ANSYS

SVS FEM

Your partner in computing

Proceedings of

22nd SVSFEM ANSYS Users' Group Meeting and Conference 2014

25th – 27th of June 2014, Jasná, Slovak Republic

Sponsors:

sgi

hp

ISBN: 978-80-905525-1-7

http://aum.svsfem.cz

Content

ANALYSIS OF TOLERANCE FIELD IMPACT ON CRADLE BEARING OF SWASH PLATE DESIGN AXIAL PISTON PUMP.

PAVOL BALCO, MICHAL MASNY
Engineering CAE, High Power Closed Circuit, Hydrostatic Division, Danfoss Power Solutions a. s., Považská Bystrica

Abstract: Swash plate design is the common used in axial piston pumps. One of the solutions for supporting of Swash-plate is Unitized Cradle bearing. This type of bearings is loaded mainly static. Tolerances of Inner and Outer race are closely associated with distribution of contact pressure and corresponding bearing life. In this paper there is shown how FEA approach could be used to analyze the issue of tolerance impact into the contact pressures, from pre-processing to post-processing.

Keywords: FEA, axial piston machine, bearing, cradle bearing, roller, swash-plate, contact pressure, tolerance field, clearance.

1 Introduction

Hydrostatic machines are commonly used in wide range of applications in mobile industry. Advantages of hydrostatic machines are impressive in many cases, but demands of the market and requests of the customers drive the manufacturers to provide better products, offering higher performance, working at higher pressures. Hydrostatic machine contains a lot of rotating parts and all this parts are supported by bearings. It means that choice of bearings is very important task.

Axial piston pumps (Image 1) are the most commonly used pumps when variable displacement is required for a machine. They possess many advantages especially in region of higher operating pressure. A demerit of piston pumps is relatively high number of moving parts.

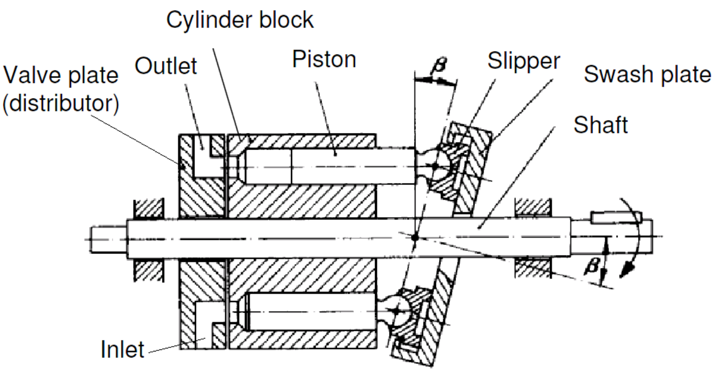

Image 1- Axial piston machine of Swash Plate design [1]

Bearings are currently used in numerous applications important in everyday life. Main goal of bearing is to reduce friction between moving parts or to support moving loads. It is known two basic types of mechanical bearings used in machinery: Sleeve bearings and Rolling bearings. Cylindrical roller bearings are the best solution for exceptionally heavier-duty applications.

Variable displacement pump require an adjustable Swash-plate. A frequently used design for support of Swash-plate in radial roller bearing is depicted in the Image 2, known as “Cradle bearing”.

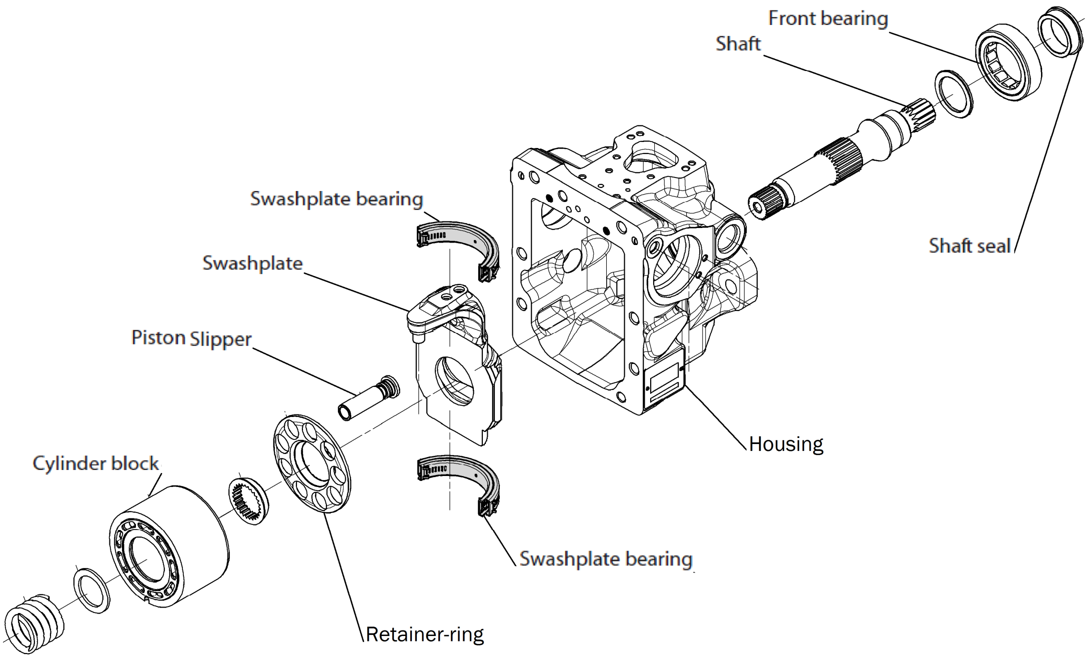

Image 1 - Partial exploded model of the Hydrostatic units Swash Plate design

2 Motivation and scope of the paper

Clearance between Housing and Swash plate has influence on the contact pressure and reaction forces distribution within the bearing – in each roller interaction. This contribution is focused on the CAE approach how this similar issue can be analyzed from FEA point of view.

3 Numerical FE simulations of bearing in an axial piston pumps

3.1 FE model

The analysis contained three modifications which reflect three positions in the tolerance field from tolerance stack up analysis point of view. Cumulative effect form the stack up analysis shows two worst cases – minimum and maximum clearances. Additionally, assembly with nominal dimensions has been also used for the FEA (Image 3).

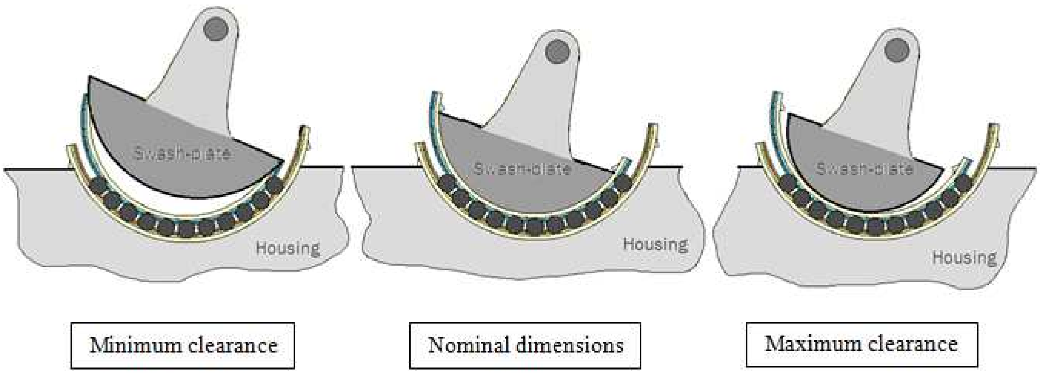

Image 3 - All three modifications from tolerance field.

Simplified geometry prepared for calculation is shown on the Image 4. Angle of the Swash plate has been tilted at maximum displacement together with Cradle bearing.

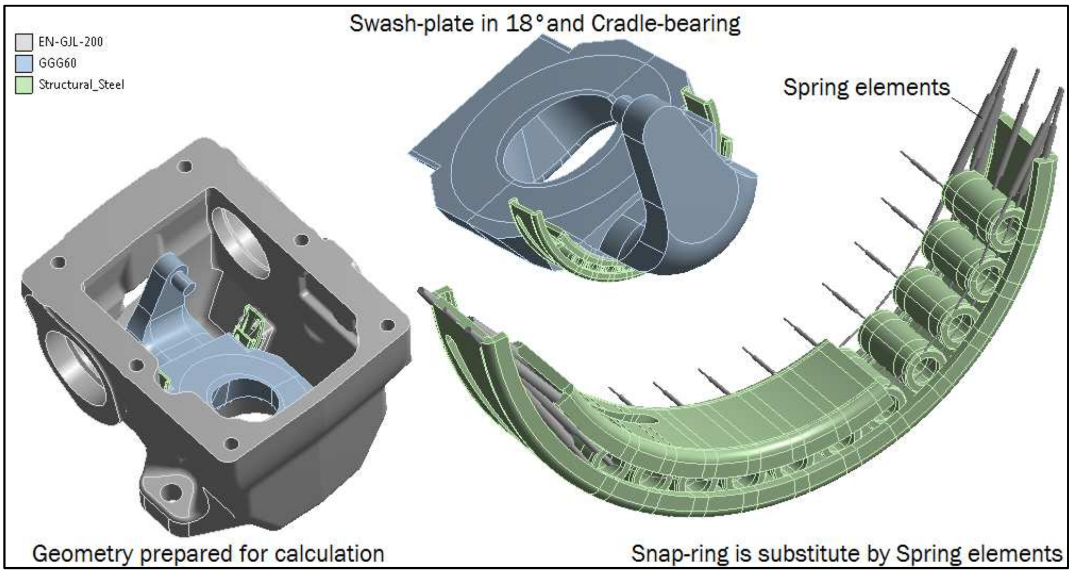

Image 4 – Simplified CAD and FE model

Bearing cage of Cradle bearing is substituted by spring elements COMBIN14. Two types of spring's elements with different stiffness has been used: 1) first type of spring elements have fixed the rollers on right position – substitution of bearing cage; 2) second type of spring elements reduced rigid body motion of the rollers and others parts. The stiffness of spring's elements is different to the previous one. The first type had 20 times higher stiffness than second one - springs has been used for stabilization of the calculation.

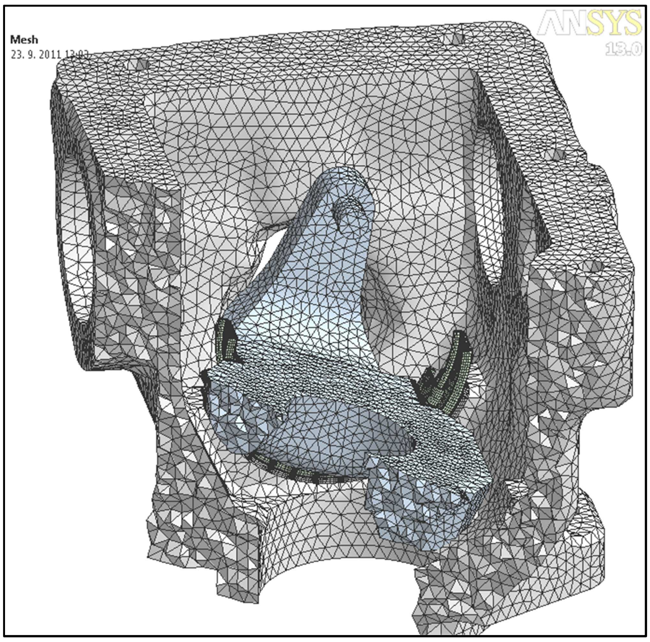

Image 5 – Cross-sectional view on the FE model

Sectional view of corresponding FE model is presented on the Image 5. In the model there is used combination of linear/quadratic solid hexagonal and tetrahedral elements.

The Inner and Outer bearing ring have been meshed by high order solid element SOLID186 to obtain hexagonal mesh. Next volumes, Housing and Swash-plate have been meshed by low order element SOLID185. Linear solid hexagonal mesh has been crated for the volumes of Swash plate under the contact region. Tetrahedral elements have been used for the rest volumes of the FE model.

The volumes of Rollers have been split due to creating quadratic solid hexagonal mesh in contact area using the element type SOLID186. The inner volumes have been removed from the rollers and this volume was replaced by “Multi-point constrains equation” with “pilot” point in the center of roller (Image 6). Behavior of surface connected with pilot point was adjusted as “Rigid”. Diameter of removed volume is calculated from Hertz’s elastic theory of contact. This practice saves a lot of number of degrees of freedom. This approach is suitable for relative comparison of contact pressures and reaction forces distribution for all three variants of the tolerance field.

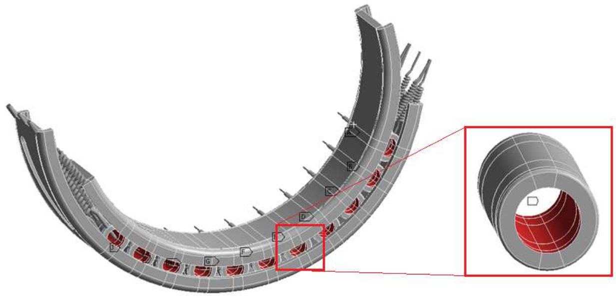

Image 6 – Simplification of rollers with rigid inner surface + pilot point

The FE model contains linear and quadratic shape function elements, therefore bonded contacts between the parts of various shape function meshes has been used. All parts which interacts each other have been defined as frictional contact.

All three clearances from the tolerance zone mentioned above have been represented by “Contact offset settings” of contact between Rollers and Inner race. The contact offset corresponds with the values from tolerance field. It means that the maximum clearance has been represented by the positive value of contact offset and vice-versa, for minimum clearance, the contact offset has been represented by the negative value.

3.2 FEM results of contact analysis

One of the major results from this analysis is outcomes related with the contact results, especially contact pressures and contact forces distribution. Results presented on the underlying elements of each roller are contact pressure and contact force distribution on the Inner bearing race. Results are presented on the picture Image 7. The results show the most loaded roller and its contact pressure. This information are very important for estimation of load bearing capability and fatigue life with respect of whole range of tolerance field.

4 Conclusion

Clearance between Housing and Swash plate has influence on the contact pressure and reaction forces distribution within the Cradle bearing. It can lead to one of the major impacts to the endurance and also on noise and vibration of whole unit. This contribution is very briefly focused on the CAE approach and method how to do the FEA on this similar issue.

Valuable outcomes from this analysis can lead the design engineers to making an decisions about tolerances of Swash-plate and Housing and also to reducing final costs and increasing endurance of the Cradle bearing and also the hydrostatic unit.

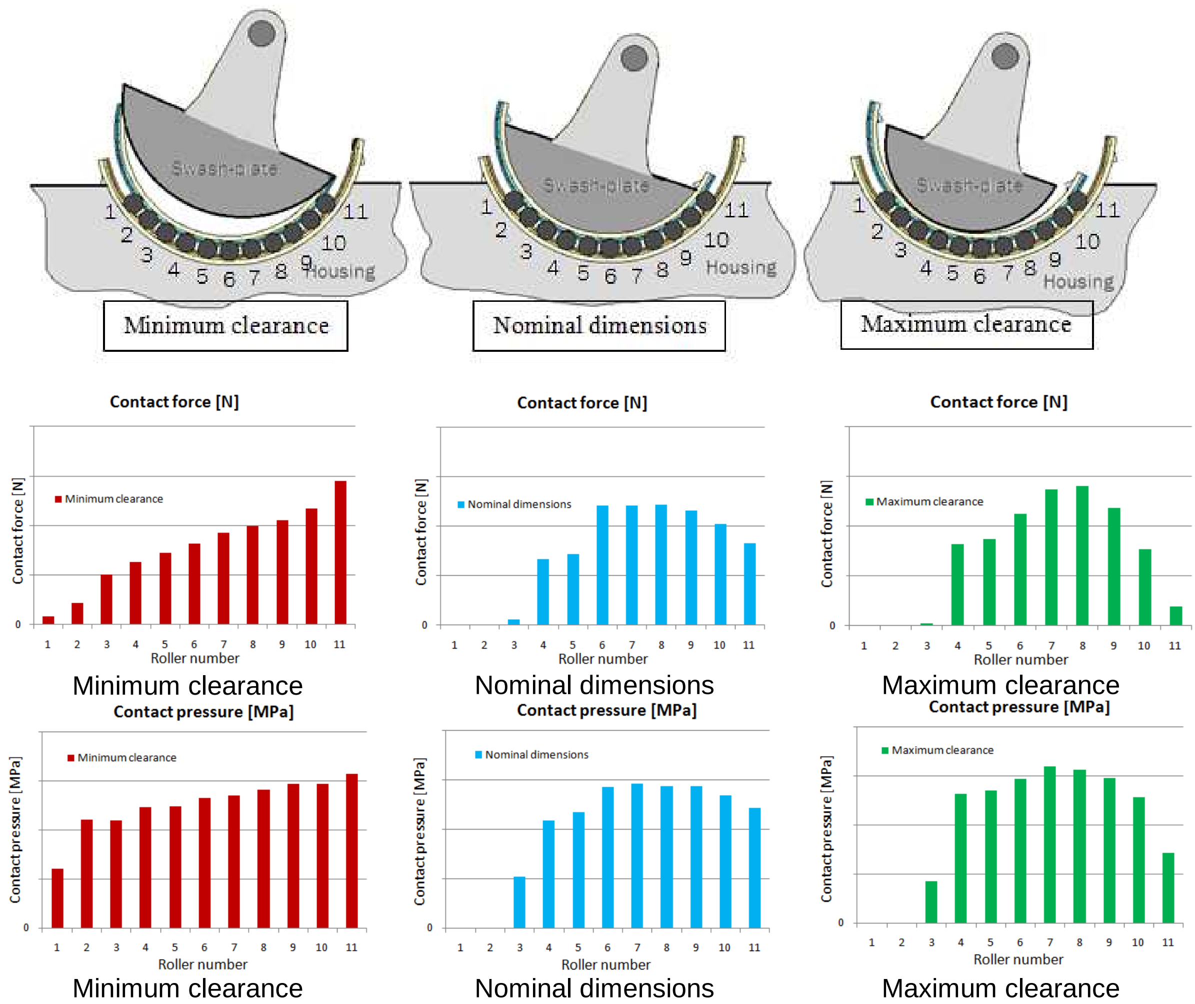

Image 7 – Contact force and Contact pressures distribution on inner race of each roller interaction

References

IVANTYSYN J., IVANTYSYNOVA M., 2001. Hydrostatic pumps and motors: principles design, performance, modeling, analysis, control and testing. New Delhi, India: ABI Overseas Limited. 512 s. ISBN 81 855 221 62

BATHE K. J., 1995. Finite Element Procedures. New Jersey: Prentice Hall, Englewood Cliffs

ANSYS Release 15, Documentation.

Contact address:

Ing. Pavol Balco
Danfoss Power Solutions a. s., Kukučínova 2148-84, Považská Bystrica, Slovakia.

APPLICATION OF THE DIFFERENT COMPUTATIONAL MATERIAL MODELS OF POLYMER MATERIAL FOR EXPLICIT SOLUTION OF FEM IN LS-DYNA

MARTIN DOBEŠ, JIŘÍ NAVRÁTIL
Development of fuel delivery modules – CAE simulations, Robert Bosch spol. s.r.o.

Abstract: This article deals with the experimental measuring of material data used for computational FEM analyses. Obtained material computational models are used in common engineering work. The focus is on the strain rate dependence of the tensile behavior of the Polymer materials. Acquired results are demonstrated on the problem of crash test of the fuel tank with fuel supply module. The applied loading is from real crash tests.

Keywords: finite element method, LS-DYNA, polymer, strain rate dependence, fuel supply module

1 Introduction

Fuel supply module, which consists of fuel pump, filter system, rail of the fuel, regulation system and flange belongs between main components of the fuel system of the car. The majority of all parts is made from Polymer materials. The materials based on TSCP (typical semi-crystal polymer) are the most common ones in this automotive branch. The development approach based on FEM calculations is commonly used in present time. This approach offers financial and time saving during development process; the number of tests can be reduced, due to virtual testing based on simulations.

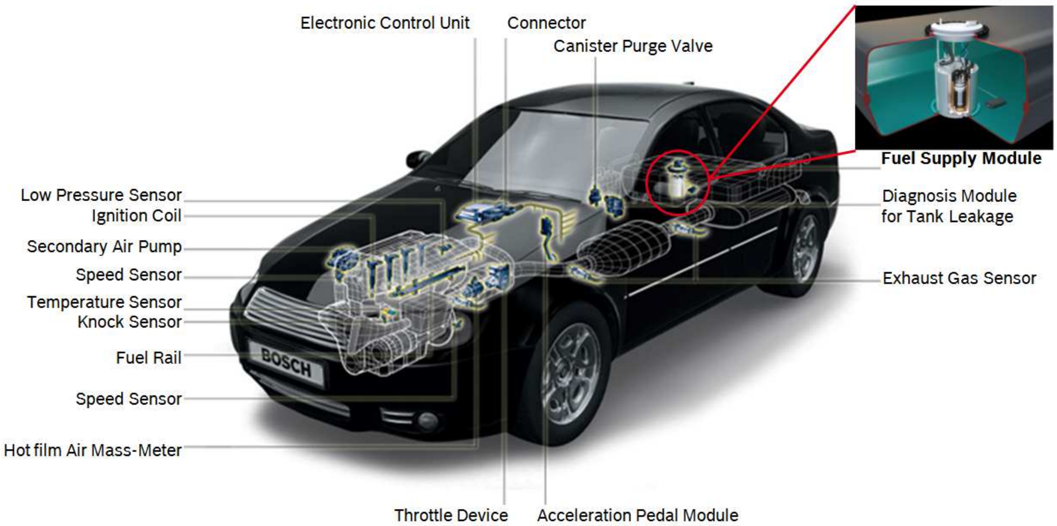

Image 2 – Position of the fuel supply module in the car

The basic precondition for correct FEM analyses are correct input material data. This paper deals with obtaining suitable material data with strain rate dependency and their using in different cracking models in software LS-DYNA. These data are later used in simulations of parts from polymer materials (TSCP) loaded by impact signal. It is demonstrated in chapter 5 where the response of the fuel supply module in the fuel tank from crash car loading is shown.

2 Experimental measurements – model of material *MAT_24

This type of material model is in LS-DYNA material library as MAT_24. This material model was made in collaboration with company 4A engineering GmbH. The aim was to specify material model, which is tuned directly for software LS-DYNA. There were made many experimental measurings for correct fitting of this computational model on the experimental results. The main tests were static, quazi-static, dynamic 3-points bending test, 4A Impetus Impact test, 3-points bending test with fixing and static tensile test. All of these tests were simulated by using FEM. A lot of trials was made to get good fitting of material models. The fitting is based on minimalization of deviation between force-displacement relationship obtained from experiment and simulation. The material model was created for a concrete type and size of finite element. This choice should be respected in future using of this material model in simulations.

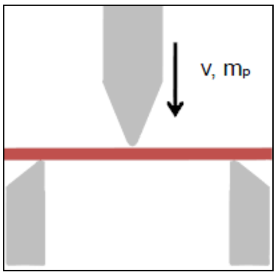

3 points bending test

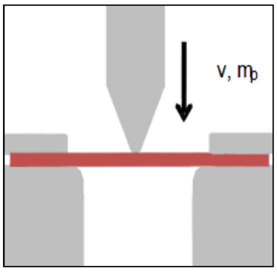

3 points bending test with fixing

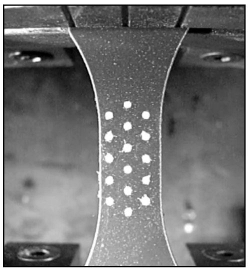

Tensile test

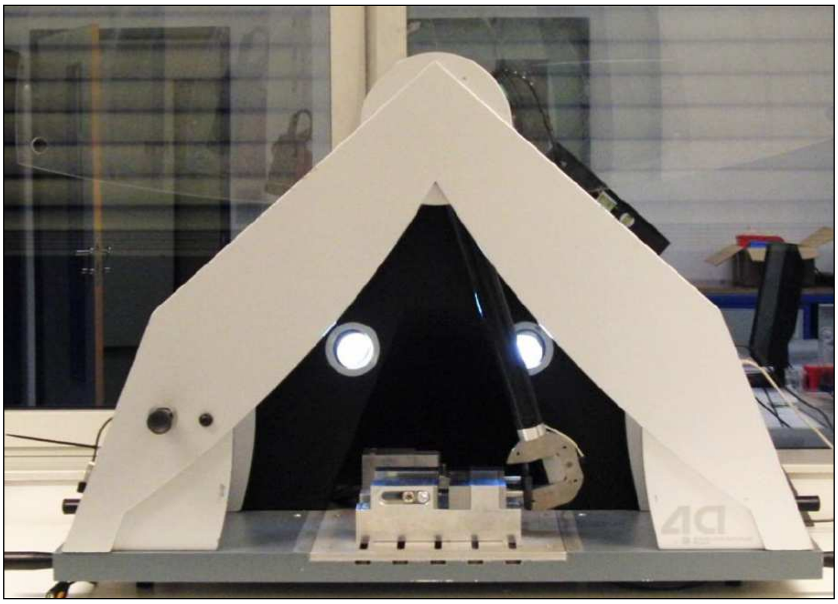

4a Impetus test machine; test velocity: 5m/s, swing hammer mass: 438g

Image 2 – Necessary testing methods

2.1 Results of the experiments

For example the fitting process of the computational material model for strain rate $\dot{\varepsilon}^{*}=0.01\text{-}100s^{-1}$ will be introduced. The experimental curves (Image.3) correspond to 3 point bending test for different velocity of the testing machine. It can be seen fitted curves for defined test area of the strain range of the real tests on the following graph. The results from 4A Impetus Impact hammer were used for higher strain rates $\dot{\varepsilon}^{*}=1000\text{-}10000s^{-1}$. The evaluation of the loading force and displacement is made by using simply mathematics relations:

The force we obtain from known mass of the weight and from measured acceleration on the forehead of the weight

$$F = m_{Pendular} \cdot a_{Pendular} \tag{1}$$

Conversion of the angle to length is made by using relation (2); pendulum

$$s_i = s_{i-1} + \frac{\Delta\alpha \cdot \pi \cdot l_{Pendular}}{180} \tag{2}$$

The impact velocity will be calculated on the base of relation (3);

$$v_0 = \frac{\Delta s_{1-2Peak}}{\Delta t_{1-2Peak}} \tag{3}$$

It can be obtained material model in true stress/strain formulation in such a way. This material reflects dependence on the loading velocity. Resulting material model is used in the practical part of this paper where the fuel supply module is loaded by impact generated within car crash.

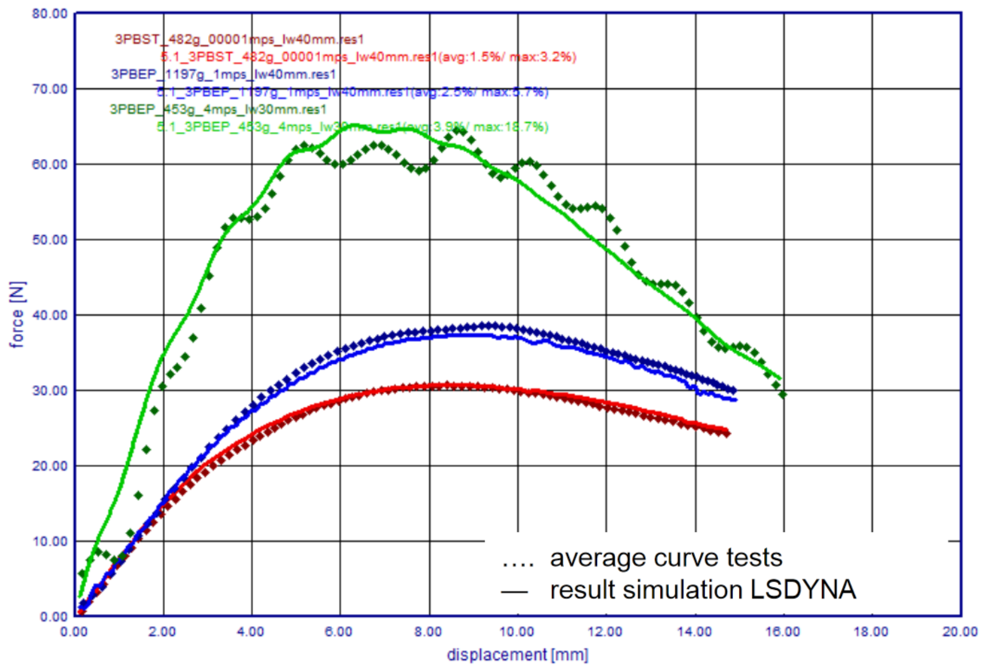

Image 3 - Experimental and simulation data from 3 points bending test

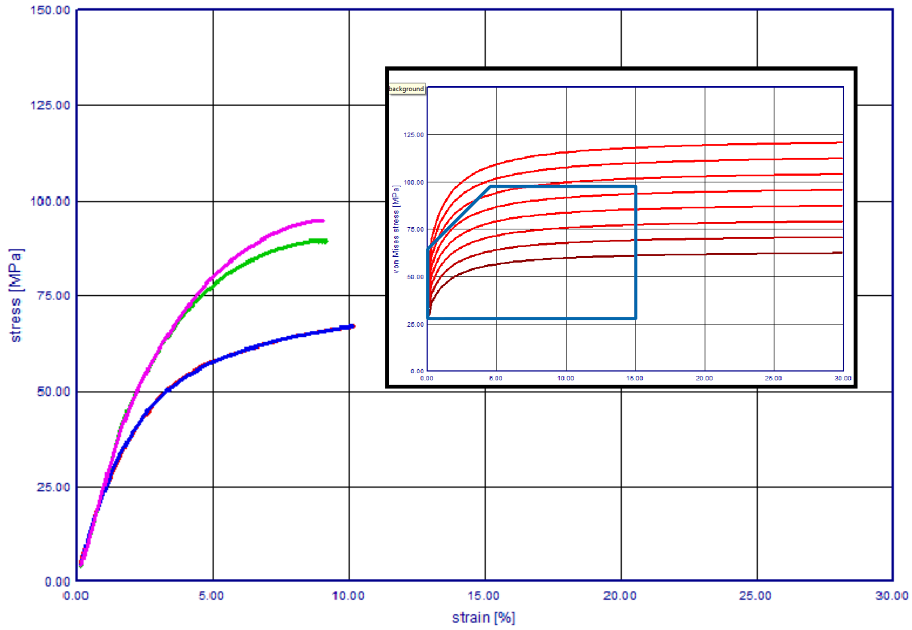

Image 4 - Obtained tensile curves from validated experimental data (blue box)

3 Basic computational models of the material damage in LS-DYNA with focus on the polymer materials

Usually FEM software proposes more possibilities of material damage. In the case of the LS-DYNA it can be used for example simple erosion of elements based on particular material criteria like strain, stress or time. It is dealt with some types of the damage models like *MAT_ADD_EROSION, *MAT_123, *MAT_187 (SAMP-1). Selecting models are evaluated on the standard tensile specimens for plastics (cross area 2x10mm).

3.1 *MAT_ADD_EROSION

There are many constitutive models of materials in LS-DYNA, which have not failure or erosion of elements. The option *MAT_ADD_EROSION provides failure models for these material models. It can be used a lot of failure criteria and these criteria can be independent or dependent. These requirement criteria can be set up by option NCS. Next important option is number of integration points (NUMFIP), where if the “failing condition” is fullfiled (e.g. strain limit) the element is deleted (eroded) from calculation. This option has significant effect on the crack propagation in the calculation model. This option is very sensitive on the size of the mesh. This material model provides some type of the damage model - GISSMO and other options of damage function. It is shown further sensitivity of the NCS, combination of the criteria on the failure and stress, strain evaluation in simulation of the tensile test (validation experiment).

Widely spread criteria in Polymer materials are stress and strain limit value. It can be chosen from many options of strain and stress. The usable stress criteria are value of Maximum principal stress at failure (SIGP1), Maximum pressure at failure (MXPRES), Equivalent stress at failure (SIGVM) and other. These criteria are very common. The strain criteria are suitable for very ductile materials, as non filled polymers. They can be selected from many possibilities like the most used Maximum principal strain at failure (MXEPS), Maximum effective strain at failure (EFFEPS), and Volume strain at failure (VOLEPS). It is considered usually tensile failure, so the criteria based on tensile characteristic of failure are chosen. Some criteria are defined as follows.

Maximum effective strain at failure (EFFEPS) is defined by

$$\varepsilon_{eff} = \sqrt{2/3\varepsilon_{ij}^{dev}\varepsilon_{ij}^{dev}} \tag{4}$$

and Volumetric strain at failure (VOLEPS) as

$$\varepsilon_{vol} = \varepsilon_{11} + \varepsilon_{22} + \varepsilon_{33} \tag{5}$$

This type of the strain can be a positive or negative number; this effect considers failure in tension or compression respectively. It can be considered damage model GISSMO in material model *MAT_24. The GISSMO damage model is a phenomenological formulation that allows for an incremental description of damage accumulation. The input data are directly from the experiments in table form. The model is based on an incremental formulation of damage accumulation:

$$\Delta D = \frac{DMGEXP \times D^{\left(1-\frac{1}{DMGEXP}\right)}}{\varepsilon_f}\Delta\varepsilon_p \tag{6}$$

D ..Damage value (from 0 to 1)

ε_f ..Equivalent plastic strain, as function triaxility value η

$\Delta\varepsilon_p$ ..Equivalent plastic strain increment

This type of the model is suitable mainly for metalic materials; so it is not used for Polymer materials.

3.2 *MAT_MODIFIED_PIECEWISE_LINEAR_PLASTICITY_RTCL

LS-DYNA material library contains *MAT_123. This elastic-plastic material is defined by stress-strain curve(s) and can use strain rate dependence. This material model is very similar to material model *MAT_24, but it implements more sophisticate model of the failure. For objectives of this paper option RTCL for failure is used. The option RTCL is damage function, which is defined by

$$\Delta f_{damage} = \frac{1}{\varepsilon_0} f\left(\frac{\sigma_H}{\bar{\sigma}}\right)_{RTCL} d\,\bar{\varepsilon}^p \tag{7}$$

where

ε_0 ..unaxial fracture strain / critical damage value

σ_H ..hydrostatic stress

$\bar{\sigma}$ ..effective stress

$d\varepsilon^p$ ..effective plastic strain increment

The elements are deleted from calculation, if function damage is higher than 1.0. This algorithm is used during calculation, if the plastic strain increment is greater than zero. The inside function of the stress distribution is divided by following:

$$f\left(\frac{\sigma_H}{\bar{\sigma}}\right)_{RTCL} = \begin{cases} 0 & \text{for } \dfrac{\sigma_H}{\bar{\sigma}} \le -\dfrac{1}{3} \\ 2\dfrac{1+\dfrac{\sigma_H}{\bar{\sigma}}\sqrt{12-27\left(\dfrac{\sigma_H}{\bar{\sigma}}\right)^2}}{3\dfrac{\sigma_H}{\bar{\sigma}}+\sqrt{12-27\left(\dfrac{\sigma_H}{\bar{\sigma}}\right)^2}} & -\dfrac{1}{3} \le \dfrac{\sigma_H}{\bar{\sigma}} \le -\dfrac{1}{3} \\ \dfrac{1}{1.65}\exp\left(\dfrac{3\sigma_H}{2\bar{\sigma}}\right) & \dfrac{\sigma_H}{\bar{\sigma}} \ge \dfrac{1}{3} \end{cases} \qquad (8)$$

In case option (_RATE) is used failure limits with strain rate dependency can be used.

4 Verification of the material models with experimental data – tensile tests

Tensile test up to damage was used for verification of computational material models. There were used different types of obtained tensile curves in analysis. These curves were compared with experimental data for loading velocity v_L=*1000mm/s* (velocity of the fixing plate). This high loading velocity has big effect on the values of stress and ductility of the TSCP material. Generally, it can be said, that the material has higher tension, but material became less ductile (Image 6.1). It was tested material model with static tensile curve from producer in engineering stress-strain values (A), static tensile curve in true stress-strain values (B), experimental curves from measurement of company 4A engineering (C), article 2, (Image 6.2). Different computational models of the damage on some material models were compared. The relationship of force and displacement was used for comparison and validation of the computational material models.

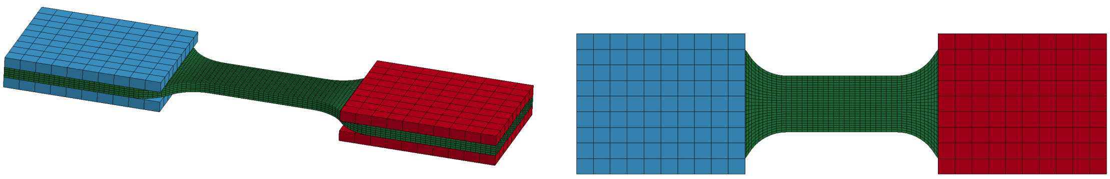

Image 5 – Geometry of tensile specimen for LS-DYNA specimen

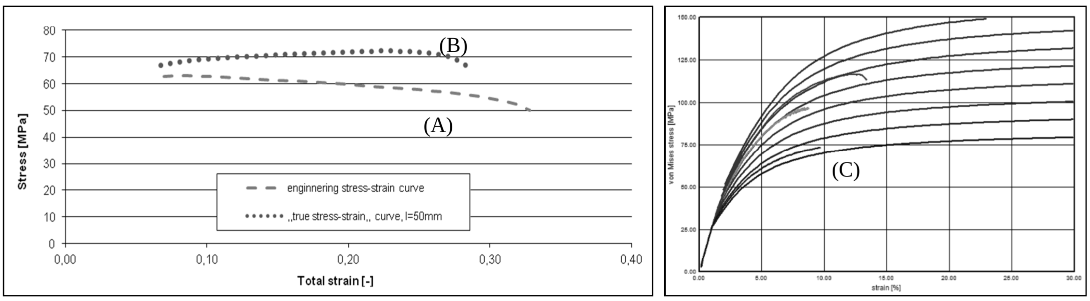

Image 6 – Example of the considered variants of tensile curves
(6.1. Plastic part of tensile curves, 6.2. Strain rate dependency)

It can be seen, that difference is significant between material models. The most conservative approach is using of the material (A). Better solution gives material model (B). The best computational model from these available is (C) material model – with strain rate dependence. There were further applied different computational models of the damage. The most simple is *MAT_24 with material erosion (*MAT_ADD_EROSION), in this case used with criteria Maximum principal stress *(S1max=100 MPa)*. The element becomes deleted if this criterium is fullfiled. The approach with using *MAT_123 – RTCL appears more correct. This material model is described in article 3.2. This model considers the type of the stress in the critical area. This material computational model is one of the most precise ones from simple group of computational models of damage in LS-DYNA for polymer materials.

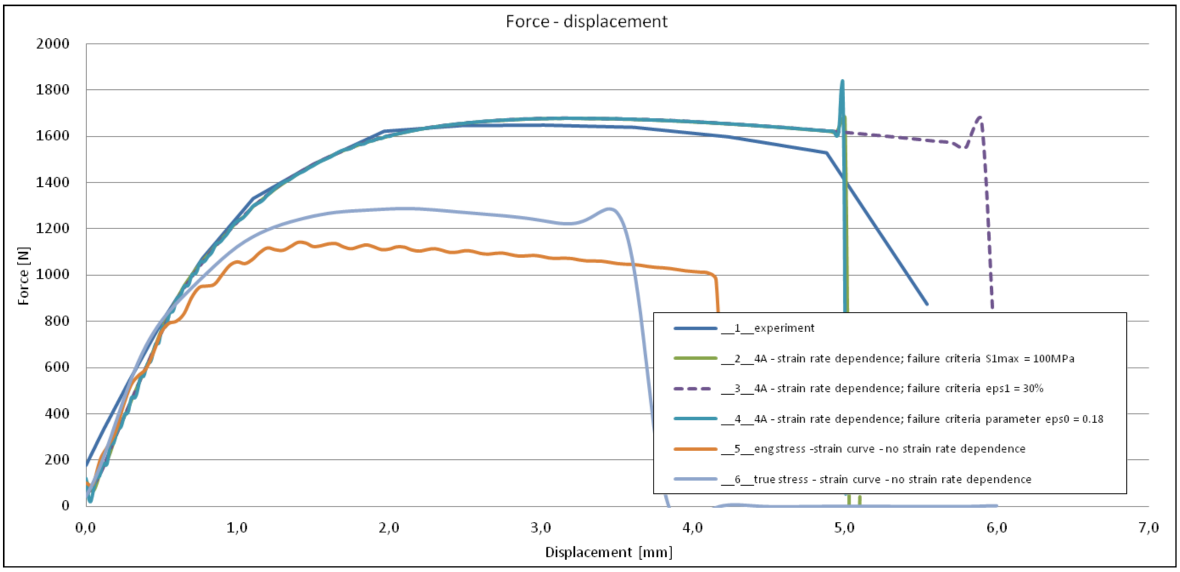

Legend:

__1__ experimental measurement, loading velocity *1000mm/s* (strain rate $\varepsilon^{s}=50s^{-1}$)

__2__ material model created for LS-DYNA solver for *MAT_24 with strain rate dependence, as failure limit was used Maximum principal stress (*S1max=100MPa*)

__3__ material model created for LS-DYNA solver for *MAT_24 with strain rate dependence, as failure limit was used Maximum principal strain (*eps1=30%)*

__4__ material model created for LS-DYNA solver for *MAT_24 with strain rate dependence, as failure limit was RTCL parameter (*eps0=0.18*)

__5__ material model obtained from material producer in engineering data, without strain rate dependence

__6__ material model obtained from material producer, but recalculated to true stress –strain values without strain rate dependence

Image 7 – Results of the simulations of the tensile test for loading velocity $v_L = 1000mm/s$

Image 7 shows, that curves 5 and 6 do not correspond with experiment data. The character of these curves is very different. This effect is caused by independence of the stress on the loading velocity. In this case the material model does not harden. The best solutions are variant 2,4, where the displacement in the time of the failure corresponds with failure time from experiment. The variant 3 with failure criteria Maximum principal strain 30% is based on strain limit from data sheet (ductility in %). This criterion is too simplified. For impact and fast loading generally, where the dependence of the stress and strain on loading velocity is very important material data with strain rate dependence should be used. There is a lot of more correct material models for polymers in LS DYNA but before mentioned variants are quite simple and they does not need any special testing for good description of material behaviour.

5 Practical problems – using of the material model with damage

Fuel supply module must ensure safety during all situations of real traffic. The module is designed for usage in ordinary traffic, but it must guarantee fuel system tightness in unexpected situations like accidents too. Reliability is described by two requirements:

- Low velocity crash – module must survive without damage
- High velocity crash – module is out of service, but tank tightness must be kept.

Crash conditions are mostly based on customer demands. Data from real crash test (tank kinematics) are the best input for explicit simulation. Front and side crash is tested according to Euro NCAP. Simulations are performed in driving direction and in seven other directions with angle step of 45°. This loading should cover almost all possible impact directions.

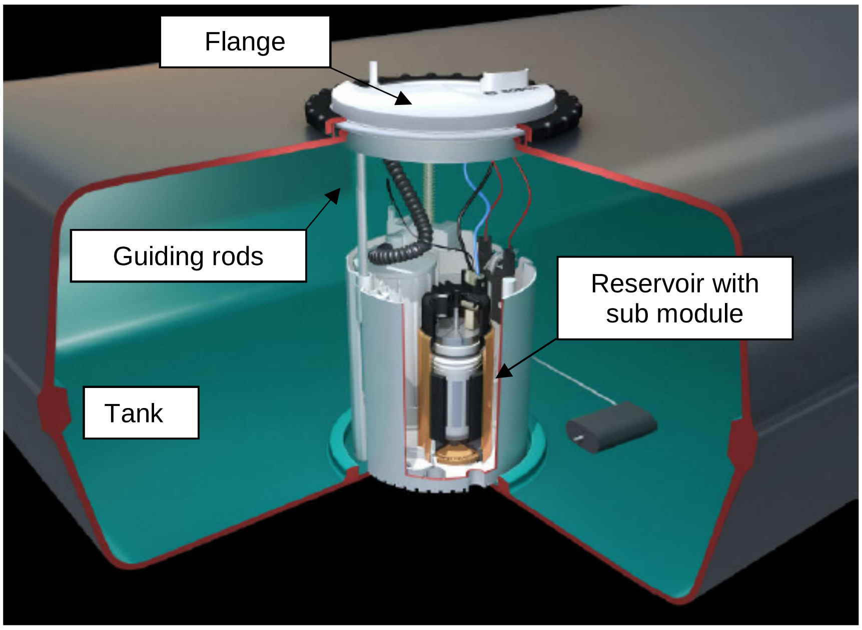

Image 8 – Fuel supply module scheme

5.1 Underside impact, steel guiding rods

Underside impact is simplified substitution of real crash. Guiding rods are bended by rigid tool till flange damage. Damage area must occur on rod bosses, but not on the bottom of the flange. This test is a verification of the design quality from cracking zone point of view on the guiding rod bosses. The cracking continues over the body of the guiding rod bosses in the case of proper design. The flange must be 100% tight after this test. This test is the worst case loading on the cracking zones; The impact loading on plastic component is used in this case. The other possible test is impact test with acceleration signal, for example a_i=800G per t=1.5ms. The geometrical shape of this signal is approximately triangle. The area under this curve is kinetic energy, which the flange can absorb during this impact loading. Real crash test with car can have acceleration signal with time duration about t=60-80ms and amplitude about a_r=50-80G. It means previous underside impact test serves mainly for verification of the design of the cracking zones.

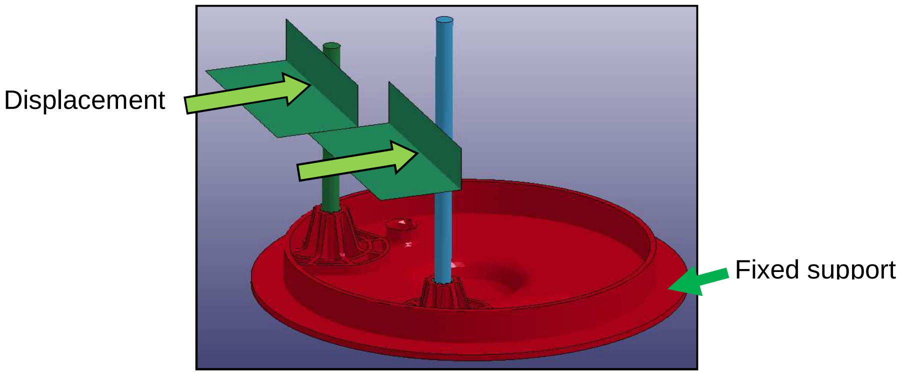

Image 9 – Boundary conditions

Correct behavior during underside impact is shown in (Image 10). Crack initialization occurs on boss ribs curvature. It can be assumed crack propagation through rod boss only. Flange leakage should not occur.

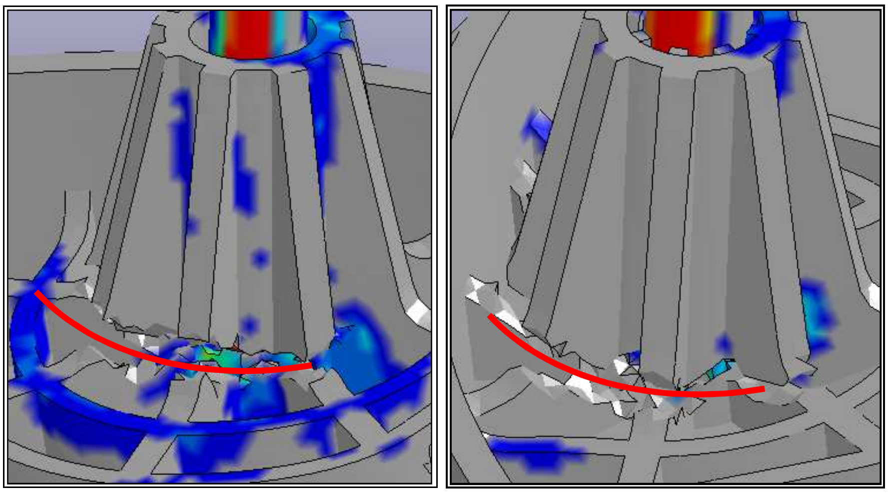

Image 10 – Rod housing damage

5.2 Underside impact, plastic guiding rods

Simulation of underside impact where influence of flange - tank connection is taken into account is carried out.

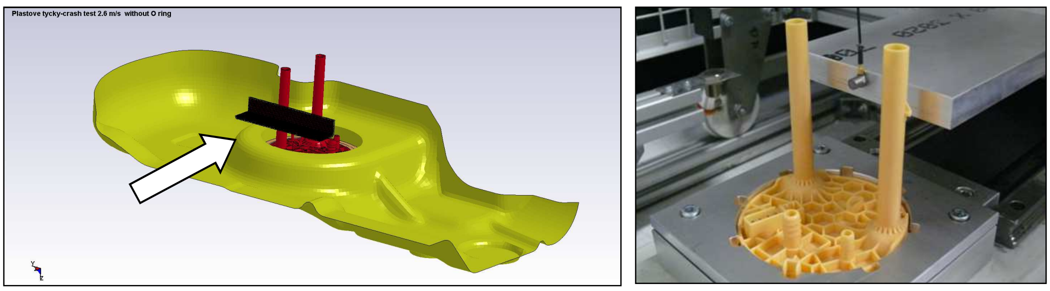

Image 11 – Impact test for concept with plastic guiding rods

The left image 12 depicts the computational model after impact moment, the failure limit Maximum principal stress *S1max=100MPa* is considered in this simulation. The cracking zones correspond with cracking zones in real experiment, right image 12. The failure has brittle character and used type of the failure limit in simulation considers this brittle behavior.

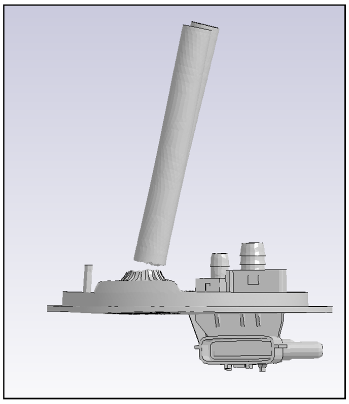


Image 12 – The results of the failure from simulation and test

6 Conclusion

This paper shows some approaches of the modeling of the failure in explicit simulation by LS-DYNA. The computational models were tested for polymer materials TSCP. It can be implemented a lot of many computational models of the failure, but sophisticated models are very demanding on the input experimental data. Basic computational models of the failure (*MAT_ADD_EROSION, *MAT_123-RTCL) were used for calculation. These basic types are suitable for polymer materials, but correct type of the failure limit must be selected. Proper values of these limit for material TSCP were found. These computational models were verified by tensile test and on the real problems in engineering practice. Experiments and explicit simulations of these experiments correspond mutually and cracking zones are in the same areas of the design. The subject of following work will be computational model SAMP-1, which was added to material library before several years. This type of the model is necessary to check and validate for concrete types of the polymer materials. It is quite hard to fit this material model on the experimental data. A lot of experiments like tensile tests for several levels of the strain rates, compression test, shear test and other should be carried out.

References

HOLZAPFEL, Gerhard A. Nonlinear Solid Mechanics: A continuum Approach for Engineering. John Wiley, 2000, ISBN 04-718-2319-8.

HUBERTH, F., HIERMAIER, S., NEUMANN, M. Material Models for Polymers under Crash Loads – Existing LS-DYNA Models and Perspective, *Proceedings of the 4th Ls-DYNA Forum*, Bamberg, Germany, ISBN 3-9809901-1-7, H-I-1-12, 2005

Finite-element analysis of quasi-static characterization tests in thermoplastic materials: Experimental and numerical analysis results correlation with ANSYS, 25 October 2006, number 26, pages 284-305.,www.sciencedirect.com

Material characteristics of the TSCP, http://www.basf.com/group/corporate/en/

Contact address:
Ing. Martin Dobeš**,** Development of fuel delivery modules – CAE simulations, Robert Bosch spol. s.r.o., Roberta Bosche 2678, 370 04 České Budějovice

Ing. Jiří Navrátil**,** Development of fuel delivery modules – CAE simulations, Robert Bosch spol. s.r.o., Roberta Bosche 2678, 370 04 České Budějovice

COMPARISON OF CALCULATION OF PARAMETERS IN FRACTURE MECHANICS

DUŠAN DROBNÝ, OĽGA IVÁNKOVÁ

STU in Bratislava, Faculty of Civil Engineering, Department of Structural Mechanics

Abstract: The main purpose of this paper is an analysis of fracture parameters on 3-point loaded beam with a crack. The aim is to compare the computational procedures and results of calculating by variety of loads and crack geometry according to depth of the sample examined. Three computational procedures are used. ANSYS and Mathcad were used for getting finally presented fracture parameters.

Keywords: Fracture mechanics, Stress intensity factor, J-integral, Crack driving force, crack tip

1 Introduction

The main aim of designers and technicians after some accidents is to analyse its causes. As a result od an investigation, it was found that most of the disorders were caused by cracks. Cracks can appear either directly in the materials as like material defects, or by improper design or execution, retention, bad use, or maintenance of the weather. The materials contain microscopic cracks but just one crack steeply developing may cause the destruction of the whole structure.

To investigate the relationships between the stress, crack and crack toughness is the branch of Fracture Mechanics. The first pioneer was A. A. Griffith who established the relationship between the stress and the crack size 1920. This approach, however, was only suitable for fragile materials. In the 1950´s G. R. Irwin developed for towing materials an energetic concept, which defined the parameter *G* (crack driving force) as a change of the potential energy in the vicinity of the cracks root for linearly elastic materials. If the value of *G* reaches G_c (critical value), the crack is growing. Using a similar approach, another parameter *K* – crack paramaeter (the coefficient of the stress intensity). In the sixties of the nineteenth century, scientists focused their study to plastic deformation in the vicinity of the cracks root. In 1968, J. R. Rice created an processing model of non-linear material behaviour in the vicinity of the cracks root and defined an independent integral, *J-integral*, on the basis of energy access. In between, A. Wells defined the *CTOD* parameter (the opening of the crack root). These are the parameters that have led the EPFM research (Elasticko-Plastic Fracture Mechanics).

At present, the issue of fracture mechanics is not closed. Extensive research being developed on the definition of the fracture parameters due to dynamic loads [1]. It si proven that for towing material there is not enough to know only one fracture parameter for the developing and spreading the cracks. On this basis, the *T-strain* as the second parameter theory of for solution of tasks in fracture mechanics, was developed [2].

2 Modeling of Solids Having Cracks

For this purpose some loaded beams supported in three points having a crack were modelled in ANSYS using the 2-D model, when selecting 2-D PLANE 183 elements. These elements allow to model the singularity around the crack root, and obey the calculation the fracture parameters directly in ANSYS. They may be 8- or 6-pointed, while enabling a quarter of shift in middle points of the edges.

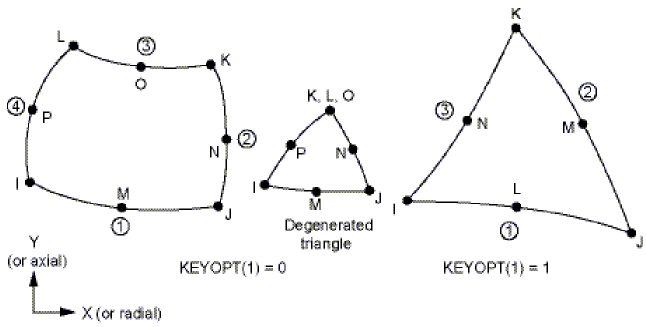

Fig. 1 Element PLANE 183

2.1 Characteristics of Models

We have chosen the steel as the material of the beam as a typical isotropic material having the modulus of elasticity of 210GPa and Poisson's number of 0.3. The model was discreted by triangular PLANE 183 elements (Fig. 1). The length of the edges of the finite element in the root of the cracks was 1 mm. The beam was divided into 9186 2-D elements having completely 18677 points.

3 Calculus

Values of the K (coefficient of stress intensity) were calculated and compared. The model was loaded by forces *F* = 50N, *F* =100N, *F* = 150N, *F* = 200N, respectively. The calculations were carried out for α from 0.2 to 0.8, where α is the ratio between the depth of the beam W and the length of the crack a. Values of K were calculated in three ways:

- using the calculation according to the Catalogue of the fracture characteristics [3]
- using an extrapolating method built in ANSYS
- using the method of *J-integral* built in ANSYS

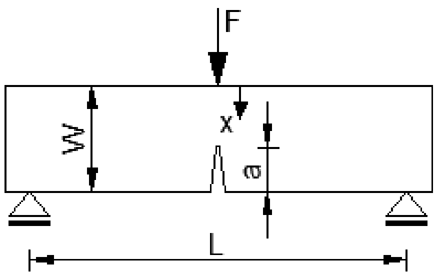

Fig. 2 Model of 3-point loaded beam having a crack

3.1 Calculation by the Catalogue [3]

Opening of cracks are caused particularly by stress in y direction. The value of the stress along the crack edge was calculated according to (2).

$$\alpha = a/W \tag{1}$$

$$\sigma_y = \frac{3.F.L}{2.W^2} \tag{2}$$

A singularity in the forehead of the crack was taken into account using a shape function F_p given in (3).

$$F_p(\alpha) = 1.090 - 1.735\alpha + 8.2\alpha^2 - 14.18\alpha^3 + 14.57\alpha^4 \tag{3}$$

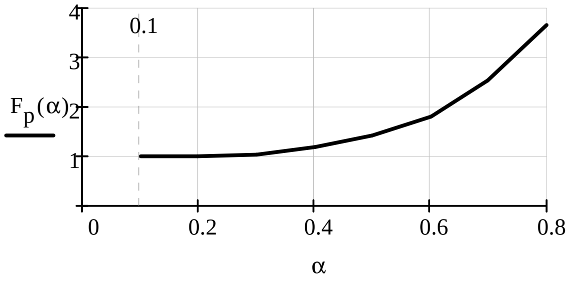

Diagram 1 Function $F_p(\alpha)$

The coefficient of the stress intensity may be calculated by (4).

$$K(\alpha) = \sigma_y.\sqrt{\pi.a(\alpha)}.F_p \tag{4}$$

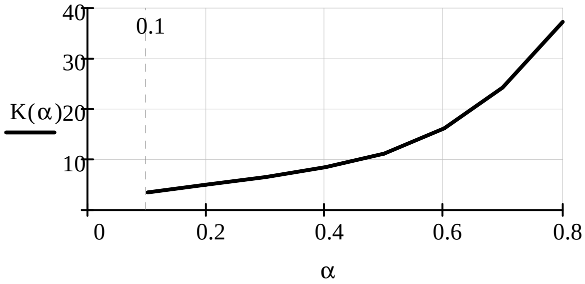

Diagram 2 The *K(α)* function

Then we know, using an equation valid for a linearly elastic material, determine the value of the motive power of the cracks (*G*), where *E* is the modulus of elasticity, referred in (5).

$$G(\alpha) = \frac{K(\alpha)^2}{E} \tag{5}$$

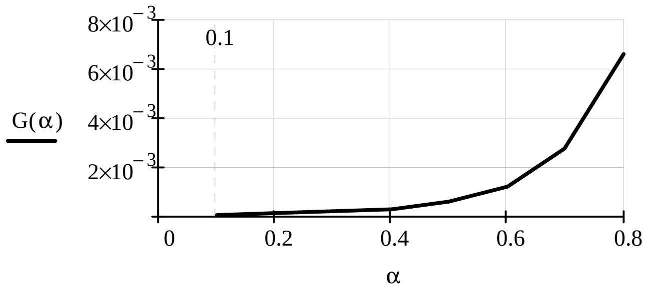

Diagram 3 The function $G(\alpha)$

3.2 Calculation using ANSYS

3.2.1 Extrapolating Method

The coefficient of stress intensity was calculated using the extrapolating method given in (6) a (7), when modus I and II were taken into account:

$$K_I \begin{Bmatrix} \cos\theta(\kappa - \cos\theta) \\ \sin\theta(\kappa - \cos\theta) \end{Bmatrix} = 2\mu\sqrt{\frac{2\pi}{r}} \begin{Bmatrix} u^I \\ v^I \end{Bmatrix} \tag{6}$$

$$K_{II} \begin{Bmatrix} \sin\frac{\theta}{2}(2 + \kappa - \cos\theta) \\ \cos\frac{\theta}{2}(2 - \kappa - \cos\theta) \end{Bmatrix} = 2\mu\sqrt{\frac{2\pi}{r}} \begin{Bmatrix} u^{II} \\ v^{II} \end{Bmatrix} \tag{7}$$

where $$\mu = \frac{E}{2+(1+\nu)} \tag{8}$$

When the planar stress state occurs

$$\kappa = \frac{E}{3(1-2\nu)} \tag{9}$$

E – the modulus of elasticity of material

ν - the Poisson's number

When the planar strain state occurs: $\kappa = 3-4\nu$ (10)

The resulting value of the coefficient of stress intensity we may obtain by (11).

$$K = K_I + K_{II} \tag{11}$$

This is an extrapolating method through the displacements. Its advantage comparing with a stress method is, that values of displacements are not influenced by singularities in the edge of the crack so significantly like stress values.

3.2.2 The J-integral Method

Using the ANSYS the *J-integral* values were calculated as well. By LEFM (Linear Elastic Fracture Mechanics) we may suppose:

$$J = G \tag{12}$$

Substituting the (12) to (5) and expressing *K* we may get (13).

$$K = \sqrt{EJ} \tag{13}$$

The *J-integral* is defined like an independent integral by the curve (14).

$$J = \int_{\Gamma} W.d_y - \int_{\Gamma} (t_x \frac{\partial u_x}{\partial x} + t_y \frac{\partial u_y}{\partial y}) ds \tag{14}$$

W – the density of the energy

t_x, t_y – vectors along *x, y* directions

$$t_x = \sigma_x n_x + \sigma_{xy} n_y \tag{15}$$

$$t_y = \sigma_y n_y + \sigma_{yx} n_y \tag{16}$$

σ_x, σ_y – stress components in *x, y* directions

n_x, n_y – components of a unit vector of the normal line to the integrating line Γ

u_x, u_y – components of displacements

s – length of the integrating line

In Fig. 4 the stress components in x direction are plotted. Some emergency of plastic zones in the point of the crack root can be observed. This stress in finite element method consists of a singularity, going to infinity. The progress of stress σ_x around the crack root is plotted in Fig. 5. The progress of stress components σ_x and σ_y going from the top of the crack to the loaded edge of the sample is plotted in diagrams 4 and 5.

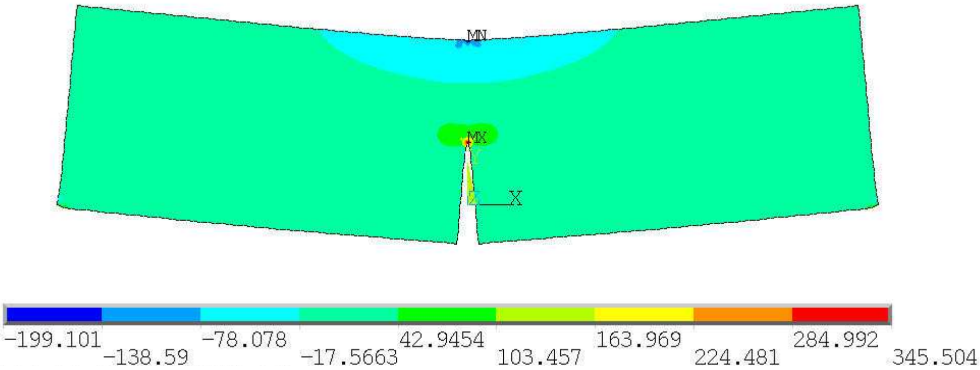

Fig. 4 Model of 3-pointed beam having a crack, stress σ_x

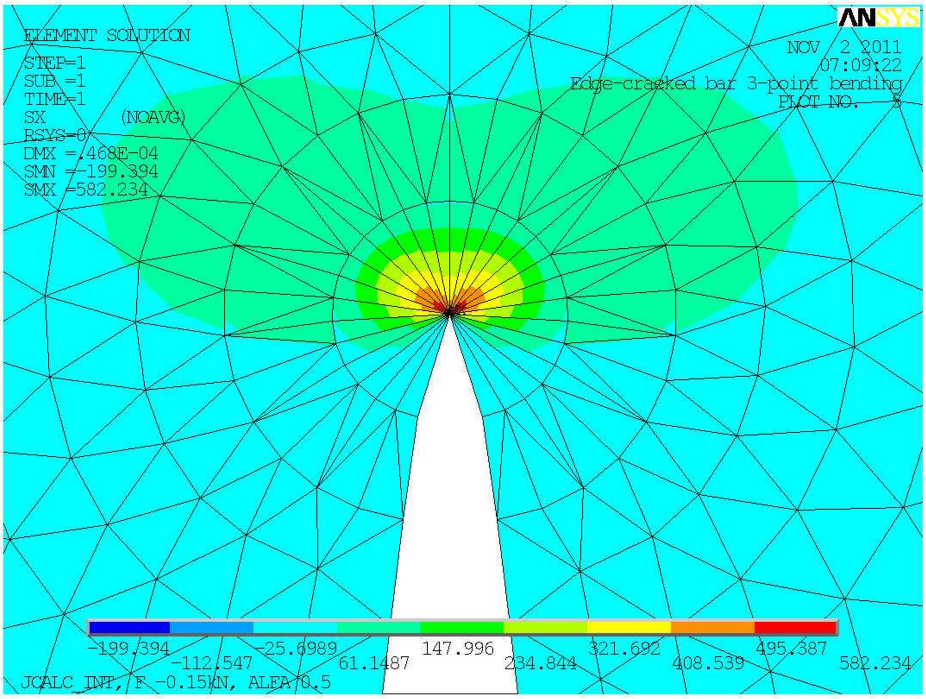

Fig. 5 Model of 3-pointed beam having a crack, detail in a crack root

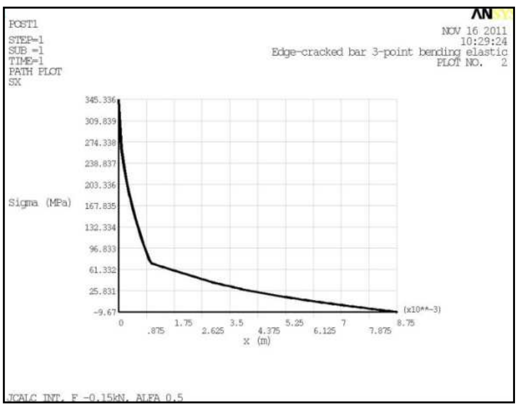

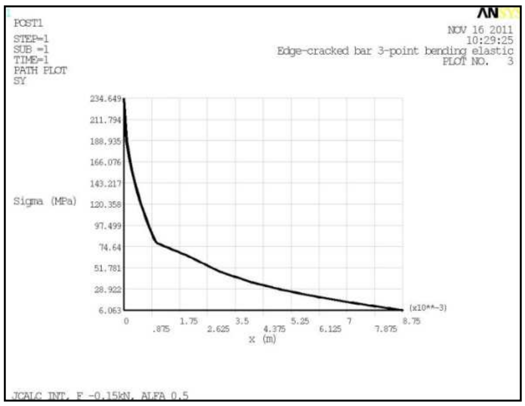

Diagram 4 Stress σ_x Diagram 5 Stress σ_y

4 Analysis of Results

The results of different methods and input values of the calculation.

Tab. 1 Values *K* by *F*=50N

α=a/R	K			Ansys method of the J-integral
	By[3]	Ansys extr. method $K=K_I+K_{II}$	K=√J.E	
0.2	1.247	1.2275	1.2423	7.35E-06
0.3	1.623	1.6294	1.6185	1.25E-05
0.4	2.109	2.1685	2.1074	2.11E-05
0.5	2.835	2.9925	2.8264	3.80E-05
0.6	4.021	4.4223	4.0076	7.65E-05
0.7	6.012	7.3687	6.2449	1.86E-04
0.8	9.299	15.4680	11.6020	6.41E-04

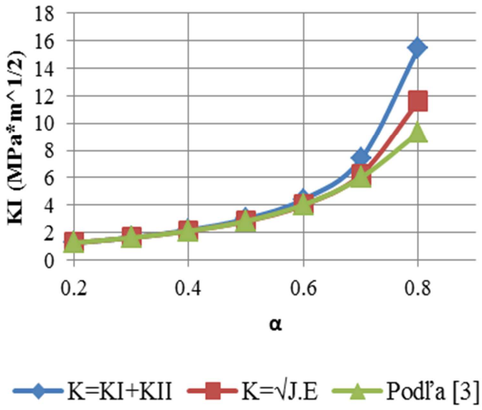

Diagram 6 Comparison of *K* values by by *F* = 50N

Tab. 2 Values *K* by *F=100N*

α=a/R	K			Ansys method of the J integral
	By [3]	Ansys extr. method $K=K_I+K_{II}$	K=√J.E	
0.2	2.494	2.4551	2.4846	2.94E-05
0.3	3.246	3.2587	3.2369	4.99E-05
0.4	4.219	4.3369	4.2148	8.46E-05
0.5	5.670	5.9849	5.6528	1.52E-04
0.6	8.042	8.8446	8.0152	3.06E-04
0.7	12.023	14.7370	12.4899	7.43E-04
0.8	18.597	30.9360	23.2039	2.56E-03

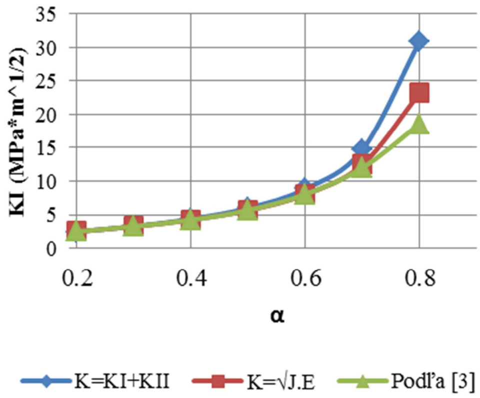

Diagram 7 Comparison of *K* values by *F* = 100N

Tab. 3 Values *K* by *F=150N*

α=a/R	K			Ansys method of the J-integral
	By [3]	Ansys extr. method $K=K_I+K_{II}$	K=√J.E	
0.2	3.740	3.6826	3.7269	6.61E-05
0.3	4.870	4.8881	4.8554	1.12E-04
0.4	6.328	6.5054	6.3221	1.90E-04
0.5	8.505	8.9774	8.4791	3.42E-04
0.6	12.063	13.2670	12.0228	6.88E-04
0.7	18.035	22.1060	18.7348	1.67E-03
0.8	27.896	46.4040	34.8059	5.77E-03

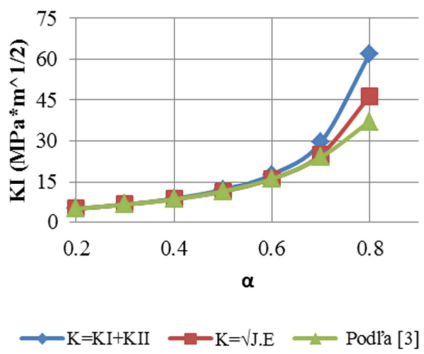

Diagram 8 Comparison of *K* values by *F* = 150N

Tab. 4 Values *K* by *F=200N*

α=a/R	*K*				Ansys method of the *J- integral*
	By [3]	Ansys extr. method $K=K_I+K_{II}$	*K=√J.E*		
0.2	4.987	4.9102	4.9693		1.18E-04
0.3	6.493	6.5174	6.4739		2.00E-04
0.4	8.438	8.6738	8.4296		3.38E-04
0.5	11.340	11.9700	11.3056		6.09E-04
0.6	16.084	17.6890	16.0305		1.22E-03
0.7	24.046	29.4750	24.9799		2.97E-03
0.8	37.194	61.8721	46.4086		1.03E-02

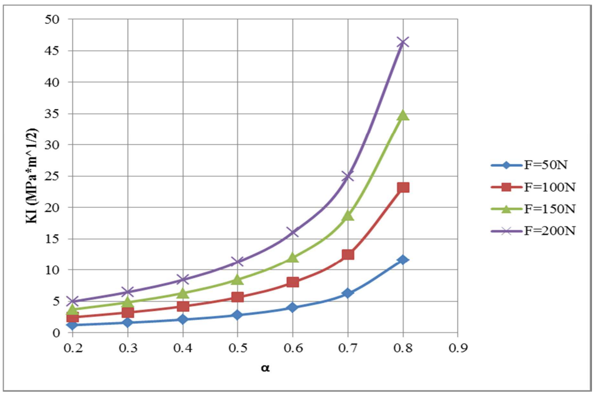

Diagram 9 Comparison of *K* values by *F* = 200N

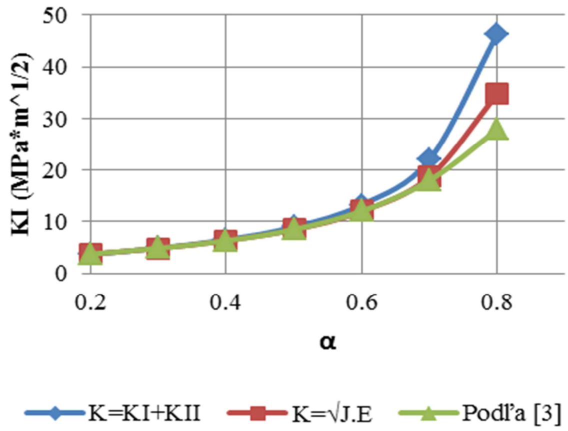

Diagram 10 Comparison of *K-values* due to different loads

5 Conclusions

In this paper some values of *K*-coefficient of stress intensity on the 3-point loaded beam loaded by forces of *F* = 50N, *F* = 100N, *F* = 150N and *F* = 200N, respectively, were compared. The values were calculated by three different methods.

The values of K-coefficient, obtained for α from 0.2 to 0.7, have very similar values because of the approximate methods used for their calculation. When *α* = 0.8, the dispersion of obtained coefficients is larger because of non-negligible plastic deformations obtained in the crack root and in the point of F loads as well.

References:

[1] XU, L. Roy - HUANG, Yonggang Y - ROSAKIS, Ares J. *Dynamic crack deflection and penetration at interfaces in homogeneous materials: experimental studies and model predictions*. Journal of the Mechanics and Physics of Solids 51 : Elsevier. 2003. 461-486.

[2] SLADEK, J. - SLADEK, V. *Evaulations of the T-stress for interface cracks by the boundary element method*. Engineering Fracture Mechanics Vol. 56, No. 6: Elsevier Science Ltd. 1997. 813 - 825.

[3] SIRATORI, M. – MIES, T. – MACUSITA, Ch. *Vyčisliteľnaja mechanika razrušenia*. Moskva: Mir. 1986. 334.

[4] IVÁNKOVÁ, O. *Vybrané problémy z lomovej mechaniky.* Habilitačná práca zo študijného odboru aplikovaná mechanika. Slovenská technická univerzita v Bratislave , Vydavateľstvo STU. 2007. 85. 978-80-227-2681-8.

[5] SLADEK, J. – SLADEK, V. – DRŽÍK, M. *Elastoplastic crack analysis by boundary integral method and surface spectrum measurement*. International Journal of Fracture 71: Kluwer Academic Publishers. 1995. 165-176.

[6] Manuál ANSYS.

Acknowledgement

This paper was written with the support of Slovak Grant Agency VEGA. Registration number of the project is 01/1186/12.

Kontaktná adresa:

Ing. Dušan Drobný
Katedra stavebnej mechaniky, Stavebná fakulta STU, Radlinského 11, 813 68 Bratislava
doc.Ing. Oľga Ivánková, PhD.
Katedra stavebnej mechaniky, Stavebná fakulta STU, Radlinského 11, 813 68 Bratislava

MODELING OF A CAPACITIVE MICRO ACCELEROMETER WITH FE METHOD

GABRIEL GÁLIK, VLADIMÍR KUTÍŠ
Institute of Automotive Mechatronics
Faculty of Electrical Engineering and Information Technology
Slovak University of Technology in Bratislava

Abstract: The article deals with the modelling of a micro-accelerometer using the finite element method. Micro accelerometers are used to measure the acceleration of objects, collisions, gravity and frequency of self-oscillation. Various methods exist for the transfer of acceleration into an electrical signal. To simplify and accelerate the development process, numerical analyses of the modelled system were implemented using the finite element method. FEM was used to obtain the characteristic properties of the modelled system. The article concludes with the evaluation of the modelled accelerometer for possible use based on its acquired characteristics.

Keywords: FEM, Micro-accelerometer, Finite element, Structural analysis

1 Introduction

The work deals with the use of finite element modelling for issues in micro-electromechanical systems. Micro-electromechanical systems or MEMS are used as sensors or actuators. Commonly contain integrated electronics for processing input and output electrical signals. Representatives of MEMS systems are for example miniature acceleration sensors, micro-accelerometers. Microaccelerometer's advantage is low weight and small structure size. They are used for the measurement of acceleration of objects, collisions, gravity and frequency of self-oscillation. Lightweight system means a fast response sensor and minimal impact on the properties of the measured system. There are various methods for conversion of acceleration to electrical signals, each structure comprises from a seismic mass, its inertia is used to determine the magnitude of acceleration. Various methods use different physical phenomena to detect inertial force or displacement of the seismic mass. Sensor characteristics are determined by the mechanical structure configuration. To simplify and accelerate the development process, the finite element method was implemented for analyses of the modeled system. Finite Element Method or FEM was used to calculate the system response to external loads. The model and analyses in this work were created using ANSYS system package.

2 Micro-accelerometers

Sensor is a device that changes its output electrical signal based on changes in the detected physical quantity (Fraden, 2010). Microaccelerometers are electromechanical systems that sense acceleration caused by external forces or gravity. Accelerometers have very wide application. They are used for the detection of acceleration from smartphones to space shuttles, for exact determination of gravity, as Seismographic sensor or as a rotation sensor in intelligent systems such as modern mobile phones. Microaccelerometers structure can be divided into two main parts: mechanical and electronic. The mechanical part of the micro-accelerometer converts the measured acceleration into an easily measurable quantity. The design of the mechanism determines the characteristic properties of the sensor. The sensing element can have almost any shape to have the desired characteristics. Electronic part ensures the conversion of the measured quantity into a usable electrical output signal.

2.1 Sensing structure

Sensing structure consists of a seismic mass, which is attached to the substrate via multiple springs while the system also exhibits damping properties, which depend on the structure and viscosity of the gas that fills the chamber containing the sensing element. A schematic representation of the sensing structure is represented in Image 3.

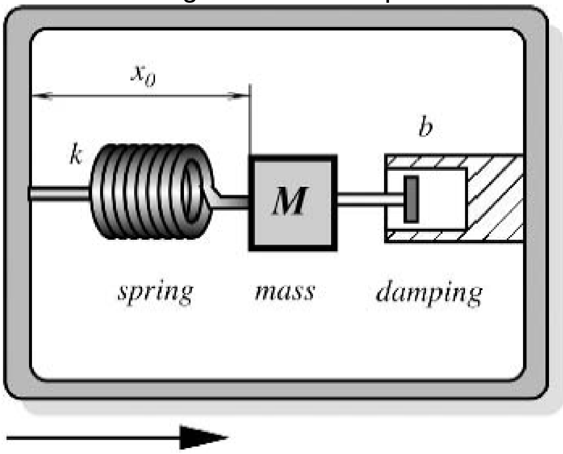

Image1- Schematic representation of mechanical structure

The main task of the sensing member is the conversion of acceleration magnitude into seismic mass displacement. The response of the system can be described by equations characteristic of individual parts. Newton's second law applies for the seismic mass m, which determines its response to acceleration a:

$$F = m.a \tag{2}$$

Spring supports are used for anchoring the seismic mass and to ensure its linear displacement x as a function of innertial forces F. Value characterizing the spring is called the coefficient of stiffness k.

$$F = kx \tag{3}$$

Under static load, displacement of the seismic mass depends only on the balance of forces. Equation (3) describing the response of the system to constant acceleration can be obtained by substitution from equations (1) and (2):

$$\Delta x = -ma/k \tag{4}$$

Damping effect in a micro-accelerometer ensures system stability and prevents unstable oscillations. Damping coefficient b is determined by filling gas viscosity.

$$F = bv \tag{5}$$

Damping force is linearly dependent on the velocity v of the seismic mass, and always directed against movement. The value of damping strongly influences the system's behaviour during transient loading. The value of b depends on the properties of the fluid surrounding the system, these properties can be dependent on temperature and the result is that the frequency response of the system can be temperature-dependent. Equation describing the micro-accelerometer as a dynamic system in differential form represents the correlation between force balance and seismic mass displacement and takes the form of:

$$m\frac{d^2x}{dt^2} + b\frac{dx}{dt} + kx = 0 \tag{6}$$

Equation (5) only applies if we consider a system with one degree of freedom. Unidirectional micro-accelerometer detecting acceleration in the x-direction experience adverse effects caused by seismic mass displacement caused by an acceleration in the y or z directions. The design should ensure that the spring stiffness in y and z-directions is significantly higher than the stiffness in the x-direction, the sensing element thus has a greater sensitivity in this direction.

.

2.2 Displacement sensors

For the system to be used as an acceleration sensor, the displacement of the seismic mass must be measured. Capacitive detector constitutes the most widely used type of displacement sensor, which uses the behaviour of plate capacitor of micrometer dimensions. The advantages of capacitive sensors are thermal stability and simple structure. A capacitive detector can be formed from any electrically conductive material, for micromechanical systems they are usually constructed from an identical material as the seismic mass. The most common material is mono or polycrystalline doped silicone. The shape of the electrodes represents a plate capacitor with dimensions in the scale of micrometers.

$$C = \varepsilon S/d \tag{7}$$

From equation (6) we can see that the capacity is directly proportional to the overlapping area S between the two electrodes and is inversely proportional to the distance d between them. The constant ε is the electric permittivity of fluid, filling the chamber around the sensing element. For the capacitive detector to have a linear dependence on acceleration, one of the properties - surface or distance - has to be constant. Technically, it is impossible to create a structure with constant properties, but it is possible to ensure sufficient stability. Capacitive sensors can be divided into two main types according to the principle of capacity change, sensors based on the change of capacitance by intersection area change or by change in electrode distance. Based on the design of the electrodes sensors can be divided into: sensors with plate electrodes and sensors with inter-digital electrode structure.

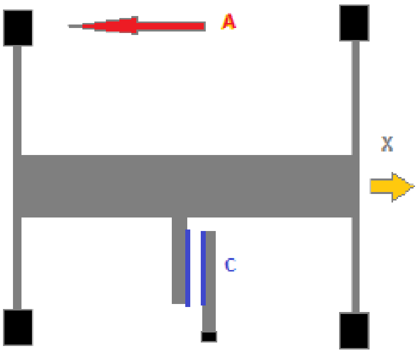

Image2- Inter-digital electrode structure with variable distance

The sensitivity of the capacitive detector is directly proportional to the size of changes in capacity for a given amount of displacement. Increasing the capacity could be realized by increasing the area of parallel electrodes or increasing the number of electrode pairs. The main drawback of capacitive detectors are electrostatic forces between the electrodes. If the electrode pairs are divided into two sets of separate directionality, than they can be connected into a differential capacitive sensor. Differential capacitive sensors minimalize the effects of electrostatic forces.

2.3 Dynamic properties

The modelled structure is a spatially distributed system, therefore it has to be described with different equation systems, which can be represented as tensors or matrices. Settling time output value is the time required for the system to stabilise the output value to the level defined by the measured quantity. Real accelerometers are under-damped systems, damping is provided by the inter-digital structure and viscosity of the filling gas. Damping of mechanical systems can be described using Rayleigh's formulae of material damping (Kandge G. M., 2007). The first component is due to damping in the material from which the system is created and it is determined by the coefficients α and β according to equation (8), where M is the mass matrix and K the stiffness matrix.

$$M\ddot{x} + C\dot{x} + Kx = F(t) \tag{8}$$

$$C = \alpha M + \beta K \tag{9}$$

The second component is the damping of ambient fluids around the mechanical structure. In a micro-accelerometer with capacitive detector a so-called "squeeze-film" phenomenon can occur by the extrusion of gas from the gap between electrodes during their movement. Damping coefficient is calculated according to equation (9)

$$c = \frac{\mu f(h/l) h^3 l}{d^3} \tag{10}$$

μ- gas viscosity, h- layer thickness, l- electrode intersection length, d- fluid gap width

Relation (9) shows the damping coefficient of one electrode set, to determine the total damping it must be multiplied by the number of electrode sets. The value of function f(h/l) is given in Table 1.

Table1 Function f(h/l) value

h/l	0	0.1	0.2	0.3	0.4	0.5	0.6	0.7	0.8	0.9	1
f()	1	0.92	0.85	0.78	0.72	0.65	0.60	0.55	0.50	0.45	0.41

3 Material and model properties

The aim of the simulation using the finite element method is to obtain the characteristic properties of the modelled system. The accuracy of the obtained values is affected by the quality of simulation and manufacturing quality. The resulting simulation with a given tolerance represents the real system without manufacturing defects. Finite element method can determine the impact of manufacturing defects on the characteristics of only if they are included in the model. Both models and material properties were defined separately for the performed structural and electrostatic analyses.

3.1 Topology properties

To create the model we used scripted instructions, the sequence of instructions is stored in a macro (*.mac) file. The advantage of using scripts is the possibility of quick changes in the properties of the model. To determine the properties of the system depending on geometrical dimensions, it is necessary to generate the simulation model using scripted instructions. Geometrical properties entered in the script are shown in Table2.

Table2 Dimensions (Baharodimehr et. al., 2009; Zimmermann et. al., 1995; Xiong et.al., 2005)

Dimension	Value	Units
Width of seismic mass	200	μm
Length of seismic mass	1485	μm
Number of mass reduction holes	14	
Length of holes	100	μm
Width of holes	50	μm
Seismic mass	0.962	μg
Number of springs	4	
Length of spring	455	μm
Width of spring	1.5	μm
Layer thickness	15	μm
Support area	20x50	μm^2
Middle electrode length	270	μm
Upper electrode length	270	μm
Lower electrode length	240	μm
Spacing of identical electrodes	21.9	μm
Electrode width	5	μm
Number of electrode sets	2x67	
Electrode clearance	2.3	μm
Length of interface area	240	μm
Bumper distance	2.3	μm
Bumper length	200	μm
Total bounding area	1530x1200	μm^2

The system is modelled in 2D and is oriented in the xy plane. Geometry is modelled using the element PLANE 182. Thickness of the silicon layer is represented in the model by the properties of the meshed element. The properties of the materials forming the structure of the sensing element are shown in Table 3.

Table3 Material properties

Property	ANSYS Ab.	Value	Unit
Anisotropic elastic modulus poly-Si	C11	165.7	GPa
	C12	63.9	GPa
	C13	52	GPa
	C33	155	GPa
	C44	79.6	GPa
Density poly-Si	DENS	2.329E-15	kg/(μm)2
Ultimate Stress poly-Si		2-3	GPa
Air viscosity (20°C)		18.23E-6	Ns/m2
Resistance poly-Si	RSVX	1.0E-6	TΩμm
Relative permittivity poly-Si	PERX	11.7	pF/ μm
Resistance of Air	RESX	1.0E9	TΩμm
Relative permittivity of Air	PERX	1	pF/ μm

3.2 Mechanical analysis model

The resulting mechanical sensing element model shown in Image 3 includes a movable structure suspended by four springs, stationary electrodes and their supports and bumpers. Bumper blocks are designed to restrict the amplitude of the seismic mass displacement in both directions to a value less than the air gap between the movable and stationary electrodes.

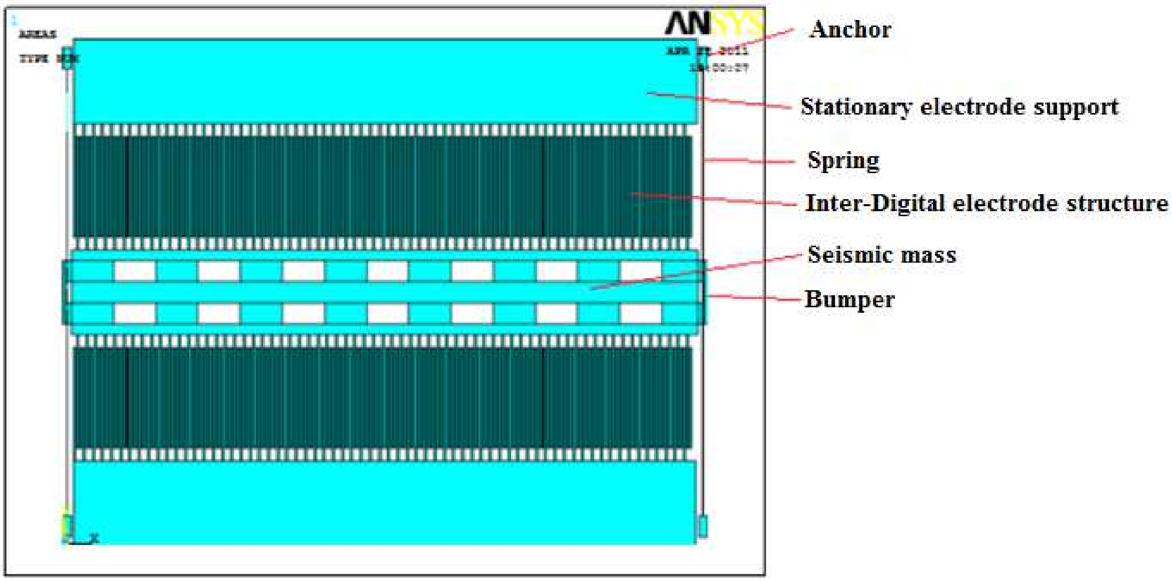

Image3- Mechanical model Topology

The mechanical structure is sensitive to acceleration in the x direction, displacement of the seismic mass is detected by differential capacitive sensor. Damping coefficients have to be defined to obtain accurate dynamic characteristic properties of the mechanical system from the analysis. Finding the values of the coefficients α and β is difficult without measurement on the real system. However, it is possible to calculate the ambient damping coefficient and use it as a minimal damping value. The calculated value of damping coefficient according to the characteristics of the mechanical system is **3.211e-4 Ns/m**. The dimension of its unit is equal to μNs/μm, therefore the value is directly applicable to μMKS unit system. Elements PLANE182 (11,898pcs) and COMBIN14 (4pcs) were used to create the model mesh for static and dynamic mechanical analyses.

3.3 Electrostatic analysis model

The characteristic function of the differential capacitive sensor gives the dependence of capacity difference on the displacement of the central movable electrode. It is sufficient to model one set of electrodes to determine the response of the entire inter-digital structure. The model also incorporates the mesh of the filler fluid between electrodes.

Image4 contains the model used in the electrostatic analysis, the model consists of PLANE121 (2825pcs) elements.

Image4- Model for electrostatic analysis

Capacity values are obtained using CMATRIX, the macro calculates capacity based on material properties and geometry. The analysis requires a model meshed with electrostatic elements. The model has all its main dimensions defined as parameters and contains a variable parameter that determines the amount of displacement of the central electrode.

4 Steady-State Analyses

The aim of steady-state analysis is to determine the characteristic function of the sensing member. The sensing of acceleration consists of two value conversions, the first is the conversion of acceleration to displacement, the second is the conversion of displacement to capacity difference. The characteristic properties of the sensor can be determined by the superposition of the two conversion characteristics.

4.1 Structural Analysis

Static analysis is used to obtain the characteristic function of the mechanical system. Characteristic function is defined as the dependence of displacement on acceleration. Static analysis uses the same model as modal analysis, and the same element. Acceleration of the substrate is modelled as external loading using gravity in the direction of the x axis.

Table4 Selected values from characteristic function

Acceleration [g]	Displacement [μm]
0	0
200	0.44797
400	0.89594
600	1.344
800	1.792
1000	2.24
1030	2.30

In Table 4 we can see the maximum displacement that occurs during acceleration of 1030g. Greater acceleration causes the seismic mass to contact the bumpers this causes the distortion of the output signal. The graph in Image 5 represents the characteristic function and it is linear, the sensitivity of the mechanical structure is given by the gradient and has a value of 0.00224μm / g.

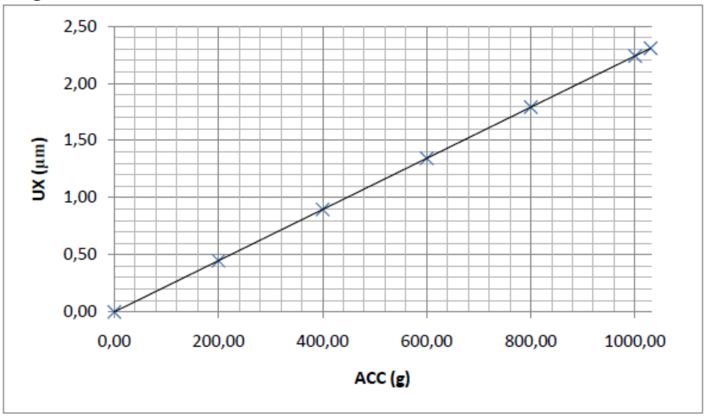

Image5- Characteristic function with regression curve

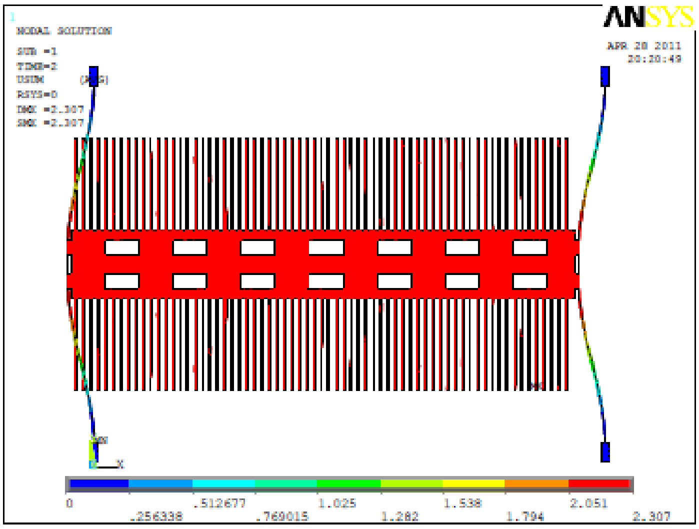

Image6- Structure displacement in axis X

Image 6 shows the deformation of the system during maximum acceleration in automatic displacement scaling. Expanded scale causes overlay in the model during rendering.

4.2 Electrostatic Analysis

Image 7 (a) and (b) contain the potential distribution and the intensity of the electric field at zero displacement, images (c) and (d) contain the potential distribution and the intensity of the electric field with the central electrode offset by 2μm.

(a)

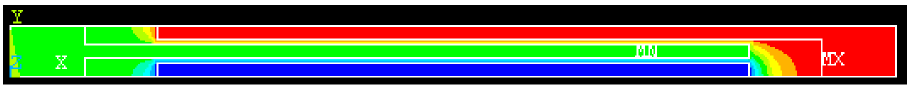

(b)

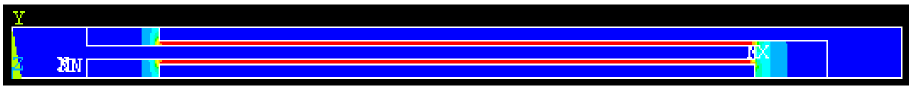

(c)

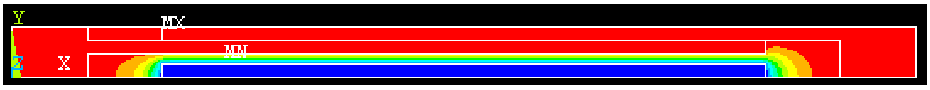

(d)

Image7- Distribution of electric potential (a,c) and electric field intensity (b,d)

Table5 Acquired values for different displacements

Displacement [μm]	c1 [pF]	C1t [pF]	c2 [pF]	C2t [pF]	Δc [pF]	ΔC [pF]	U [V]
0	0.142×10^{-1}	28.694	0.141×10^{-1}	28.503	0.95×10^{-4}	0.190	0.175×10^{-1}
0.44797	0.176×10^{-1}	35.490	0.119×10^{-1}	23.921	0.057×10^{-1}	11.575	0.976
0.89594	0.231×10^{-1}	46.623	0.102×10^{-1}	20.618	0.129×10^{-1}	26.005	1.937
1.344	0.338×10^{-1}	68.134	0.901×10^{-2}	18.121	0.248×10^{-1}	50.012	2.902
1.792	0.634×10^{-1}	127.44	0.804×10^{-2}	16.170	0.553×10^{-1}	111.27	3.876
2.24	0.532	1070.32	0.726×10^{-2}	14.602	0.5252	1055.7	4.866

The obtained values are calculated per unit length of one set of electrodes. Table 5 contains important features of the capacitive sensor. Non-zero capacity difference at zero displacement is caused by geometrical asymmetry and creates a zero offset in the characteristic function. Voltage values in Table 5 are the voltage between the center electrode and ground, with the top electrode connected to 5V and the lower electrode connected to -5V. The graph in Image 8 represents the dependency of capacity difference on the displacement of the central electrode, the dependence is exponential. Theoretically, at maximum displacement the capacity difference would be infinite, but in a real system at maximum displacement an electrical contact occurs between the central and stationary electrode. Macro CMATRIX cannot calculate a capacity value width zero gas gap. The dependence is almost linear for smaller displacement than 1μm.

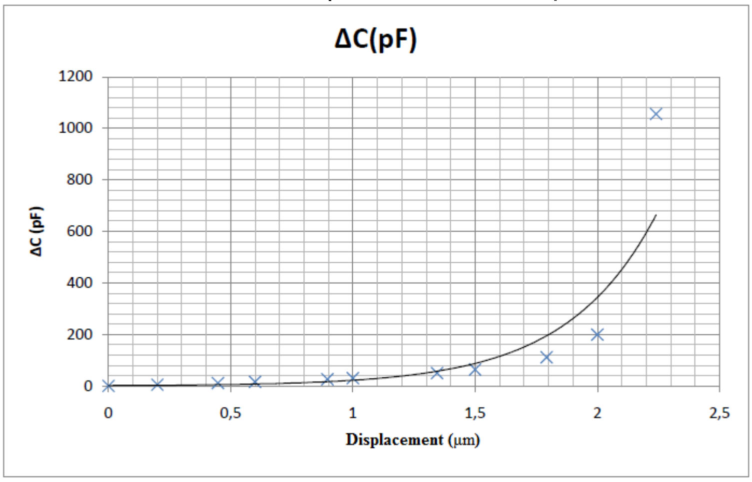

Image8- Characteristic function of differential capacitive displacement sensor with regression curve

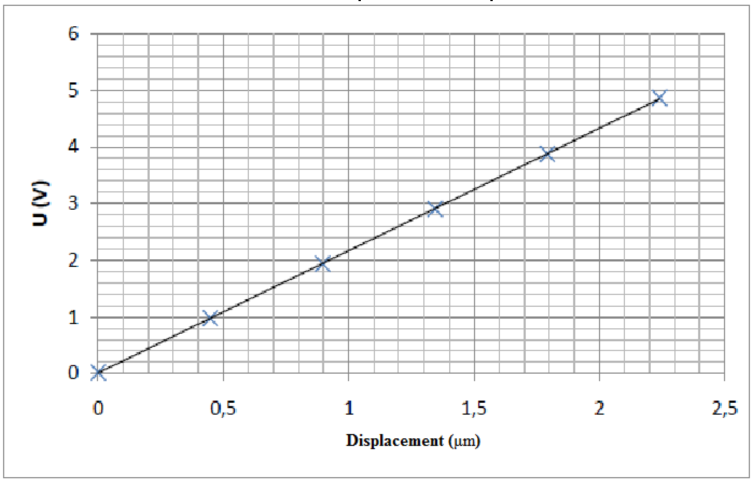

Image9- Characteristic function of differential capacitive displacement sensor with regression curve

Image 9 shows the characteristic function of the differential capacitive divider. The voltage dependence on the displacement of the center electrode is linear, its gradient is equal to 2.1725 V/μm. The resulting sensor characteristic function is obtained by superposition of mechanical and capacitive characteristics and has a value of 4.866×10^{-3} V/g for symmetric differential capacitive sensor voltage supply of ± 5V.

4.3 Modal analysis

The input parameters for modal analysis are the number of desired eigenfrequencies and eigenmodes and the required frequency spectrum. ANSYS offers a variety of algorithms to compute the natural frequencies in this simulation we used the algorithm with damping. Modal analysis requires a model with defined material properties, defined boundary conditions and constraints without external loads. Due to the time-consuming nature of the analysis calculation, it is sufficient to determine the properties of the moving structure.

Table6 Eigenfrequencies

Eigenfrequency	**Frequency [Hz] w/o damping**	**Frequencz [Hz] w/ damping**
1	10552	10552
2	148944	148944
3	231608	231608
4	232668	232667

5	232972	232972

Eigenfrequencies obtained by simulation are shown in Table 6. The first eigenfrequency represents the natural frequency of oscillation of the seismic mass in the direction of the x-axis. The first natural frequency of the system determines the upper limit of sensor bandwidth, a mechanical system driven by its first natural frequency reaches resonance and has disproportionate displacements. The value of damping coefficient has minimal impact on the value of the modal frequencies. By increasing the coefficient of damping, the modal frequencies slightly shift to lower frequencies. The eigenmode of oscillation of a mechanical system with the first natural frequency is visible in the Image10.

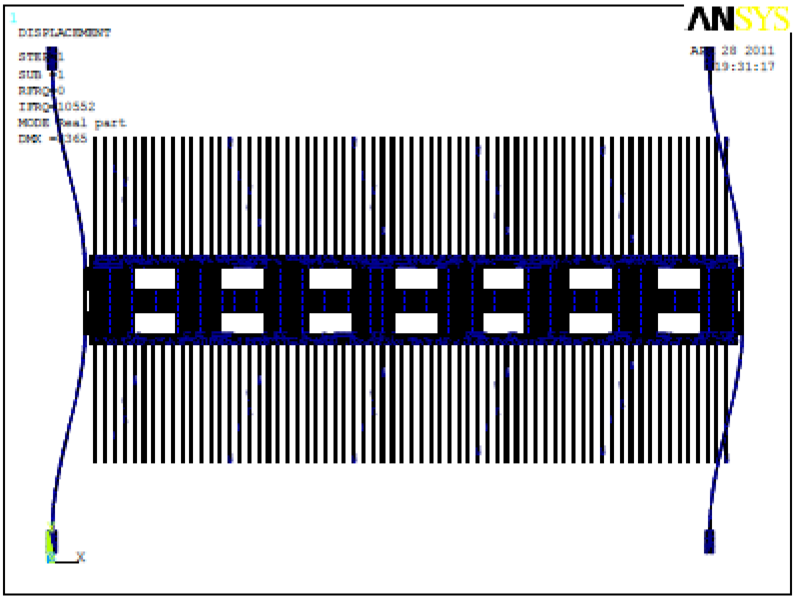

Image10- First eigenmode vibration

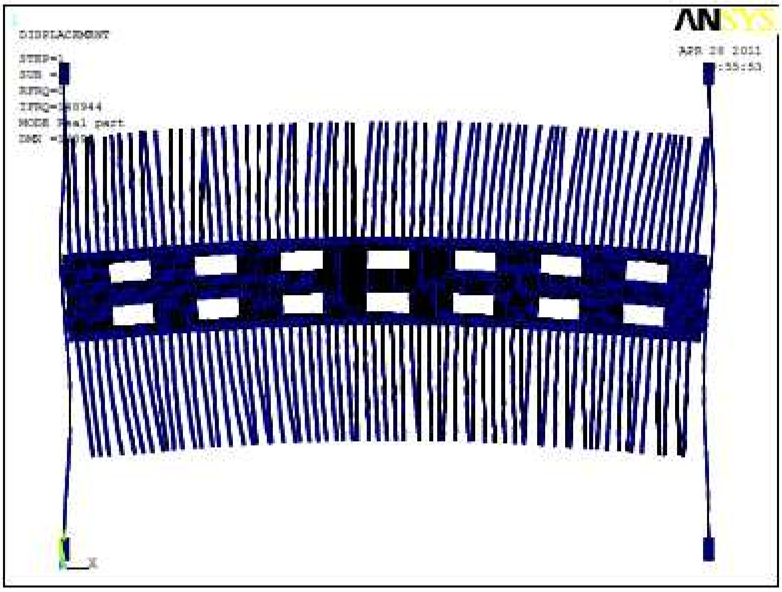

Image11- Second eigenmode vibration

Higher frequencies cause a torsional vibration of the mechanical system as shown in Image 11. Size distortions and displacements visible in the Image 10 and Image 11 are normalized, their numerical values do not represent actual values of oscillation.

5 Time - transient analyses

Time-transient analyses are used to determine the dynamic characteristics of a mechanical system and the system's response to time-transient loading. Two important properties that need to be determined to characterize the system are settling time and the transmission bandwidth. Transient analysis is used for determining the settling time and a harmonic analysis is performed for determining the frequency bandwidth.

5.1 Transient structural analysis

Transient Analysis examines the mechanical response of the structure to a step change in acceleration. Damping of the mechanical system has a major impact on the step response. an undampened system would vibrate with its first natural frequency and constant amplitude. Any real system, however, has some damping properties that cause the amplitude to steadily decrease into a steady state. Ambient damping coefficient can be defined in the model using COMBIN14 element that is inserted between the seismic mass and the bumper. Damping coefficient is than defined as a real-constant. The graph in Image 13 contains the time course of the mechanical system response to a step change in acceleration from zero to 10g.

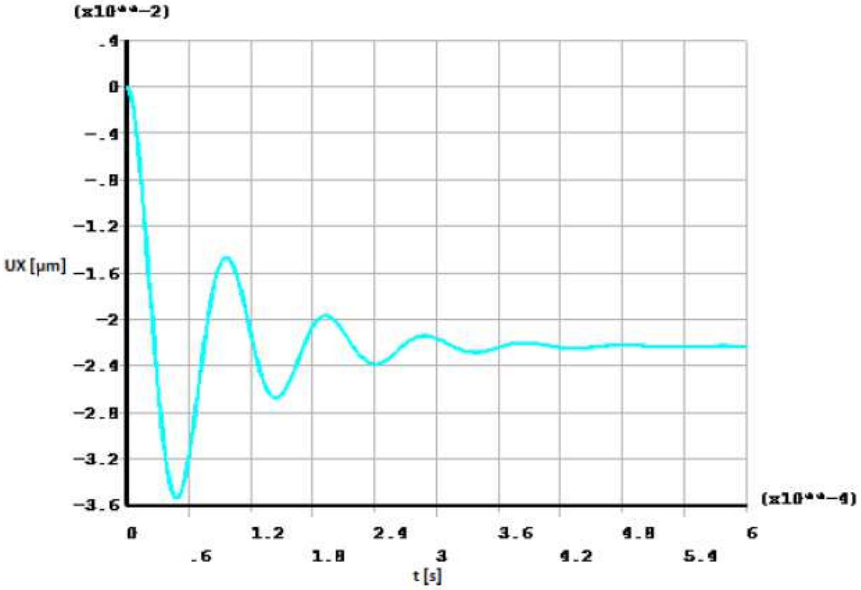

Image12- Step response characteristics

From the step response we can determine that the system will reach steady-state in 0.6ms and a state of minor fluctuations of 5% in less than 0.24ms. The peak of the first overshoot for the step change of 10 g reaches a value of about $3.55x10^{-2}$μm, which represents 154% of the steady-state value. The overshoot can be so large that it causes a contact between the seismic mass and the bumper, therefore the dynamic input range of the mechanical system is ± 650 g.

5.2 Harmonic - response analysis

The result of a harmonic analysis is the frequency response of the mechanical system. Frequency response describes the dependence of displacement amplitude of the seismic mass from the excitation frequency of harmonic acceleration. If an undamped system is driven by its own natural frequency it reaches resonance and vibration amplitude of the seismic mass should theoretically be infinite. The vibration amplitude of mass around its natural frequency drops sharply. Using the frequency characteristics it is possible to determine the upper limit of the transmission band. Transmission band is the part of the frequency response where the output amplitude is not affected by resonant frequency effects.

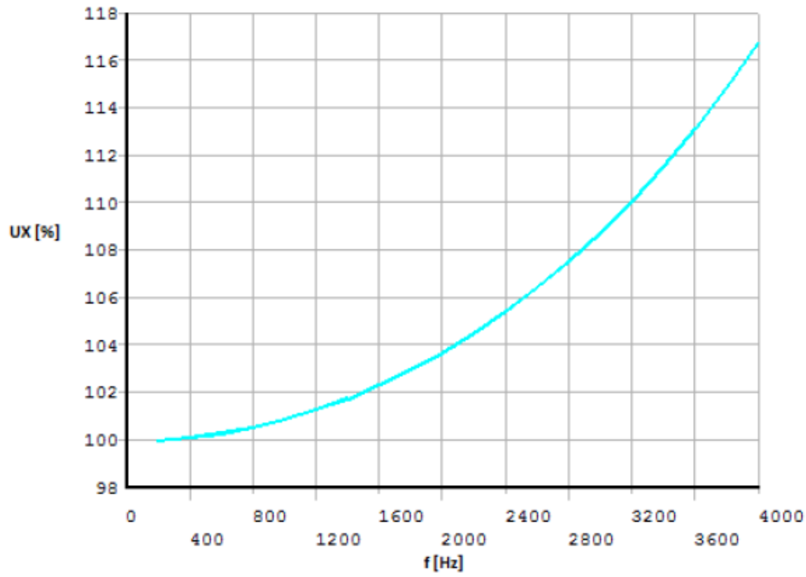

Image13- Amplitude-frequency characteristics in transfer band

Image 13 represents the percentual change in amplitude based on frequency of vibration of the mechanical system with damping, the value of 100% represents the displacement value at 0Hz (static) load. Oscillation amplitude increase of 5% occurs at a frequency of 2.4kHz and increase in amplitude by 10% at 3.2kHz. The upper frequency limit of the transmission bandwidth of the mechanical system is 3.2khz.

6 Conclusions

Based on the acquired characteristics of the modelled system, the given mechanical structure could form the core of microaccelerometers used as a crash sensor in airbag system control units or as a sensor for active suspension control systems. Dynamic characteristics were analyzed using the minimum ambient damping coefficient, damping in real sensors may be greater. The shape and dimensions of the modelled geometry were ideal, the resulting properties of real accelerometer may vary due to manufacturing inaccuracies. The properties of the output electric signal are also influenced by integrated electronics which is used for shaping the output signal. As a future work we would like to determine the impact of manufacturing tolerances on the characteristic properties of the modelled system.

References

BAHARODIMEHR A.; ABOLFAZL SURATGAR A., SADEGHI H., 2009, Capacitive MEMS accelerometer wide range modeling using artificial neural network, Journal of Applied Research and Technology, Vol. 7, No. 2, pp. 185-192, ISSN 1665-6423

FRADEN, J., 2010, Handbook of modern sensors: physics, designs, and applications. 4th ed. ISBN 978-1441964656

KANDGE G. M., 2007, Influence of Mode Dependent Rayleigh Damping on Transient Stress Response. University of Ljubljana, Faculty for mathematics and physics, Department of physics ISRN BTH-AMT-EX--2007/D-01--SE

Xiong X., Lu D. and Wang W., 2005,A Bulk-micromachined Comb Accelerometer with Floating Interconnects, Proc. of the 48th IEEE International Midwest Symposium on Circuits & Systems (MWSCAS’05), pp. 147-150, Cincinnati Ohio USA, Aug 7-10, 2005.

ZIMMERMANN L., EBERSOHL J. PH. et. al., 1995, Airbag application: a microsystem including a silicon capacitive accelerometer, CMOS switched capacitor electronics and true self-test capability, Sensors and Actuators A: Physical, Issues 1-3, pp. 190-195

Acknowledgement

This work was supported by Grant Agency VEGA, grant No. 1/0228/14, Grant Agency KEGA grant No. 015STU-4/2012 and Slovak Research and Development Agency under the contracts APVV-0450-10

Contact address:

Ing. Gabriel Gálik
Slovak University of Technology
Faculty of Electrical Engineering and Information Technology
Ilkovičova 3, SK-812 19 Bratislava, Slovakia

STRUCTURAL MULTIBODY DYNAMICS USING ANSYS – ADAMS INTERFACE

V GOGA

Institute of Automotive Mechatronics
Faculty of Electrical Engineering and Information Technology
Slovak University of Technology
Ilkovičova 3, 81219 Bratislava, Slovak Republic

Abstract: This paper presents two ways how to solve structural multibody dynamics problems in software ANSYS. The first one is the classical method using structural transient analysis in ANSYS Workbench. The second way is using ANSYS – ADAMS interface. ADAMS is special software for dynamic analysis of rigid multibody systems. Time dependent loads, forces and moments from ADAMS analysis can be imported to ANSYS and applied on finite element model of selected body and perform the structural analysis. Dynamic structural analysis can be also performed directly in ADAMS on finite element model created in ANSYS.

Keywords: multibody dynamics, ANSYS – ADAMS interface, finite element model, structural analysis, crank mechanism

1 Introduction

Crank mechanism is used for transform the linear motion of the piston to rotary motion of the crankshaft and vice versa (Vlk, 2003). Piston is connected with crankshaft with piston rod, which is the most stressed part of the crank mechanism. Crank mechanism was subjected to finite element dynamic analysis (Zienkiewicz, 2013). Stress analysis was performed just for piston rod.

3D geometrical model of the crank mechanism is shown in IMAGE 1. Model consists from four bodies: piston, piston pin (just pin), piston rod (just rod) and crankshaft. From the kinematics point of view the most important parameters of crank mechanism are crank radius *R* and rod length *L*. Weights *m* and moments of inertia *I* of individual bodies are important for dynamic analysis. These physical quantities are dependent on the material density *ρ* and whole geometry of the bodies. For stress analysis is also necessary to know material Young's modulus *E* and Poisson's ratio *ν*.

All important parameters for crank mechanism model are presented in TABLE 1. All bodies are made from steel but the density of piston and pin is intentionally 100 times higher due to the increased effect of inertia forces.

Table 7 Parameters of the crank mechanism

crank radius *R*	[mm]	15.5			
piston rod length *L*	[mm]	54			
		piston	pin	rod	crankshaft
density *ρ*	[kg.m^{-3}]	785 000	785 000	7 850	7 850
Young's modulus *E*	[MPa]	2.1×10^5	2.1×10^5	2.1×10^5	2.1×10^5
Poisson's ratio *ν*	[-]	0.3	0.3	0.3	0.3

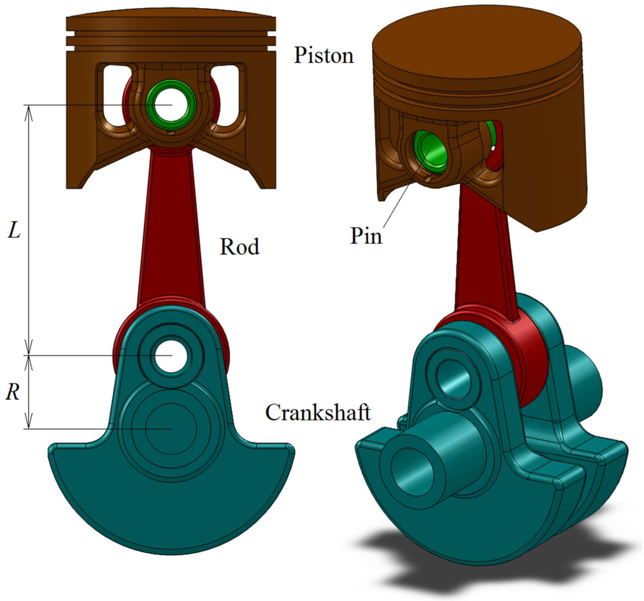

Image 4 – CAD model of the crank mechanism

2 Rigid multibody dynamics

Only kinematic parameters (displacement, velocity and acceleration) of the bodies and reaction forces in the joints can be calculated from rigid multibody dynamics. There is no possible to perform stress analysis. This analysis was performed in ANSYS Workbench using module Rigid dynamics.

CAD model was imported into ANSYS and all material properties were specified. Three revolute joints were defined between: ground - crankshaft, crankshaft - rod and rod - pin. One translate joint was created between ground and piston.

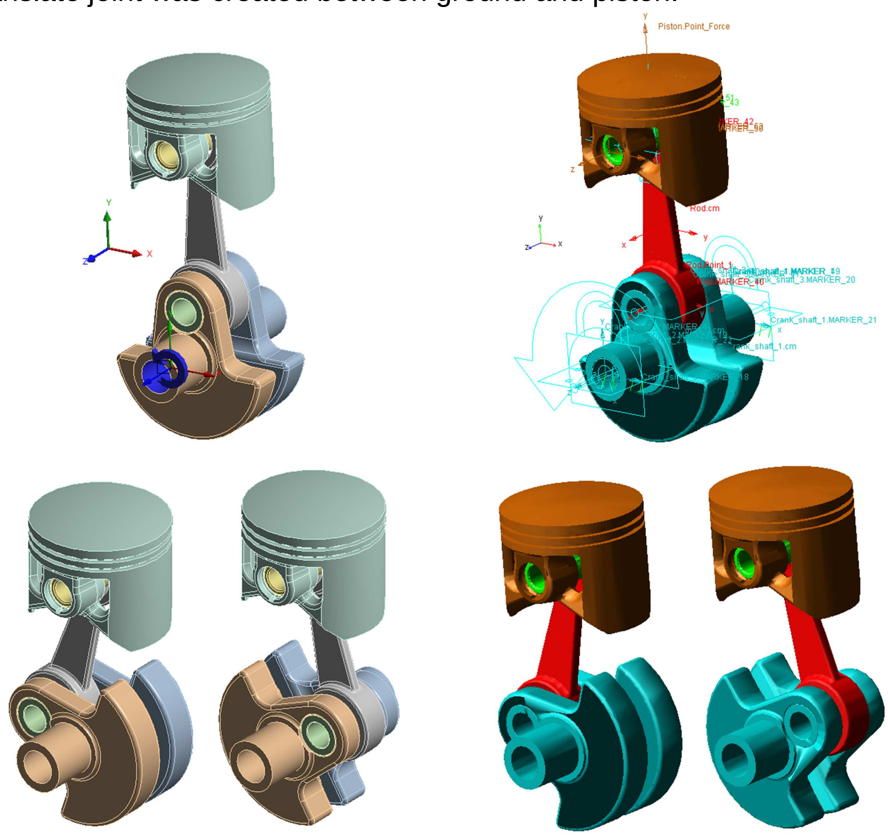

Image 2 – Models for rigid dynamic simulations: ANSYS (left) and ADAMS (right)

Motion of the mechanism was prescribed with crankshaft constant angular velocity equal to 800 RPM (ω = 83.776 rad.s^{-1}). Simulation was carried out for two turns of crankshaft which correspond to the simulation time around 0.15 s (time step was defined to 0.001 s). The same analysis was also performed in module ADAMS/View. Simulation models from ANSYS and ADAMS are shown in IMAGE 2.

Results of the piston movement (displacement, velocity and acceleration) and reaction forces in rod's upper joint are presented in IMAGE 3 and 4, respectively. All results are good agreement, therefore the both simulation models can be considered as equivalent and correct.

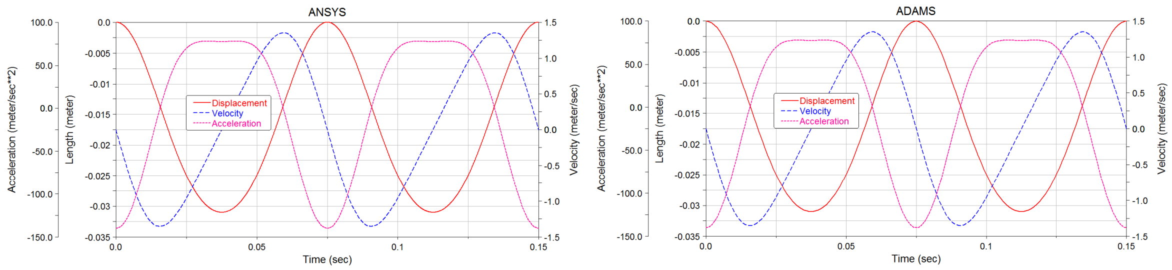

Image 3 – Piston movement results: ANSYS (left) and ADAMS (right)

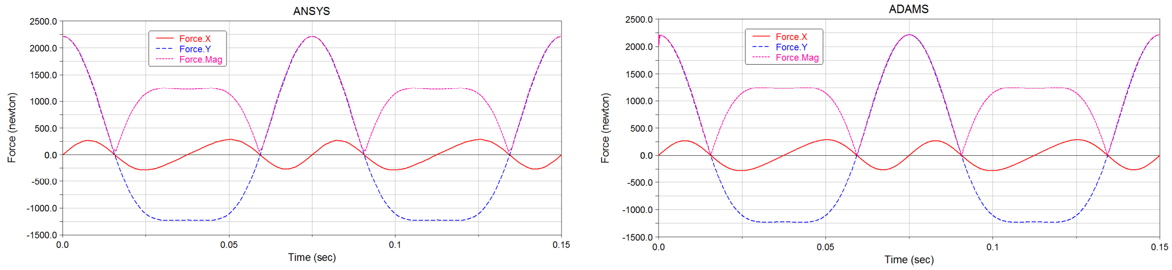

Image 4 – Reaction forces in rod's upper joint: ANSYS (left) and ADAMS (right)

3 Structural multibody dynamics in ANSYS Workbench

Inertial forces induce mechanical stresses in all bodies of the crank mechanism. The most stressed is the piston rod. Therefore stress analysis of the rod was performed in module Transient structural in ANSYS Workbench. The same model was used as in previous rigid dynamic analysis but the rod was set as flexible body. Rod was meshed by element type SOLID187 (tetrahedron solid element with 10 nodes), see IMAGE 5. Program ANSYS automatically added further necessary elements to the model (contact and target elements CONTA174 and TARGE170, mass elements MASS21 and joint elements MPC184). Total number of solid elements and nodes was 16 766 and 27 861, respectively.

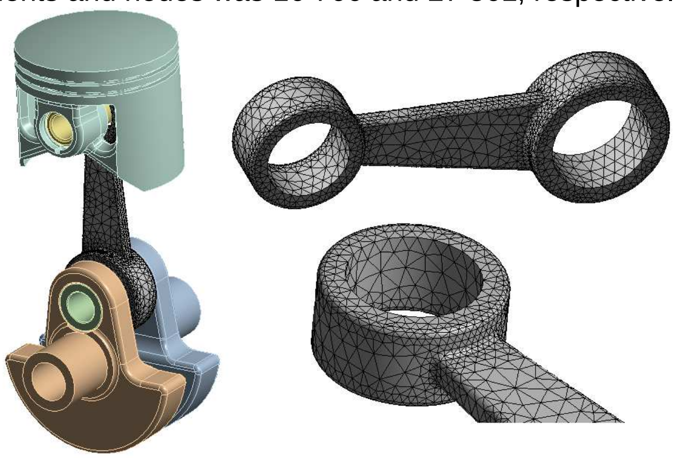

Image 5 – Flexible rod in ANSYS Workbench

Simulation time was 0.09 s what represents approximately one and quarter turn of the crankshaft (time step was 0.001 s).

Von Mises stress was monitored. Stress distribution in rod for three different time moments is shown in IMAGE 6. Stress values for some selected nodes on the rod in the most critical time moment t_c = 0.075 s and in the random time t_r = 0.063 s are shown in IMAGE 7. These results will be compared with results from simulation performed using ANSYS – ADAMS interface.

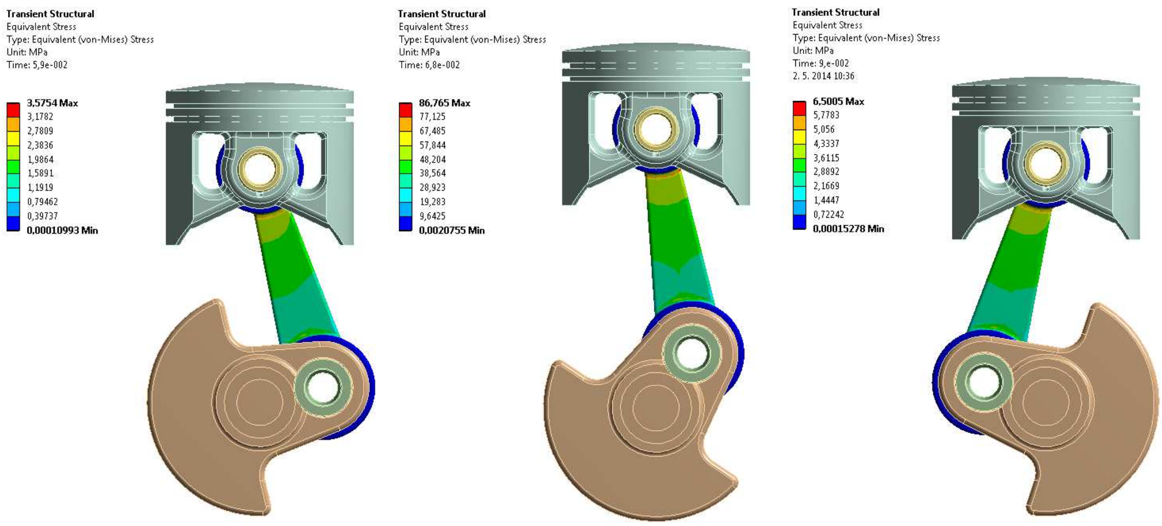

Image 6 – Von Mises stress distribution in rod (ANSYS Workbench)

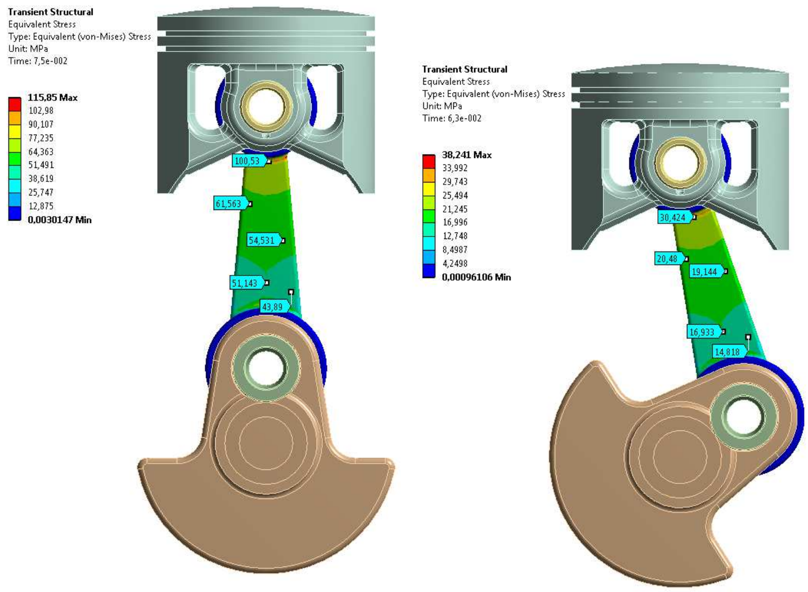

Image 7 – Stress values (ANSYS Workbench) in critical time t_c (left) and in random time t_r (right)

4 Structural multibody dynamics using ANSYS – ADAMS interface

ADAMS software is predominantly used for dynamic analysis of the multibody systems created from rigid bodies (Adams Help 2007). It is also possible to create flexible bodies in ADAMS, but their geometry must be very simple (for example: prismatic rectangular or circular rod).

Finite element (FE) model of flexible body with more complex geometry must be created in some finite element software such as the program ANSYS. FE model can be then imported into ADAMS in form Modal Neutral File (MNF). The algorithm used to create MNF is based on a formulation called component mode synthesis (also known as dynamic substructuring). ADAMS uses the approach of Craig Bampton with some slight modifications. According to this theory, the motion of a flexible component with interface points is spanned by the interface constraint modes and the interface normal modes. Constraint modes and interface normal modes together are referred to as component modes. (ANSYS Help 2012)

Geometry model of the piston rod was imported into ANSYS Classic and meshed with element type SOLID187 (total number of elements and nodes was 23 499 and 40 123, respectively). Next two nodes were created in the middle of rod's pins. These nodes are called interface points. Interface points are very important because only in these points can be applied forces or joints in ADAMS. Connection of the interface points to the structure is usually performed with spider web of beams. Element type BEAMS188 was used for creating spider webs. Material properties for beam element was $E = 2.1\times10^{15}$ MPa, $\nu = 0.3$ and $\rho = 10$ kg.m^{-3}. Beam's great rigidity and lightweight should ensure minimal impact on the rod stress analysis. Complete rod FE model for ADAMS is shown in IMAGE 8.

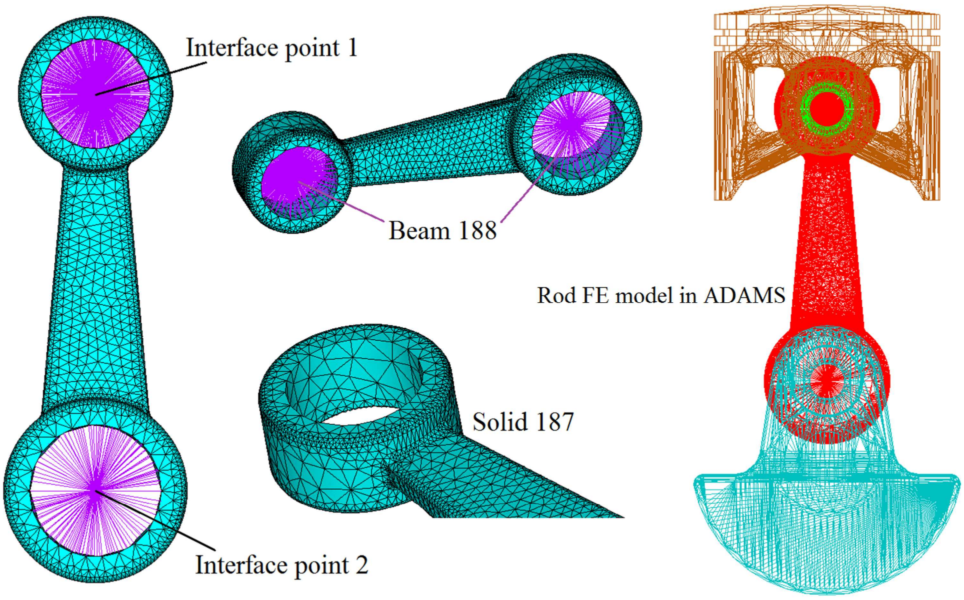

Image 8 – Rod finite element model (ANSYS Classic) for ADAMS simulation

After importing rod FE model into ADAMS, this model was connected to other bodies in interface points using revolute joints. Simulation with the same settings as in the previous ANSYS transient structural analysis was performed and results of von Mises stress distribution are shown in IMAGE 9.

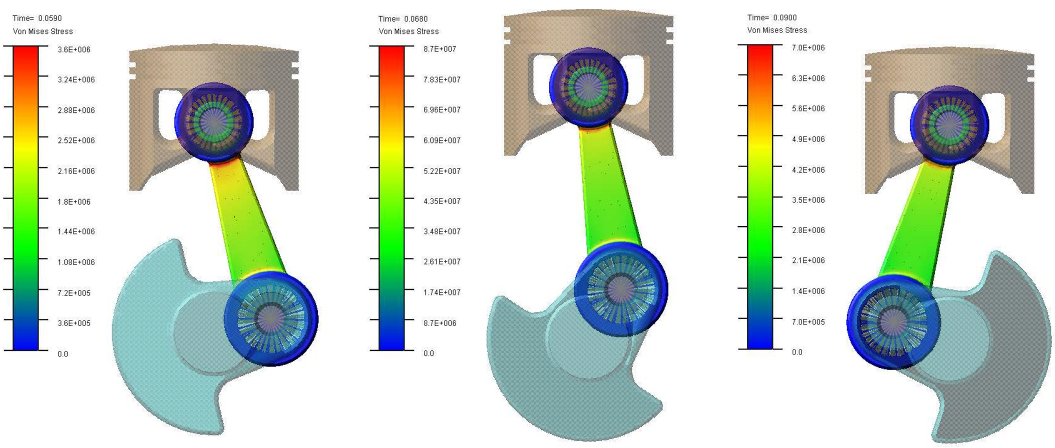

Image 9 – Von Mises stress distribution in rod (ADAMS)

For precise stress analyses, it is possible to export loads from interface points back to ANSYS Classic. Loads from interface points can be exported from rigid or flexible ADAMS model and applied to FE model in ANSYS Classic. We used first option and loads from ADAMS rigid body model were exported to ANSYS Classic. Results from ANSYS simulation are presented in IMAGE 10 and 11.

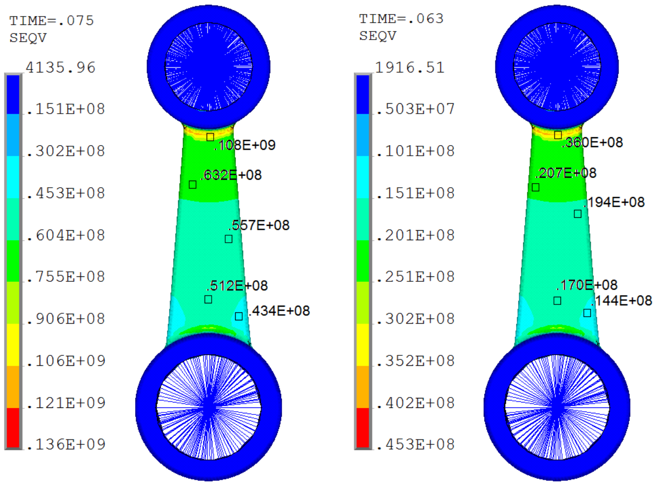

Image 10 – Stress values (ADAMS) in critical time t_c (left) and in random time t_r (right), unit: Pa

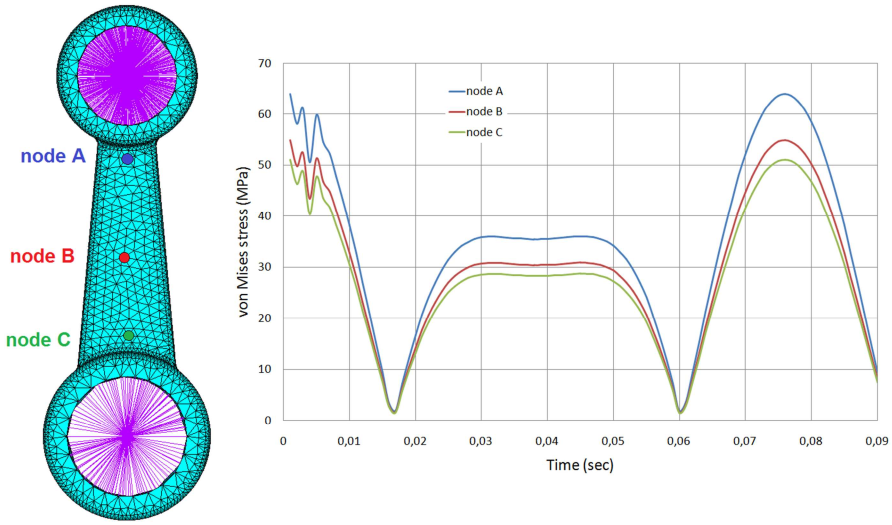

Image 11 – Stress versus time for three selected nodes (ANSYS Classic)

5 Simulation model for mechatronic systems

ADAMS model with finite element body created in ANSYS can be used for creation of simulation model for mechatronic systems. ADAMS mechanical model can be imported into program MATLAB/Simulink, where it is possible to build the control system for regulation its function.

Example: regulation of the solid flexible beam which base is moved by motion with target function shown in IMAGE 12. Free end point of the beam starts vibrate due to inertia forces, IMAGE 13.

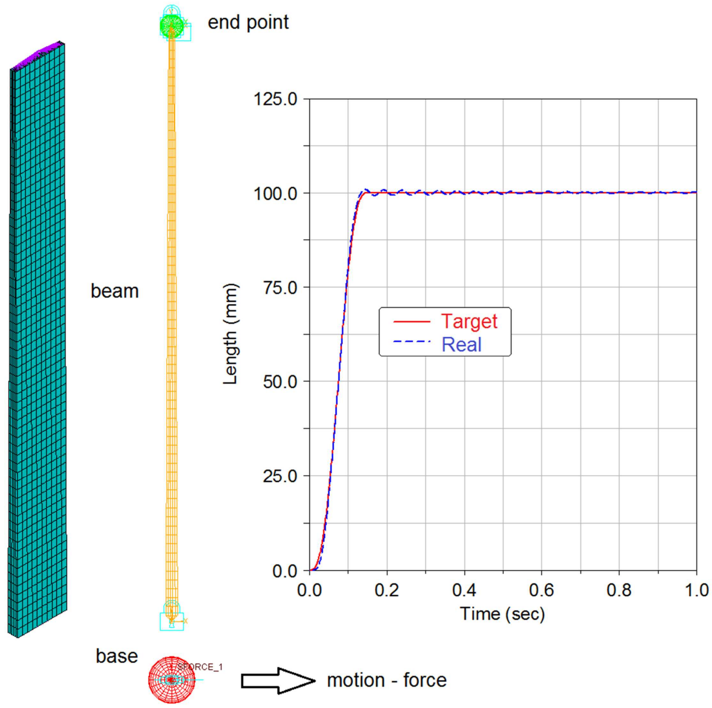

Image 12 – Motion of solid flexible beam – target and real position of the end point

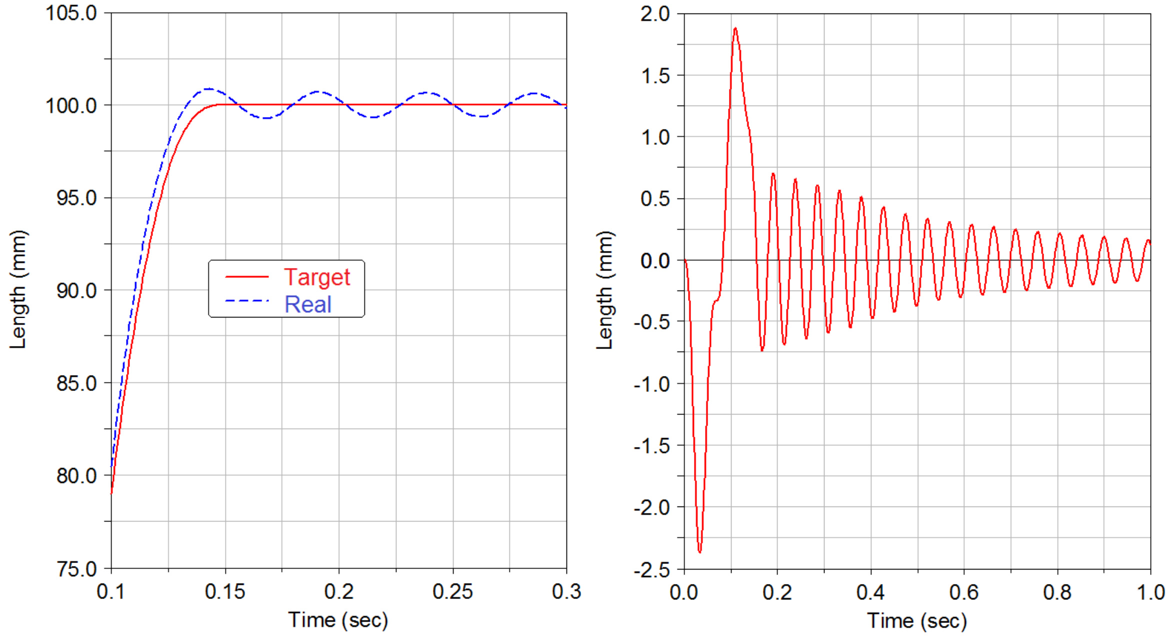

Image 13 – Point movement (detail view, left) and point vibration (right)

The aim of control was eliminate the end point vibration. Control system with PID regulators was applied for ADAMS model, see IMAGE 14. Detail view of point vibration after regulation and acting force generated from control system are shown in IMAGE 15.

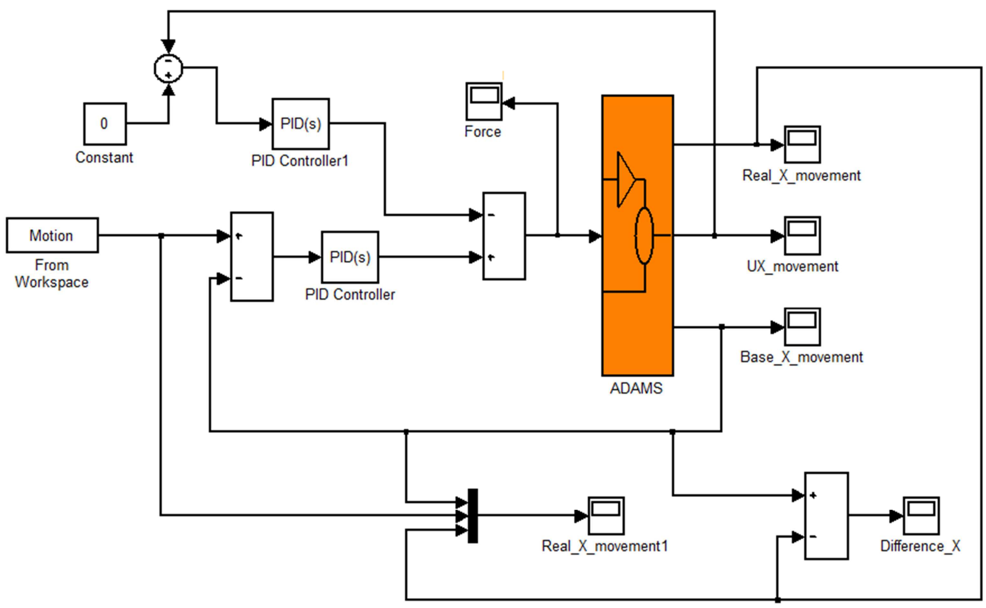

Image 14 – Control system in MATLAB/Simulink

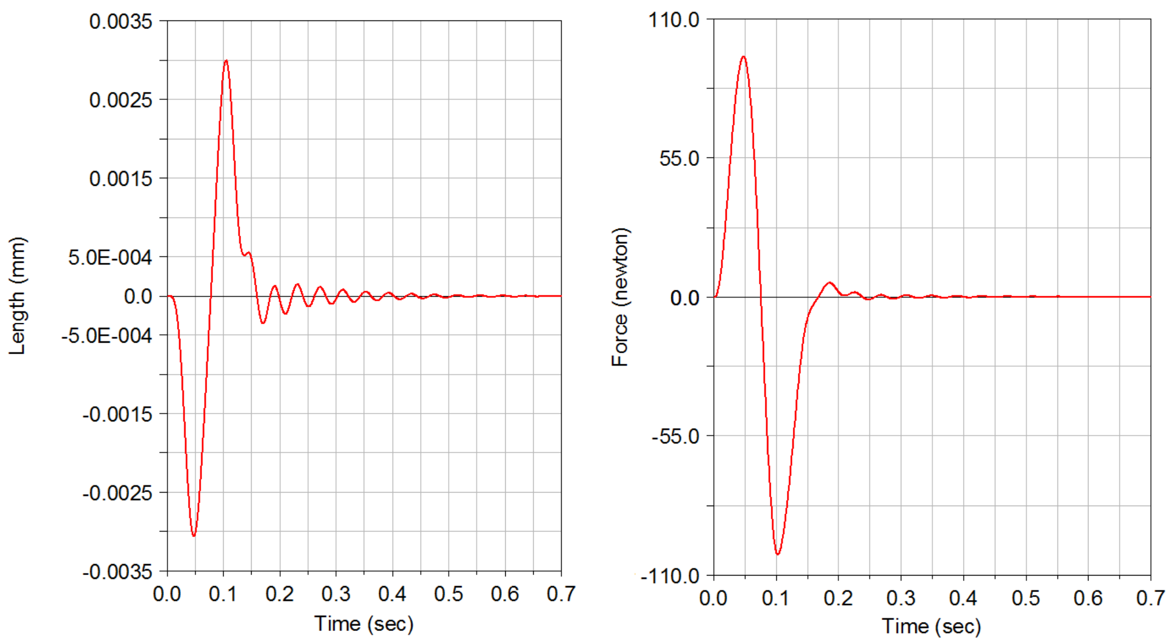

Image 15 – Point vibration (left) and acting force (right) after regulation

6 Conclusion

This paper presented the possibility to solve multibody dynamics using ANSYS – ADAMS interface. This approach allows faster solution for dynamic analysis of multibody mechanical systems and of course there is possibility to make structural analysis of these systems. Results from ANSYS and ADAMS simulations were in good agreement.

Another advantage is that the ADAMS model with flex bodies from ANSYS can be imported into MATLAB/Simulink and deal with it in terms of system control, thereby creating the simulation model for mechatronic systems.

References

ADAMS Help 2007
ANSYS Help, 2012
VLK F., 2003. *Automobilová technická příručka.*Brno, 791 p. ISBN 80-238-9681-4
ZIENKIEWICZ O.C., TAYLOR R.L., FOX D.D., 2013. *The Finite Element Method for Solid and Structural Mechanics.* Butterworth-Heinemann, 672 p. ISBN 978-1856176347

Acknowledgement
This work was supported by: Slovak Research and Development Agency under contracts APVV-0450-10, Grant Agency KEGA 015STU-4/2012 and grant VEGA 1/0228/14.

Contact address:

Ing. Vladimír Goga, PhD.
Institute of Automotive Mechatronics
Faculty of Electrical Engineering and Information Technology
Slovak University of Technology, Ilkovičova 3, 81219 Bratislava, Slovak Republic
e-mail: vladimir.goga@stuba.sk

LOAD-BEARING CAPACITY OF FRICTIONAL JOINTS IN STEEL ARCH YIELDING SUPPORTS

PETR HORYL, PAVEL MARŠÁLEK
VŠB-Technical University of Ostrava, IT4Innovations National Supercomputer Centre

Abstract: Yielding steel arch supports of roadways are widely used mainly in coal mines. The support consists of several segments, joined by friction bolt connections. A loading capacity of arch support and its pliability (ability to accept deformations of surrounding rock mass) is much influenced by a function of connections, first of all by tightening of bolts. The results can be obtained in laboratory in difficult way. Only an expensive research on whole support structure can give relevant knowledge. The contribution therefore deals with computer modelling of behaviour of yielding bolt connections with different tightening of bolts. The aim is to determine the load bearing at different tightening screws. Another parameter that significantly affects loading capacity is the value of friction coefficient in contacts between elements of joints.

Keywords: yielding arch support, mining roadways, bearing capacity, FEM, ANSYS

1 Introduction

The loading capacity of a friction connection (maximal value of normal forces borne by connection without slip of segments) plays important role in a static design of arch supports. The construction of connection as regards to strength of its different parts and tightening of screws introduce meaningful technical aspects of a function of yielding supports. Opinions on the optimal value of screw tightening are not unified. Therefore we modeled the most applied screw connection with three pairs of bolts (used in Germany, Poland and Czech Republic (Junker et al., 2009) – Figure 1 and 2. We investigated behaviour and condition of single parts with three values of tightening moment and relations between values of screw tightening and bearing capacity of connection for different friction coefficients.

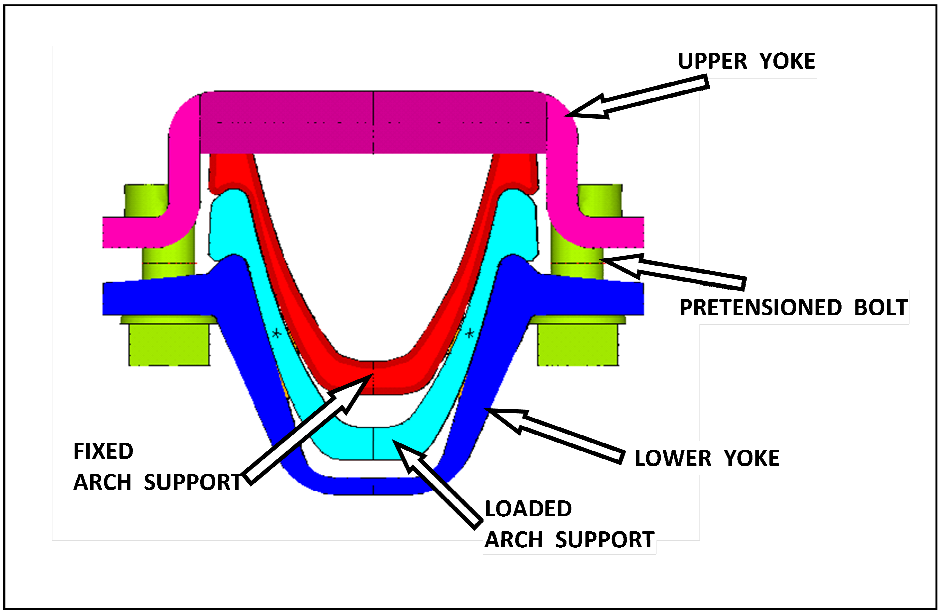

Image 5 – Yielding connection, front view

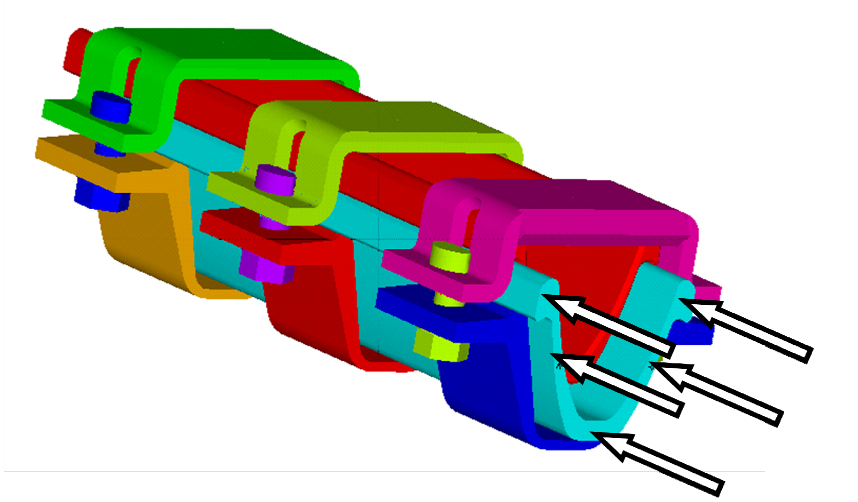

Image 2 – Yielding connection, 3D view

2 Methodology

Computer modeling of clamp connections was performed using finite element program ANSYS. The issue of finding a clamp static loading capacity was hard non-linear structural problem (Horyl and Snuparek, 2012). Because we have here large displacements and strains, non-linear steel properties and a lot of contacts. Large displacements means that stiffness matrix of the whole structures depends on unknown deformation parameters. For non-linear material behaviour we used bilinear material properties with three values: E Young's modulus of elasticity, σ_y yielding stress and ET tangent modulus of plasticity. Our structure has three kinds of materials, Table 1.

Table 8 Material properties of steel parts

Structure Part	Material properties		
	Young's modulus of elasticity E [MPa]	Yielding stress σ_y [MPa]	Tangent modulus of plasticity E_T [MPa]
Steel support	200,000	350	1,680
Upper yoke and lower yoke		295	1,783
High strength connecting screw		640	2,170

The geometry of computer model was created from designs of all four parts our structure. It was made in Wokbench Ansys 14.0. Because all boundary conditions were symmetric we created only one half of structure, see Figure 3. Discretization was done with solid, contact and pretensioned bolt elements Table 2.

Table 2 Used finite elements

Type of Elements	ANSYS Finite Elements	Number of Elements
Solid elements	SOLID186, SOLID187	75,941
Contact elements	CONTA174, TARGE170	26,311
Pretensioned bolts	PRETS179	3

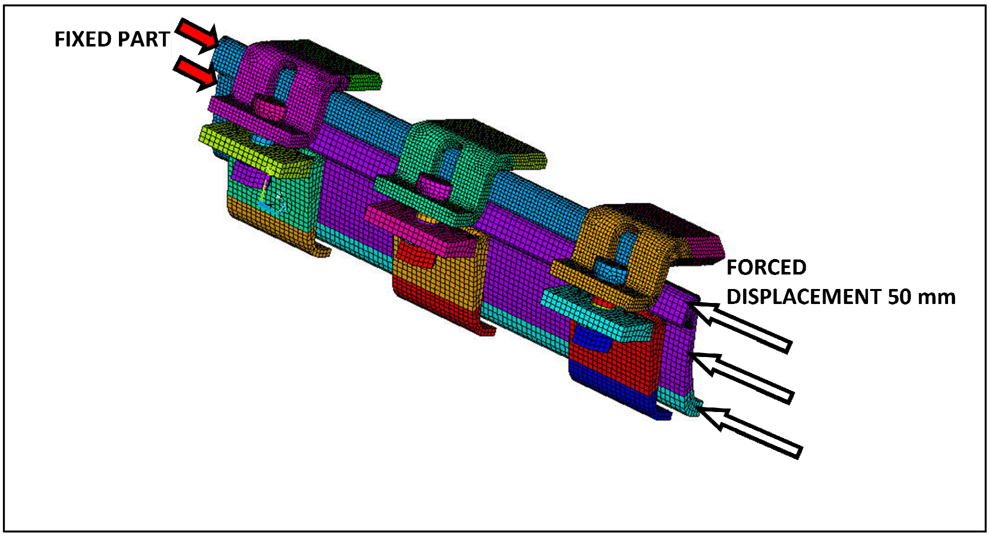

Image 3 – Mesh of finite elements and displacement loading

The total number of structure elements was 102,255, 308,643 nodes and 920,035 number of equations. Number of equations is the number of unknown deformation parameters of the system. The load was divided in two loading steps: pretension of connecting bolts and deformation loading one support. The second support was fixed. The three torque values were applied on screws, namely 350 Nm, 400 Nm and 450 Nm. These values of torque correspond next values of preload forces, namely 100,966 N, 115,390 N and 129,814 N. Outside torque values affects mainly the value of loading capacity coefficient of friction in the contacts pairs. That is why calculations were performed with a coefficient of friction from 0.12 to 0.32 in steps of 0.04. For solution was chosen full Newton-Raphson method. Calculations were carried out on a computer of Supercomputing Centre VSB-Technical University of Ostrava, number of used cores was 9. One calculation took between 11 - 15 hours.

3 Results

An important factors for the assessment of mechanical structures after the loading are primarily total displacement, value equivalent plastic strain ε_{pl} and von Mises stress σ_e . Equivalent stress (also called von Mises stress) is often used in design work because it allows any arbitrary three-dimensional stress state to be represented as a single positive stress value. Equivalent stress is part of the maximum equivalent stress failure theory used to predict yielding in a ductile material. The equivalent plastic strain gives a measure of the amount of permanent strain in an engineering body. The equivalent plastic strain is calculated from the component plastic strain (Ansys Release 14.0, 2011).

3.1 Load step 1 - Implementation bolt preload

Deformed structure after tightening the screws for 450 Nm shown in Figure 4.

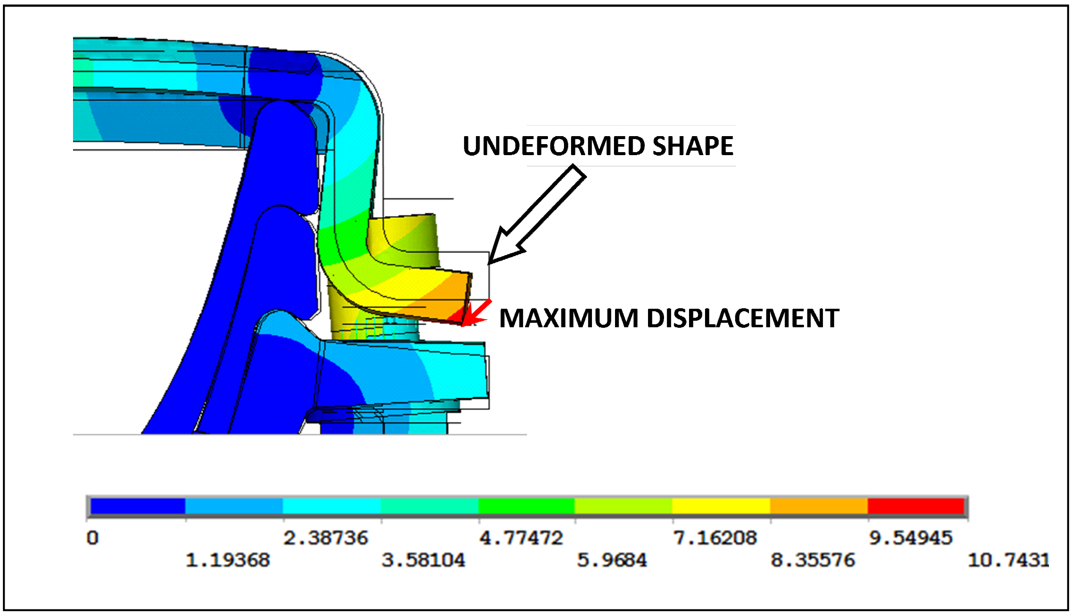

Image 4 – Deformed structure, place of maximum deformation

The largest displacement was found at the end of the upper yoke and up to 10.7 mm. Although the offset value is significant to touch other parts of the joints does not occurs. The functionality of the joint is maintained. Mainly results for the first load step are grouped within Table 3.

Table 3 Mainly results from bolt preload

Description of the Variables		Values		
Torque [Nm]		350	400	450
Maximum displacement [mm]		8.1	9.2	10.7
Support	σ_e [MPa]	409	414	402
	ε_{pl} [1]	0.005	0.01	0.03
Upper yoke	σ_e [MPa]	572	623	710
	ε_{pl} [1]	0.16	0.183	0.24
Lower yoke	σ_e [MPa]	326	344	363
	ε_{pl} [1]	0.02	0.03	0.04
Bolts	σ_e [MPa]	1064	1125	1254
	ε_{pl} [1]	0.197	0.22	0.28

It should be noted that in all parts of the clamp is exceeded the yield point. This means that even after unloading remain in the construction permanent deformation. As will be discussed below, it is usually a very small area, which should not affect the functionality of the coupling. Location of very small plastic areas for steel support are given in Figure 5. The upper yoke plastification occurs in small areas of contact of the head bolt, see Figure 6. But value of equivalent plastic strain is high, it means that in these areas arise dimples. Few intensive areas plastification occurring on lower yoke, Figure 7. A high degree of plastification is on the bolt, but it is a small area in contact with the screw head in Figure 8.

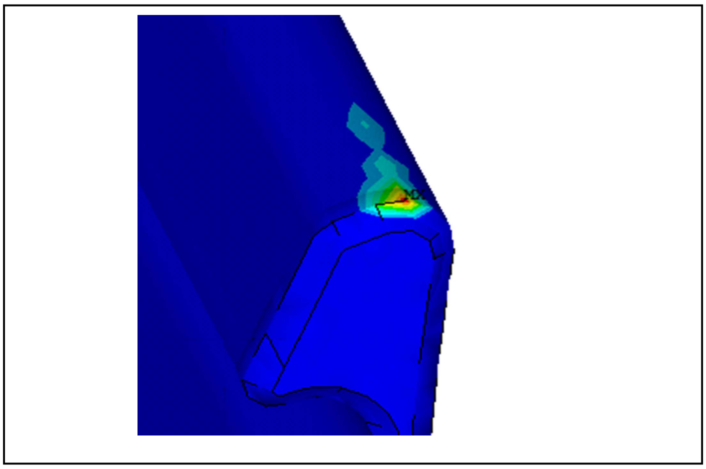

Image 5 – Plastic areas on steel support, ε_{pl} = 0.026

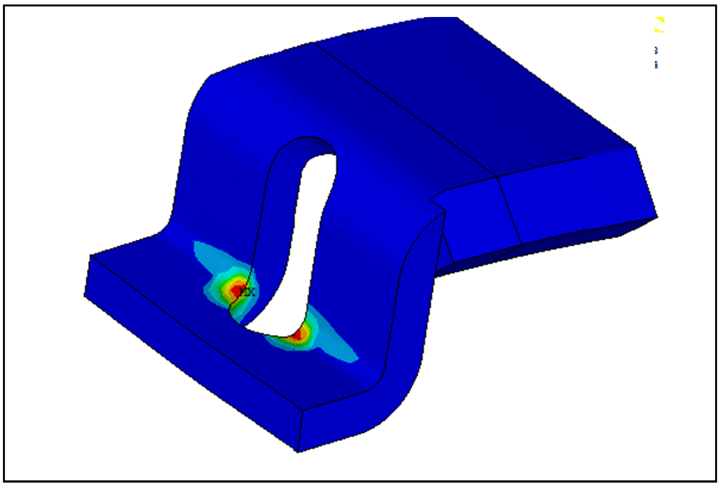

Image 6 – Plastic areas on upper yoke, ε_{pl} = 0.24

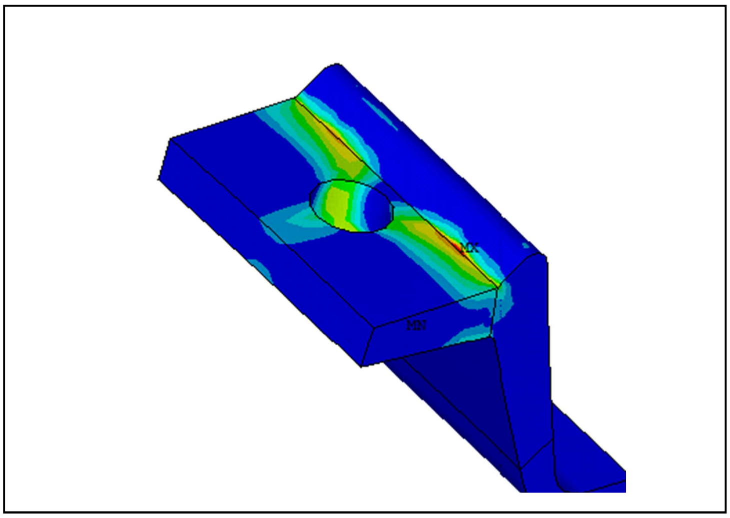

Image 7 – Plastic areas on lower yoke, ε_{pl} = 0.04

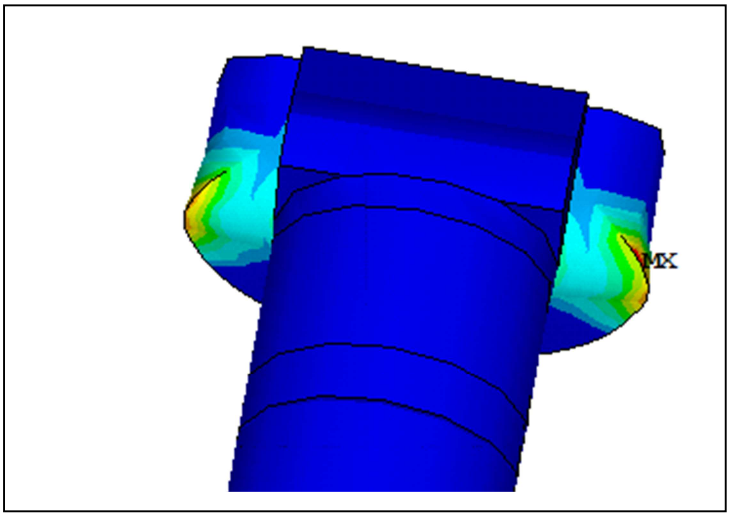

Image 8 – Plastic areas on bolts, $\varepsilon_{pl} = 0.28$

3.2 Load step 2 - Implementation of forced displacement

Courses nonlinear calculations are documented in the following two pictures. The first convergence calculation is displayed depending on the gradual loading, Figure 8. The second picture shows speed of load increment, Figure 9.

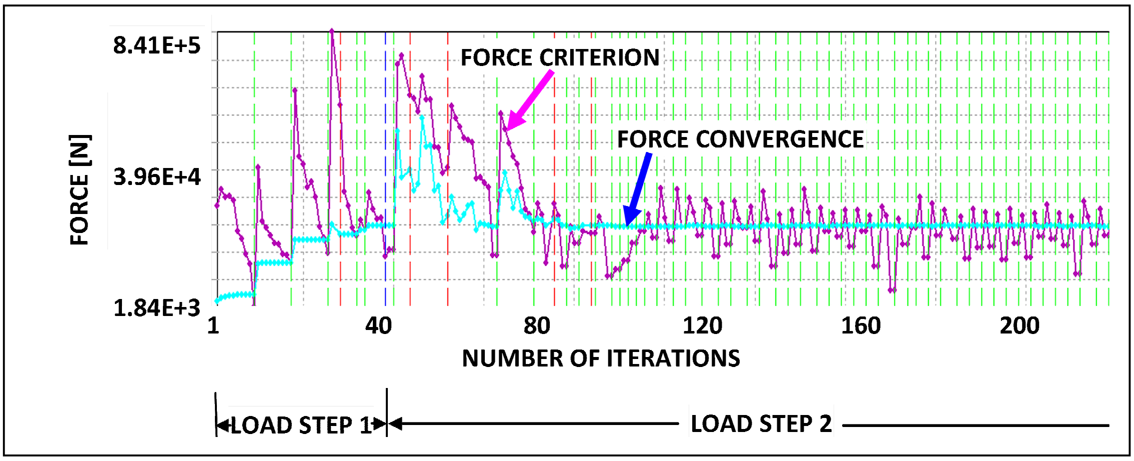

Image 9 – The typical course of force convergence

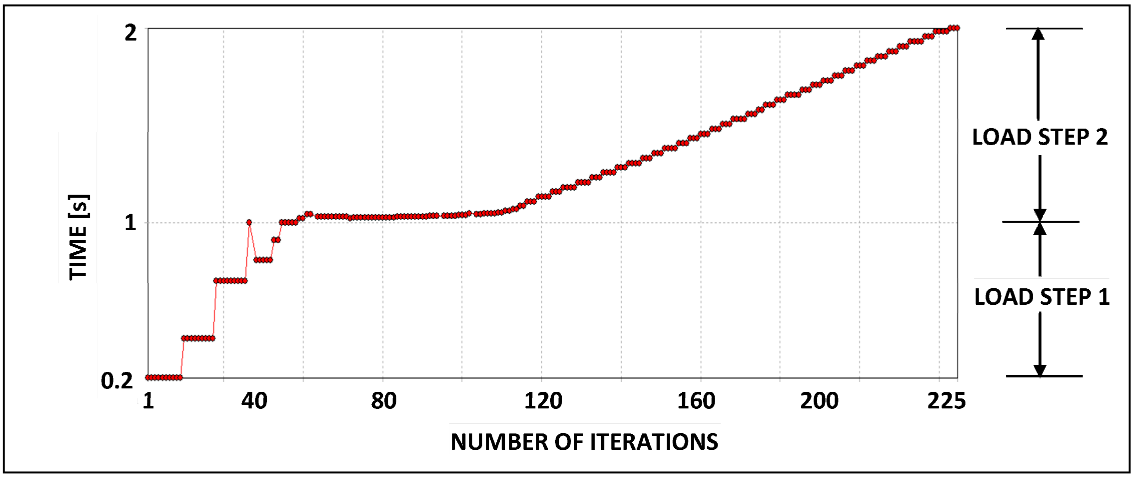

Image 10 – Speed of load increment

Convergence in each substep of the Newton-Raphson method is satisfied when in all nodes of model is fulfilled force convergence condition. Another criterion is the increment value of equivalent plastic deformation, maximum could be less then 0.15. Load step 1 was calculated in the range of 4 to 7 substeps, while the second load step from 26 to 36 substeps. In each substeps had to be calculated a few iterations to achieve convergence. Total number of iterations was around 225.

The main results of the numerical simulations are shown in Figure 10. Values of the critical axial force are shown, which occurs when the joint is slipping. We are speaking about loading capacity of yielding connection. The values are dependent on the coefficient of friction in the contacts and the values of torque. Dependencies are almost linear.

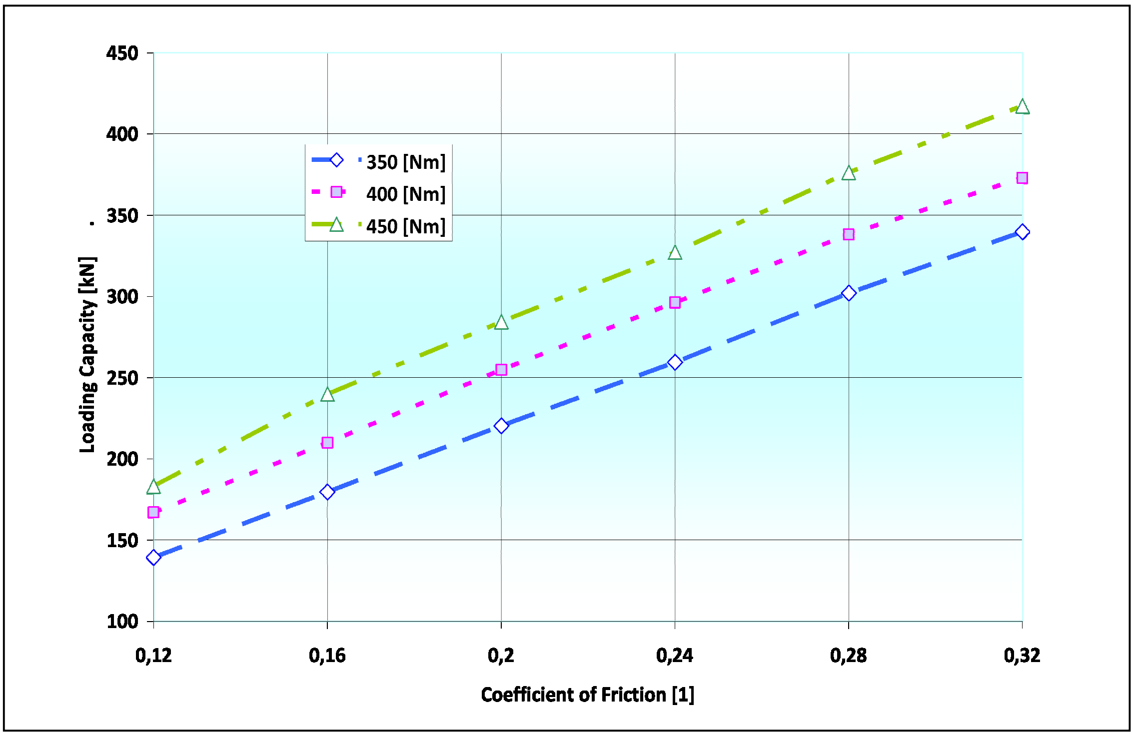

Image 11 – Dependence loading capacity of yielding connections on the values of the friction coefficient and torque

Resistance values are consistent with those published in the literature (Šňupárek and Konečný, 2010; Janas, 1990). The ranges of these values and their high dependence on the coefficient of friction in contacts have not yet been published. The minimum value of resistance was 139 kN to 350 Nm of torque and the friction coefficient 0.12, the highest value of 417 kN to 450 Nm of torque and the friction coefficient 0.32.

Areas of plastification in this load step do not change significantly. Decisive for the formation of plastic regions is load step 1.

4 Conclusions

Load the preload screw causes the creation of plastic areas in all parts of the connection. They are just a very small areas, which should not affect the functionality of the connection. The ranges of loading capacity of yielding connections values and their high dependence on the coefficient of friction in contacts have not yet been published. The minimum value of resistance was 139 kN to 350 Nm of torque and the friction coefficient 0.12, the highest value of 417 kN to 450 Nm of torque and the friction coefficient 0.32.

References

ANSYS® Mechanical, 2011, Release 14.0, Help System, ANSYS, Inc.

HORYL P., SNUPAREK R., 2012. Reinforcing Measures of Steel Roadway Support in Rockburst Prone Areas. *Archives of Mining Sciences,* Vol. 57 No. 1, pp. 193-208.

JANAS P., 1990. Dimensioning of roadway supports in conditions of Ostrava-Karvina Coalfield. In.: *Proceedings of World Mining Congress,* Novosibirsk, Russia, pp 124-129.
JUNKER et al., 2009. *Strata control in in-seam roadways*. Essen: VGE Verlag GmbH.
SNUPAREK R., KONECNY P., 2010. Stability of roadways in coalmines alias rock mechanics in practice. *Journal of Rock Mechanics and Geotechnical Engineering,* Vol. 2 No. 3, pp. 281-288.

Acknowledgement

The paper has been done in connection with project IT4Innovations Centre of Excellence project, reg. no. CZ.1.05/1.1.00/02.0070, supported by Operational Programme "Research and Development for Innovations" funded by Structural Funds of the European Union and state budget of the Czech Republic.

Contact address:

prof. Ing. Petr Horyl, CSc. dr.h.c.
VŠB – TU Ostrava, 17. listopadu 15, 708 33 Ostrava-Poruba

MATERIAL PARAMETERS ESTIMATION OF SMALL PUNCH TEST BY TWO VARIANTS OF GENETIC ALGORITHMS

JOZEF HRABOVSKÝ[1], PETR LOŠÁK[2], JAROSLAV HORSKÝ[1]

1) Heat transfer and fluid flow laboratory, 2) Institute of solid mechanics, mechatronics and biomechanics, Brno University of technology

Abstract:

The issue of material data and obtaining parameters is fundamental to all engineering applications. To perform required analyses and obtain relevant results it is necessary to have sufficient input data and information. For designing and solving a given problem it is crucial to know material properties. We have several methods for obtaining material data. One method is the Small Punch Test (SPT). This method is considered non-destructive. The experimental samples for SPT have small dimensions and therefore can be obtained from a tested structure without significant destruction. When respecting certain assumptions, this method can be considered equivalent to tensile experimental procedure. By using this method it is possible to measure the same parameters as when using a tensile test. The typical results of the SPT measurements are force-deflection curves. It is possible to use numerical simulation to convert a force-deflection curve to a stress strain curve. This paper presents two methods of determining suitable material parameters for transformation of force-deflection curves to stress-strain curve for defined steel at elevated temperature at the Ansys Workbench. To determine the appropriate transformation, two types of material models (Ramberg-Osgood model, Chaboche model) and two variants of genetic algorithms were used. For the first variant, the optimization toolbox implemented in the Ansys Workbench was used. For the second variant, a genetic algorithm from the Python scripting language into the Ansys Workbench was implemented. The presented results show the advantages and disadvantages of considered methods and it is possible to select a method for many engineering applications. The estimation of the material parameters were studied for steel with a higher content of silicon.

Keywords: Small Punch, Chaboche model, Ramberg-Osgood model, genetic algorithm

1 Introduction

To obtain relevant mechanical properties it is possible to use several methods. Most widely used methods of studying the mechanical properties are tensile tests, bending tests or impact tests. All these methods are so-called destructive. The specimen for measurement have relatively high dimensions. Therefore it is not possible to create the specimen without destruction of the initial part. If it is needful to maintain the original part and measure some changes in mechanical properties it is possible to use nondestructive measurement. One of these methods is Small Punch Test (SPT) [1].
Generally this test is used in energy industry, when it is necessary to determine the mechanical properties of material that has been exposed to environmental influences or load without significant damage of the device. SPT can be classified into two types of tests. The first type of test is pushing of the specimen at a constant speed. The results of this test are the relationships of force on displacement. This type of test is considered as equivalent to tensile test because it is possible to find the same material characteristics. Small Punch Test at constant deflection rate is referred to as the SPT-CDR. The second type of SP test is pushing of the specimen at constant force. This type of test is used as a creep test and it is referred to as the CF-SPT. The result of this test is the time relationship of deflection [2]. For both tests it is typical that the specimen is pushed up to rapture. The major benefits of these tests are small specimens and simple possibility of measurements at elevated temperatures.

Applied method was designed to identify the mechanical properties of selected steel. As already written the typical result of the SPT is force – deflection curve. To obtain typical mechanical properties (Young´s modulus, yield strength and so on) it is necessary to convert measured force – deflection curve to stress – strain curve. It is possible to use two basic approaches for the conversion of measured curve. The first approach is based on the empirical equations. This approach is very easy but not universal because the equation was defined for specific conditions and material. The second method which is more complicated but appropriate for universal application is FEM analysis combined with optimization. In this paper the second approach was used. The FEM analyses and optimization were prepared in Ansys Workbench. Two types of material models and two types of optimization methods were applied. The first method was based on the possibilities of Ansys Workbench. The Chaboche´s material model defining the monotonic history of sample loading and direct optimization was used. For the second method the owned Ramberg – Osgood model and optimization tool were created into the Ansys Worbench through the Python script language. For both methods the genetic algorithm was used as optimization approach. Described methods were applied on tested specimen at elevated temperature 600°C.

2 Experimental procedure

As already mentioned in the introduction chapter, Small Punch Test (SPT) was chosen to study the mechanical properties. Experimental measurements of mechanical properties were prepared to make it possible to measure the mechanical characteristics of defined steel. For preparation of samples the steel with higher silicon content was selected. The selected steel was subjected to chemical analysis and chemical composition is given in Table 1.

Table 9 Chemical composition of studied steel

	C (%)	Mn (%)	Si (%)	P (%)	S (%)	Cr (%)	Cu (%)	Sn (%)
Specimen	0.010	0.240	1.140	0.006	0.011	0.050	0.030	0.010

The small punch tests have been performed on the experimental apparatus constructed by IPM ASCR (see Image 1). Schematic illustration of dimension and position of the specimen at the SPT is shown in Image 2. The SPT can be simply described as following: between the upper and lower die specimen is fixed, then the specimen is loaded through the ball until the material failure occurs. In this case the ceramic ball for loading has been used. SPT was carried out at elevated temperature 600°C.

For measurement of required mechanical properties the SPT at constant speed was considered. The value of speed at measurements was set to 0.006 mm/s. The speed of deflection was measured through sensor Hottinger-Baldwin. This measurement also considered the elastic deformation of bottom frame of SPT apparatus. It is possible to neglect the elastic deformation at measurement of small values of forces.

Measured curve at elevated temperature is presented in Image 3. The force – deflection curve is very important characteristic, but even more useful characteristic for engineering applications is the stress – strain curve. The conversion of the force – deflection curve to stress – strain curve methodology is descripted in next chapter.

Image 6 SPT apparatus

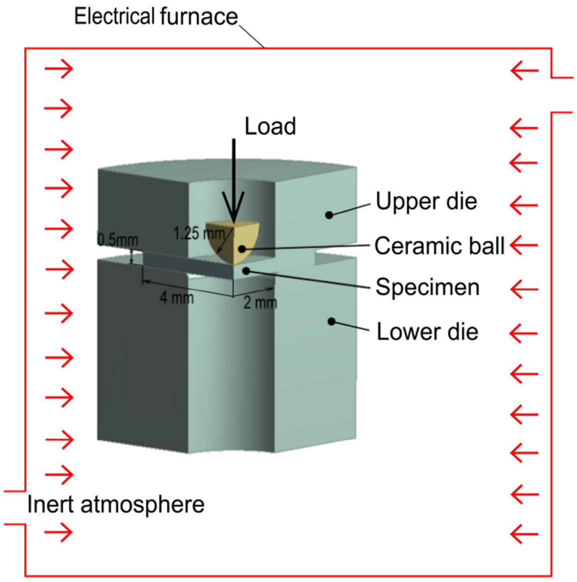

Image 7 Schematic illustration of specimen fixation

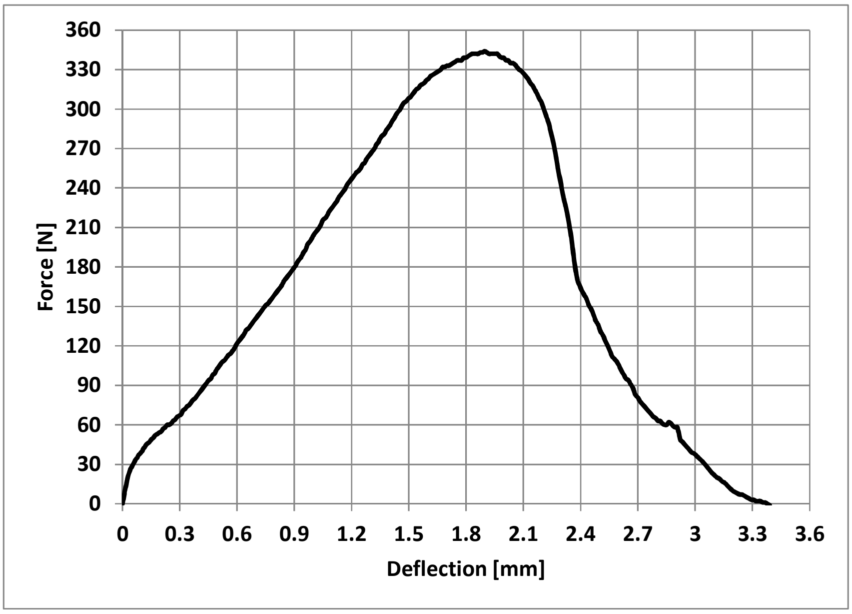

Image 8 Measured force –deflection curve at elevated temperature 600°C

3 Optimization of material parameters

The aim of optimizing the material parameters was to find suitable parameters for converting the measured curve to curve describing the mechanical response of the material on the loading. To find appropriate parameters and to obtain basic characteristics, which are the Young´s modulus and the yield stress, ANSYS Workbench was selected. In the classical SP test carried out on samples of steel, characteristics of the steel (such as Young´s modulus, yield stress, ultimate stress) are usually known from conventional tensile tests on which it is possible to correlate SPT measurements with a tensile test. Because in this case SPT measurement was carried out at elevated temperature, these basic characteristics of studied steel were not known, therefore it was necessary to include them between searched parameters for optimization.

3.1 FE model

FE model for the numerical simulation of the optimization task was based on the actual geometry of the experimental equipment of SP tests. For the numerical model the upper and lower die were considered, the specimen with a defined thickness that was measured for each sample and the indenter (ceramic balls) see Image 4. The whole task was designed as a two-dimensional and therefore the model of geometry was prepared as two-dimensional axisymmetric. The actual model was axisymmetric, so it was possible to apply this simplification and significantly reduce the computational complexity tasks with regard to the relevance of the description of material properties of the sample. The components were coherent and their properties corresponded to real conditions. Individual components of the numerical model of geometry were connected through the contact surfaces. Contact areas were thus defined between the bottom and top of the sample with bottom respectively upper and lower die. Further contact was then defined between the top of the sample and the puncher. All contacts were set up as contacts with friction. Frictional coefficient between the specimen and the die was defined by the value of 0.5. Friction coefficient between the indenter and the specimen was considered as one of the parameters. The corresponding geometry models are presented in Image 4.

On this model an optimization task for finding suitable parameters describing material behavior of the specimen was carried out and transformation of measured curve force vs. deflection to stress strain curve was performed.

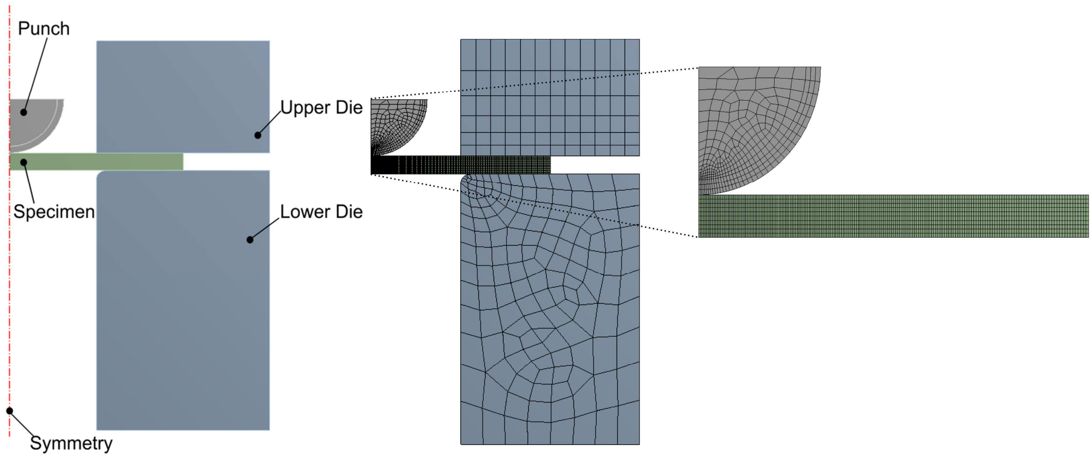

Image 9 Model of geometry (left), FE model (right)

3.2 FE analalysis with optimization procedure (case 1)

For FE analysis the material model of each part of geometry was applied. For upper and lower die and ceramic ball the linear-elastic model was considered. The Chaboce´s kinematic material model was used for specimen. Chaboche´s material model can be defined by five kinematic hardening models for simulation of complex cyclic deformation behavior of materials. This material model contains several parameters describing the material behavior. Due to the combination and the inclusion or deletion of the parameters it is possible to capture the phenomena. With appropriate treatment it is possible to use this material model to describe a monotonic uniaxial loading [3]. In this case, the equation with only two kinematic models and parameter γ_2 equal to zero was considered. From the general equation of the material model it is then possible to derive a simplified form for the description of monotonic loading, which was also loading during the SP test, equation (1) [4]. Individual members of the equation determine the slope and the course of the stress strain curve. For the formation of Chaboche´s model it is necessary to have experimental data from which the necessary coefficients of Chaboche´s model are identified. Estimation of parameters can be performed by using mathematical approaches such as nonlinear regression with initial estimate of required coefficients [5]. In numerical modeling and finding the optimal parameters for the specimen measured during the SP test the value of stress depending on the strain were not known, as usual, but the curve was measured as a function of the deflection. Therefore, the necessary parameters of Chaboche´s model were parameterized and searched by optimization method based on several values of force and corresponding to the value of deformation selected from the whole measured process.

$$\dot{\alpha} = \sum_{i}^{n} \dot{\alpha}_i = \frac{2}{3} \sum_{i}^{n} C_i \dot{\varepsilon}^{pl} - \gamma_i \alpha_i \dot{\hat{\varepsilon}}^{pl} + \frac{1}{C_i} \frac{dC_i}{d\theta} \dot{\theta} \alpha_i \tag{1}$$

$$\sigma_x = \sigma_Y + \frac{C_1}{\gamma_1}(1 - e^{-\gamma_1 \varepsilon_{px}}) + C_2 \varepsilon_{px} \tag{2}$$

For optimization process a total of six parameters were considered. Two basic parameters as Young´s modulus, frictional coefficient between ceramic ball and specimen and four parameters as yield strength, C_1, γ_1, C_2 which represent the Chaboche´s material model. All these parameters were imported into the optimization procedure. The optimization procedure was based on the toolbox Direct Optimization which is part of Ansys Workbench. This toolbox allows to use several optimization methodologies for example screening method, “NLPQ” – gradient method and “MOGA” – iterative multi-object genetic alghoritm. This “MOGA” methodology was applied as optimization method to find the appropriate values of selected parameters. The “MOGA” is a hybrid variant of the NSGA-II (Non-dominated Sorted Genetic Algorithm-II) based on controlled elitism concepts. The Pareto ranking scheme is done by a fast, non-dominated sorting method that is an order of magnitude faster than traditional Pareto ranking methods. The constraint handling uses the same non-dominance principle as the objectives, thus penalty functions and Lagrange multipliers are not needed. This also ensures that the feasible solutions are allways ranked higher than the unfeasible solutions. [5]

The results of optimization of material parameters for specimen at appropriate temperature are presented in Tab. 2 and Image 5. In Image 5 the comparison of the measured and optimized force – deflection curve is shown. The average difference between selected measured and calculated points is 6.64%. The Chaboche´s material model parameters obtained from optimization procedure are presented in Table 2. The optimized parameters were used in equation 2 and the stress – strain curve was created (see Image 6).

Table 10 Optimized material parameters (MOGA method)

Temperature [°C]	Friction Coefficient [-]	E [MPa]	Yield Strenght [MPa]	C_1 [MPa]	γ_1 [-]	C_2 [MPa]
600	0.3374	24633.0	56.1	4551.4	141.5	125.9

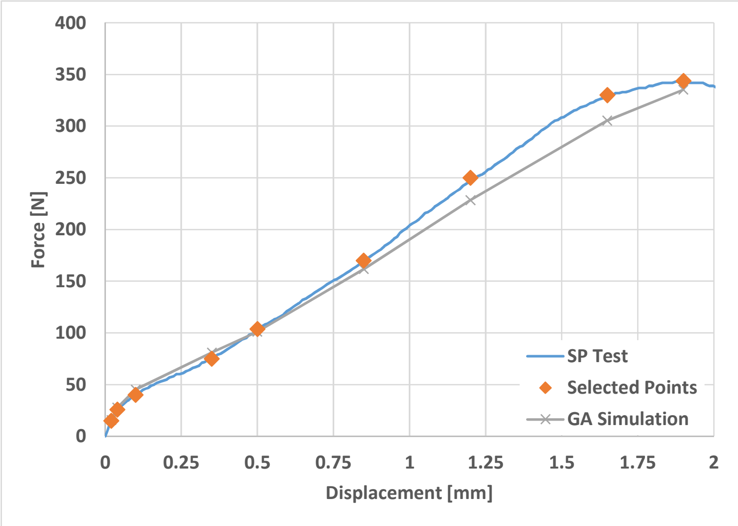

Image 10 Comparison of measured and optimized force – deflection curve (MOGA method)

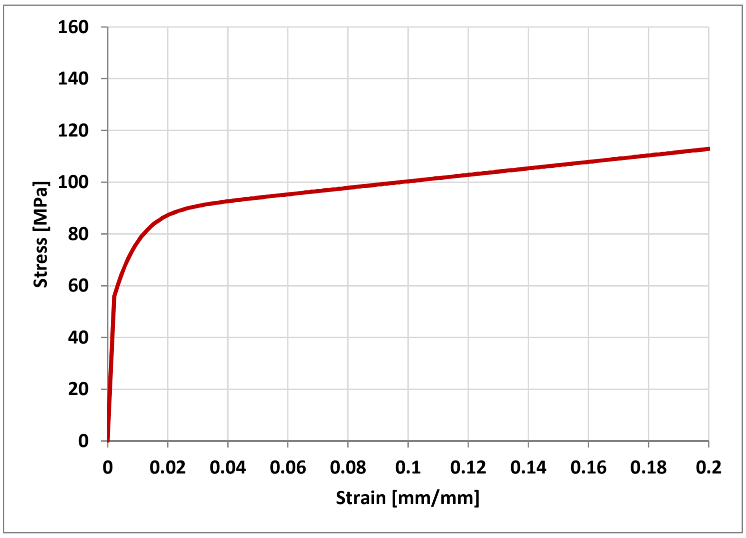

Image 11 Evaluated stress – strain curve (MOGA method)

3.3 FE analalysis with optimization procedure (case 2)

The model of geometry and material of each part, except for the specimen, remained the same as in the case 1. For the specimen, the material described by the Ramberg-Osgood relation (3) was used. The relation is derived and described in detail for example in [6]

$$\varepsilon = \frac{\sigma}{E} + K\left(\frac{\sigma}{E}\right)^n \tag{3}$$

K and *n* are Ramberg-Osgood's parameters. The first member in the equation, σ / E, describes the linear portion of the material behavior and the second member describes the plastic portion of the total deformation.

According to [6], the equation can be modified using the proof stress $\sigma_{0.2}$ which yields in form (4).

$$\varepsilon = \frac{\sigma}{E} + 0.002\left(\frac{\sigma}{\sigma_{0.2}}\right)^n \tag{4}$$

Thus in the optimization process it was sufficient to find only Young's modulus *E*, exponent *n* and the proof stress $\sigma_{0.2}$. The fricion coefficient between the specimen and the ceramic ball was also included in the optimization variables. The objective function (5) was used to assess the appropriateness of the idividual values of the optimization variables.

$$\Psi = \sum_{i=1}^{n} \left|F_{si} - F_{ei}\right| w_i \tag{5}$$

n is number of the steps of the numerical simulation, F_{si} is the force which the puncher was acting on the specimen in i-th step. F_{ei} is the force obtained from experiment which corresponds to the same displacement. Parameter w_i is the weight coefficient that allows to modify the significance of the particular points on the force-displacement curve.

Since model of material based on the Ramberg-Osgood relation is not implemented into the ANSYS Workbench environment, the special Python script was written. Based on the relation (4) the script fills the table of multilinear material model by the plastic strains and corresponding stresses. Python script also controls the optimization algorithm, in this case Genetic Algorithm (GA), which is described in detail for eg. In [7]. The result of optimization procedure is shown in Image 7. Found coefficients of Ramberg-Osgood relation are summarized in Table 3. The average difference between selected measured and calculated points is 5.96%.The optimized parameters were applied in equation 4 and the stress – strain curve was created (see Image 8).

Table 11 Optimized material parameters (GA method)

Temperature [°C]	Friction Coefficient [-]	E [MPa]	Yield Strenght [MPa]	n [-]
600	0.284	104090.0	26.8	2.798

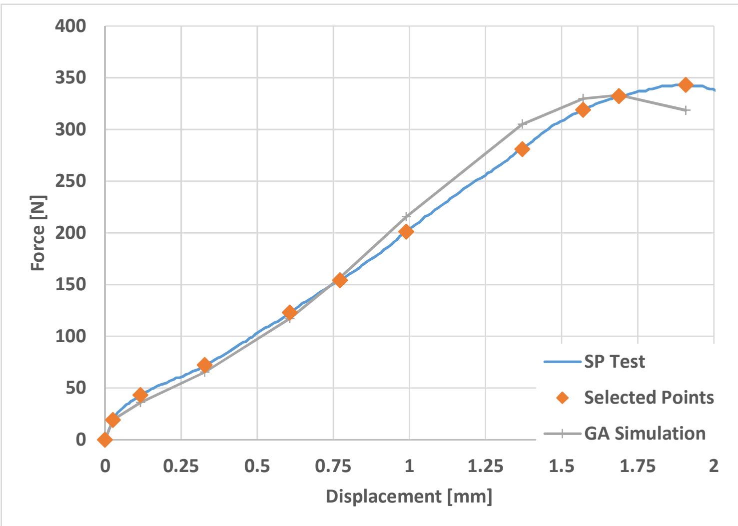

Image 12 Comparison of measured and optimized force – deflection curve (GA method)

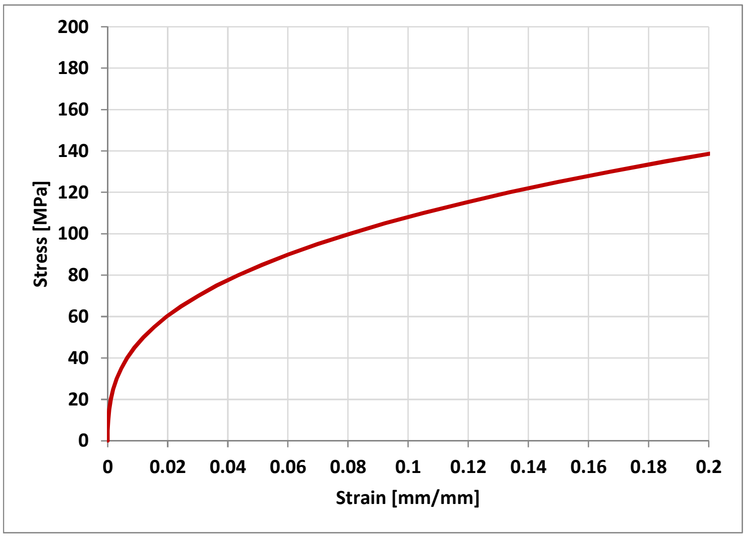

Image 13 Evaluated stress – strain curve (GA method)

4 Conclusion

The presented work is focused on the material parameters estimations which define mechanical properties. The material parameters estimation was carried out for result obtained from Small Punch test. The SP test was performed on selected steel at elevated temperature (600°C). To obtain the mechanical properties of material, curve measured during SP test and optimization task in computational program ANSYS Workbench was prepared. The optimization task was combined with numerical analysis and aimed to find suitable material parameters so that the response during punching of the specimen best fitted the measured force vs. deformation curve. When finding suitable parameters it was possible to reconstruct the stress - strain curve. The estimation of material parameters were carried out in two cases. For the first case the Chaboche´s material model for material behavior definition and MOGA optimization method were used. In the second case the Ramberg – Osgood description of material behavior with GA optimization procedure were applied. For the second case Ansys Workbench with Python scripts defined the Ramberg – Osgood model and GA alghoritm was used. The optimization procedures which were performed in both cases led to required results. For both cases the correlation between measured and calculated force – deflection curves was done and average difference between measured and calculated values do not exceed 10%. Based on the obtained results from optimization process it was possible to reconstruct the stress – strain curve of tested material. From all optimized variables of both cases just E, Yield Strength and Frictional Coefficient can be directly compared. All these variables show high differences. The first reason of the differences in results can be produced by combination of material and temperature. The material which was tested is not suitable to be used at elevated temperatures. This means that the measured curve can be affected by unstable phases in material at elevated temperatures. The second reason is more obvious and relates to used material model in both cases. In the first case the fully-fledget Chaboche´s material model was used and in the second case just the description of stress – strain curve through the Ramberg – Osgood mathematical model was considered. This qualitative difference of both approaches have impact on the results. The big advantage which was presented in this paper is methodology of direct material parameters estimation through the Ansys Worbench without additional programs.

References

[1] KAMEDA J., MAO X., 1992, Small-punch and TEM-disc testing techniques and their application to characterization of radiation damage, Journal of materials science, 27, 983-989

[2] MILIČKA K., DOBEŠ F., 2006. Small punch testing of P91 steel. Int. J. Pressure Vessels Piping, 83, 625–634.

[3] HALAMA R., ROBOVSKÁ H., et al., 2007. Stanovení konstant Chabocheova nelineárního kinematického modelu zpevnění, 9th International scientific conference, Applied mechanics, Malenovice, Czech Republic.

[4] IMAOKA S., 2008. Chaboche nonlinear kinematic hardening model, Memo Number:STI0805A, Ansys Release: 12.0.1

[5] ANSYS Release: 15.0 help, ANSYS, Inc. http://www.ansys.com/

[6] RAMBERG W., OOSGOOD W.R, 1941. Determination of Stress-strain Curves by Three Parameters, Technical Note No. 503, National Advisory Committee on Aeronautics, (NACA),

[7] HAUPT R.L., HAUPT E.H., Practical Genetic Algorithms, A Wiley-Interscience publication, ISBN 0-471-45565-2

Acknowledgement

"This work is an output of research and scientific activities of NETME Centre, regional R&D centre built with the financial support from the Operational Programme Research and Development for Innovations within the project NETME Centre (New Technologies for Mechanical Engineering), Reg. No. CZ.1.05/2.1.00/01.0002 and, in the follow-up sustainability stage, supported through NETME CENTRE PLUS (LO1202) by financial means from the Ministry of Education, Youth and Sports under the „National Sustainability Programme I“."
The paper presented has been supported by project CZ.1.07/2.3.00/30.0005 of Brno University of Technology.

Contact address:

Ing., Ph. D, Jozef Hrabovský
Heat transfer and fluid flow laboratory, Brno University of technology, Technická 2896/2, 616 69 Brno, Czech Republic

STUDIE VLIVU MÍRY ROZTRŽENÍ TĚSNÍCÍHO SVARU LAMELOVÉ PÁSNICE NA VELIKOST FAKTORU INTENZITY NAPĚTÍ

PAVEL HRUBÝ, ONDŘEJ KRŇÁVEK, ALEŠ NEVAŘIL, LUCIE TOTKOVÁ
Centrum AdMaS, Fakulta stavební, VUT v Brně, Veveří 95, 602 00 Brno, Česká republika

Abstract: This study deals with cracks in welded joints of lamellar flanges of the steel-concrete composite bridge. The main emphasis is put on the comparison of stress intensity factors for different crack configurations. Four variants of bottom surface rupture of seal weld are analyzed. The task is solved comprehensively with the use of submodeling technique. Boundary conditions for four different submodels with cracks are obtained by analysing the global behavior of the bridge. In the final part of study are presented stress intensity factor waveforms along the length of the weld.

Keywords: crack, lamellar flange, steel-concrete composite bridge, stress intensity factor, welded joint

1 Úvod do problematiky

Dnešní stavitelství se člení do mnoha různých odvětví, přičemž jedním z těch tradičních je stavitelství mostní. V rámci tohoto oboru se můžeme setkat s několika základními typy mostních děl, a to včetně mostů vzpěradlových, jež jsou často navrhovány za účelem překlenutí hlubokých údolí (Stráský, 2001, s. 25). Modifikace tohoto typu mostu byla zvolena též pro přemostění Lochkovského údolí, které kříží trasu jihozápadního okruhu Prahy dokončeného v roce 2010. Zmíněný most o celkové délce 461 metrů je tvořen železobetonovou spodní stavbou spolu se spřaženou ocelobetonovou nosnou konstrukcí. Ta je představována jednokomorovým otevřeným ocelovým průřezem doplněným o dvojici vnějších a jeden vnitřní vzepřený podélník, jež jsou společně s horními pásnicemi komory spřaženy s železobetonovou mostovkou.

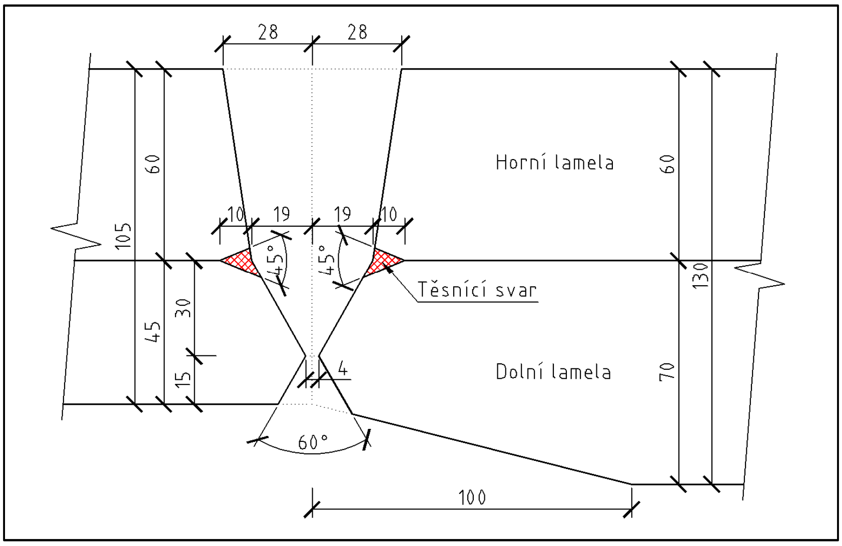

Obrázek 14 – Schéma svarového spoje 7213

Jeden ze základních rysů mostů přes hluboká údolí tvoří relativně velké délky mostních polí, přičemž v případě výše zmíněného mostu činí délka nejdelšího, středního pole 99,3 metru. Tato skutečnost ve spojení s navrženým nosným systémem a konstrukčním uspořádáním příčného řezu měla za následek nutnost návrhu velkých dimenzí horních pásnic ocelové komory mostu, a to především v oblastech nad podporami. Praktická realizace ocelových pásnic velkých tlouštěk však naráží na problémy s výrobou, a proto byla v případě mostu přes Lochkovské údolí zvolena možnost návrhu pásnice lamelové. Tento konstrukční prvek je přitom tvořen několika na sobě umístěnými ocelovými lamelami svařenými po obvodě konstrukčními těsnícími svary. Spojování jednotlivých montážních dílů pásnice po délce mostu je pak prováděno za pomoci nosných (tupých) výplňových svarů (viz obrázek 14).

V průběhu montáže mostu přes Lochkovské údolí byla po provedení jednotlivých výplňových svarů realizována ve shodě s předpisy jejich nedestruktivní kontrola. Při těchto kontrolních zkouškách byla v rámci přiléhajících těsnících svarů zjištěna ve spojích 6014, 7213 a 7214 přítomnost několika přípustných i nepřípustných indikací (Vejvoda, 2011). Předmětem následující studie je vliv míry a polohy roztržení dolního líce těsnícího svaru spoje 7213 na velikost vypočteného faktoru intenzity napětí.

2 Teorie výpočtu faktorů intenzity napětí

Použítí klasických postupů metody konečných prvků k zachycení chování v okolí kořene trhliny je vzhledem k přítomnosti singularity v dané oblasti velmi obtížné. Z tohoto důvodu byly navrženy speciální přístupy, které jsou schopny dané chování v kritickém okolí čela trhliny postihnout. Jedná se například o použití speciálních konečných prvků, metodu virtuálního prodloužení trhliny, metodu J-integrálu, metodu interakčního integrálu a dalších přístupů, jejichž shrnutí i bližší popis uvádí například Kuna (2013).

Při řešení úloh v rámci studie bylo využito metody interakčního integrálu (Stern, 1976). Tato metoda má řadu výhod: je využitelná pro komplexní geometrie, anizotropní materiály i nehomogenní konstrukce a lze ji relativně snadno aplikovat do FEM kódů. Dále pak umožňuje vyčíslení faktorů intenzity napětí i pro trhliny zatížené ve smíšeném módu.

V následující části bude stručně nastíněno odvození interakčního integrálu. Podrobnější pojednání lze nalézt například u Walterse (2005), či případně v další odkazované literatuře.

Interakční integrál vychází z klasického J-integrálu, který byl odvozen na konci šedesátých let (Cherepanov, 1967), (Rice, 1968). Ten je možné zapsat jako

$$J(s) = \lim_{\Gamma\to 0} \int_{\Gamma} (W\delta_{1i} - \sigma_{ij}u_{j,1})n_i d\,\Gamma, \qquad (11)$$

kde $W = 1/2\sigma_{ij}\varepsilon_{ij}$ je hustota deformační energie, σ_{ij} je Cauchyho tenzor napětí, ε_{ij} je tenzor deformace, u_i je vektor přemístění a δ_{1i} je Kroneckerovo delta.

V kontextu metody konečných prvků je vyčíslování křívkových, případně plošných integrálů s dimenzí nižšího řádu, než je dimenze okrajové úlohy velmi problematické (Kuna, 2013). Shih (1986) odvodil vztah pro $\bar{J}(s)$, energii uvolněnou při jednotkovém nárůstu lomové plochy, kterým transformoval výše uvedený vztah (11) do tvaru s klasickými objemovými integrály:

$$\bar{J}(s) = \int_V (\sigma_{ij}u_{j,1} - W\delta_{1i})q_{,i}\,\mathrm{d}V + \int_V (\sigma_{ij}u_{j,1} - W\delta_{1i})_{,i}q\,\mathrm{d}V - \int_{S^+ + S^-} t_j u_{j,1} q\,\mathrm{d}S, \qquad (12)$$

kde t_j jsou komponenty trakční síly (components of traction) působící na povrchu trhliny a q je skalární váhová funkce. Hlavní nevýhodou klasické formulace J-integrálu je nemožnost přesného vyčíslení faktorů intenzity napětí pro trhlinu zatíženou ve smíšeném módu. Jak již bylo uvedeno výše, interakční integrál tímto limitem netrpí.

Metoda interakčního integrálu (někdy též M-integrálu) je založena na superpozici dvou zatěžovacích stavů, přičemž první zatěžovací stav představuje skutečné zatížení konstrukce s trhlinou a druhý zatěžovací stav odpovídá libovolnému pomocnému řešení se známými faktory intenzity napětí. Vzájemnosti interakční energie obou stavů je dosaženo za pomoci Bettiho teorému. Superponováním obou výše zmíněných stavů lze pro všechny veličiny psát

$$u_i^S = u_i + u_i^{\mathrm{aux}},\ \sigma_{ij}^S = \sigma_{ij} + \sigma_{ij}^{\mathrm{aux}} \quad \text{atd.}, \qquad ($$

13)

kde σ_{ik}^{aux}, $\varepsilon_{ik}^{\text{aux}}$ a u_i^{aux} jsou pomocná pole napětí, přetvoření a přemístění v okolí trhliny získaná například z Williamsova řešení (Williams, 1956). Horní index S ve výše uvedeném vztahu značí superponovanou veličinu. Dosazením vztahu (13) do vztahu (12) získáme:

$$\bar{J}^S(s) = \int_V \left[(\sigma_{ij} + \sigma_{ij}^{\text{aux}})(u_{j,1} + u_{j,1}^{\text{aux}}) - W^S\delta_{1i}\right]q_{,i}\,\mathrm{d}V + \int_V \left[(\sigma_{ij} + \sigma_{ij}^{\text{aux}})(u_{j,1} + u_{j,1}^{\text{aux}}) - W^S\delta_{1i}\right]_{,i} q\,\mathrm{d}V - \int_{S^+ + S^-}(t_j + t_j^{\text{aux}})(u_{j,1} + u_{j,1}^{\text{aux}})q\,\mathrm{d}S. \quad (14)$$

Po upravě je možné rovnici (14) rozdělit do tří částí:

$$\bar{J}^S(s) = \bar{J}(s) + \bar{J}^{\text{aux}}(s) + \bar{I}(s), \quad (15)$$

přičemž $\bar{J}(s)$ odpovídá skutečnému stavu, $\bar{J}^{\text{aux}}(s)$ stavu pomocnému a $\bar{I}(s)$ interakčnímu integrálu, ve kterém dochází k interakci proměnných odpovídajících stavu skutečnému a pomocnému. Vhodnou definicí pomocných polí a po dalších dílčích úpravách pak lze interakční integrál vyjádřit následovně:

$$\bar{I}(s) = \int_V (\sigma_{ij}u_{j,1}^{\text{aux}} + \sigma_{ij}^{\text{aux}}u_{j,1} - \sigma_{jk}\varepsilon_{jk}^{\text{aux}}\delta_{1i})q_{,i}\,\mathrm{d}V + \int_V \left[\sigma_{ij}(u_{j,1i}^{\text{aux}} - \varepsilon_{ij,1}^{\text{aux}}) + \sigma_{ij}^{\text{aux}}u_{j,1}\right]q\,\mathrm{d}V - \int_{S^+ + S^-} t_j u_{j,1}^{\text{aux}} q\,\mathrm{d}S. \quad (16)$$

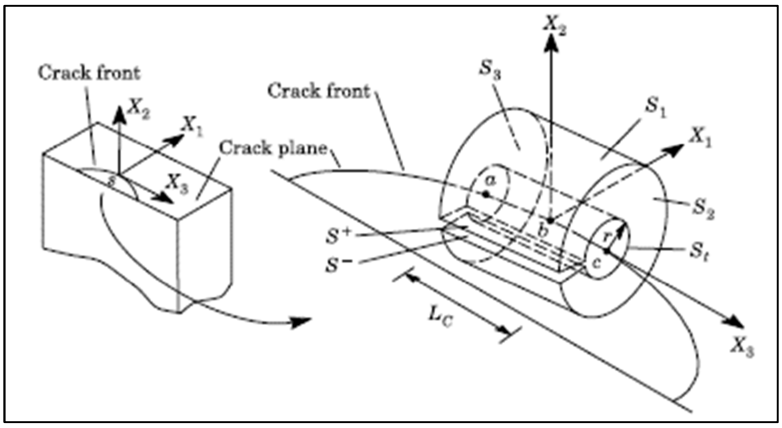

Obrázek 15 – Domény používané pro výpočet plošných a objemových integrálů na čele trhliny ($s = b$), rozprostírající se na délce L_c od bodu a do bodu c. Povrchy S_t a S_1 (válcové plochy), S_2 a S_3 (rovinné boční plochy) a S^+ a S^- (horní a dolní plochy na čele trhliny) tvoří povrch S a vymezují objem V. Pro obecný případ zatížení se povrch S_t musí zmenšit na čelo trhliny, tj. $r \to 0^+$. (Walters, 2005)

Pro případ přímé trhliny, kvazistatické zatížení, elastické homogenní materiály a bez uvažování trakcí na ploše trhliny (crack-face tractions) druhý a třetí integrál ve výrazu (16) vymizí. Protože je segment L_c velmi malý, lze předpokládat, že se interakční integrál $I(p)$ mění na daném segmentu pomalu. Proto je $I(p)$ možné nahradit konstantní hodnotou $I(s)$, přičemž

$$I(s) = \frac{\bar{I}(s)}{\int_{L_c} q(s)\mathrm{d}s}. \quad (17)$$

Uvážíme-li klasický vzorec vyjadřující rychlost uvolňování energie v závislosti na faktorech intenzity napětí smíšeného módu namáhání (Anderson, 2004), platí

$$J(s) = \frac{K_I^2 + K_{II}^2}{E'} + \frac{1+\nu}{E}K_{III}^2, \quad (18)$$

kde $E' = E$ pro rovinnou napjatost, $E' = E/(1-\nu 2)$ pro rovinnou deformaci a ν je Poissonův součinitel.

Dosazením $K_N^S = K_N + K_N^{\mathrm{aux}}$ do vztahu (18) a výběrem interakčních členů lze vyjádřit:

$$I = \frac{2}{E'}\left(K_I K_I^{aux} + K_{II} K_{II}^{aux}\right) + \frac{2(1+\nu)}{E} K_{III} K_{III}^{aux}. \tag{19}$$

Dosadíme-li do výše uvedeného vztahu pomocné faktory intenzity napětí $K_I^{aux} = 1$ a $K_{II}^{aux} = K_{III}^{aux} = 0$ obdržíme hodnotu hledaného faktoru intenzity napětí K_I. Obdobným způsobem lze získat též hledané hodnoty pro zbývající faktory K_{II} a K_{III}.

3 Modelované varianty roztržení těsnícího svaru

V rámci studie byl jako zájmový vybrán těsnící svar umístěný nad dolní lamelou o tloušťce 45 mm (viz obrázek 14 vlevo), přičemž byly modelovány celkem čtyři varianty roztržení dolního líce tohoto těsnícího svaru:

a) 3 mm trhlina na horním okraji dolního líce těsnícího svaru (u kořene svaru),

b) 3 mm trhlina ve středu dolního líce těsnícího svaru,

c) 3 mm trhlina na dolním okraji dolního líce těsnícího svaru,

d) dolní líc těsnícího svaru plně porušený trhlinou.

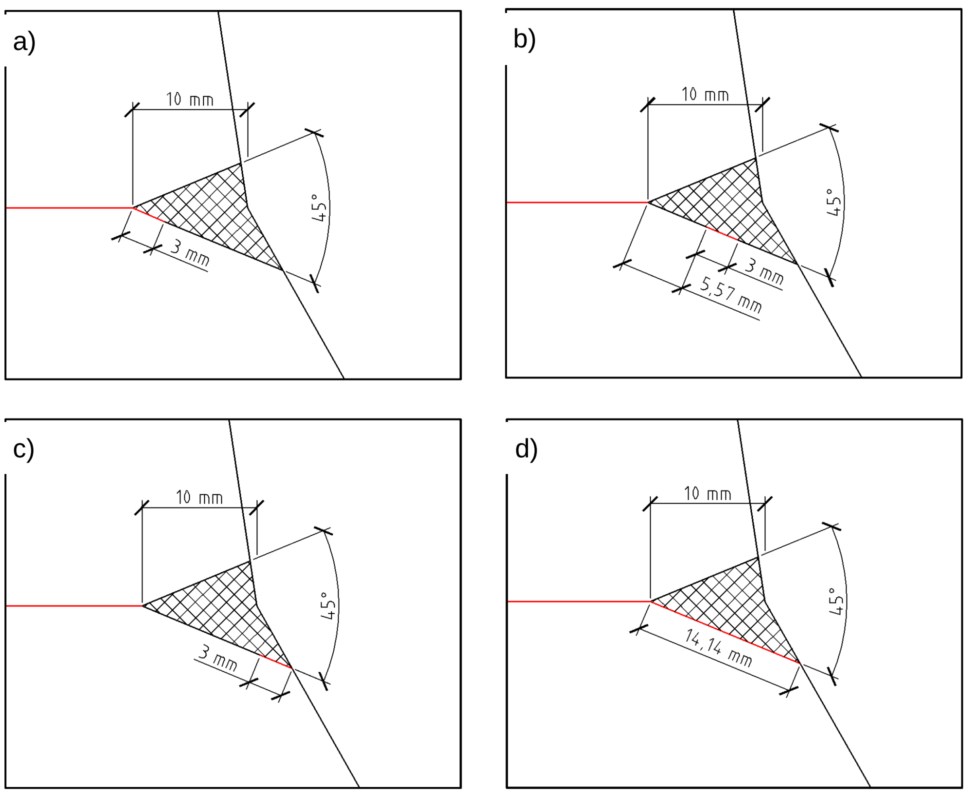

Obrázek 16 – Modelované varianty roztržení těsnícího svaru

Zmíněné varianty roztržení jsou schématicky zobrazeny na obrázku 16. Pro všechny modelované případy byla uvažována trhlina procházející po celé délce svaru.

4 Výpočtové modely

V rámci prováděných matematických simulací byla využita metoda submodelů. Tato metoda vyžaduje tvorbu dvou typů konečněprvkových modelů. V první řadě se jedná o model globální, který slouží primárně pro získání okrajových podmínek pro podrobnější model druhého typu a v daném případě postihoval chování celého mostu. Globální model byl přitom s výhodou sestaven tak, aby disponoval nižší výpočtovou náročností. Druhý typ modelu pak představuje submodel postihující vždy jen malou zájmovou oblast a její bezprostřední okolí. Submodel se přitom oproti modelu globálnímu vyznačuje větší podrobností a v daném případě i vyšší výpočtovou náročností. V rámci studie tento typ modelu zastupovaly čtyři modely svarových spojů lamelových pásnic, pro něž byly okrajové podmínky získány za pomoci jednoho modelu globálního. Více informací o dané problematice dále zmiňuje Hrubý (2013).

4.1 Globální model mostu

Pro potřeby modelování globálního chování mostu byl využit konečněprvkový výpočtový model vytvořený v době zpracování projektu mostu přes Lochkovské údolí. Tento model byl z důvodu získání odpovídající formy okrajových podmínek zmodifikován, přičemž byly v oblastech zájmu nahrazeny původní jednoduché pásnice pásnicemi lamelovými. Kromě těchto úprav byly dále provedeny též některé další změny umožňující například modelování postupné výstavby mostu. Zmíněný výpočtový model byl vyhotoven ve velkém detailu jako prostorový MKP model, při jehož tvorbě byly využity především skořepinové elementy SHELL181 a objemové elementy SOLID185. V rámci modelu byly dále využity též prutové, příhradové, kontaktní a další konečné prvky. Podrobnější popis globálního modelu mostu lze nalézt ve výše uvedené literatuře.

V rámci modelování zatížení konstrukce byl zjištěn významný vliv postupné montáže mostu na výslednou napjatost vznikající v horních pásnicích jeho ocelové komory. Z tohoto důvodu byly pro účely získání odpovídajích okrajových podmínek provedeny simulace postupné výstavby mostního díla (Krňávek, 2013). Na výsledky těchto simulací bylo dále navázáno, vypočtená data byly porovnána s měřením probíhajícím na mostě, a dle daných požadavků byly příslušné hodnoty napětí v modelu kalibrovány za pomoci silového zatížení. Zavedení této úpravy bylo provedeno za účelem zahrnutí vlivů, jež nebyly v rámci prováděných simulací zohledněny (zejména účinky zatížení poklesem podpor, výsuvem ocelové konstrukce, reziduální napětí z výroby, atd.)

4.2 Submodely

Jak již bylo zmíněno výše, v rámci studie byly pro potřeby detailního modelování svarových spojů lamelových pásnic vytvořeny celkem čtyři submodely. Rozměrové uspořádání těchto modelů bylo přitom voleno tak, aby byla postižena celá délka zájmových svarů (na šířku pásnice) a aby byl zajištěn korektní přenos okrajových podmínek. V příčném směru byl tedy zvolen rozměr 600 mm (300 mm na obě strany od podélné osy spoje). Obdobným způsobem byla určena i výška submodelů, přičemž byla kromě vlastních pásnic modelována i přiléhající 300 mm vysoká část betonové mostovky a rozměrově shodná část ocelové stojiny komory mostu. Používané submodely byly vypracovány ve vysokém detailu včetně koutových obvodových těsnících svarů (viz obrázek 17).

Při tvorbě submodelů bylo využito převážně objemových prvků SOLID185. Pro tvorbu sítě koutových obvodových svarů přiléhajících k oblastem roztrženého dolního líce těsnícího svaru pak byly doplňkově použity též prvky SOLID186. Jelikož bylo v průběhu simulace zapotřebí postihnout také vliv tření mezi horními a dolními lamelami a mezi horní lamelou a přiléhající betonovou mostovkou, byly při tvorbě submodelů použity též kontaktní prvky typu TARGE170 a CONTA174. Spřažení mostovky s ocelovou komorou mostu reálně prováděné za pomoci spřahovacích trnů pak bylo simulováno s použitím CP vazeb.

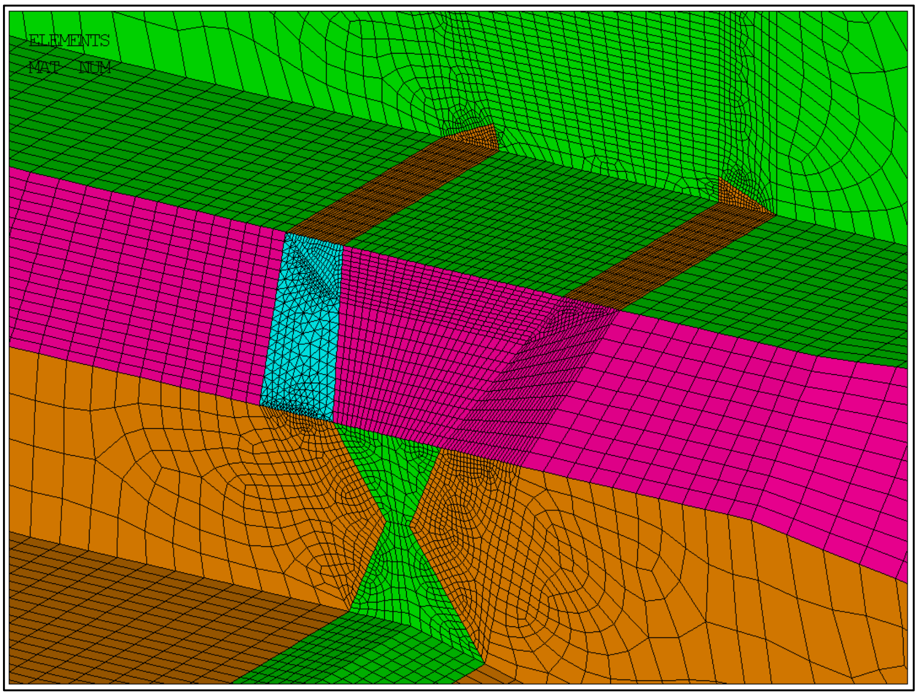

Obrázek 17 – Koutový obvodový těsnící svar submodelu

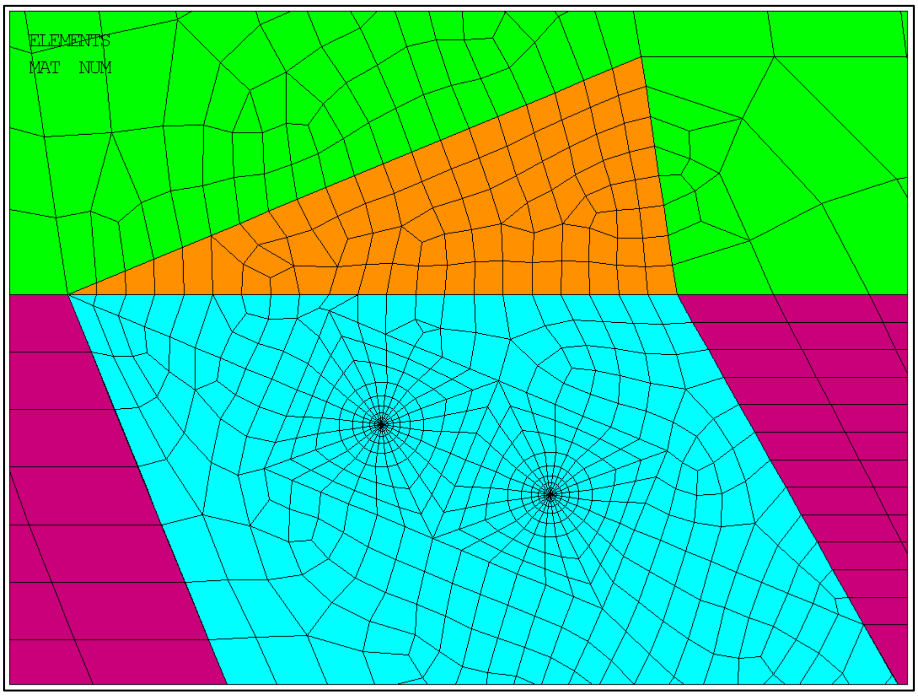

Obrázek 18 – Síť konečných prvků v okolí analyzované trhliny (varianta 3 mm trhlina ve středu dolního líce těsnícího svaru)

Pro modelování sítě v okolí trhlin byly využity opět osmiuzlové prvky SOLID185. Tato část sítě, zobrazená na obrázku 18, byla přitom vytvořena odděleně a s přiléhající sítí spojena za pomoci výše uvedených typů kontaktních elementů. Jak je z uvedeného obrázku zřejmé, počet kontur vytvořených okolo čel trhlin pro výpočet faktorů intenzity napětí byl zvolen na šest. Z důvodu zajištění větší přesnosti výpočtu bylo přitom realizováno odstupňování velikosti elementů směrem od kořene trhlin, a to v poměru 1:3. Na tomto místě je dále třeba uvést, že v průběhu všech výpočtů byl používán lineárně elastický materiál, a že směr šíření trhlin byl uvažován ve směru rovnoběžném s dolním lícem těsního svaru.

Jelikož povaha úlohy nezajišťovala otevření trhliny vždy po celé její délce, bylo nutné zabránit případné nežádoucí penetraci obou povrchů trhliny. K tomuto účelu bylo využito opět prvků TARGE170 a CONTA174. Na tuto skutečnost však navazoval problém s výpočtem hodnot J-integrálu a faktorů intenzity napětí. Výpočet těchto veličin je totiž podmíněn vyloučením přítomnosti kontaktních prvků v okolí analyzované trhliny (ANSYS Inc., 2013). Zmíněný problém bylo proto nutné vyřešit tak, že v první fázi výpočtu byla řešena strukturální analýza submodelu s trhlinou bez výpočtu J-integrálu a faktorů intenzity napětí a v návaznosti na tento krok byl dále analyzován zmenšený model s vyloučením kontaktních elementů zatížený deformacemi vypočtenými v předchozí fázi. Druhá výpočetní fáze již zahrnovala samotný výpočet J-integrálu a faktorů intenzity napětí.

5 Výsledky studie

V průběhu provedené numerické simulace byly s využitím interakčního integrálu zmíněného v kapitole 2 získany hodnoty faktorů intenzity napětí pro namáhání v módu I (tahové namáhání) a módu II (smykové namání v rovině trhliny), jejichž průběhy po šířce lamely jsou prezentovány na obrázcích 19 a 20. Faktor intenzity napětí odpovídající módu III, vyšel řádově nižší, a proto mu v prezentovaných výsledcích nebude věnována pozornost.

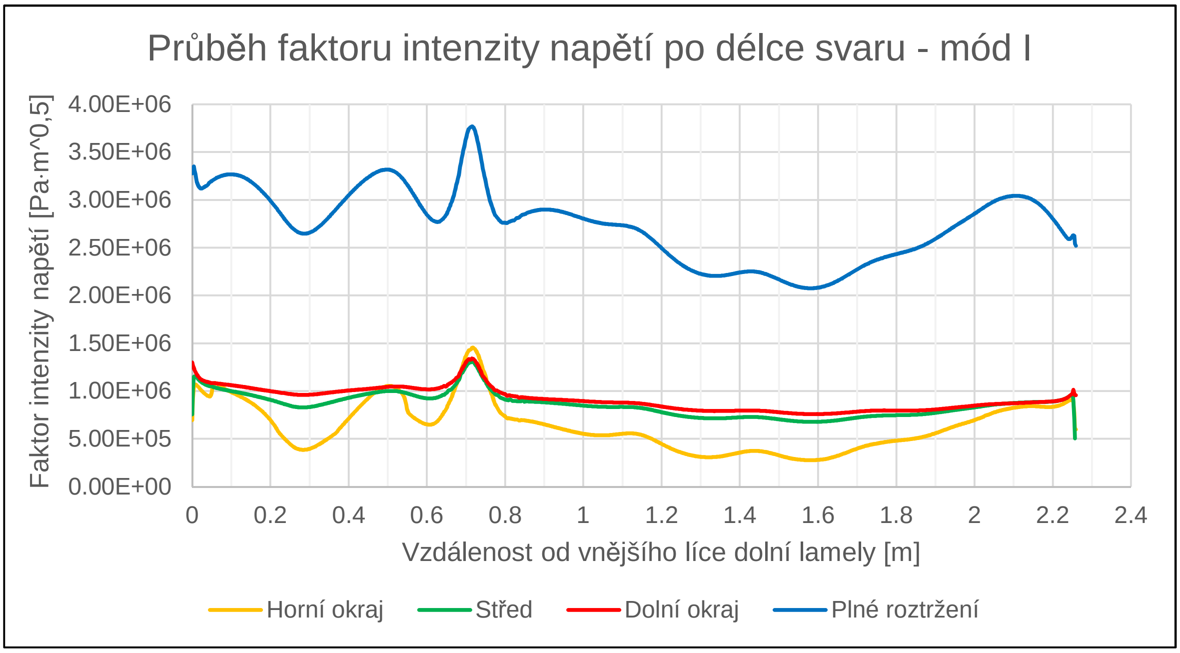

Obrázek 19 – Průběh faktorů intenzity napětí po délce svaru – mód I

Z výsledků všech simulací je patrný významný vliv napojení lamelových pásnic na stěnu komory mostu. V místě napojení, které se v uvedených grafech nachází v poloze 0,71 m, nabývají faktory intenzity napětí odpovídající oběma módům maximální hodnoty. Z uvedených výsledků je dále patrné, že dominantní je faktor intenzity napětí v módu II, jehož hodnoty jsou více než dvakrát větší než ty odpovídající módu I. Dle očekávání bylo nejvyšších faktorů intenzity napětí dosaženo v případě varianty s trhlinou vedenou po celém dolním líci těsnícího svaru. Konkrétně bylo dosaženo maximální hodnoty faktoru K_{II} o velikosti $9{,}36 \cdot 10^6$ Pa·$\sqrt{\text{m}}$, faktor intenzity napětí K_I pak dosahoval extrémní hodnoty $3{,}77 \cdot 10^6$ Pa·$\sqrt{\text{m}}$. Extrémy faktorů intenzity napětí ve zbývajících simulovaných variantách vykazují blízké hodnoty, a to v rozmezí $1{,}31\text{-}1{,}45 \cdot 10^6$ Pa·$\sqrt{\text{m}}$ pro faktor K_I a $3{,}13\text{-}3{,}53 \cdot 10^6$ Pa·$\sqrt{\text{m}}$ pro faktor K_{II}.

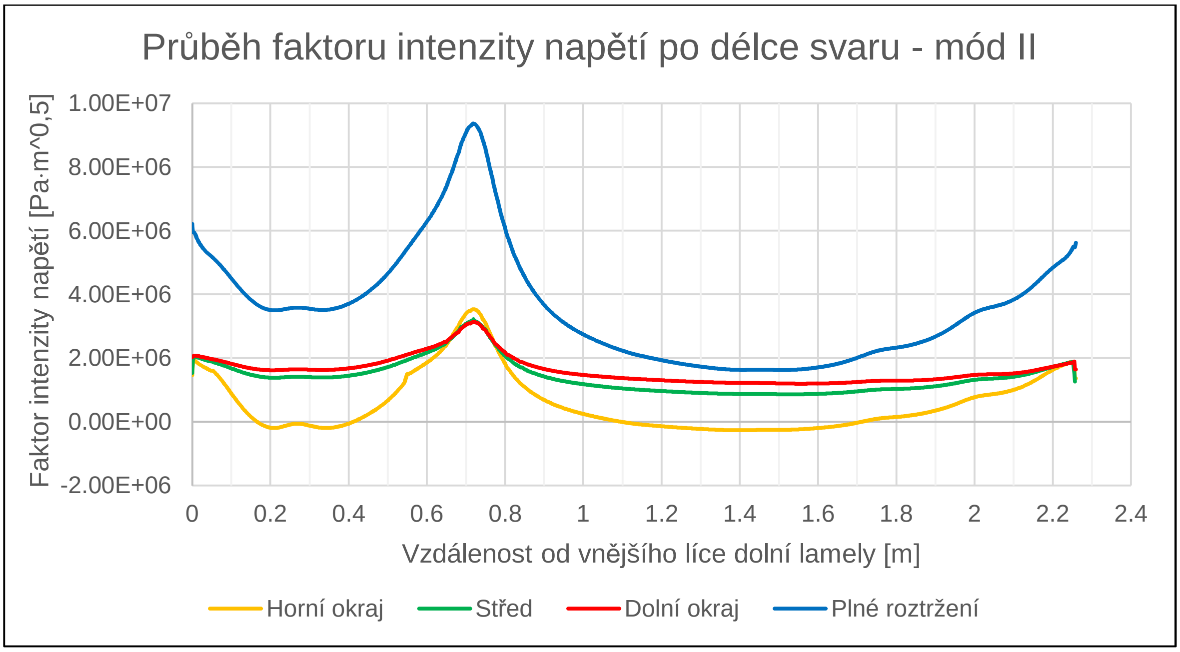

Obrázek 20 – Průběh faktorů intenzity napětí po délce svaru – mód II

Maximální hodnoty faktorů intenzity napětí pro jednotlivé případy shrnuje tabulka 12.

Tabulka 12 – Extrémní hodnoty faktorů intenzity napětí

Varianta	Faktor intenzity napětí [Pa·$\sqrt{m}$]	
	Mód I	Mód II
Horní okraj	1 454 900	3 533 700
Střed	1 313 400	3 215 400
Dolní okraj	1 340 400	3 129 200
Plné roztržení	3 768 800	9 362 400

6 Závěr

V rámci příspěvku byla prezentována metodika výpočtu faktoru intenzity napětí v těsnícím svaru lamelové pásnice mostního díla. Byl proveden výpočet faktoru intenzity napětí pro čtyři zvolené teoretické varianty poškození těsnícího svaru. Výpočtová metodika zahrnovala využití globálního modelu mostu pro určení namáhání v oblasti se zkoumaným svarem. Dále byl využit detailní lokální model, který obsahoval kontaktní prvky v oblasti poškození svaru. Vzhledem k nemožnosti přímého výpočtu faktoru intenzity napětí za pomoci modelu s kontakty bylo nutné odpovídající napjatostní stav vytvořit na dalším submodelu, který již kontaktní prvky neobsahoval. Tento model již umožnil výpočet faktoru intenzity napětí. V příspěvku jsou prezentovány obdržené faktory intenzity napětí pro mód I a II po celé délce těsnícího svaru skrze šířku lamelové pásnice.

Literatura

ANDERSON, T., 2005. *Fracture mechanics: fundamentals and applications*. 3rd ed. Boca Raton: Taylor, 621 s. ISBN 08-493-1656-1

ANSYS, Inc. *ANSYS 15.0 Help*. Release 15.0. USA, Canonsburg, 2013 [cit. 2014-05-30]

CHEREPANOV G., 1967. Rasprostranenie trechin v sploshnoi srede. *Prikladnaja matematika i mechanika*. Moskva: Akademia nauk SSSR, roč. 31.

HRUBÝ P., KRŇÁVEK O., NEVAŘIL A., TOTKOVÁ L., 2013. Submodelling Technique and the Detail Structural Analysis. In.: *Sborník příspěvků z 2. mezinárodní vědecké konference*

Structural and Physical Aspects of Civil Engineering, Štrbské Pleso, SR, 27.-29.11.2013. Košice: Stavebná fakulta Technickej univerzity v Košiciach, 10 s.

KRŇÁVEK O., NEVAŘIL A., 2013. Modelling of steel-concrete composite bridge assembly. In.: *Sborník příspěvků z 29. konference s mezinárodní účastí Výpočtová mechanika 2013*, Špičák, ČR, 4.-6.11.2013. Plzeň: Katedra mechaniky, Fakulta aplikovaných věd, Západočeská univerzita v Plzni.

KUNA M., 2013. *Finite elements in fracture mechanics Theory--Numerics--Applications*. Dordrecht: Springer. ISBN 978-940-0766-808

RICE J. R., 1968. A Path Independent Integral and the Approximate Analysis of Strain Concentration by Notches and Cracks. *Journal of Applied Mechanics*, vol. 35, issue 2. DOI: http://dx.doi.org/10.1115/1.3601206.

SHIH C., MORAN B., NAKAMURA T., 1986. Energy release rate along a three-dimensional crack front in a thermally stressed body. *International Journal of Fracture*, roč. 30, č. 2.

STERN M., BECKER E., DUNHAM R., 1976. A contour integral computation of mixed-mode stress intensity factors. *International Journal of Fracture*, roč. 12, č. 3.

STRÁSKÝ J., 2001. *Betonové mosty*. Praha: Šel, 103 s. ISBN 80-864-2605-X.

VEJVODA S., MAŘÍK P., 2011. Posouzení indikací ve svarech lamelových pásnic mostu přes Lochkovské údolí. In: *Silnice železnice* [online]. [cit. 2014-05-25]. Dostupné z: http://www.silnice-zeleznice.cz/clanek/posouzeni-indikaci-ve-svarech-lamelovych-pasnic-mostu-pres-lochkovske-udoli.

WALTERS M. C., PAULINO G. H., DODDS R. H., 2005. Interaction integral procedures for 3-D curved cracks including surface tractions. *Engineering Fracture Mechanics*, vol. 72, issue 11, s. 123-154. DOI: http://dx.doi.org/10.1533/9780857094803.123.

WILLIAMS M. L., 1957. On the Stress Distribution at the Base of a Stationary Crack. *Journal of Applied Mechanics*, vol. 24, č. 1.

Poděkování

Tento článek byl vypracován v rámci projektu FR-TI4/430 za finanční podpory Ministerstva průmyslu a obchodu České republiky.

Kontaktní adresa:
Ing. Pavel Hrubý
Ing. Ondřej Krňávek
Ing. Aleš Nevařil, Ph.D.
Lucie Totková
Centrum AdMaS, Fakulta stavební, VUT v Brně, Veveří 95, 602 00 Brno, Česká republika

CFD ANALYSIS OF FUEL ASSEMBLY USING ANSYS CFX CODE

JAKUB JAKUBEC, VLADIMÍR KUTIŠ, JURAJ PAULECH

Institute of Automotive Mechatronics, Faculty of Electrical Engineering and Information Technology

Abstract: The paper deals with CFD modeling and simulation of coolant flow in fuel assembly of nuclear reactor VVER 440. The influence of coolant flow through bypass and the mixing grid position on temperature distribution at the output of fuel assembly and pressure drop is investigated. Only steady-state analyses are performed. Generated thermal power in fuel rods is prescribed individually for each rod with axial distribution of power. ANSYS CFX is chosen as a main CFD software tool, where all analyses are performed.

Keywords: CFD, fuel assembly, VVER 440, parametric study, ANSYS CFX

1 Introduction

Detailed knowledge of the thermo-hydraulic processes in fuel assembly of nuclear reactor is very important from operational safety point of view. Modern computer simulation techniques, like CFD [Ch. Hirsch,2007], [T. J. Chung, 2010] or FEM [J. Donea, 2003], can be very useful in detail study of such processes, because after verification and validation processes [W. L. Oberkampf,2002] of CFD model, you can relatively easily change boundary and initial conditions, or other input parameters of the model.

The flow field in fuel assembly of nuclear reactor VVER 440 is very complex mostly in fuel assembly head, where the thermocouple is placed. In the fuel assembly head main hot coolant stream from the fuel rods area is mixed with colder coolant from central tube and bypass. Thermocouple as the only source of coolant temperature measurement in fuel assembly has to register average coolant temperature at the outlet. In our research, we focused on modeling and simulation of thermo-hydraulic processes in fuel assembly, where the distribution of temperature field in coolant and various influences of boundary conditions, generated heat power and different turbulent models on obtained results are investigated. All CFD analyses were performed by ANSYS CFX software [ANSYS CFX. 2010], which computes basic thermo-hydraulic differential equations by Finite Volume Method [H. K. Versteeg, 1995]. Three different types of analyses are performed. First type of analysis does not consider flow of coolant through the bypass, i.e. all coolant flows across fuel assembly. In the second type of analysis, flow of coolant through bypass is considered and the flow is defined by mass flow through bypass and outlet bypass temperature as parameters. The influence of both parameters on temperature distribution at the output of fuel assembly is investigated. The last type of analysis were focused on mixing grid position. The influence of mixing grid position on temperature distribution and the data registered by the thermocouple was investigated.

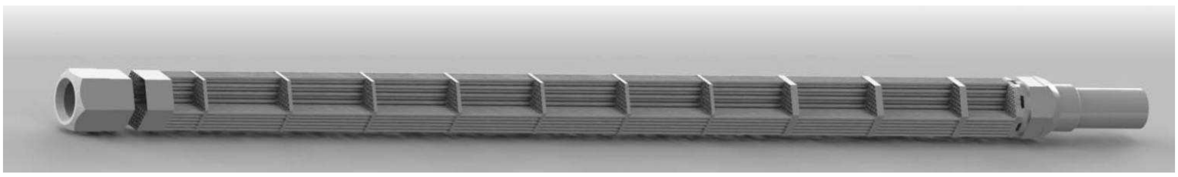

Image 1 – Detailed 3D CAD model of fuel assembly

2 Geometry model

To perform thermo-hydraulic analysis of fuel assembly of reactor VVER440, it is necessary to create 3D geometry model of coolant in the fuel assembly. Creating of geometry model of coolant is divided into three steps. In the first step, geometry model of fuel assembly with all details is created. This first geometry model represents the basic geometry model, that can be used not only in geometry creation for CFD analysis, but also for structural analysis of individual components of fuel assembly. Image 1 shows fully detailed 3D CAD model of fuel assembly.

In second step, detailed geometry model of fuel assembly is simplified. The simplification of fuel assembly geometry model is necessary, because our discretized models are limited by hardware, that are used to CFD computations. Simplifications are performed on input and also on output part of fuel assembly. Image 2 shows example of simplifications made on input and output parts.

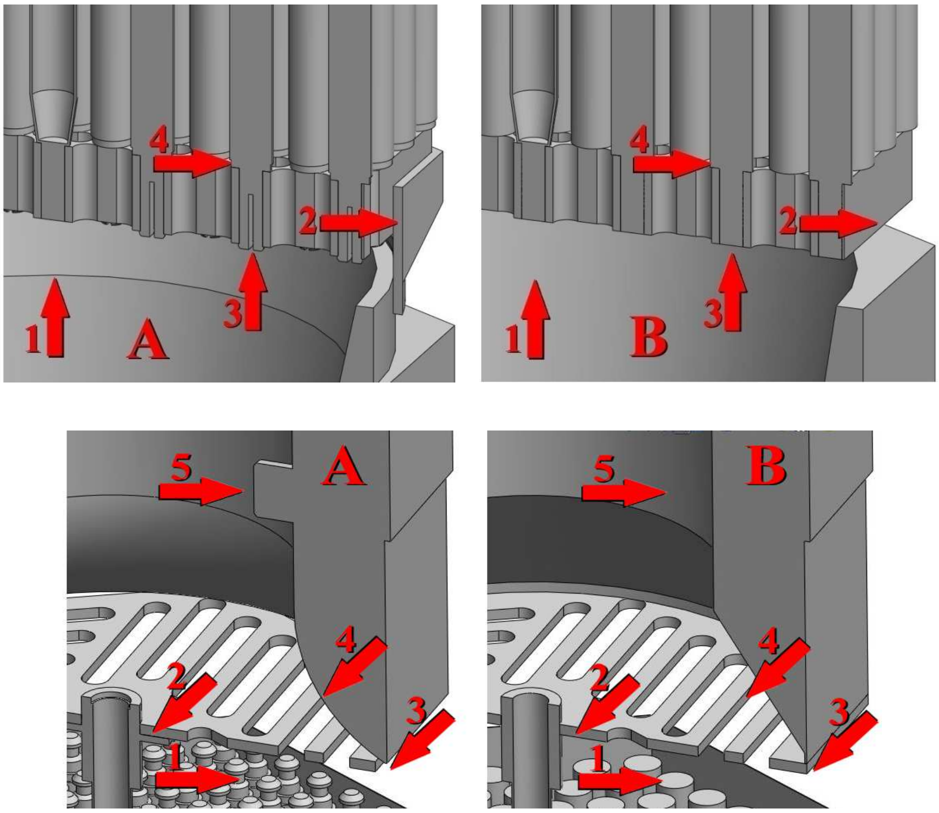

Image 2 – Simplifications made on the input parts (top) and on the output parts (bottom)

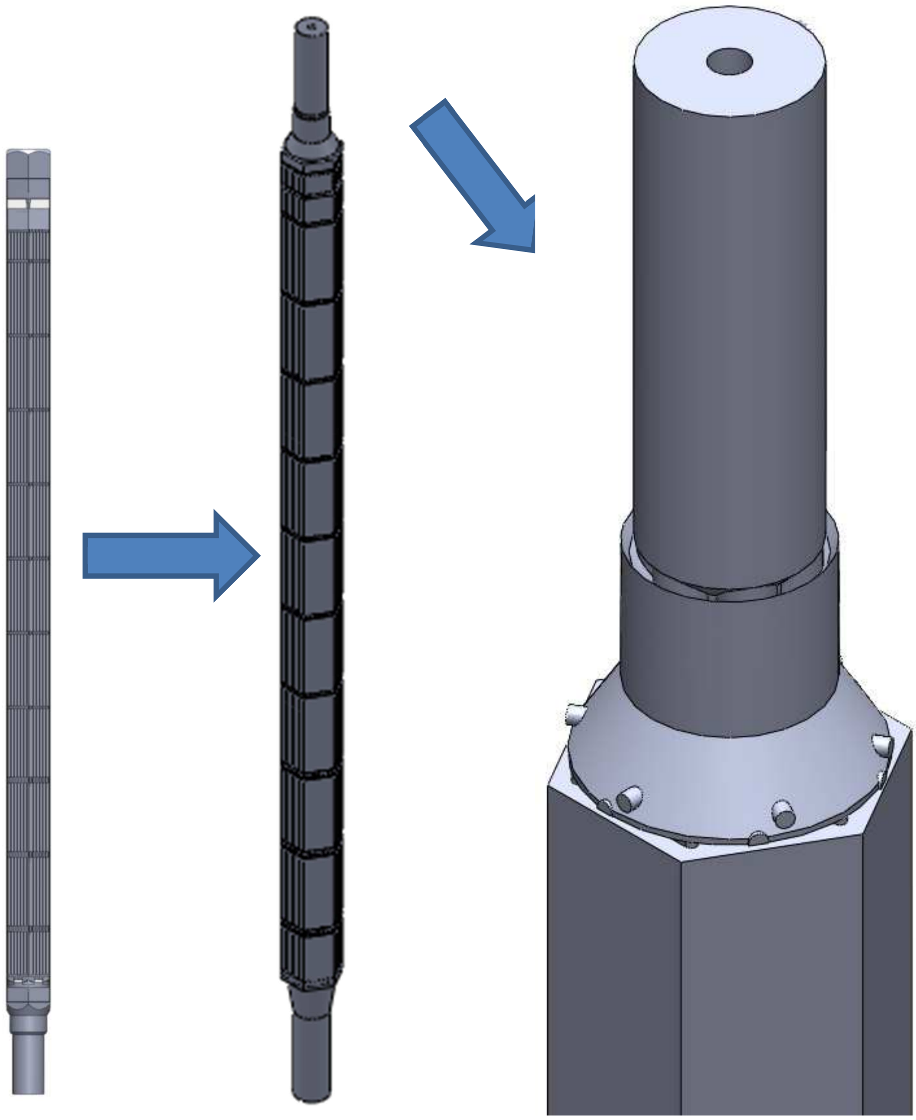

Image 3 – Geometry model of coolant in fuel assembly with thermocouple housing

In third step, negative volume of fuel assembly, which represents the volume of coolant, is created. In this step, also the geometry of channel in upper core supporting plate is modeled, where also the thermocouple housing is created.

Final geometry model of coolant in fuel assembly with thermocouple housing is shown in Image 3. The final geometry model of coolant contains not only all internal fuel assembly components like supporting grid, spacer grid or mixing grid, but there is also modeled coolant flowing across central tube and central tube itself as a solid part.

3 Discretization of model

To solve Reynolds Averaged Navier-Stokes equations (RANS) by Finite Volume Method (FVM), division of the geometry of coolant into small cells is necessary. The cells can directly represents finite volumes – if FVM uses Cell Centered formulation, or finite volume is created from several parts of adjacent cells – if FVM uses Vertex Centered formulation. The process of discretization was performed in mesh tool ANSYS ICEM CFD where blocking strategy was used. In order to use this strategy on most of the geometry, the whole geometry of coolant was divided into 9 parts (from a to i) – see Image 4.

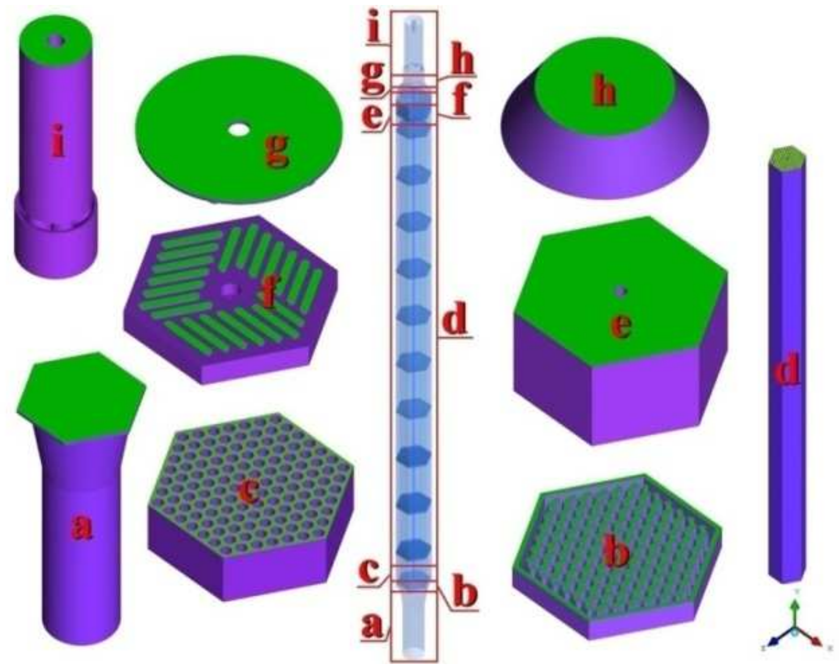

Image 4 – Parts of coolant used in meshing process

Each part was meshed separately and examples of mesh is shown in Image 5

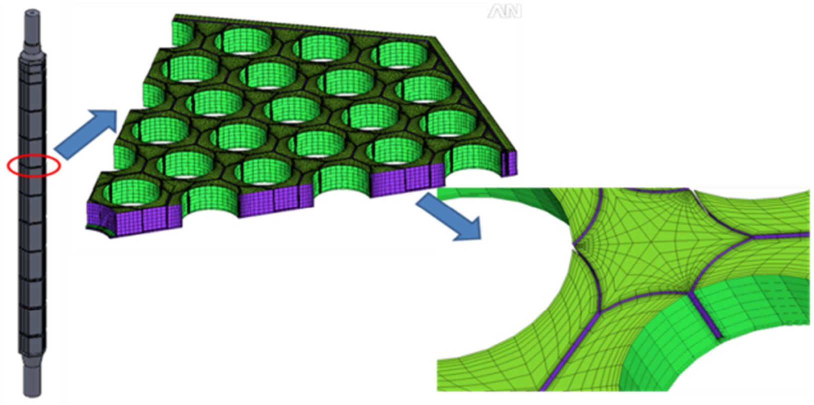

Image 5 – Mesh near supporting grid

All meshed parts were connected by GGI connection in ANSYS CFX. The discretized model of coolant in fuel assembly contains approximately 70 millions of nodes and 65 millions of cells. These numbers represents the limit of our hardware and software configuration, that was used for CFD computations.

4 CFD simulation and obtained results

Theree types of parametric CFD analyses were performed:

1. analysis: different bypass mass flow
2. analysis: different bypass outlet temperatures
3. analysis: diffferent mixing grid postion

Boundary conditions for the first and the second type of analysis are defined as follows (Image 6-a):

- nominal inlet mass flow: 25kg/s
- inlet temperature: 266.9°C
- output pressure: 12.17MPa

Bypass parameters:

- inlet and outlet mass flow: 3-7% mass flow
- outlet temperature: 266.9-281°C

Turbulent models:

- SST, k-ω, BSL

Prescribed thermal power distribution in fuel rods (Image 6-b):

- total thermal power = 5.82MW
- prescribed as the heat flux in 42 axial locations (nodes)
- each fuel rod has its own heat flux axial profile

Bondary conditions fot the last type of analyses (mixing grid position) are defined by following Russian experiment investigating same problem [L.L. Kobzar, 2006]:

- nominal inlet mass flow: 21.7kg/s
- inlet temperature: 100.7°C
- output pressure: 9.73MPa

Bypass parameters:

- no bypass

Turbulent models:

- SST, k-ω, BSL

Prescribed thermal power distribution in fuel rods (Image 6-c):

- total thermal power = 663.5kW
- prescribed as the heat flux for each fuel rod (each calculation has its own distribution according to mixing grid position)

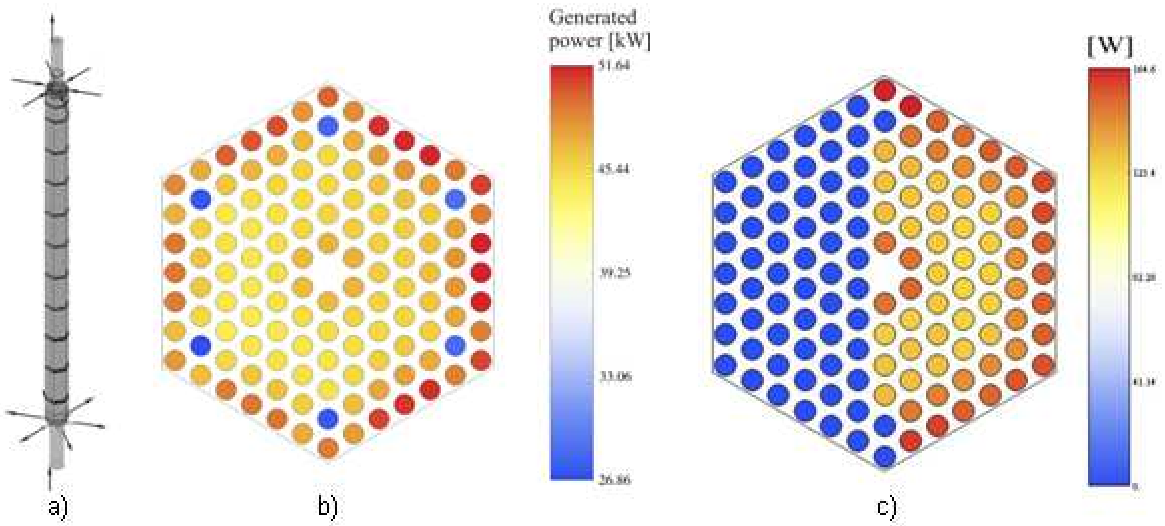

Image 6 – a) inlet and outlet boundary conditions, b) prescribed thermal power for analysis 1 and 2, c) prescribed thermal power for analysis 3

All simulations were performed as steady state, ANSYS CFX was chosen as CFD tool for all simulations. The model contains two domains: fluid and solid. Solid domain is used only for modeling of heat transfer across the wall of central tube. The connection between individual mesh parts is realized by GGI connection. Material parameter of coolant (water) were defined by ANSYS CFX material library IAPWS-IF97.

4.1 Results of first and second analysis type

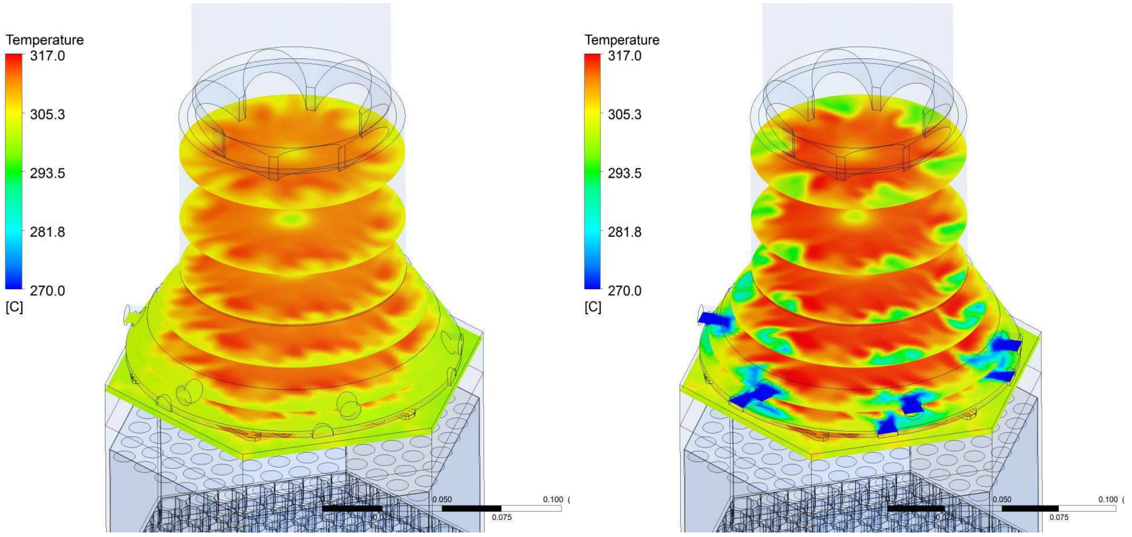

Image 7 - Coolant temperature at the output in individual cross-section planes, left - without bypass, right - with bypass (5% of nominal mass flow)

Image 7 shows obtained results, i.e. distribution of temperature in coolant at the output of fuel assembly. Left part of Image 7 represents results depicted in individual cross-section planes of CFD model, where bypass was not considered, and right part of Image 7 represents results of CFD model, where nominal bypass flow was considered. Similar results are shown in Image 8. As we can see from Image 7 a Image 8, bypass but also the flow in central tube influence the distribution of temperature at the outlet region of fuel assembly. The influence is studied parametrically and dependencies are shown in graphs.

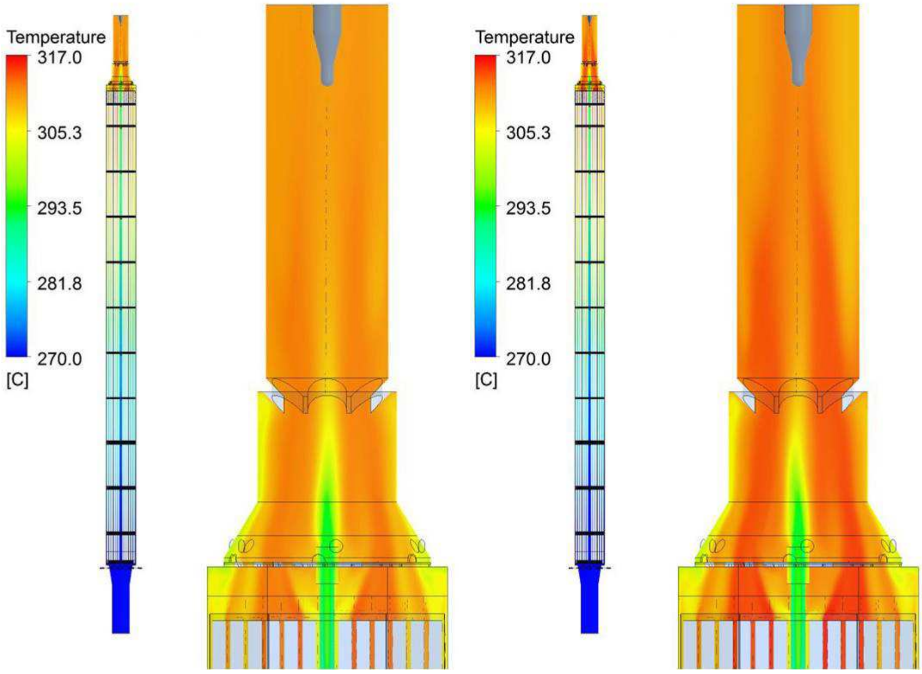

Image 8 - Coolant temperature at the output, left - without bypass, right - with bypass (5% of nominal mass flow)

The influence of mass flow through bypass on temperature at three different locations - thermocouple, outlet from fuel rods area and outlet from fuel assembly is shown in Image10. In all these computations the temperature of coolant at the output of bypass was set up 266.9°C.

As we can see from Image 9, in spite of the temperature at the thermocouple housing and temperature a the fuel rods area are different, the corelation between these two temperatures is evident.

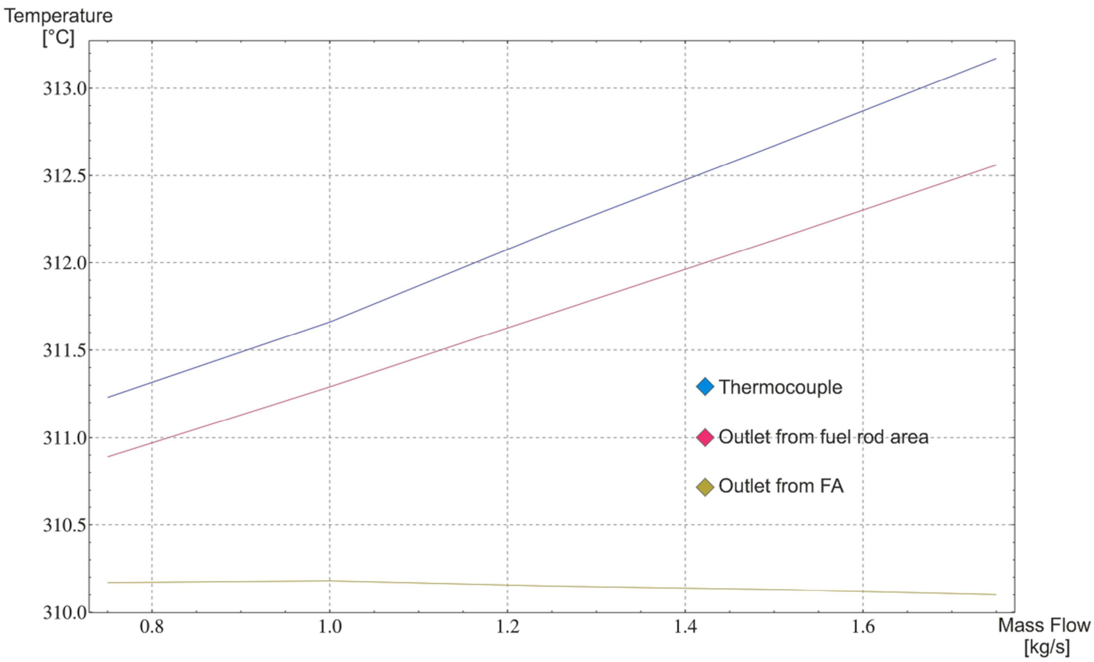

Image 9 - Monitored temperatures dependence on coolant Mass flow through bypass

(t_{bypass}=266.9 °C)

The dependece of thermocouple temperature and temperature at the outlet from fuel assembly on bypass temperature is shown at Image 10.

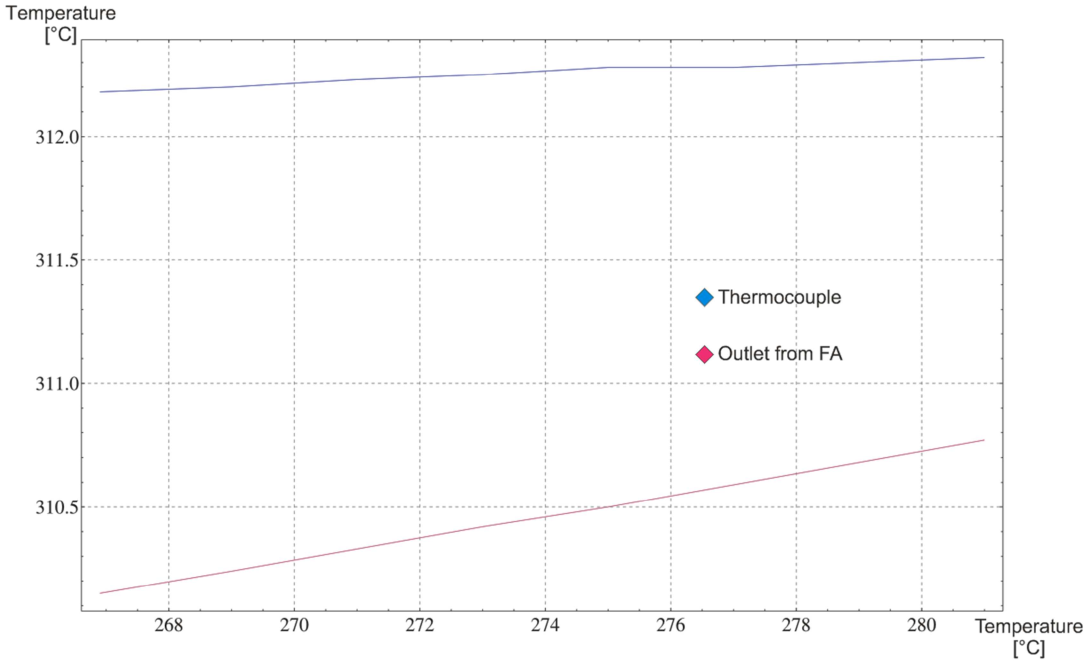

Image 10 - Monitored Temperatures dependence on coolant Temperature in bypass ($\dot{m}_{bypass}$=5% of nominal)

As we can see from Image 10, temperature at the outlet from fuel assembly is more sensitive on bypass outlet temperature than thermocouple housing temperature.

The dependence of pressure drop on mass flow of coolant through bypass is shown in Image 11. In these simulations the temperature at the bypass outlet was set up 266.9°C. The Pressure drop decreases if the bypass mass flow increases.

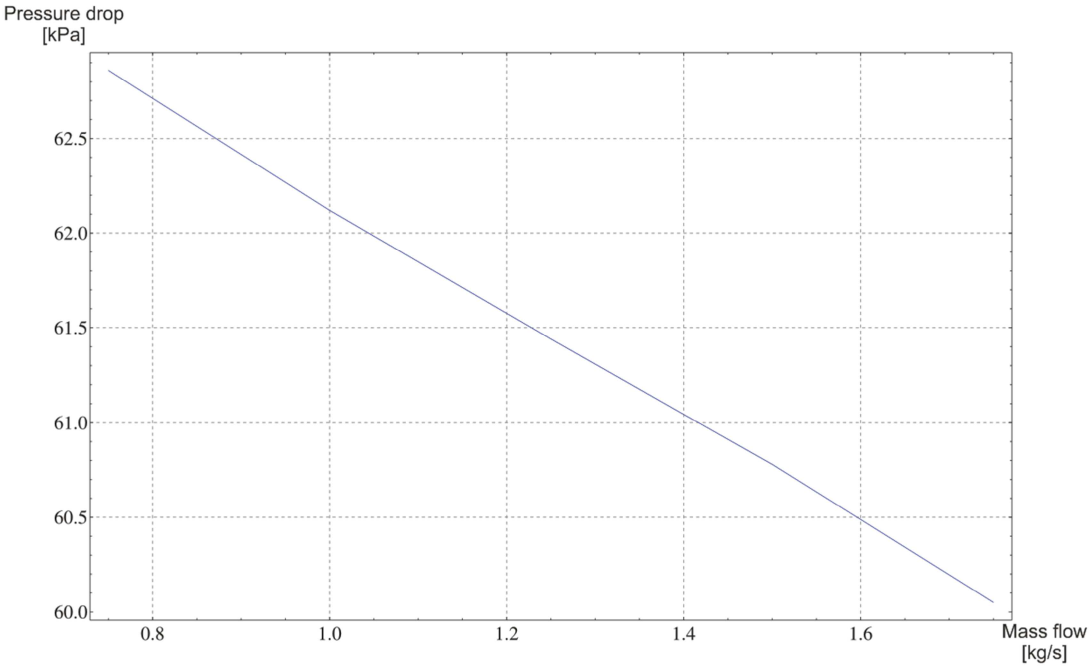

Image 11 - Dependence of Pressure drop on Mass flow of coolant through bypass

(t_{bypass} = 266.9 °C)

The distribution of pressure drop through the fuel assembly height is show at Image 12.

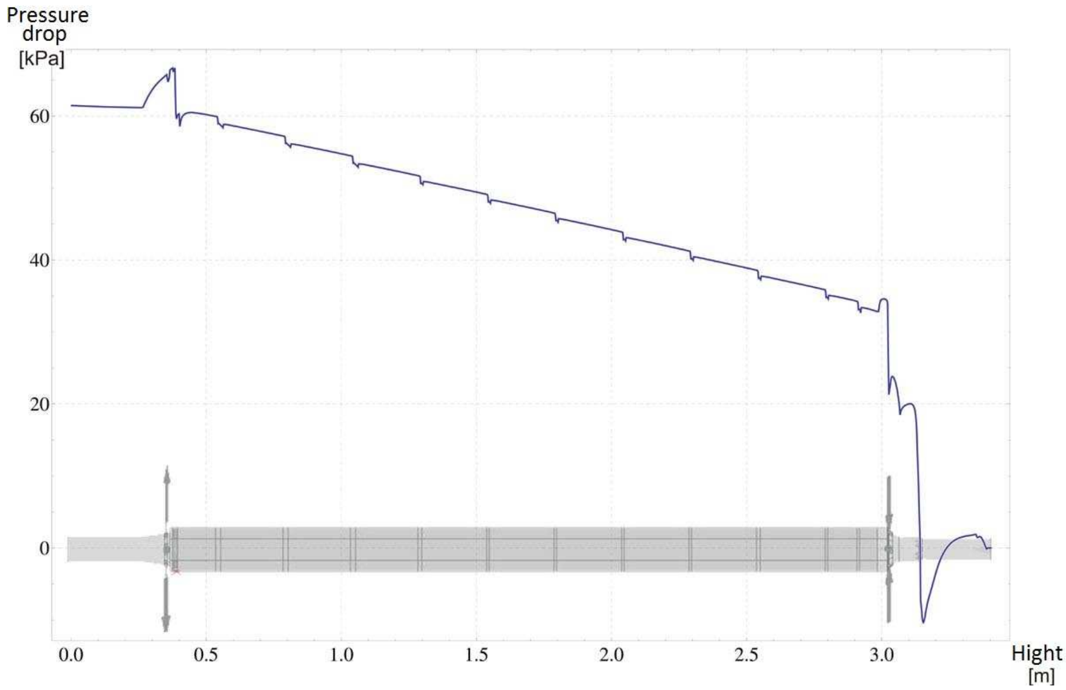

Image 12 - Dependence of Pressure drop along the FA Height

($\dot{m}_{bypass}$=5% of nominal, t_{bypass}=266.9 °C)

4.2 Results of third analysis type

Four positions of the mixing grid were achieved by changing boundary conditions of the fuel rods.

In all four simulations we achieved same results except temperature measured by the thermocouple (see Table 1). Outlet temperature (107.32 ˚C), pressure drop (44.28 kPa) and same outlet velocity (5.19 m/s)

Table 13 Main results

case	1	2	3	4
thermo [C]	106.77	106.70	107.26	108.37
outlet [C]	107.32	107.32	107.32	107.32
outlet velocity [m/s]	5.19	5.19	5.19	5.19
pressure loss [kPa]	44,28	44,28	44,28	44,28

Table 1 shows data measured by thermocouple dependency on mixing grid position.

Image 13 displays coolant temperature distribution before mixing grid in first simulation. In all other cases is the temperature distribution same.

From the Image 14 is clearly visible effect of the mixing grid position on the flow mixing processes. Difference between case 1 and case 3 is that mixing grid is shifted by 120 degrees. In cases 2 and 4 mixing grid mirrors case 1 and 3.

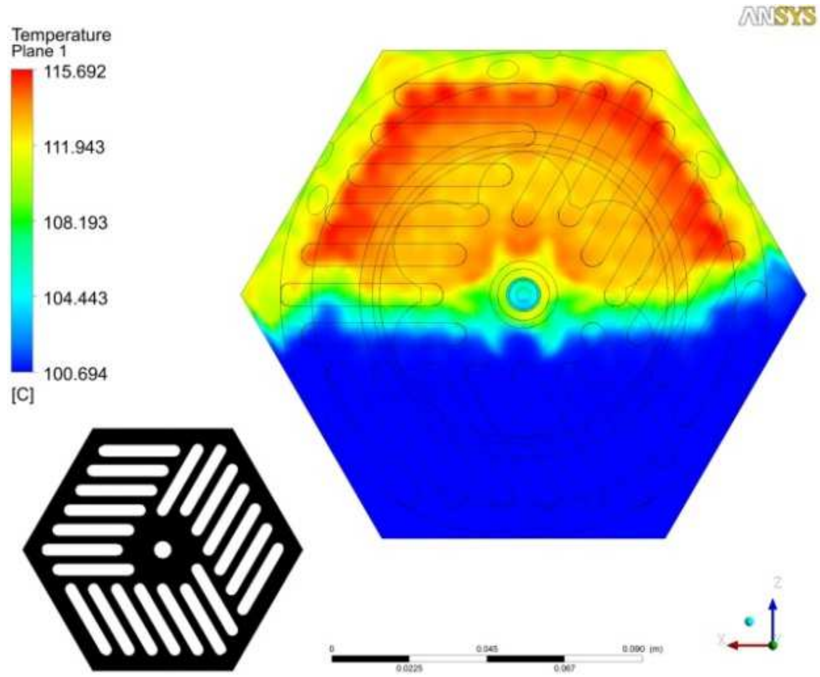

Image 13 - Coolant temperature distribution before the mixing grid (case 1)

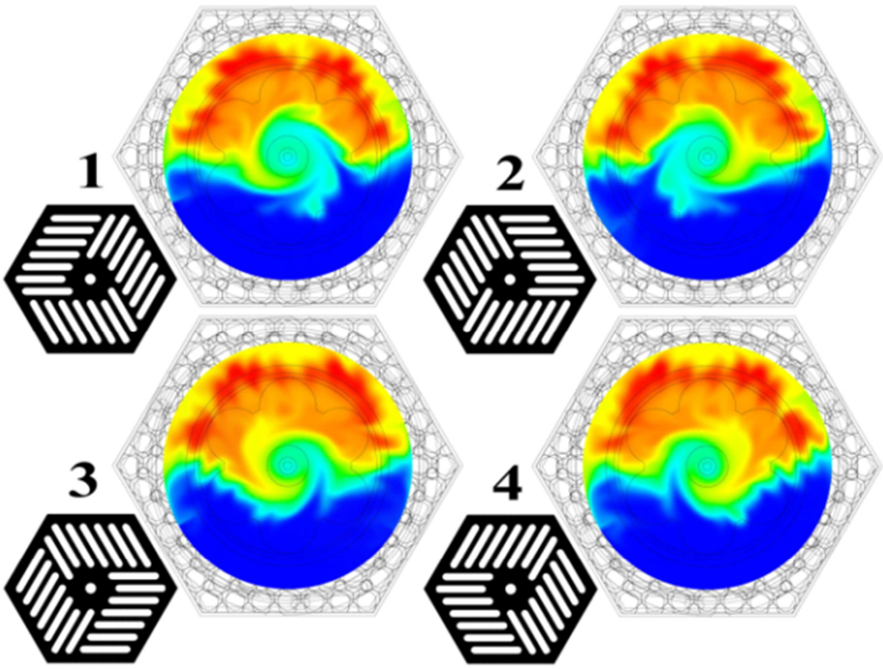

Image 14 - Coolant temperature distribution after the mixing grid of all investigated cases

Image 15 displays coolant temperature distribution along fuel assembly and in the fuel assembly outlet in two cross sections. This picture captures influence of coolant stream from the central tube on the thermocouple.

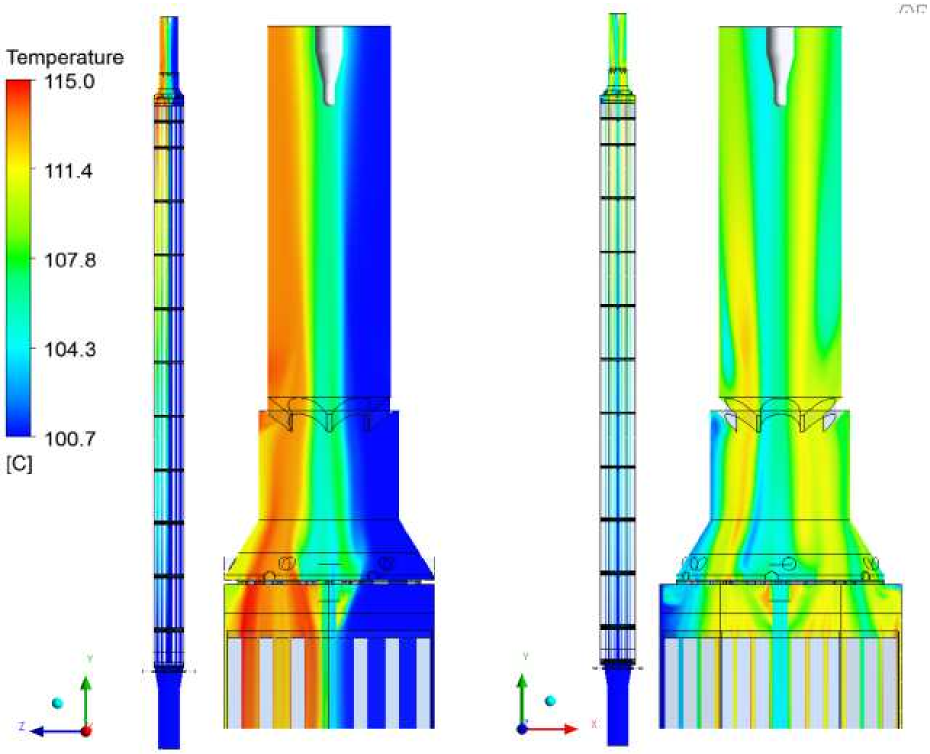

Image 15 - Coolant temperature distribution along fuel assembly (case 1)

5 Conclusion

The paper presents CFD modeling and simulation of coolant flow in fuel assembly of nuclear reactor VVER 440. The discretized model of coolant geometry contains over 60 millions cells. To perform CFD analyses ANSYS CFX software was chosen. In the model, also the flow in central tube as well as heat transfer across the wall of central tube were considered. Only steady-state analyses were performed. Generated thermal power in fuel rods was prescribed individually for each rod with axial distribution of power. Total radial heat power distribution was not symmetrical.

In the first and the second type of nalaysis , the influence of mass flow through the bypass and temperature at the outlet of bypass on fuel assembly output temperature, thermocouple housing temperature and pressure drop were investigated.

Achieved results in the third type of analysis correspond with experimental results from experiment of Kurchatov Institute [L.L. Kobzar, 2006]. Result also suggest significant influence of mixing grid on data measured by the thermocouple when power performance of the fuel rods is not symmetrical.

This study also suggest to investigate influence of central tube on thermocouple.

References

ANSYS CFX, Theory manual, 1280 pages.

Hirsch, Ch.: Numerical Computation of Internal and External Flows: The Fundamentals of Computational Fluid Dynamics. Butterworth-Heinemann, Oxford, 680 pages, ISBN: 978-0-7506-6594-0

Chung, T. J.: Computational Fluid Dynamics. Cambridge University Press, Cambridge, 1056 pages, ISBN: 9780521769693

Donea, J., Huerta, A.: Finite Element Methods for Flow Problems. John Wiley & Sons, West Sussex, 362 pages, ISBN: 978-0-471-49666-3

L.L. Kobzar, D.A. Oleksyuk, Experiments on simulation of coolant mixing in fuel assembly head and core exit channel of VVER-440 reactor, 16th Symposium of AER on VVER Reactor Physics and Reactor Safety

Oberkampf, W. L., Trucano, T. G.: Verification and Validation in Computational Fluid Dynamics. Sandia National Laboratories, Albaquerque, 790 pages, ISBN: 978-0521837583

Versteeg, H. K., Malalasekera, W.: An introduction to Computational Fluid Dynamics, The Finite Volume, 520 pages, ISBN: 978-0131274983

Acknowledgement

This work was supported by Grant Agency APVV-0450-10, VEGA 1/0228/14, KEGA 015STU-4/2012

Contact address:
Ing. Jakub Jakubec
xjakubecj@stuba.sk

DYNAMICKÁ ANALÝZA ŽELEZOBETÓNOVEJ VALCOVEJ NÁDRŽE

NORBERT JENDŽELOVSKÝ, ĹUBOMÍR BALÁŽ

Katedra stavebnej mechaniky,Stavebná fakulta, STUv Bratislave

Abstract: This paper deals with a problem of eigenfrequencies of cylindrical tank rested on elastic foundation. For an ANSYS analysis of eigenfrequencies some numerical models of gravel subgrade are used and finally results got by these models are compared. In final part of the paper some crucial results are presented both in a graphical and numerical way.

Keywords: CylindricTank, Dynamic Analysis, Ansys, Eigenfrequencies, Custom shape of oscillation

1 Úvod

V tomto článku budeme prezentovať výpočet vlastnýćh tvarov a frekvencií valcových nádrží pomocou programu ANSYS, pričom sme použili štyri odlišné teórie počítačového modelovania náplne valcovej nádrže. Všetky tieto modely boli postupne analyzované na pevnom podklade aj pružnom podloží. Parametre výpočtu pružného podkladu boli prevzaté z reálnej konštrukcie štrkového vankúša pod valcovou nádržou. Podložie bolo modelované Winklerovým modelom podložia.

V prvej časti sme overili hodnotu prvej vlastnej frekvenicie podľa empirických vzťahov. Išlo ov zťah pre nádrž z pevným podopretím (1) a o nádrž z pružným podopretím (2).

$$f = \sqrt{\frac{3 \cdot EI}{4 \cdot \pi^2 \cdot h^3 \cdot m}} \tag{1}$$

$$f = \frac{1}{4 \cdot \pi^2} \cdot \frac{3 \cdot EI \cdot \pi \cdot r^2 \cdot k}{h^2 \cdot \left(\pi \cdot r^4 \cdot h \cdot k + 12 \cdot EI\right) \cdot m} \tag{2}$$

Nasledne sme modelovali nádrže pomocou MKP v progreme Ansys.

Náplň v nádrži sme postupne modelovali štyrmi spôsobmi:

Hmota rozdelená do hmotných bodov po plášti nádrže (model A) (Kotrasová,2010, Kotrasová,2012).

Rozdelením hmoty na dve časti, spodná hmota pevne spojená s konštrukcioiu a druha hmota pri hornokm povrchu spojená cez pružné prvky s plášťom (model B) (Juhásová,2002).

V tretiom a štvrtom modely bol objem kvapalinovej oblasti modelovaný pomocou elementov FLUID30 a FLUID80, tieto prvky sú špecialne určené na modelovanie tekutiny (model C a D).

Parametre modelu valcovej nádrže

Priemer nádrže:	8.23 m
Hrúbka dna:	0.4m
Hrúbka steny:	0.4 m
Výška nádrže:	6.0 m
Betón:	C 30/37
Zaťaženie:	voda (γ =10 kN/m^3)

Postupne sme určili prvé vlastné tvary a frekvencie valcovej nádrže, ktorej výpočtový model bol stanovený podľa parametrov skutočnej konštrukcie. Takáto valcová nádrž je postavená v závode na výrobu bioplynu v obci Budča okres Zvolen, Slovenská republika

2 Model železobetónovej valcovej nádrže

V programe ANSYS sme vytvorili konečno-prvkový model valcovej nádrže podľa preddefinovaných parametrov, priestorový model sme vytvorili ako 3D teleso rovnakých rozmerov ako je skutočná valcová nádrž. Na modelovanie steny a dna valcovej škrupiny sme použili škrupinový prvok SHELL63. Objem kvapalinovej oblasti bol vytvorený osemuzlovým konečným prvkom FLUID30 a osemuzlovým prvkom FLUID80. v modeloch C a D. V Modeloch A a B bol na modelovanie hmoty použitý prvok MASS21

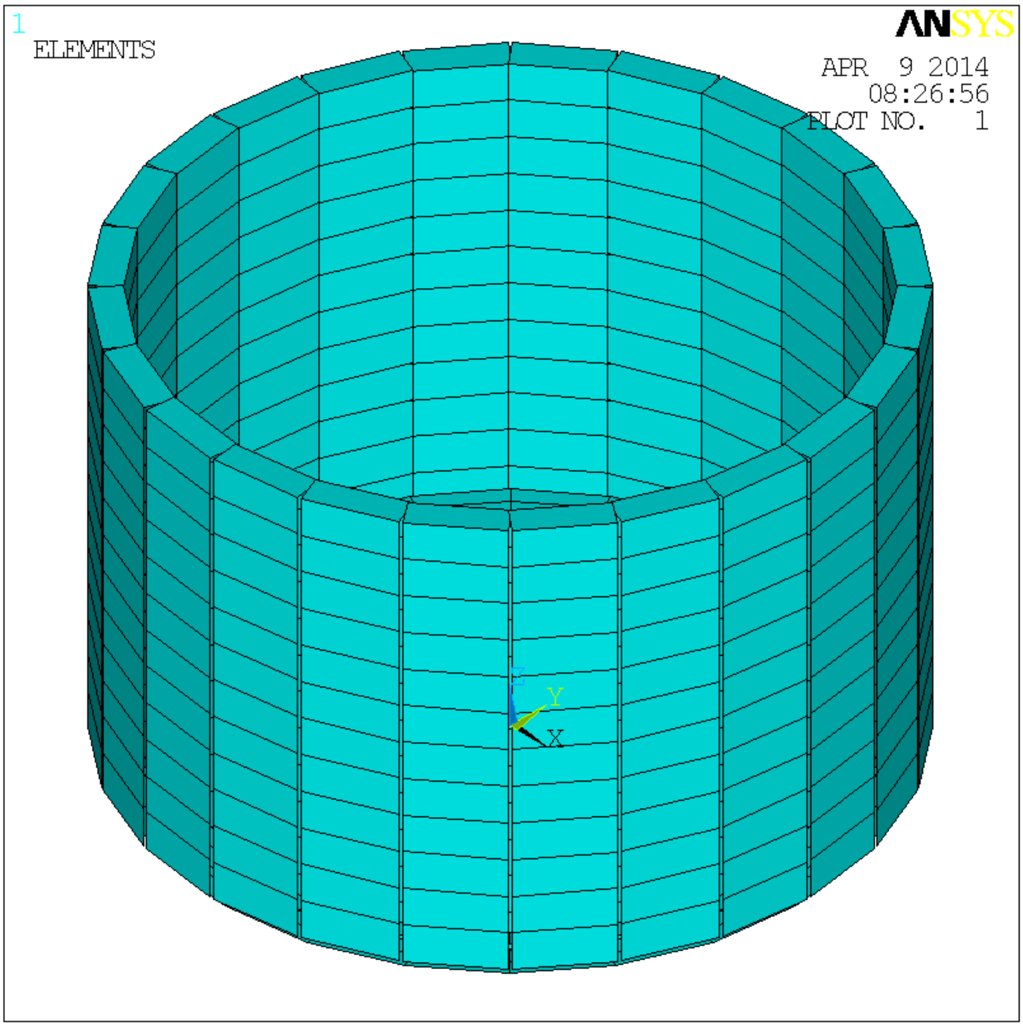

Obrázok 21 – Model valcovej nádrže

3 Rovnomerne rozmiesnená hmota

V ďalšej časti sme hmotu vody rozdelili rovnomerne do uzlov plášťa valcovej nádrže model A. Na obr. 2 je zobrazený model valcovej nádrže a prvý vlastný tvar kmitania pre pevné podopretie. Obr. 3 prezentuje prvý vlastný tvar na pružnom podloží pre model s rovnomerne rozmiestnenou hmotou vody do plášťa nádrže – model A.

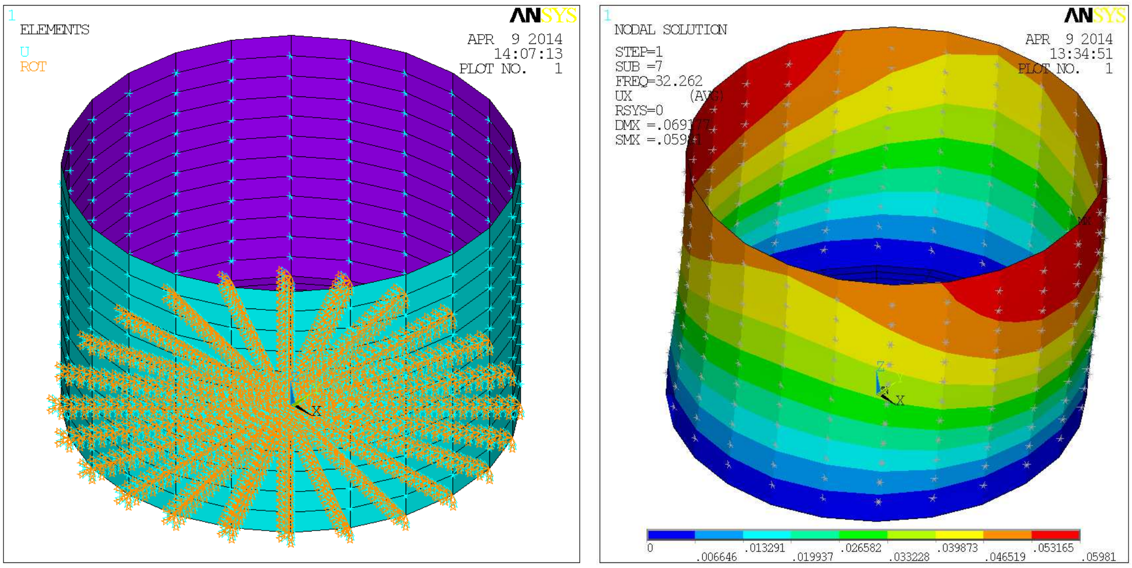

a) b)

Obrázok 2 – a) Model valcovej nádrže; b) Prvý tvar kmitania

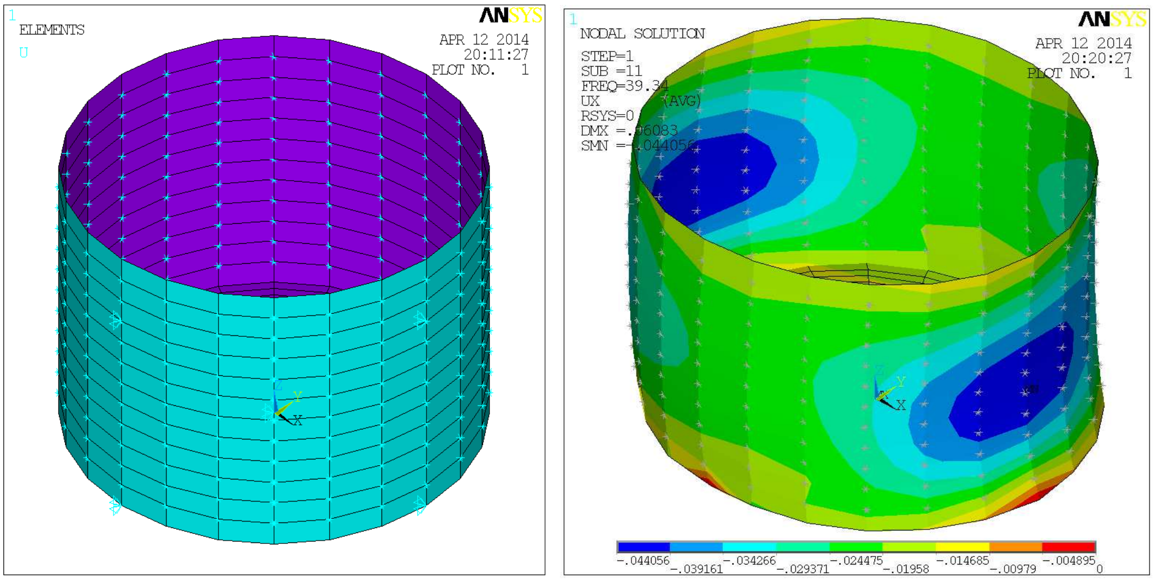

a) b)

Obrázok 3 – a) Model valcovej nádrže; b) Prvý tvar kmitania

4 Housner – Epsteinova metóda

Ak je celková hmota kvapaliny v nádrži $\boldsymbol{m_{tot}}$ urýchlená prostredníctvom základne v horizontálnom smere potom sa jej istá časť $\boldsymbol{m_1}$ chová ako impulzná hmota, ktorá je pevne spojená s obklopujúcou stenou nádrže. Housner uvažoval nádrž ako tuhú konštrukciu, takže pohyb kvapaliny $\boldsymbol{m_I}$ je v tomto prípade synchronizovaný s horizontálnym pohybom dna. Pretože priamym dôsledkom seizmického budenia je aj kmitanie voľnej hladiny kvapaliny existuje tiež takzvaná konvektívna hmota kvapaliny $\boldsymbol{m_k}$, ktorá je so stenou nádrže spojená pružne a jej pohyb má autonómny nízkofrekvenčný charakter. Výsledný hydrodynamický tlak je potom zložený z tlaku vyvolaného hmotou $\boldsymbol{m_I}$ *resp.* $\boldsymbol{m_k}$ Pôvodnú Housnerovu hypotézu zjednodušil Epstein (Jendželovský,2012).

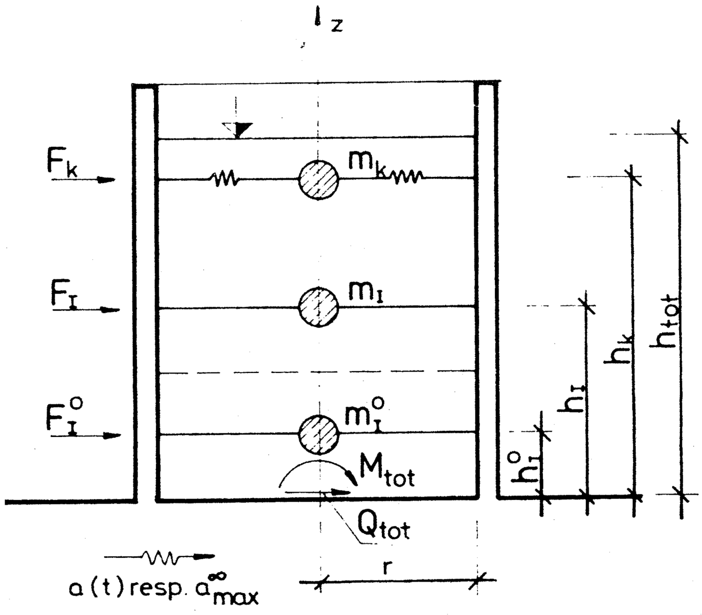

Obrázok 4 – Označenie veličín pre výpočet

1. Označenie všetkých veličín je znázornené na obr. 6. Okrem toho $\boldsymbol{\rho}$ je merná hmotnosť kvapaliny a $\boldsymbol{T}$ je perióda vlastných kmitov voľnej kvapaliny v nádrži. Podľa prevrátenej hodnoty, určíme s príslušného spektra odozvy pre približne 5% útlm odpovedajúce zrýchlenie $\boldsymbol{a_K}$. Ďalej vo vzťahoch (10) a (12) $\boldsymbol{a_{max}}$ je takzvané zrýchlenie pri nulovej perióde (nádrž je tuhá), čo je asymptotická hodnota v spektre odozvy. Pri $\boldsymbol{f=\infty}$ alebo $\boldsymbol{T=0}$ predstavuje amplitúdu zrýchlení základne v tomto prípade v horizontálnom smere.
2. Veličiny označené indexom * sa používajú pre približné vyjadrenie hydrodynamického účinku kvapaliny na dno nádrže čím sa zväčšuje celkový ohybový moment v základovej škáre z $\boldsymbol{M_{tot}}$ (bez účinku na dno)na $\boldsymbol{M^*_{tot}}$ (v rátane tohto účinku).
3. Vodorovná sila $\boldsymbol{Q_{tot}}$ a ohybový moment $\boldsymbol{M_{tot}}$ resp. $\boldsymbol{M^*_{tot}}$ vyjadrujú iba hydrodynamický účinok kvapaliny v nádrži a nie jej vlastný zotrvačný účinok, ktorý je v prípade dokonale tuhej nádrže evidentný. Pretože vodorovné seizmické zrýchlenie môže meniť svoju orientáciu, je potrebné počítať s analogickou zmenou smeru pôsobenia sily $\boldsymbol{Q_{tot}}$ a ohybového momentu $\boldsymbol{M_{tot}}$ resp. $\boldsymbol{M^*_{tot}}$.

Ďalšie zobecnenie Housnerového či uvedeného Epsteinovéhoho algoritmu spočíva napr. v uvážení nie len prvého základného tvaru kmitania, ale aj vyšších tvarov kmitania voľnej hladiny v nádrži. To môže mať niekedy význam ak si uvedomíme, že základná frekvencia kmitov voľnej hladiny býva okolo *0,5 Hz*, takže až vyššie frekvencie a im odpovedajúce vlastné tvary môžu rezonovať s dominantnými frekvenciami seizmického budenia (Sumec,2008, Mrózek,2009).

Na obr. 5 je zobrazený model B valcovej nádrže a prvý vlastný tvar kmitania pre pevné podložie. Obr. 6 prezentuje prvý vlastný tvar na pružnom podloží pre modely s pružne pripojenou koncentrovanou hmotou náplne.

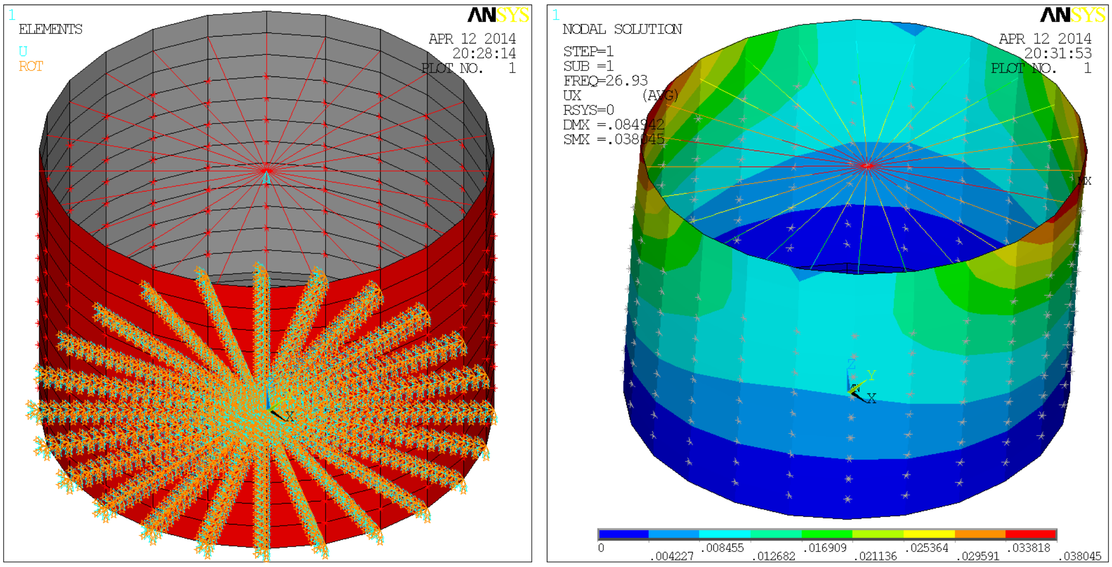

a) b)

Obrázok 5 – a) Model valcovej nádrže pevné podopretie; b) Prvý tvar kmitania

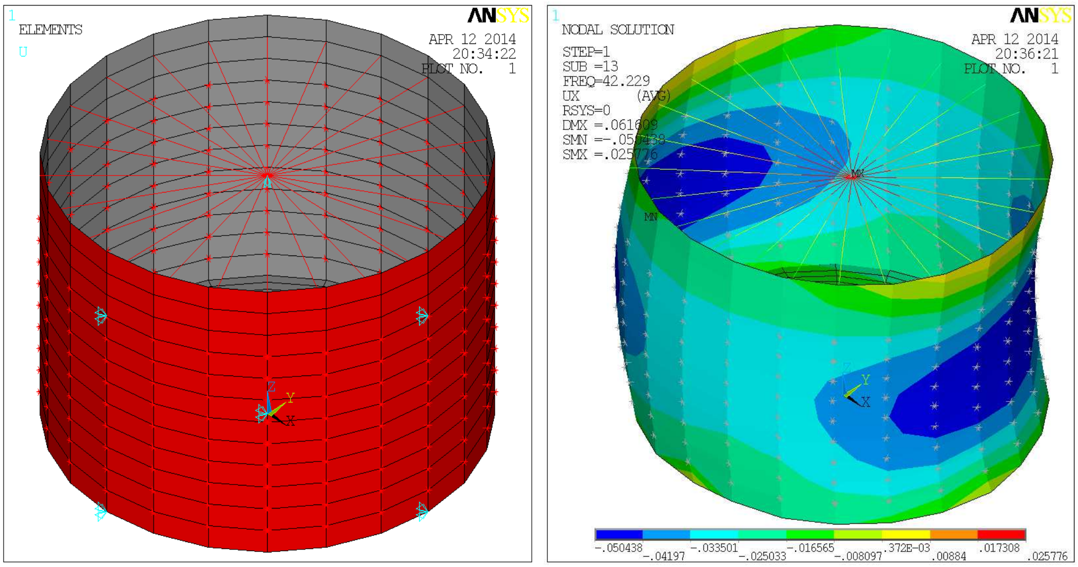

a) b)

Obrázok 6 – a) Model valcovej nádrže pružné podložie; b) Prvý tvar kmitania

5 Modelovanie pomocou konečných prvkov FLUID30

V treťom prípade sme pristúpili k modelovaniu s použitím prvku FLUID30. Na nasledujúcich obrázkoch je zobrazený model železobetónovej valcovej nádrže a následne prvý vlastny tvar kmitania pre pevné podopretie (obr.7) a pružné podložie pod valcovou nádržou (obr.8). Na modelovanie samotnej konštrukcie valcovej nádrže sme použili konečný prvok SHELL63.

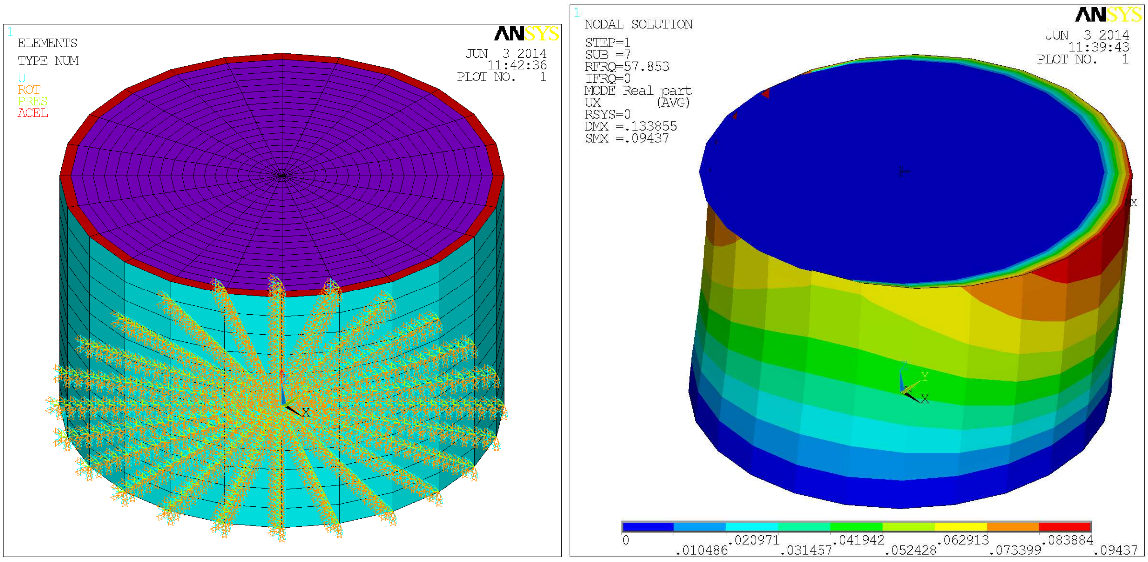

a) b)

Obrázok 7 – a) Model valcovej nádrže – FLUID30 pevne podopretie; b) Prvý tvar kmitania

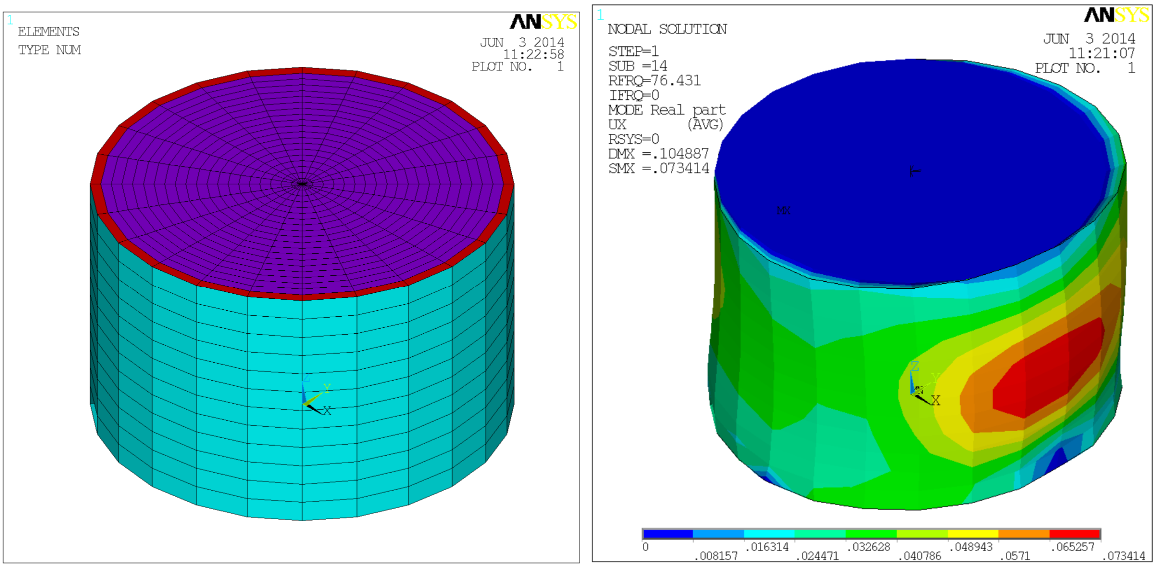

a) b)

Obrázok 8 – a) Model valcovej nádrže – FLUID30 pružné podložie; b) Prvý tvar kmitania

6 Modelovanie pomocou konečných prvkov FLUID80

V poslednom prípade sme pristúpili k modelovaniu valcovej nádrže a jej náplne pomocou konečného prvku FLUID80. Na nasledujúcich obrázkoch je zobrazený model železobetónovej valcovej nádrže a následne prvý vlastny tvar kmitania pre pevné podopretie (obr.9) a pružné podložie pod valcovou nádržou (obr.10).

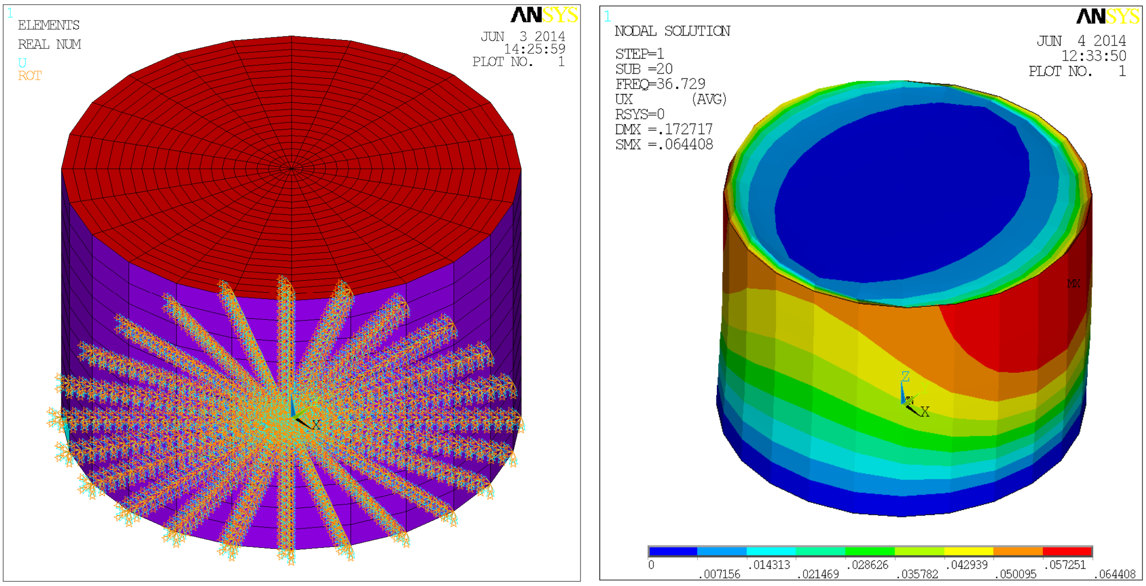

a) b)

Obrázok 9 – a) Model valcovej nádrže – FLUID80; b) Prvý tvar kmitania

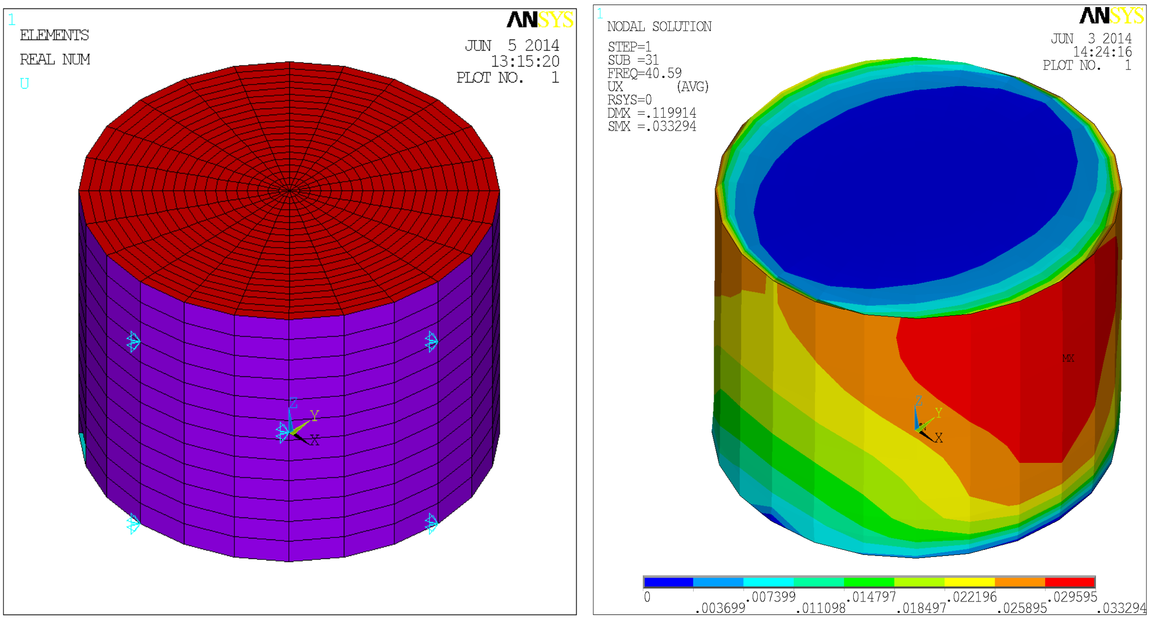

a) b)

Obrázok 10 – a) Model valcovej nádrže – FLUID80; b) Prvý tvar kmitania

7 Záver

V tomto príspevku sme porovnávali štyri spôsoby modelovania náplne valcovej nádrže s výpočtom pomocou vzťahov (1) a (2), a ich vplyv na veľkosť vlastných frekvencií. Pri tejto analýze sme použili pevné aj pružné podložie pod základovou doskou plnej valcovej nádrže.

Numerickým modelovaním v metóde konečných prvkov sme upresnili výpočet vlastných frekvencií plnej valcovej nádrže podla vzťahov (1) a (2), ktoré sa nachadzajú v literature a technických normách.

Model C je rádovo odlišný od ostatných pretože pri tomto výpočte vzniká nesymetrická sústava rovníc z čoho vzniká nárčný výpočet vlasných čísel a vlastných vektorov. Z tohto dôvodu je zložité hľadanie vlastných frekvencií kmitania valcovej nádrže.

Tabuľka 14 Vlastné frekvencie plnej valcovej nádrže

VLASTNÉ FREKVENCIE KMITANIA					
	“Model A”	**“Model B”**	**“Model C”**	**“Model D”**	**equation (1) a (2)**
pevné podopretie	**32,26 Hz**	**26,93 Hz**	**57,85 Hz**	**36,72 Hz**	**41,00 Hz**
pružné podložie k = 16 000 kN/m^3	**39,34 Hz**	**42,29 Hz**	**76,43 Hz**	**40,59 Hz**	**60,00 Hz**

Literatúra

JENDŽELOVSKÝ N., BALÁŽ Ľ., 2012. *Dynamic Analysis of a Cylindrical Tank, Proceedings of the 6th International Conference on Dynamics of Civil Engineering and Transport structures and Wind Engineering, DIN-WIND 2012.*

JUHÁSOVÁ E., BENČAT J.,KRIŠTOFOVIČ V.,KOLCÚN Š., 2002. Expected seismic response of steel water tank. *12th European Conference on Earthquake Engineering*,2002 London.

KALA J., SALAJKA V., HRADIL P., 2012. Investigation of eigenvalue problem of water tower construction interacting with fluid. *Journal of Vibroengineering* Volume 14, Issue 3, Pages 1151-1159

KALA J., SALAJKA V., HRADIL P., 2012. Response of water tower on wind induced vibration considering interaction of fluid and structure. *2nd International Conference on Engineering and Technology Innovation 2012*, ICETI 2012; Kaohsiung; Taiwan; 2 November 2012 through 6 November 2012 Volume 284-287, 2013, Pages 1269-1272

KOTRASOVÁ K., KORMANÍKOVÁ E., 2010. Frequency analysis of the base plate on Winkler model subsoil model, *Pozemné komunikácie a dráhy* 1-2/2010 roč. 6, (in Slovak).

KOTRASOVÁ K., KORMANÍKOVÁ E., 2012. Frequency analysis of fluid in rectangular ground- supported tank, *12th International Multidisciplinary Scientific GeoConference and EXPO, SGEM 2012*, June 2012. Varna, Bulgaria, Volume 3, p. 693-69817.

MISTRÍKOVÁ Z., JENDŽELOVSKÝ N., 2012. Static Analysis of the Cylindrical Tank Resting on Various Types of Subsoil. *Journal of Civil Engineering and Management*, Vol. 18, Issue 5 pp. 744-751.

MRÓZEK M., NEVAŘIL A., ČADA Z., BRAŤKA M., 2009. Contemporary approaches to seismic analysis of tank with fluid, *Engineering mechanics 2009, National conference with international participation*, Svratka, CR, 11.-14.5.2009, Praha, Czech Republic, p. 186-187.

SUMEC J., JENDŽELOVSKÝ N., 2008 Seismic analysis of reinforced concrete water tank, *Proceedings of the 4th International Conference on Dynamics of Civil Engineering and Transport structures and Wind Engineering, DIN-WIND 2008.*

Poďakovanie
-Tento príspevok vznikol za finančnej podpory grantovej agentúry MŠ SR, ako projekt VEGA01/0629/12.
-Prepojenie vedeckého výskumu a stavebnej praxe umožnila spoločnosť Bioplyn Budča spol. s.r.o. Elektrárenská 1 Bratislava 831 04.
Zodpovedný: Ing. Viliam Bendel, Šípová 3/A , Bratislava, t.č. +421 903900654,
e-mail : bendel@europea.sk

Kontaktná adresa:
Prof. Ing. Norbert Jendželovský,PhD., Katedra stavebnej mechaniky, Stavebná fakulta
Slovenská technická univerzita v Bratislave, Radlinského 11, 813 68 Bratislava.
e-mail:norbert.jendzelovsky@stuba.sk

Ing. Ľubomír Baláž., Katedra stavebnej mechaniky, Stavebná fakulta
Slovenská technická univerzita v Bratislave, Radlinského 11, 813 68 Bratislava.
e-mail:lubomir.balaz@stuba.sk

DETERMINISTIC AND PROBABILISTIC ANALYSIS OF STEEL HALL COLLAPSE LOADED UNDER EXTREME WIND LOADS

J. KRÁLIK

Abstract: Engineering structures are designed to resist all expected loadings without failure. However, structural failures do happen occasionally, mainly due to inadequate design and construction, especially for extreme loads. The main aim of this contribution is to find out the maximum load carrying capacity of the steel frame. Account is taken of nonlinear material behaviour and geometry of member, in combination of the stability analysis.

Keywords: Extreme snow, nonlinearity, probability, sensitivity, LHS, ANSYS

1 Introduction

This paper deals with the resistance of the steel hale frame of the nuclear power plant (NPP) in locality J.Bohunice. The international organization IAEA in Vienna (IAEA, 1995 to IAEA, February 2003) set up the design requirements for the safety and reliability of the NPP structures. The extreme environmental events (e.g. wind, temperature, snow, explosion...) (IAEA, February 2003; NUREG-1150, 1990; NUREG/CR-4839, 1992; SHMU, 2012 and UJD SR 2011) are the important loads from the point of the NPP safety performance. The extreme wind loads are defined with the probability of mean return period equal to one per 10^4 years (IAEA, February 2003). This paper deals with the analysis of the steel frame loaded with extreme wind load. The IAEA (IAEA, 1995) and NRC standards (NRC, RG 1.200, 2009; NUREG-1150, 1990 and NUREG/CR-4839) require setting up the probability of the structure failure during the extreme loads. The critical steel frame of NPP hall structure was investigated (Image 1).

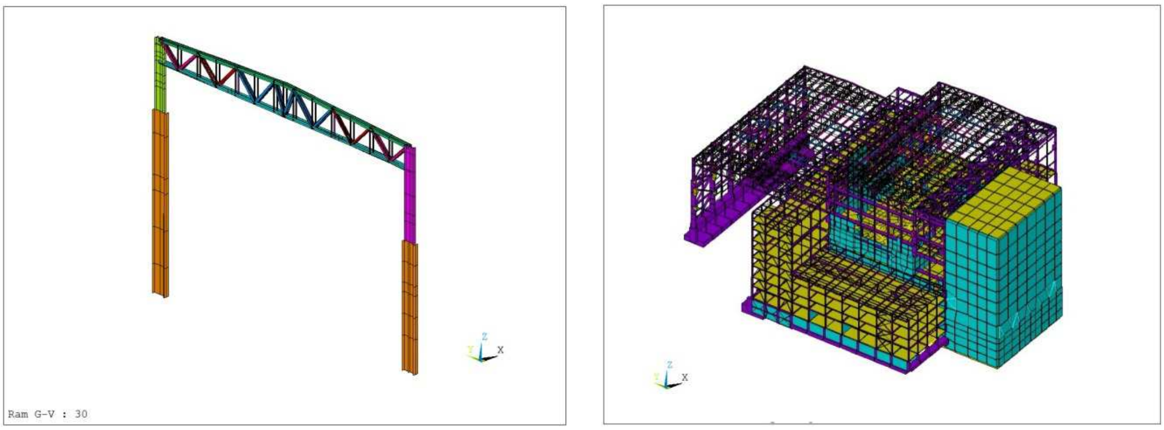

Image 1 - Calculation Model of the Frame (left), Scheme of the Steel Hall (right)

The FEM model of the steel hall frame consist the beams and mass elements of ANSYS program - BEAM188 and MASS21 (Image 1).

2 Loads and load combinations

The load combination of the deterministic calculation is considered according to Eurocode (EN 1990, 2002) and IAEA requirements (IAEA, 1978) for the ultimate limit state of the structure as follows:

Probabilistic method – extreme design situation

$$E = G + Q + W_E = g_{var}.G_k + q_{var}.Q_k + a_{var}.W_{Ek} \quad (1)$$

where g_{var}, q_{var}, a_{var}, t_{var} are the variable parameters defined in the form of the histogram calibrated to the load combination in compliance with Eurocode (EN 1990, 2002). And G_k is the characteristic value of the permanent dead loads, Q_k - the characteristic value of the permanent live loads, $W_{Ed.k}$ - the characteristic value of the extreme wind loads.

3 Wind load

The load on a structure due to the wind will depend on both wind velocity and terrain roughness (EN 1991-1-4, 2003). The wind velocity and the velocity pressure are composed of a mean and a fluctuating component. The mean wind velocity v_m should be determined from the basic wind velocity v_b which depends on the wind climate and the height variation of the wind determined from the terrain roughness and orography. The fluctuating component of the wind is represented by the turbulence intensity. The extreme wind load is defined for the probability of 10^{-4} by year on the base of the IAEA requirements (IAEA, 2011) twice the characteristic wind load value:

$$v_A = 2.v_b = 0.48\ m/s \quad (2)$$

To extrapolate the maximum quantity of rainfall from meteorological measurement results on the quantity of rainfall (measured in the time period from 12 to 48 hours), for a mean time of recurrence 10^2 or 10^4 years, it is recommended to use the Gumbel probability distribution with the requirement that the probability of the excess quantity of rainfall with mean time repeat 10^2, respectively 10^4 years, during the design of the power plant lifetime is less than 0.5, respectively 0.005.

4 Nonlinear analysis

The limit state of the steel frame was considered to utilise the geometric and material nonlinearity in program ANSYS (Králik, J., 2009). The geometric nonlinearity is based on the theory of the large strain, which is often used for elastic-plastic elements. The elastic-plastic model of steel material was taken in compliance with the Von Mises yield function. The Newton-Raphson iteration method to solve nonlinear equations was taken. The plasticity model is defined as shown on Image 2, as multilinear isotropic hardening material model.

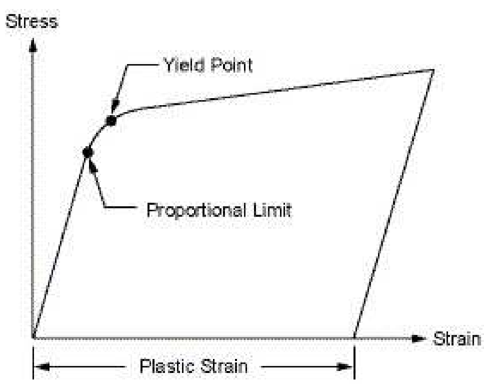

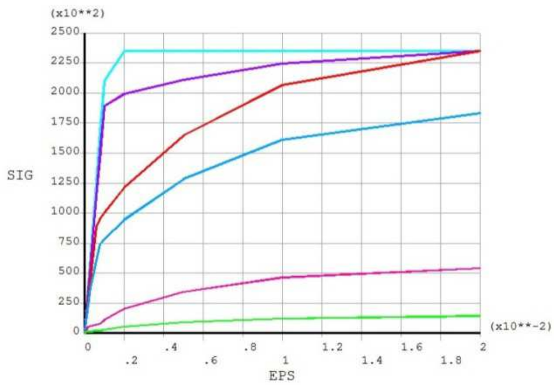

Image 2 - Elasto-Plastic Stress-Strain Curve (left), Nonlinear Material Properties (right)

5 The probabilistic approach

Most problems concerning the reliability of building structures are defined today as a comparison of two stochastic values, loading effects *E* and the resistance *R*, depending on the variable material and geometric characteristics of the structural element (Janas, P., Krejsa, M., Krejsa, V., 2009; Kala, Z., 2011; Králik, J., 2009; Krejsa, M., 2012; Melchers, R. E., 1999; Novák, D. Vořechovský, M. Rusina, R., 2003 And Suchardová, P., Bernatík, A., SuchardA, O., 2012). The variability of those parameters is characterized by the corresponding functions of the probability density $f_r(x)$ and $f_e(x)$. In the case of a deterministic approach to a design, the deterministic (nominal) attributes of those parameters R_d and E_d are compared.

6 Uncertainties of input data

The uncertainties of the input data – action effect and resistance are for the case of the probabilistic calculation of the structure reliability defined in (JCSS-OSTL/DIA/VROU-10-11-2000, 2000) and Eurocode (EN 1990, 2002). The stiffness of the structure is determined with the characteristic value of Young's modulus E_k and variable factor e_{var}. Loads are represented by theirs characteristic values G_k, Q_k, $A_{E,k}$, and variable factors g_{var}, q_{var} and w_{var}. The resistance of the steel is delimited by the characteristic values of the strength f_{sk} and the variable factor f_{var}. The uncertainties of the calculation model are considered by variable model factor θ_R and variable load factor θ_E for Gauss's normal distribution.

7 Failure wind loads of frame

The failure capacity of frame on extreme wind load is obtained from plastic calculation of frame (Králik, J., 2009). The fragility curve of the extreme wind was calculated on the base of the nonlinear deterministic analysis of the steel frame for median values of input data. The probability of the structure failure was calculated for the various levels of the wind loads. The density of probability and the cumulative probability function were determined using simulation on the base of LHS method (Novák, D. Bergmeister, K. Pukl, R. Červenka, V., 2009). The Image 3 shows results for 10x the value of extreme wind velocity which was 48 m/s. After several calculations we discovered that the maximum carrying capacity of frame is between 2,2x and 2,3x the value of extreme wind without automatic time stepping.

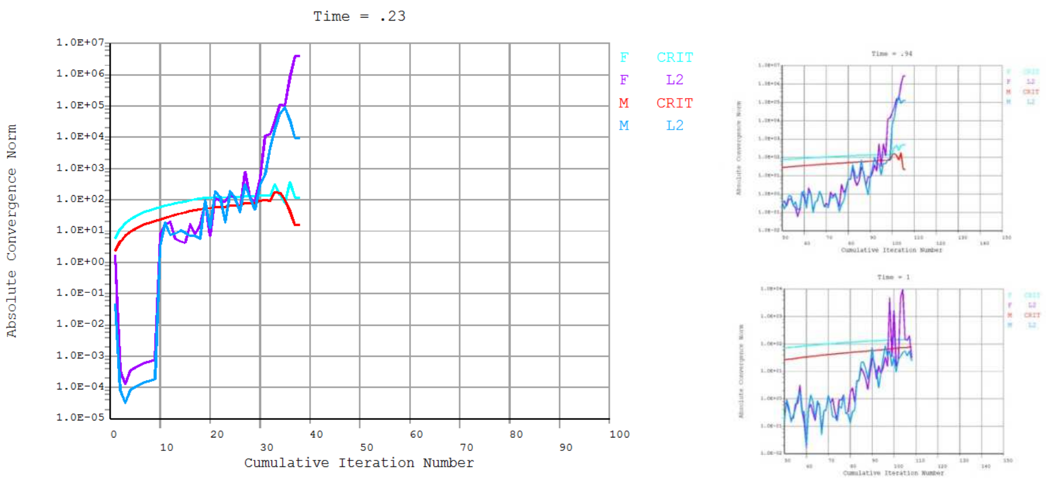

Image 3 - Max. Capacity for Extreme Wind Values 10x (left), 2,3x (up), 2,2x (down)

8 Wind fragility curve of frame

The probability of the frame failure was determined by the probabilistic analysis by the simulation in LHS method using program FReeT (Novák, D. Bergmeister, K. Pukl, R. Červenka, V., 2009). The fragility curve was calculated for various levels of wind loads using the results from the nonlinear analysis of the steel hall frame. The wind fragility curve of the steel hall frame is presented in Image 4. This curve was calculated by LHS method using the program FReeT.

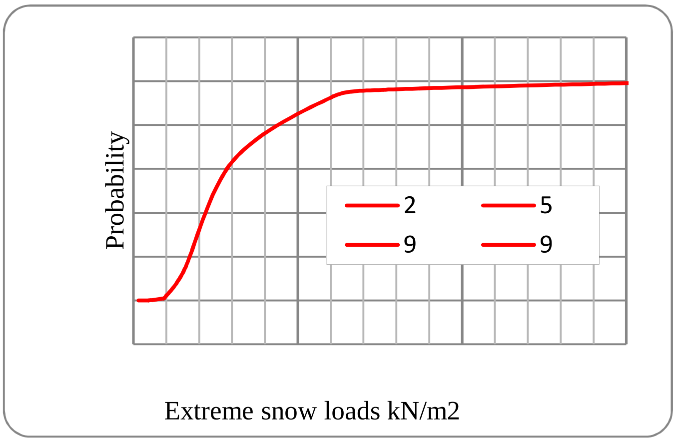

Image 4 - Wind Fragility Curve of the Steel Hall Frame

9 Conclusion

This paper presents the reliability analysis of the steel hall frame resistance due to extreme wind loads (SHMU, 2012). The extreme loads were defined for mean return period equal to one per 10^4 years in accordance of the IAEA requirements for NPP structures (IAEA, 1995 to IAEA, 2011). The geometric and material nonlinearity were taken into account. The deterministic and probabilistic analysis of the structure failure was investigated. The limit state (frame collapse) was obtained from deterministic analysis for the factor $\eta_u=2.3$. The probability of failure was calculated on program FReeT using LHS method (Novák, D. Vořechovský, M. Rusina, R., 2003). The probability of failure value is lower than 10^{-6}. In the case of the wind load multiplied by factor $\eta_u=2.3$ the probability of failure is equal to 0.0087. The wind fragility curve of the steel hall frame was determined using LHS method for various level of the wind load.

References

EN 1990, Eurocode – *Basis of structural design*. Bruxelles.

EN 1991-1-4, CEN 2003. *Eurocode 1 - Actions on structures - Part 1-4: General actions - Wind loads*.

EN 1993-1-1, CEN 2003. *Eurocode 3: Design of steel structures. Part 1-1 General rules and rules for buildings.* ENV 1993-1-1.

EN 1990, CEN 2002. *Eurocode – Basis of structural design*. Bruxelles.

IAEA, 1995. Safety Guide 50-SG-QA6, Rev. 1, "*Quality Assurance in the Design of Nuclear Power Plants*".

IAEA , November 1978. Safety Standards Safety in Nuclear Power Plant Siting, *A Code of Practice*, No. SS-50-C-S, Vienna.

IAEA, 1991. Safety Guide SO-SG-Sl, Rev. 1, "*Earthquakes and Associated Topics in Relation to Nuclear Power Plant Siting*".

IAEA, 2000. *Safety of Nuclear Power Plants: Design, Safety Standards Series* No. NS-R-1, Vienna.

IAEA, February 2003. *Safety Standards, External Events Excluding Earthquakes in the Design of Nuclear Power Plants*, No. NS-G-1.5, Vienna.
IAEA, March 2003. *Safety Standards, Extreme external events in the design and assessment of nuclear power plants*, No. IAEA-TECDOC-1341, Vienna.
IAEA, February 2003. *Safety Standards, Meteorological Events in Site Evaluation for Nuclear Power Plants*, No. NS-G-3.4, Vienna.
IAEA, February 2006. *Safety Standards, Advanced nuclear plant design options to scope with external events*, IAEA-TECDOC-1487, Vienna.
IAEA, 2011. *Safety Standards, Meteorological and Hydrological Hazards in Site Evaluation for Nuclear Installations*, No. SSG-18, Vienna.
JANAS, P., KREJSA, M., KREJSA, V., 2009. Structural Reliability Assessment Using Direct Determined Probabilistic Calculation. In: Proceedings of the *Twelfth International Conference on Civil, Structural and Environmental Engineering Computing*, paper 72, Topping, Costa Neves & Barros (eds), Funchal, Madeira, Portugal. Civil-Comp Press,. ISBN 978-1-905088-31-7.
JCSS-OSTL/DIA/VROU-10-11-2000, 2000. *Probabilistic Model Code, Part 1 Basis of Design*, Working material, http://www.jcss.ethz.ch.
KALA, Z., 2011. Sensitivity analysis of steel plane frames with initial imperfections. *Engineering Structures*, 33, 8, pp.2342-2349.
KAZAKOV K., YANAKIEVA, A., 2012. Computational Effectivness of the Augmented Lagrange Method in the FE Simulations of Pull-out of Steel Bar and Concrete. *Comptes rendus de l'Académie bulgarie des Sciences,* Tome 65 (2), p. 219-224.
KRÁLIK, J. KRÁLIK, J., ml., 2006. Reliability and Sensitivity Analysis of Tall Building Structures Considering the Soil-Structure Interaction. In: *International Conference VSU 2006*, Sofia, Bulgaria, May 22-23.. Vol. I. pp. I- 197-203. ISBN – 10: 954-331-009-2.
KRÁLIK, J., 2009. *Safety and Reliability of Nuclear Power Buildings in Slovakia. Earthquake-Impact-Explosion*. In: Monograph. Edition STU Bratislava, 305 p.
KRÁLIK, J., 2009. *Reliability Analysis of Structures Using Stochastic Finite Element Method*. Edition STU Bratislava, pp. 143.
KRÁLIK, J. KRÁLIK, J., jr., 2009. Deterministic and Probabilistic Analysis of Non-symmetrical Wind Effects to Symmetrical High Rise Buildings. In: *Proceedings ESREL, Reliability, Risk and Safety, Theory and Applications*, CRC Press/A.Balkema Book, Taylor&Francis Group, Prague, Czech Republic, 7-10 September. Vol.2, p.1393-1396.
KREJSA, M., 2012. Stochastic Modelling of Fatigue Crack Progression using the DOProC Method, In: *Proceedings of the Eleventh International Conference on Computational Structures Technology*, ©Civil-Comp Press, 2012 B.H.V. Topping, (Editor), Civil-Comp Press, Stirlingshire, Scotland, Full text in CD, pp.18.
MELCHERS, R. E., 1999. *Structural Reliability: Analysis and Prediction*, John Wiley & Sons, Chichester, U.K.
NOVÁK, D. BERGMEISTER, K. PUKL, R. ČERVENKA, V., 2009. Structural assessment and reliability analysis for existing engineering structures, theoretical background. *Structure and infrastructure engineering*, 9, n. 2, p. 267-275.
NOVÁK, D. VOŘECHOVSKÝ, M. RUSINA, R., 2003. Small-sample Probabilistic Assessment – software FReET, *ICASP 9, 9th International Conference on Applications of Statistics and Probability in Civil Engineering*, San Francisco, USA, July 6-9. pp. 91-96.
NRC, RG 1.200, 2009. An approach for determining the technical adequacy of probabilistic risk assessment results for risk-informed activities, U.S. Nuclear Regulatory Commission, Washington, DC.
NUREG-1150, 1990. *Severe Accident Risks: An Assessment for Five US Nuclear Power Plants*, Final Summary Report, Vol.1 and 2, US NRC.
NUREG/CR-4839, 1992. "*Methods for External Event Screening Quantification: Risk Methods Integration and Evaluation Program (RMIEP) Methods Development*," Report , Sandia National Laboratories and U.S. Nuclear Regulatory Commission.
SHMU, 2012. *Súhrnná správa SHMÚ pre lokalitu Jaslovské Bohunice*, Bratislava, január.

SUCHARDOVÁ, P., BERNATÍK, A., SUCHARDA, O., 2012. Assessment of loss results by means of multi - Criteria analysis. In: *Advances in Safety, Reliability and Risk Management - Proceedings of the European Safety and Reliability Conference, ESREL 2011*. London: CRC PRESS-TAYLOR & FRANCIS GROUP, pp. 1563-1570. ISBN 978-0-415-68379-1.

UJD SR, 2011. *The stress tests for Nuclear Power Plants Slovakia*, Bratislava, september.

Acknowledgement

This paper was written with the support of Slovak Grant Agency VEGA. Registration number is 1/1039/12.

Contact address:

Ing. Juraj Králik, PhD.
Institute of Constructions in Architecture and Engineering Structures, Faculty of Architecture,
Slovak University of Technology in Bratislava,
Námestie Slobody 19,
812 45 Bratislava 1,
Slovak Republic.

NONLINEAR PROBABILISTIC ANALYSIS OF THE REINFORCED CONCRETE STRUCTURES USING ANSYS-CRACK SOFTWARE

JURAJ KRÁLIK

Abstract: The paper presents an application of the nonlinear analysis of reinforced concrete structures under extreme static loads. The evaluation is based on an extension of the smeared crack model developed on the basis of Kupfer's bidimensional failure criterion and implemented into the ANSYS system as program CRACK. The nonlinear analysis was considered for the median values of the input data and the probabilistic analysis models the uncertainties of loads, material resistance and other modelling issues. Results show that the effect of thermal load are relevant mainly for the bubble condenser and at the interface between the floor of hermetic zone and the rooms beneath

Keywords: ANSYS, CRACK, concrete, nonlinear, probability, extreme load

1 Introduction

The reinforced concrete structures of nuclear power plants under the extreme static loads (internal and external temperature, overpressure during the accident and other effects) is cracked in tension or crushed in compression zone and the behaviour of the structures is nonlinear. The properties of the concrete depends on the type of the damage and the orientation of the cracks. The SOLID65 element in the system ANSYS is capable for nonlinear analysis (Musmar et al., 2014). The multi linear isotropic concrete model uses the von Mises failure criterion along with Willam and Warnke model to define the failure of concrete. ANSYS allows entering three reinforcement bars materials in the concrete, each rebar material corresponds to the x, y, and z directions of the smeared element (Kohnke, 2008). Cracking and crushing are determined by a failure surface. The failure surface for compressive stresses is based on William-Warnke failure criterion (William et al., 1975, 2001) which depends on five material parameters. Tensile stress consists of a maximum tensile stress criterion: a tension cutoff. Unless plastic deformation is taken into account, the material behavior is linear elastic until failure. When the failure surface is reached, stresses in that direction have a sudden drop to zero, there is no strain softening neither in compression nor in tension. The experiances of the various users with this element are positive as well as negative. The principal problem is the loss of the convergence after cracking in three direction in one element or after degradation of stiffnes in one node in the cracking zone. The positive experiances are with the application on the reinforced concrete beam or wall. The negative experience are in the case of the plane or space structures exposed on membrane and bending effects (Králik, 2009, 2013). The element SOLID65 is working in elastoplastic state when the stress state is lower as the failure criterion and in elastic limited state with the zero stiffneess in the direction perpendicular on the crack. From this reason the program CRACK based on the layered shell element was developed by me and incorporated in ANSYS system (Králik, 2009).

2 Non-linear model of reinforced concrete structure

The theory of large strain and rate independent plasticity were proposed during the high overpressure loading using the SHELL181 layered shell element from the ANSYS library (Kohnke, 2008).

The vector of the displacement of the l^{th} shell layer $\{u^l\} = \{u_x^l, u_y^l, u_z^l\}^T$ is approximated by the quadratic polynomial (Králik, 2009) in the form

$$\{u^l\} = \begin{Bmatrix} u_x^l \\ u_y^l \\ u_z^l \end{Bmatrix} = \sum_{i=1}^{4} N_i . \begin{Bmatrix} u_{xi} \\ u_{yi} \\ u_{zi} \end{Bmatrix} + \sum_{i=1}^{4} N_i . \frac{\zeta . t_i}{2} . \begin{bmatrix} a_{1,i} & b_{1,i} \\ a_{2,i} & b_{2,i} \\ a_{3,i} & b_{3,i} \end{bmatrix} . \begin{Bmatrix} \theta_{xi} \\ \theta_{yi} \end{Bmatrix} \tag{1}$$

where N_i is the shape function for i-node of the 4-node shell element, uxi, uyi, uzi are the motion of i-node, ζ is the thickness coordinate, ti is the thickness at i-node, $\{a\}$ is the unit vector in x direction, $\{b\}$ is the unit vector in plane of element and normal to $\{a\}$, θ_{xi} or θ_{yi} are the rotations of i-node about vector $\{a\}$ or $\{b\}$.

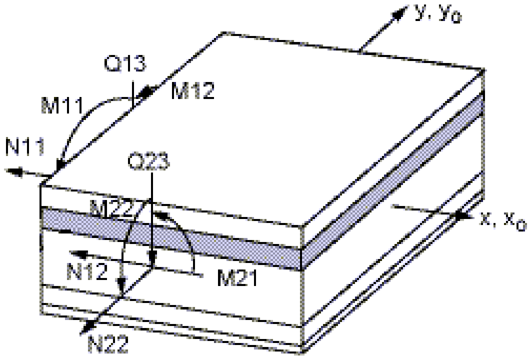

Image 1 - SHELL181 layered element

In the case of the elastic state the stress-strain relations for the l^{th} - layer are defined in the form

$$\{\sigma^l\} = [D_e^l]\{\varepsilon^l\} \tag{2}$$

where strain and stress vectors are as follows $\{\varepsilon^l\}^T = \{\varepsilon_x, \varepsilon_y, \gamma_{xy}, \gamma_{yz}, \gamma_{zx}\}$, $\{\sigma^l\}^T = \{\sigma_x, \sigma_y, \tau_{xy}, \tau_{yz}, \tau_{zx}\}$ and the matrix of the material stiffness

$$[D_e^l] = \begin{bmatrix} B^l E_x^l & B^l \mu_{xy}^l E_x^l & 0 & 0 & 0 \\ B^l \mu_{xy}^l E_x^l & B^l E_y^l & 0 & 0 & 0 \\ 0 & 0 & G_{xy}^l & 0 & 0 \\ 0 & 0 & 0 & \dfrac{G_{yz}^l}{k_s} & 0 \\ 0 & 0 & 0 & 0 & \dfrac{G_{zx}^l}{k_s} \end{bmatrix} \tag{3}$$

where $B^l = \dfrac{E_y^l}{E_y^l - (\mu_{xy}^l)^2 E_x^l}$, E_x^l (versus E_y^l) is Young modulus of the l^{th}-layer in the direction x (versus y), G_{xy}^l, G_{yz}^l, G_{zx}^l are shear moduli of the l^{th}-layer in planes XY, YZ and ZX; k_s is the coefficient of the effective shear area ($k_s = 1 + 0.2 A/25t^2 \geq 1.2$), A is the element area, t is the element thickness.

2.1 GEOMETRIC NONLINEARITY

If the rotations are large but the mechanical strains (those that cause stresses) are small, then a large rotation procedure can be used. A large rotation analysis is performed in a static analysis in the ANSYS program (Kohnke, 2008).

The strain in the *n*-step of the solution can be computed from the relations

$$\{\varepsilon_n\} = [B_o][T_n]\{u_n\} \tag{4}$$

where $\{u_n\}$ is the deformation displacement, $[B_o]$ is the original strain-displacement relationship, $[T_n]$ is the orthogonal transformation relating the original element coordinates to the convected (or rotated) element coordinates. The convected element coordinate frame differs from the original element coordinate frame by the amount of rigid body rotation. Hence $[T_n]$ is computed by separating the rigid body rotation from the total deformation $\{u_n\}$ using the polar decomposition theorem.

2.2 MATERIAL NONLINEARITY

The presented constitutive model is a further extension of the smeared crack model (Bažant et al, 2007; Červenka, 1985; Kwak, 1990; Sucharda,O. Brožovský,J., 2012), which was developed in (Králik, 2009). Following the experimental results (Červenka 1985; Jerga and Križma, 2006; Schneider, 1985) a new concrete cracking layered finite shell element was developed and incorporated into the ANSYS system (Králik, 2009). The layered approximation and the smeared crack model of the shell element are proposed.

The processes of the concrete cracking and crushing are developed during the increasing of the load. The concrete compressive stress f_c, the concrete tensile stress f_t and the shear modulus G are reduced after the crushing or cracking of the concrete (Kwak, 1990).

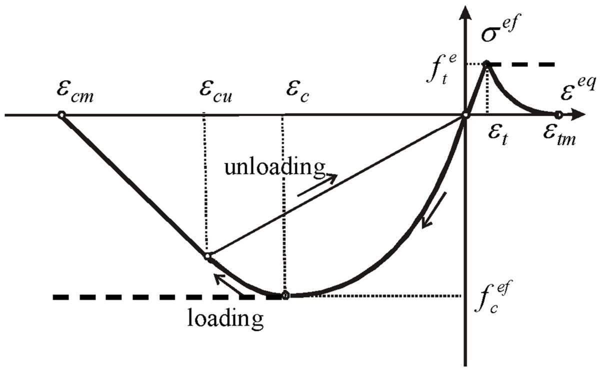

Image 2 - The concrete stress-strain diagram

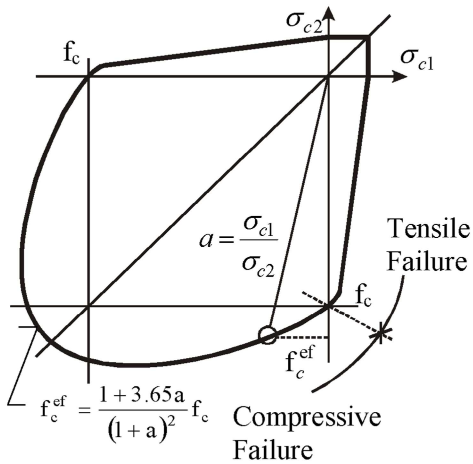

Image 3 - Kupfer's plasticity function

In this model the stress-strain relation is defined (Image 2) following STN EN 1992-1-1 (1991) (CEB-FIP Model, 1990)

➲ Loading - compression region $\varepsilon_{cu} < \varepsilon^{eq} < 0$

$$\sigma_c^{ef} = f_c^{ef}.\frac{k.\eta - \eta^2}{1.+(k-2).\eta}, \qquad \eta = \frac{\varepsilon^{eq}}{\varepsilon_c} \qquad (\varepsilon_c \doteq -0.0022,\ \varepsilon_{cu} \doteq -0.0035) \tag{5}$$

➲ Softening - compression region $\varepsilon_{cm} < \varepsilon^{eq} < \varepsilon_{cu}$

$$\sigma_c^{ef} = f_c^{ef}.\left(1 - \frac{\varepsilon^{eq} - \varepsilon_c}{\varepsilon_{cm} - \varepsilon_{cu}}\right) \tag{6}$$

➲ The tension region $\varepsilon_t < \varepsilon^{eq} < \varepsilon_m$

$$\sigma_c^{ef} = f_t.\exp(-2.(\varepsilon^{eq} - \varepsilon_t)/\varepsilon_{tm}) \qquad (\varepsilon_t \doteq 0.0001, \varepsilon_{tm} \doteq 0.002) \tag{7}$$

In the case of the plane state the strength function in tension f_t and in compression f_c were considered equivalent values f_t^{eq} and f_c^{eq}.

In the plane of principal stresses (σ_{c1}, σ_{c2}) the relation between the one and bidimensional stresses state due to the plasticity function by Kupfer (see Image 3) can be defined as follows (Kupfer, 1969):

➲ Compression-compression

$$f_c^{ef} = \frac{1+3.65.a}{(1+a)^2}.f_c, \qquad a = \frac{\sigma_{c1}}{\sigma_{c2}} \tag{8}$$

➲ Tension-compression

$$f_c^{ef} = f_c.r_{ec}, \; r_{ec} = \left(1+5.3278\frac{\sigma_{c1}}{f_c}\right), \; r_{ec} \geq 0.9 \tag{9}$$

➲ Tension-tension

$$f_t^{ef} = f_t.r_{et}, \qquad r_{et} = \frac{A+(A-1).B}{A.B}, \qquad B = K.x + A, \qquad x = \sigma_{c2}/f_c, \quad r_{et} = 1. \Leftrightarrow x = 0,$$
$$r_{et} = 0.2 \Leftrightarrow x = 1 \tag{10}$$

The shear concrete modulus G was defined for cracking concrete by Kolmar (Kolmar, 1986) in the form

$$G = r_g.G_o, \;\; r_g = \frac{1}{c_2}\ln\left(\frac{\varepsilon_u}{c_1}\right), \quad c_1 = 7+333(p-0.005), \;\; c_2 = 10-167(p-0.005) \tag{11}$$

where G_0 is the initial shear modulus of concrete, ε_u is the strain in the normal direction to crack, c_1 and c_2 are the constants dependent on the ratio of reinforcing, p is the ratio of reinforcing transformed to the plane of the crack ($0 < p < 0.02$).

It is proposed that the crack in the one layer of shell element is oriented perpendicular to the orientation of principal stresses. The membrane stress and strain vector depends on the direction of the principal stress and strain in one layer

$$\{\varepsilon_{cr}\} = [T_\varepsilon]\{\varepsilon\}, \qquad \{\sigma_{cr}\} = [T_\sigma]\{\sigma\} \tag{12}$$

where $[T_\varepsilon]$, $[T_\sigma]$ are transformation matrices for the principal strain and stress in the direction θ in the layer.

The strain-stress relationship in the Cartesian coordinates can be defined in dependency on the direction of the crack (in the direction of principal stress, versus strain)

$$[\sigma_{cr}] = [D_{cr}]\{\varepsilon_{cr}\} \text{ and } [\sigma] = [T_\sigma]^{\mathrm{T}}[D_{cr}][T_\varepsilon]\{\varepsilon\} \tag{13}$$

For the membrane and bending deformation of the reinforced concrete shell structure the layered shell element, on which a plane state of stress is proposed on every single layer, was used.

The stiffness matrix of the reinforced concrete for the l^{th}-layer can be written in the following form

$$\left[D_{cr}^l\right] = \left[T_{c.\sigma}^l\right]^{\mathrm{T}}\left[D_{cr}^l\right]\left[T_{c.\varepsilon}^l\right] + \sum_{s=1}^{N_{rein}}\left[T_s^l\right]^{\mathrm{T}}\left[D_s^l\right]\left[T_s^l\right] \tag{14}$$

where $[T_{c.\sigma}]$, $[T_{c.\varepsilon}]$, $[T_s]$ are the transformation matrices for the concrete and the reinforcement separately, N_{rein} is the number of the reinforcements in the l^{th} - layer.

After cracking the elasticity modulus and Poisson's ratio are reduced to zero in the direction perpendicular to the cracked plane, and a reduced shear modulus is employed. Considering 1 and 2 two principal directions in the plane of the structure, the stress-strain relationship for the concrete l^{th} - layer cracked in the 1-direction, is

$$\begin{Bmatrix} \sigma_1 \\ \sigma_2 \\ \tau_{12} \\ \tau_{13} \\ \tau_{23} \end{Bmatrix}_l = \begin{bmatrix} 0 & 0 & 0 & 0 & 0 \\ 0 & E & 0 & 0 & 0 \\ 0 & 0 & G_{12}^{cr} & 0 & 0 \\ 0 & 0 & 0 & G_{13}^{cr} & 0 \\ 0 & 0 & 0 & 0 & G_{23}^{cr} \end{bmatrix}_l \begin{Bmatrix} \varepsilon_1 \\ \varepsilon_2 \\ \gamma_{12} \\ \gamma_{13} \\ \gamma_{23} \end{Bmatrix}_l \tag{15}$$

where the shear modulus are reduced by the coefficient of the effective shear area k_s and parameter r_{g1} by Kolmar (11) as follows:

$G_{12}^{cr} = G_o.r_{g1}$, $G_{13}^{cr} = G_o.r_{g1}$, $G_{23}^{cr} = G_o / k_s$

When the tensile stress in the 2-direction reaches the value f_t', the latter cracked plane perpendicular to the first one is assumed to form, and the stress-strain relationship becomes :

$$\begin{Bmatrix} \sigma_1 \\ \sigma_2 \\ \tau_{12} \\ \tau_{13} \\ \tau_{23} \end{Bmatrix}_l = \begin{bmatrix} 0 & 0 & 0 & 0 & 0 \\ 0 & 0 & 0 & 0 & 0 \\ 0 & 0 & G_{12}^{cr}/2 & 0 & 0 \\ 0 & 0 & 0 & G_{13}^{cr} & 0 \\ 0 & 0 & 0 & 0 & G_{23}^{cr} \end{bmatrix}_l \begin{Bmatrix} \varepsilon_1 \\ \varepsilon_2 \\ \gamma_{12} \\ \gamma_{13} \\ \gamma_{23} \end{Bmatrix}_l \tag{16}$$

where the shear moduli are reduced by the parameter r_{g1} and r_{g2} by Kolmar (11) as follows:

$G_{12}^{cr} = G_o.r_{g1}$, $G_{13}^{cr} = G_o.r_{g1}$, $G_{23}^{cr} = G_o r_{g2}$.

The cracked concrete is anisotropic and these relations must be transformed to the reference axes *XY*. The simplified averaging process is more convenient for finite element formulation than the singular discrete model. A smeared representation for the cracked concrete implies that cracks are not discrete but distributed across the region of the finite element. The cracked concrete is anisotropic and these relations must be transformed to the reference axes *XY*. The simplified averaging process is more convenient for finite element formulation than the singular discrete model. A smeared representation for the cracked concrete implies that cracks are not discrete but distributed across the region of the finite element.

The smeared crack model (Červenka, 1985), used in this work, results from the assumption, that the field of more micro cracks (not one local failure) brought to the concrete element will be created. The validity of this assumption is determined by the size of the finite element, hence its characteristic dimension $L_c = \sqrt{A}$, where *A* is the element area (versus integrated point area of the element). For the expansion of cracking the assumption of constant failure energies $G_f = const$ is proposed in the form

$$G_f = \int_0^\infty \sigma_n(w)\,dw = A_G.L_c, \qquad w_c = \varepsilon_w.L_c \tag{17}$$

where w_c is the width of the failure, σ_n is the stress in the concrete in the normal direction, A_G is the area under the stress-strain diagram of concrete in tension. Concrete modulus for descend line of stress strain diagram in tension (crushing) can be described according to Oliver (Červenka, 1985) in dependency on the failure energies in the form

$$E_{c,s} = \frac{E_c}{1-\lambda_c}, \qquad \lambda_c = \frac{2G_f E_c}{L_c.\sigma_{\max}^2} \tag{18}$$

where E_c is the initial concrete modulus elasticity, σ_{max} is the maximal stress in the concrete tension. From the condition of the real solution of the relation (18) it follows, that the characteristic dimension of element must satisfy the following condition

$$L_c \le \frac{2G_f E_c}{\sigma_{\max}^2} \tag{19}$$

The characteristic dimension of the element is determined by the size of the failure energy of the element. The theory of a concrete failure was implied and applied to the 2D layered shell elements SHELL181 in the ANSYS element library (Kohnke, 2008). The CEB-FIP Model Code (1991) define the failure energies G_f [N/mm] depending on the concrete grades and the agregate size d_a as follows

$$G_f = \left(0.0469 d_a^2 - 0.5 d_a + 26\right)\left(f_c / 10\right)^{0,7} \qquad (20)$$

The limit of damage at a point is controlled by the values of the so-called crushing or total failure function Fu. The modified Kupfer's condition for the lth-layer of section is following

$$F_u^l = F_u^l\left(I_{\varepsilon 1}; J_{\varepsilon 2}; \varepsilon_u\right) = 0\ , \quad F_u^l = \sqrt{\beta\left(3J_{\varepsilon 2}\right) + \alpha I_{\varepsilon 1}} - \varepsilon_u = 0\ , \qquad (21)$$

where $I_{\varepsilon 1}$, $J_{\varepsilon 2}$ are the strain and deviator invariants, and ε_u is the ultimate total strain extrapolated from uniaxial test results ($\varepsilon_u = 0.002$ in the tension domain, or $\varepsilon_u = 0.0035$ in the compression domain), α, β are the material parameters determined from the Kupfer's experiment results ($\beta = 1.355,\ \alpha = 0.355\varepsilon_u$).

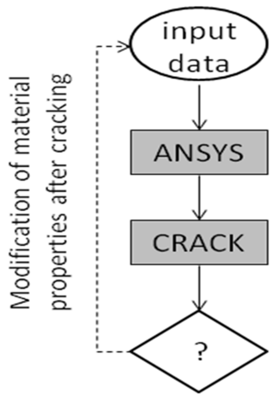

Image 4 - Non-linear calculation process

The failure function of the whole section will be obtained by the integration of the failure function through to the whole section in the form

$$F_u = \frac{1}{t}.\int_0^t F_u^l\left(I_{\varepsilon 1}; J_{\varepsilon 2}; \varepsilon_u\right) dz = \frac{1}{t}\sum_{l=1}^{N_{lay}} F_u^l\left(I_{\varepsilon 1}; J_{\varepsilon 2}; \varepsilon_u\right) t_l \qquad (22)$$

where t_l is the thickness of the l^{th} - shell layer, t is the total shell thickness and N_{lay} is the number of layers. The collapse state of the reinforced concrete structure is determined by the maximum strain ε_s of the reinforcement steel in the tension area ($\max\left(\varepsilon_s\right) \le \varepsilon_{sm} = 0.01$) and by the maximum concrete crack width w_c ($\max\left(w_c\right) \le w_{cm} = 0.3\,\mathrm{mm}$).

The program CRACK based on the presented nonlinear theory of the layered reinforced concrete shell (Image 4) was adopted in the software ANSYS (Králik, 2009, 2013). These procedures were tested in comparison with the experimental results (Králik, 2009).

Table 1 Geometric characteristics of concrete plate [P30]

Reinforc. concrete plate	Type of Load Force F [kN] or Pressure p [kN/m^2]	Plate dimensions [mm]	Reinforcements			
			Top reinfor. [mm^2]		Bottom reinfor. [mm^2]	
		$L_x/L_y/h$	Coord. X	Coord. Y	Coord. X	Coord. Y
D1	Force	1040/1040/65	193	193	397	397
D2	Force	1040/1040/65	252	133	520	273
D3	Force	1040/1040/65	283	103	520	273
D4	Pressure	3590/1190/120	-	-	402	402

The reinforced concrete plates D1-D3 (Jerga, J. Križma, M., 2006) were loaded by singular force F in plate middle supported in the plate corner and D4 were loaded by pressure p on the area of plate.

The material characteristics of plates D1-D3 are following:

Concrete - E_c = 16,4Gpa, μ = 0,2, f_c= -43Mpa, f_t= 2Mpa

Reinforcement - E_s = 201Gpa, μ = 0,3, f_s= 670Mpa

The material characteristics of plate D4 are following :

Concrete - E_c = 30.9Gpa, μ=0.2, f_c = -34.48Mpa, f_t = 4,5Mpa

Reinforcement - E_s = 210.7Gpa, μ = 0.3, f_s = 550.3Mpa.

The reinforced concrete plates D4 with the dimension 3590/1190/120mm was simple supported and loaded by pressure p on the area of plate. The plate D4 was reinforced by steel grid KARI ∅8mm a' 150x150mm at bottom.

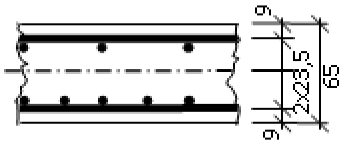

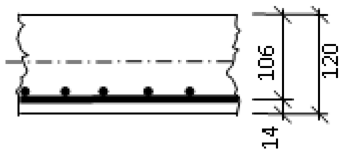

Image 5 - Section area of the tested plates - D1-D3 and D4

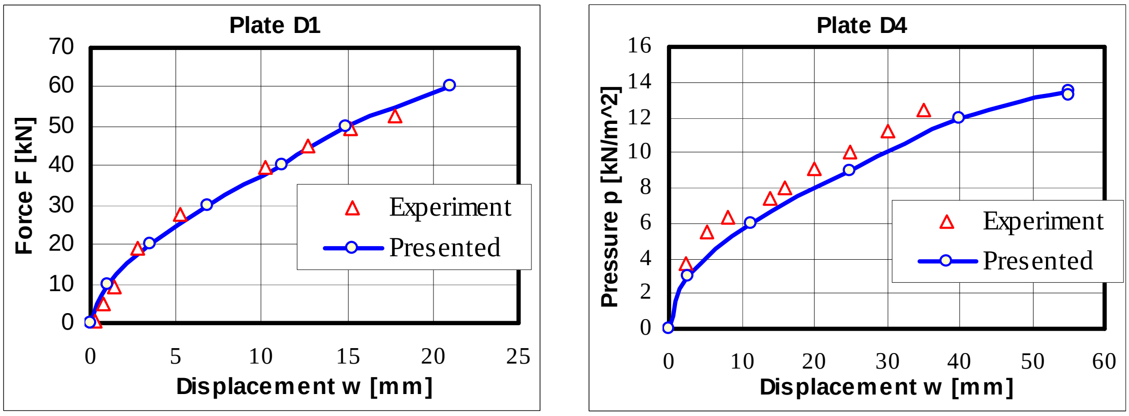

Image 6 - Comparison of experimental and nonlinear numerical analysis of plates

3 Nonlinear Deterministic Analysis

The critical sections of the structure were determined on the base of the nonlinear analysis due to the monotone increasing of overpressure inside the hermetic zone (Králik, 2009). The resistance of these critical sections was considered taking into account the design values of the material characteristics and the load. The combination load and design criteria were considered for the Beyond Design Basic Accident (BDBA) state in accordance with the international standard (IAEA, 2010).

The critical areas were identified in the walls and plate at top of the bubbler tower building. The tension forces and the bending moments were concentrated along of the middle wall. There is the effective temperature gradient equal to 60-90°C in the middle plane of the wall and the plate.

On the base of the nonlinear analysis of the containment resistance for median values of the material properties and failure function (22) the mean value of the critical overpressure was equal to 352.5 kPa and the max. strain is lower than 0,002 in the middle plane of the reinforced concrete panel.

The cracking process $(\varepsilon_1 \geq \varepsilon_t \doteq 0.0001)$ at the bottom or top section of the reinforced concrete panels starting when the overpressure was equal 250kPa.

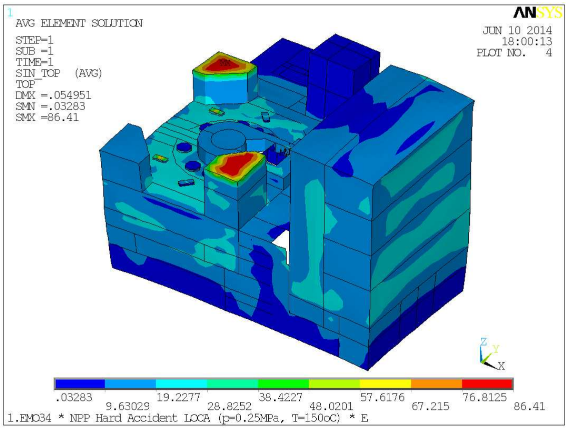

Image 7 - Stress intensity from the linear analysis

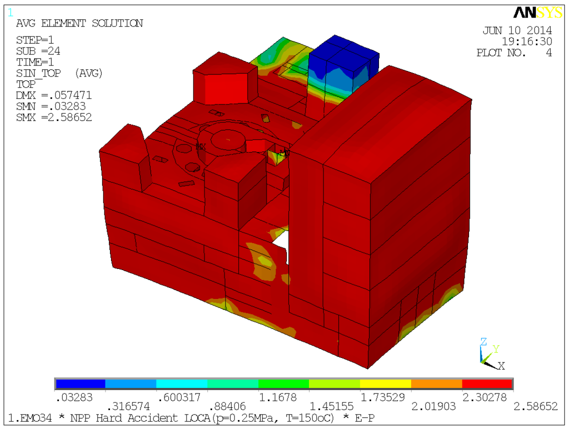

Image 8 - Stress intensity from the nonlinear analysis

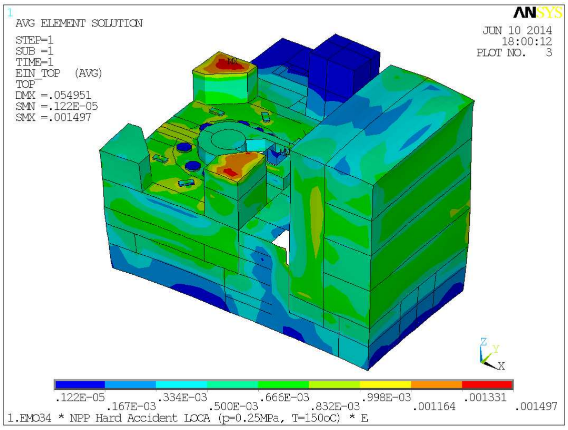

Image 9 - Strain intensity from the linear analysis

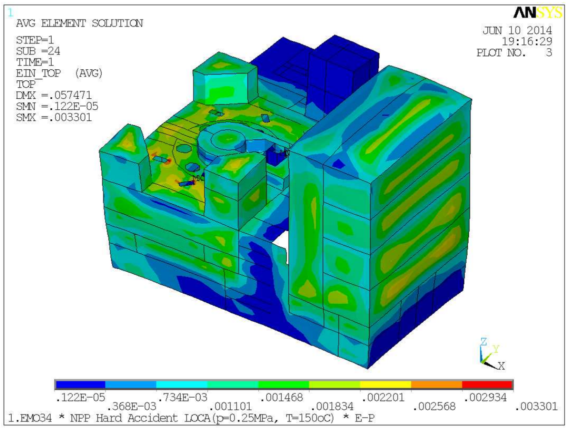

Image 10 - Strain intensity from the nonlinear analysis

The interior structures of the hermetic zone are loaded with the accident temperature equal to 150^{o}C and the outside structures in the contact with the exterior are loaded by -28^{o}C. The difference between the interior end the exterior temperature has the significant influences to the peak strain in the structures.

The comparison of the stress intensity from the linear and nonlinear solution is compared in Images 7 and 8 and the strain intensity in Images 9 and 10. The strain increase and the stress decrease in the nonlinear solution in comparison with the linear solution.

4 Probabilistic Assessment

Recent advances and the general accessibility of information technologies and computing techniques give rise to assumptions concerning the wider use of the probabilistic assessment of the reliability of structures through the use of simulation methods in the world (Haldar and Mahadevan, 2000; Čajka, R. Krejsa,M., 2013; Kala, Z. 2011; Králik, 2009, 2013; Melchers,R.E., 1999; Vejvoda, S. et al. 2003). A great attention should be paid to using the probabilistic approach in an analysis of the reliability of structures (Bažant et al., 2007; Kala, 2011; Novák et al, 2003).

Most problems concerning the reliability of building structures are defined today as a comparison of two stochastic values, loading effects E and the resistance R, depending on the variable material and geometric characteristics of the structural element. The variability of those parameters is characterized by the corresponding functions of the probability density $f_R(r)$ and $f_E(e)$.

The probabilistic definition of the reliability condition is of the form

$$RF = g\left(R, E\right) = R - E \geq 0 \tag{23}$$

where $g\left(R, E\right)$ is the reliability function.

The probability of failure can be defined by the simple expression

$$P_f = P\left[R < E\right] = P\left[\left(R - E\right) < 0\right] \tag{24}$$

The reliability function *RF* can be expressed generally as a function of the stochastic parameters X_1, X_2 to X_n, used in the calculation of *R* and *E*.

$$RF = g(X_1, X_2, ..., X_n) \tag{25}$$

The failure function *g({X})* represents the condition (reserve) of the reliability, which can be either an explicit or implicit function of the stochastic parameters and can be single (defined on one cross-section) or complex (defined on several cross-sections, e.g., on a complex finite element model).

In the case of simulation methods the failure probability is calculated from the evaluation of the statistical parameters and theoretical model of the probability distribution of the reliability function $Z = g(X)$. The failure probability is defined as the best estimation on the base of numerical simulations in the form

$$p_f = \frac{1}{N} \sum_{i=1}^{N} I\left[g\left(X_i\right) \leq 0\right] \tag{26}$$

where *N* in the number of simulations, *g(.)* is the failure function, *I[.]* is the function with value 1, if the condition in the square bracket is fulfilled, otherwise is equal 0.

The semi or full probabilistic methods can be used for the estimation of the structure failure in the critical structural areas. In the case of the semi probabilistic method the probabilistic simulation in the critical areas is based on the results of the nonlinear analysis of the full FEM model for the median values of the input data. The full probabilistic method result from the nonlinear analysis of the series simulated cases considered the uncertainties of the input data. The full probabilistic method was not applied because the various simulations have problems with the convergence of the nonlinear solution.

5 Uncertainities of the input data

The previous design analyses of the containment failure determine the critical area of the containment. The semi probabilistic method were applied for the probabilistic analysis of the containment failure in this paper. The probability of the containment failure were considered in the critical structure areas on the base of the nonlinear deterministic analysis of the containment for the various level of the overpressure. The uncertainties of the input data were thinking in accordance with the standard requirements (Table 2).

Table 2 The histograms of the input data

	Quantities		Histograms		
Input data	Charact. value	Variable value	Type	Mean μ	Deviation σ [%]
Dead load	G_k	g_{var}	*N*	1	10
Live load	Q_k	q_{var}	*Beta*	0.643	22.6
Pressure	P_k	p_{var}	*N*	1	8
Temper.	T_k	t_{var}	*Beta*	0.933	14.1
Model	E_k	e_{var}	*N*	1	5
Resist.	R_k	r_{var}	*N*	1	5

The action effect *E* were calculated considering the uncertainties of the input data

$$E = G_k g_{var} + Q_k q_{var} + P_k p_{var} + T_k t_{var} \tag{27}$$

and the resistance R we have in the form

$$R = R_k r_{\text{var}} \tag{28}$$

6 Probability of containment failure

The probability of containment failure is calculated from the probability of the reliability function RF in the form,

$$P_f = P\left(RF < 0\right) \tag{29}$$

where the reliability condition RF is defined depending on a concrete failure condition (30)

$$RF = 1 - F_u\left(I_{\varepsilon 1}; J_{\varepsilon 2}; \varepsilon_u\right) \tag{30}$$

where the failure function $F_u\left(.\right)$ was considered in the form (22).

The strain vector in the failure function (22) can be expressed in FEM following

$$\{\varepsilon\}_k = [B]\{r\}_k \quad \text{and} \quad \{r\}_k = \left[K\left(\sigma,\varepsilon\right)_n\right]^{-1}\{F\}_k \tag{31}$$

where $\{\varepsilon\}_k$ is the strain vector for the k - combination of load, $[B]$ is the shape matrix of the strian for element, $\{r\}_k$ is the vector of the deformation parameters of the element. The load vector of the element for the k-combination is

$$\{F\}_k = [X]_{ke}\{F\}_e \quad \forall \quad e = 1, n_{load} \tag{32}$$

where $[X]_{ke}$ is the matrix of the k-combination and e-load effect for n_{load} cases. The matrix of the combination $[X]_{ke}$ is defined in the form

$$\{\beta\}_k = [X]_{ke}\{\alpha\}_e \quad \text{and} \quad \{\alpha\}_e = [X]_{ke}^{-1}\{\beta\}_k\,, \tag{33}$$

where $\{\alpha\}_e$ present the input parameters of various effects and $\{\beta\}_k$ is the vector of the output parameters depended on the load combination. Therefore we have following

$$\{\varepsilon\}_e = [B]\{r\}_e \quad \text{and} \quad \{r\}_e = [X]_{ke}^{-1}\{r\}_k\ . \tag{34}$$

The strain vector $\{\varepsilon\}_e$ for the various load effects $\{F\}_e$ is used in Monte Carlo simulation depend on the uncertainties of the input data.

For the probability analysis of the containment failure the program FReET was used (Novák, D. et al. 2003.). The density of the reliability function RF was calculated using direct Monte Carlo simulation in various critical area of the hermetic zone.

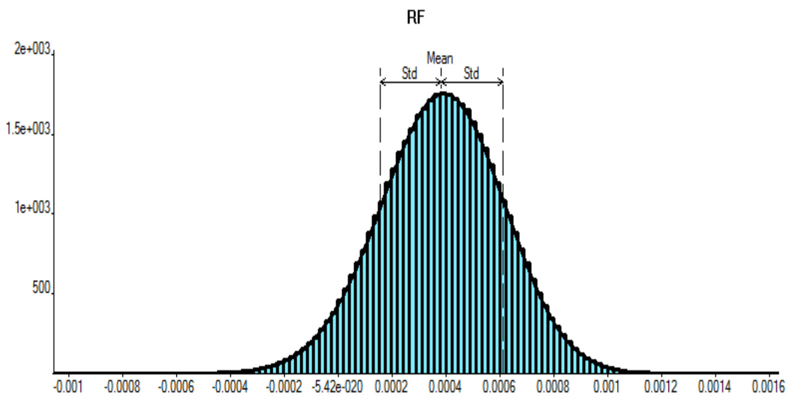

Image - 15 Density of the reliability function RF at bottom level of the BT plate at level +50.6m under overpressure Δp=275,5kPa, T_i =150^{o}C and external temperature T_e = -28^{o}C, probability P_f = 0.050422906.

7 Conclusions

The probability analysis of the loss of the concrete containment integrity was made for the overpressure loads from 250kPa to 500kPa using the nonlinear solution of the static equilibrium considering the geometric and material nonlinearities of the reinforced concrete shell layered elements. The nonlinear analyses were performed in the CRACK program, which was developed by the author and implemented into the ANSYS system (Králik, 2009, 2013). The uncertainties of the loads level (temperature, dead and live loads), the material model of the composite structure (concrete cracking and crushing, reinforcement, and liner and other influences following from the inaccuracy of the calculated model and the numerical methods were taken into account in the Monte Carlo simulations (Králik, 2009). The reliability function *RF* was defined in dependency on the failure function $F_u\left(I_{\varepsilon 1}; J_{\varepsilon 2}; \varepsilon_u\right)$ for requirements of the PSA analysis in the form (23). The probability of the loss of the concrete containment integrity is less than 10^{-6} for the original structural model. The containment failure is equal to 0.050422906 for the overpressure 275.5 kPa. The theory of the nonlinear probabilistic analysis was developed in the framework of the VEGA grant project (Králik, 2009, 2013).

References

ACI 349-90, 1990. “*Code Requirements for Nuclear Safety Related Concrete Structures*”, American Concrete Institute, Detroit.

BAŽANT, Z. P. PANG, S. D. VOŘECHOVSKÝ, M. AND NOVÁK. D. 2007. Energetic-statistical size effect simulated by SFEM with stratified sampling and crack band model. International Journal for Numerical Methods in Engineering (Wiley), 71(11):1297-1320, Rep. Dept. of Civil Eng., Northwestern University, Evanston, Illinois.

BNSI, 2006. *Requirements for the study of PSA*, BNSI.4.2.

CEB-FIP *Model Code 1990, Design Code,* Thomas Telford, ISBN 0727716964

ČERVENKA, V.,1985. Constitutive Model for Cracked Reinforced Concrete, *ACI Journal* 82, 877.

ČAJKA, R. KREJSA,M., 2013, Measured Data Processing in Civil Structure Using the DOProC, Method, *Advanced Materials Research* Vol. 859, p. 114-121, DOI 10.4028/www.scientific.net/ AMR.859.114, December, 2013 .

ENV 1992-1-1*. Eurocode 2: Design of Concrete Structures, Part 1*, Brussels: CEN 1992.

ENV 1992-1-2. *Eurocode 2: Design of Concrete Structures - Part 1-2 Fire Résistance of Concrete Structures*, CEN 1997.

HALDAR, A. MAHADEVAN, S., 2000, *Probability, Reliability and Statistical Methods in Engineering Design*, John Wiley & Sons, New York.

IAEA-SSG-4, 2010. *Development and Application of Level 2 - Probabilistic Safety Assessment for Nuclear Power Plants*. IAEA Vienna.

JCSS 2011. JCSS *Probabilistic Model Code.* Zurich: Joint Committee on Structural Safety. <www.jcss.byg.dtu.dk>.

JERGA, J. KRIŽMA, M., 2006. Assessment of Concrete Damage, *Building Research Journal* 54, p.211.

KALA, Z. 2011, Sensitivity analysis of steel plane frames with initial imperfections, *Engineering Structures,* 33, 8, pp.2342-2349.

KOHNKE, P., 2008*. ANSYS, Theory*, SAS IP Inc. Canonsburg..

KOLMAR, W. 1986 Beschreibung der Kraftuebertragung ueber Risse in nichtlinearen Finite-Element-Berechnungen von Stahlbeton-tragwerken, T.H. Darmstadt, Darmstadt.

KRÁLIK,J., 2009. *Safety and Reliability of Nuclear Power Buildings in Slovakia. Earthquake-Impact-Explosion.* Monograph. Published by STU Bratislava, 307pp. ISBN 978-80-227-3112-6

KRÁLIK,J., 2009, *Reliability Analysis of Structures Using Stochastic Finite Element Method,* Edition STU Bratislava, pp.138.

KRÁLIK,J.,2013. Nonlinear Probabilistic Analysis of the Reinforced Concrete Structure Failure of a Nuclear Power Plant Considering Degradation Effects. In: *Applied Mechanics and Materials* Vols. 249-250 (2013) pp 1087-1098, © Trans Tech Publications, Switzerland, doi:10.4028/www. scientific.net /AMM.249-250.1087.

KUPFER,H., HILSDORF, H. K. & RUESCH, H.. Behavior of Concrete Under Biaxial Stresses, *Journal ACI*, Proc.V.66, No.8, 1969, pp.656-666.

KWAK,H,G, FILIPPOU,F.C. 1990, Finite Element Analysis of Reinforced Concrete Structures under Monotonic Loads, No. UCB/SEMM-90/14, University of California Berkeley, California.

MELCHERS,R.E. 1999 *Structural Reliability: Analysis and Prediction*, John Wiley & Sons, Chichester, U.K..

MUSMAR, M. A. RJOUB, M. I. ABDEL HADI, M. A. 2014, Nonlinear Finite Element Analysis of Shallow Reinforced Concrete Beams using SOLID65 Element, *ARPN Journal of Engineering and Applied Sciences*, Vol. 9, No. 2, February.

NOVÁK, D. VOŘECHOVSKÝ, M. RUSINA, R., 2003. Small-sample Probabilistic Assessment – software FReET, ICASP 9, *9th Inter. Conf. on Applications of Statistics and Probability in Civil Engineering*, San Francisco, USA, July 6-9, pp. 91-96

SCHNEIDER,U., 1985, *Properties of Materials at High Temperatures*, Concrete, RILEM-U, Kassel, p. 21-27.

SUCHARDA,O. BROŽOVSKÝ,J., 2012, Verified Non-linear Model for Reinforced Concrete Beams. Advances in Remote Sensing, Finite Differences and Information Security: *Proceedings of the 5th WSEAS International Conference on Finite Differences - Finite Elements - Finite Volumes - Boundary Elements*, Praha, WSEAS Press, 2012, p. 27-32.

VEJVODA, S., KERŠNER, Z., NOVÁK, D. & TEPLÝ, B. 2003, Probabilistic Safety Assessment of the Steam Generator Cover, In Proc. of the *17th International Conference on Structural Mechanics in Reactor Technology (SMiRT 17)*, Prague, Czech Republic, August 17-22, in CD, M04-4, 10 pp.

WILLIAM,K.J. WARNKE, E.D. 1975, Constitutive model for triaxial behaviour of concrete, in: *Proceedings of the International Association for Bridge and Structural Engineering, ISMES,* Bergamo, Italy, 1975, pp.19/1-30.

WILLIAM K. TANABE, T.A. 2001. *Finite Element Analysis of Reinforced Concrete Structures*. American Concrete Institute, Farmington Hills, MI.

Acknowledgement

This paper was created with the support of the Ministry of Education, Science, Research and Sport of the Slovak Republic within the Research and Development Operational Programme for the project "University Science Park of STU Bratislava", ITMS 26240220084, co-funded by the European Regional Development Fund and with support of Grant Agency of the Slovak Republic (VEGA) (grant VEGA No. 1/1039/12).

Contact address:

Prof.Ing.Juraj Králik,CSc. , Authorized Civil Engineer

Faculty of Civil Engineering, STU Bratislava, Radlinského 11, 813 68 Bratislava, Slovak Republic

REMOVING HEAT FROM THERMAL SOURCE TO HEAT SINK THROUGH PRINTED CIRCUIT BOARD

ZBYNEK MAKKI, MARCEL JANDA

Brno University of Technology, Automotive Lighting s.r.o.

Abstract: The paper is focused on showing the possibility of an efficient heat removal from a thermal source to a heat sink via printed circuit board (PCB). Each solution can be described by hand calculation and simulation by Ansys Icepak software with using thermal resistance.

Keywords: Ansys Icepak, PCB (Printed circuit board), Heat conduction, Heat spread

1 Heat conduction

Conduction is heat transfer due to molecule activity. Energy is transformed from more energetic to less energetic particles due to energy gradient. Conduction is one of ways how is possible spread heat by solid materials. Empirical relation for conduction is Fourier's law. This law describes empirical relationship between conduction rate in a material and the temperature gradient in the direction of energy flow. Conduction occurs in the direction of decreasing temperature and the minus sign confirms this thermodynamic axiom.

$$\vec{q}_x = -\lambda \cdot grad\ t \tag{20}$$

Where the vector $\vec{q}_x$ is heat flux [W.m^{-2}] in the positive x-direction, *grad t* is temperature gradient [K.m^{-1}] and the proportionality constant *λ* is the thermal conductivity of the material (W/mK).

$$grad\ t = \frac{dt}{dx} \tag{2}$$

Heat transfer is better through some materials, because we can describe each of used materials for PCB construction by thermal conductivity (their conduction rate) *λ* [W/m.K]. In our case we speak about materials which are used for construction classical PCBs as their carrying material – FR4 with thermal conductivity 0.35 W/m.K and pure copper with thermal conductivity 385.6 W/m.K used for layer for electrical paths and for heat spreading by top and bottom layer.

Because we are speaking about steady-state analysis therefore we can write equation (1) as steady-state heat transfer

$$Q = \lambda \cdot \frac{t_{2(hot)} - t_{1(cold)}}{x} \cdot A \tag{3}$$

Equation (3) describes heat spread by one direction across area A [m^2] with material thickness *x* [m]. And *Q* is heat through material [W]. For our simplification we can say that Q (heat) is P (power dissipation) because J is W.s and we are speaking about steady-state analysis, therefore J is equivalent for W.

Heat or heat flow is equivalent for electrical current and such as electrical resistance we can describe for his equivalent thermal resistance.

$$R_{th} = \frac{x}{\lambda \cdot A} \tag{4}$$

Where R_{th} is thermal resistance [K/W]. Because in this paper are used VIAs for some PCB construction, therefore we can use equation (4), but as area we must imagine circle area with hole inside.

In the end from equation (3) and (4) we can write simple equation which is most important for this paper

$$t_{2(hot)} - t_{1(cold)} = P \cdot R_{th} \tag{5}$$

Now we to know every equations what we need for calculations describes in this paper.

2 Introduction for calculation

As was wrote for thermal spread exist several ways how is possible spread heat from heat source to Heat sink, but we are thinking only about heat conduction from LED (light emitting diode) through PCB to heat sink (we speak about heat spread in one direction only). Thermal source inside LED is junction temperature with power dissipation 1W which is value used for calculations in this paper.

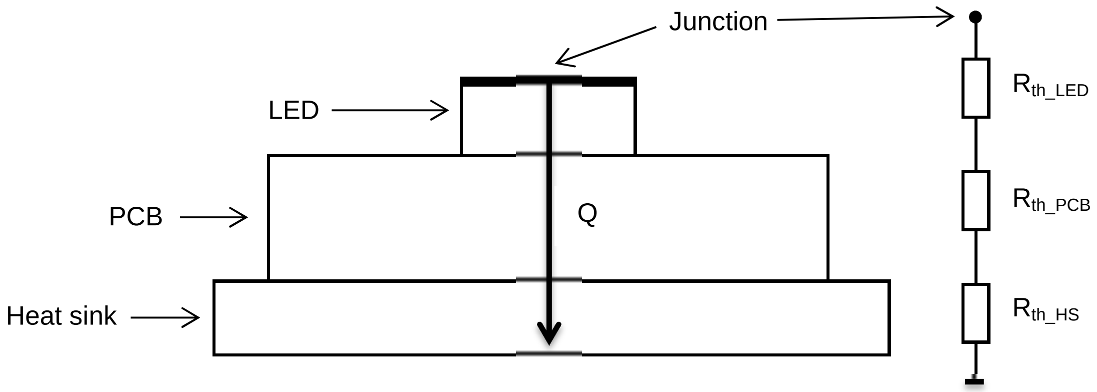

Image 22 – Heat transfer from thermal source to heat sink

From Image 1 you can see that each of parts we can describe their thermal resistance. For bigger simplification is possible to say that does not matter on LED and Heat sink properties, but we are interesting only about PCB construction and his materials. Therefore as thermal source is used area with dimension $1.05^{\times}10^{-5}$m^2 (3x3.5mm) which describes LED thermal pad.

For simple comparison were chosen several solution PCB constructions. As first simple two layer board, second is two layer board with capped and filled VIAs, third is three layer board with micro and buried VIAs, fourth is four layer board with micro and buried VIAs and last (fifth) is IMS (insulated metal substrate) board.

For cases which are used for construction we must use for hand calculation serial-parallel combinations of thermal resistance as shows Image 2. For IMS board is the same combination as for two layer board, but instead FR4 material is use some material with better thermal conductivity (around 3K/W) and smaller thickness (around 0.035mm) than for variant with FR4.

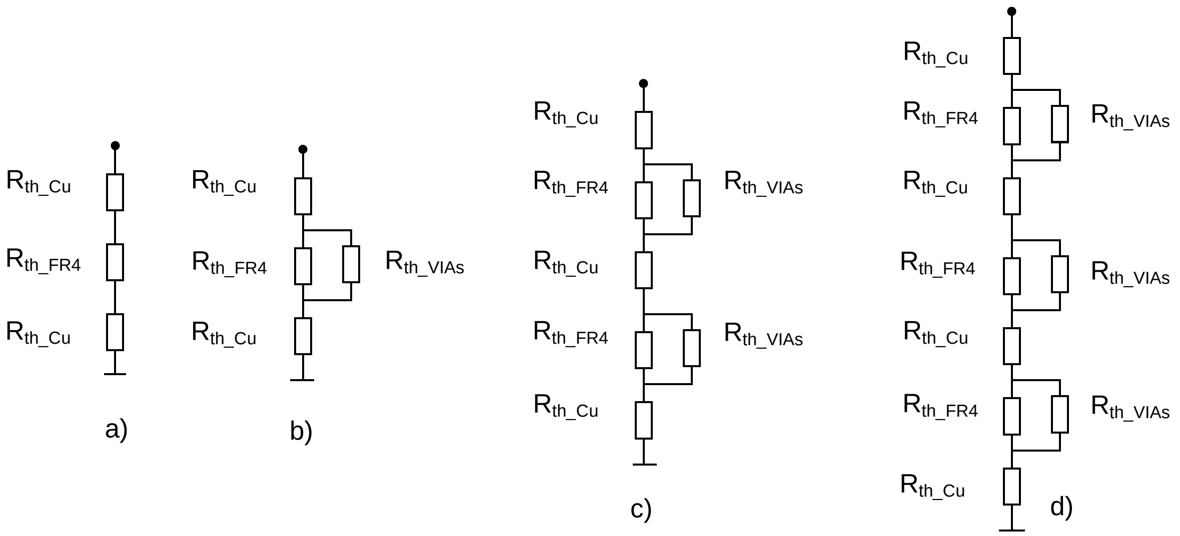

Image 2 – Combination for each of serial-parallel combination thermal resistance used for PCBs construction, a) two layer board, b) two layer with capped and filled VIAs, c) three layer board with micro and buried VIAs and d) four layer board with micro and buried VIAs

And layouts show Image 3.

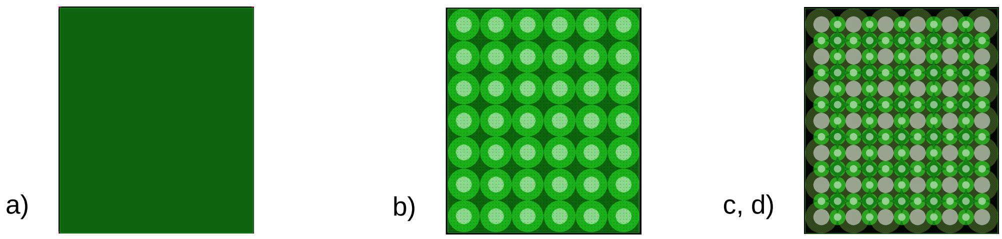

Image 3 – Layouts for each of used PCBs construction, a) two layer board, b) two layer with capped and filled VIAs, c) three layer board with micro and buried VIAs and d) four layer board with micro and buried VIAs

3 Results

For each of PCB construction was calculated thermal resistance. First calculation was by Ansys Icepak and second by hand with equation (4) and (5).

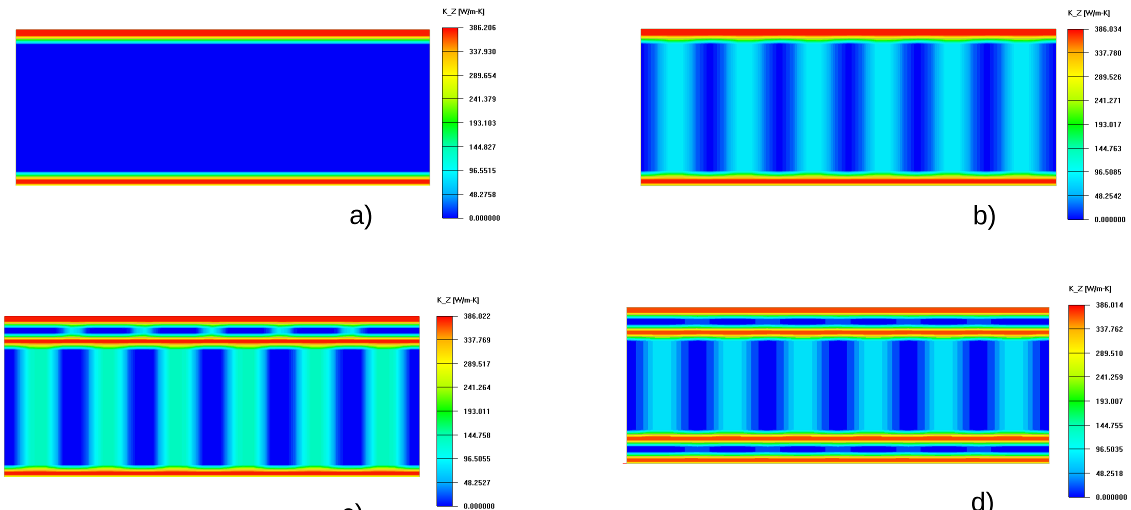

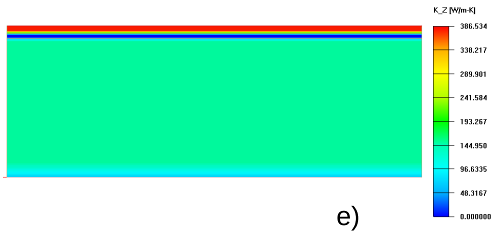

e)

Image 4 –Thermal conductivity across each of used PCBs construction, a) two layer board, b) two layer with capped and filled VIAs, c) three layer board with micro and buried VIAs and d) four layer board with micro and buried VIAs and d) IMS board

Image 4 describes how big influence has thermal conductivity for spread temperature od heat through PCBs. Blue parts means parts represent FR4 material with small number of thermal conductivity and red parts means parts represent Copper material used for layer used for thermal conductivity. Image 4 shows how big influence have thermal VIAs for thermal spreading across dielectric material (FR4).

3.1 Calculation by Ansys Icepak

Results for thermal resistance are inside Table 1.

Table 15 Thermal resistance calculated by Ansys Icepak

PCB construction		First	Second	Third	Fourth	Fifth
$\Delta T_{Cu\ Top}$	[K]	0.0262	0.0182	0.0069	0.0147	0.0147
$\Delta T_{FR4\ Inner1}$	[K]	-	-	1.1470	1.1860	1.1177
$\Delta T_{Cu\ Inner\ 1}$	[K]	-	-	0.0137	0.0149	-
$\Delta T_{FR4\ Base}$	[K]	272.0838	3.8113	3.5350	2.5486	-
$\Delta T_{Cu\ Inner\ 2}$	[K]	-	-	-	0.0149	-
$\Delta T_{FR4\ Inner2}$	[K]	-	-	-	1.1118	-
$\Delta T_{Cu\ Bottom}$	[K]	0.0384	0.0389	0.0137	0.0149	0.6184
R_{th}	[K/W]	272.1408	3.8684	4.7460	4.9049	1.7508

In Table 1 layers Inner 1 and Inner 2 represent dielectric materials inside PCB.

3.2 Calculation by hand

Results for thermal resistance are inside Table 2.

Table 2 Thermal resistance calculated by hand calculation

PCB construction		First	Second	Third	Fourth	Fifth
$\Delta T_{Cu\ Top}$	[K]	0.0160	0.0199	0.0146	0.0146	0.0138
$\Delta T_{FR4\ Inner1}$	[K]	-	-	0.9311	0.9311	1.1111
$\Delta T_{Cu\ Inner\ 1}$	[K]	-	-	0.0179	0.0179	-
$\Delta T_{FR4\ Base}$	[K]	272.1088	3.8824	3.0983	2.4098	-
$\Delta T_{Cu\ Inner\ 2}$	[K]	-	-	-	0.0179	-
$\Delta T_{FR4\ Inner2}$	[K]	-	-	-	0.9311	-
$\Delta T_{Cu\ Bottom}$	[K]	0.0160	0.0199	0.0179	0.0146	0.6184
R_{th}	[K/W]	272.1408	3.9221	4.0781	4.3257	1.7433

For better view are results compared for both of calculations in column graph – Imagine 4.

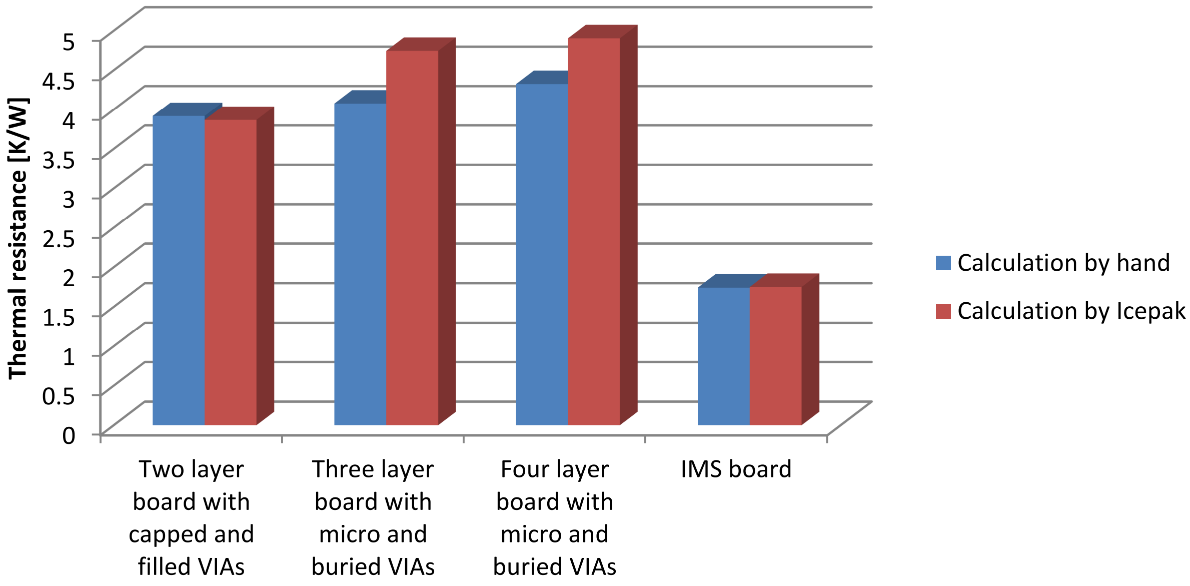

Image 5 – Thermal resistance comparison between calculation by hand and calculation by Ansys Icepak (without results for first construction variant)

4 Conclusion

The worst thermal resistance has two layers PCB which is described as first case what was chosen for comparison in this paper. From Table 1 and 2 we can see that thermal resistance for this solution is more than 68x higher than solution with two layer board with capped and filled VIAs. Therefore it is useful using PCBs with VIAs for thermal spread from thermal source directly to heat sink.

Differences between calculations by hand and by Ansys Icepak depend on mesh quality and on pattern of VIAs. The main influence have pattern of VIAs because we cannot say that VIAs are equally distribute across whole PCB, therefore results between hand calculation and Icepak calculation are little bit different. But for estimation of thermal resistance results are still good.

References

Prihoda M., Redr M., 2008. Sdileni tepla a proudeni. Ostrava, 180. ISBN 978-80-248-1748-4

DAVIES, T.W. FOURIER'S LAW. In: [online]. [cit. 2014-06-10]. DOI: 10.1615/AtoZ.f.fourier_s_law. Available from: http://www.thermopedia.com/content/781/

Fourier. J.,1955. The Analytical Theory of Heat, Dover Publications. New York.

Acknowledgement

Author(s) gratefully acknowledge(s) financial support from the Ministry of Education, Youth and Sports under projects No. LO1210 – „Energy for Sustainable Development (EN-PUR)“ solved in the Centre for Research and Utilization of Renewable Energy.

Contact address:
Ing. Zbynek Makki; Pavov 113, 568 01, Jihlava, CZ; zbynek.makki@al-lighting.com

PILOTOVÉ ZÁKLADY A VRSTEVNATÉ PODLOŽIE

ĽUBOMÍR PREKOP
Stavebná fakulta STU v Bratislave, Katedra stavebnej nechaniky

Abstract: This paper deals with the foundation of building structures on a layered subsoil using the pile structures. The attention is paid to the contact between a pile and the layered subsoil while the pile is in its head loaded by a horizontal force. Particular subsoil layers have different physical characteristics. Results are presented as the analysis of displacements and state of stress of the pile.

Keywords: Bended Pile, Layered Subsoil, Interaction

1 Úvod

Zakladanie na pilotách sa používa, ak je podložie stavebného objektu málo únosné resp. zemina je silno stlačiteľná pri hĺbke únosnej vrstvy nad 4,0 m. Málo únosnou zeminou sú najčastejšie mäkké íly, rašelinité pôdy a nezhnutnené násypy, ktorých sadanie je väčšie, ako sú prípustné hodnoty sadnutia stavby. Opreté piloty zaistia nízke hodnoty zvislého zaťaženia. Pri zakladaní na pilotách sa preto nevyskytujú väčšie diferencie pri sadnutí objektu.

Pilotový základ patrí medzi najrozšírenejšie hĺbkové zakladania. V porovnaní s plošným základom sa znižuje hmotnosť základu, rozsah výkopu, vylučuje sa debnenie a veľký spätný zásyp. Betónové piloty sa vyhotovujú z prostého betónu alebo železobetónu. Tvar piloty býva najčastejšie kruhový, štvorcový alebo mnohouholníkový. Rozmery pilot sa líšia podľa použitej technológie a sú v rozsahu od 0,3 m do 2,0 m. Druhov pilot je veľké množstvo. Vo všeobecnosti môžeme rozdeliť piloty podľa rôznych kritérií, univerzálne piloty pre všetky možné prípady neexistujú.

Závažným problémom pri projektovaní pilot je stanovenie potrebnej dĺžky pilot. Preto sú pre správny návrh potrebné čo najpresnejšie výsledky inžiniersko-geologického prieskumu, najmä pod pätou piloty. Potrebná dĺžka pilot býva často premenlivá, nakoľko povrch únosnej vrstvy býva zvlnený alebo šikmý.

2 Železobetónové piloty

Pre vystužovanie pilot je dôležité ich správne pôdorysné rozmiestnenie v pilotovom základe. Piloty sa rozmiestnia tak, aby zaťaženie pilotového základu bolo čo najbližšie dostrednému zaťaženiu. Do betónového prierezu sa podľa spôsobu namáhania navrhne nosná výstuž. Pri návrhu výstuže je potrebné zvážiť aj štáduá, ktoré vzniknú počas výroby pilot a ich dopravy na miesto použitia.

Rozmiestnenie výstuže piloty v priečnom reze je v zásade symetrické. Pozdĺžna výstuž sa umiestňuje v rohoch piloty alebo pri kruhovom pôdoryse rovnomerne po obvode a volí sa s priemerom $\varnothing$ = 18 - 32 mm. V prípade potreby sa dopĺňa medziľahlo umiestnenou výstužou s priemerom $\varnothing$ = 14 - 22 mm. Krytie výstuže je aspoň 35 mm, v prípade pilot vháňaných cez zeminy s agresívnou vodou sa krytie výstuže zvyšuje na 50 až 80 mm. Výstuž v špici piloty sa dopĺňa konštrukčnou výstužou. Rovnako pod hlavou piloty sa výstuž upravuje kvôli zväčšeniu tuhosti piloty pri baranení.

Šmyková výstuž sa navrhuje v tvare skrutkovice, prípadne v tvare uzavretých strmeňov s priemerom 5,5 až 8 mm. Výška závitu skrutkovice alebo vzdialenosť strmeňov je po výške piloty rozdielna. V spodnej a hornej časti je po 50 až 100 mm, v strednej časti piloty do 200 mm.

Monolitické piloty sa vystužujú pomocou výstužných košov, ktoré sa spúšťajú do vyrobeného otvoru. Kôš musí byť upravený tak, aby sa do otvoru mohla spustiť betónovacia rúra. Výstužné koše sa stykujú presahom.

3 Únosnosť podložia

Úlohou je čo najpresnejšie stanovenie hrúbok jednotlivých vrstiev podložia, zostrojenie geologického modelu prostredníctvom profilov a podrobné stanovenie vlastností zemín. K najdôležitejším patria pevnostné a deformačné charakteristiky, pomocou ktorých sa vypočíta únosnosť a sadanie základovej pôdy.

4 Vodorovná únosnosť piloty

Priečne zaťažené piloty sa navrhujú podľa viacerých výpočtových modeloch. Obvykle sú piloty situované zvislo a musia prenášať vodorovné zaťaženie. V prípade, ak postačuje poznať orientačne vodorvnú únosnosť, sa použijú tabuľkové hodnoty únosnosti, aby sa splnila podmienka:

$$U_{h,tab} \geq H_d \,, \tag{1}$$

kde $U_{h,tab}$ je tabuľková hodnota vodorovnej únosnosti podľa ČSN 73 1004,
H_d – vodorovná zložka extrémneho výpočtového zaťaženia.

Pri výpočtovom modeli sa pilota považuje za nosník votknutý do pružnoplastického prostredia, ktorý sa pre určitý obor deformácií môže riešiť ako nosník na pružnom podklade. Vychádza sa z predpokladu lineárneho vzťahu medzi napätím a deformáciou podľa Winklerovej hypotézy

$$\sigma = k_h . y \,, \tag{2}$$

kde k_h je modul horizontálnej stlačiteľnosti [kN.m^{-3}],
y – vodorovný posun piloty.

Veľkosť modulu k_h závisí od typu zeminy a priebeh deformácie pozdĺž piloty môže mať rôzny priebeh. Pri vodorovnom namáhaní sa pilota môže správať ako **tuhá** (nastane iba jej posun alebo pootočenie) alebo ako **poddajná** (po zaťažení sa ohne) (Turček, P., Slávik, I., 2002).

5 Vrstevnatosť podložia

Zloženie podložia pod základovou konštrukciou je zvyčajne nehomogénne, tzn. skladá sa z dvoch alebo viacerých vrstiev. Zohľadnenie vrstevnatosti pri modelovaní nám umožní vytvoriť model, ktorý lepšie vystihuje reálnu konštrukciu a následne získať presnejšie výsledky deformácií a napätí.

6 Model konštrukcie

Riešená bola pilota dĺžky $l = 8{,}0$ m. Kruhového priečneho rezu s priemerom $\varnothing = 0{,}42$ m. Pilota bola vyrobená zo železobetónu. Modul pružnosti je E = 20000 MPa. Podložie predstavuje málo únosné prostredie s modulom pružnosti E = 1,0 MPa. Poissonovo číslo pre zeminu malo hodnotu $\nu = 0{,}35$. Pre výpočet boli použité dva zaťažovacie stavy, reprezentujúce vodorvné namáhanie piloty: v prvom je pilota v hlave zaťažená vodorovne pôsobiacou silou $F_x = 100$ kN, v druhom prípade je pilota v hlave zaťažená momentom $M_y = 100$ kNm. Pre túto pilotu v homogénnom zložení podložia bolo k dispozícii analytické riešenie (Kollár, P., Mistríková, Z., 1985).

V ďalšom kroku bola tá istá pilota umiestnená vo vrstevnatom podloží, ktorého zloženie a fyzikálno-materiálové charakteristiky sú zrejmé z obr. 1. Podrobnejšie sa otázkam vrstevnatého podložia a modelovaniu kontaktu piloty a okolitého prostredia venuje príspevok (Kuzma, Hruštinec, 2002).

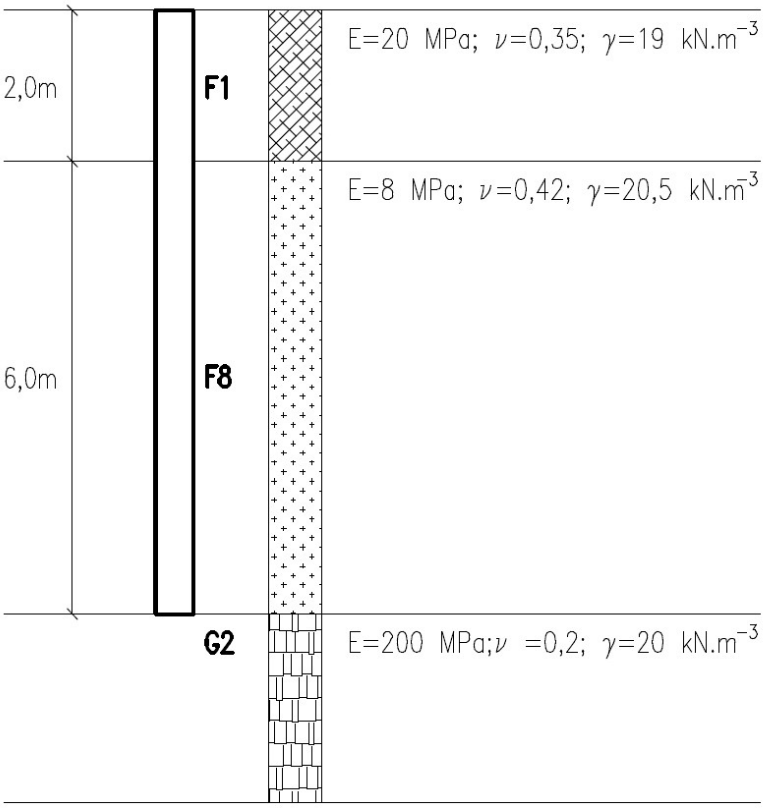

Obrázok 23 - Zloženie vrstiev podložia

Vo výpočte bola použitá pilota s voľnou pätou, opretá v päte do vrstvy únosnej zeminy. Model konštrukcie bol vytvorený ako priestorový v programe ANSYS. Železobetónová pilota bola modelovaná pomocou prvkov SOLID65 a okolitý zemný masív prvkami SOLID45. Týmto prvkom boli postupne priradené vlastnosti vrstiev podložia podľa obr. 1. Kontakt piloty a zemného masívu bol modelovaný pomocou kontaktných prvkov TARGE170 a CONTA173 (ANSYS® User’s Manual, 2011). Podrobnejšie sa otázkam modelovania kontaktu piloty a okolitého prostredia venuje príspevok (Kuzma, Hruštinec, 2003).

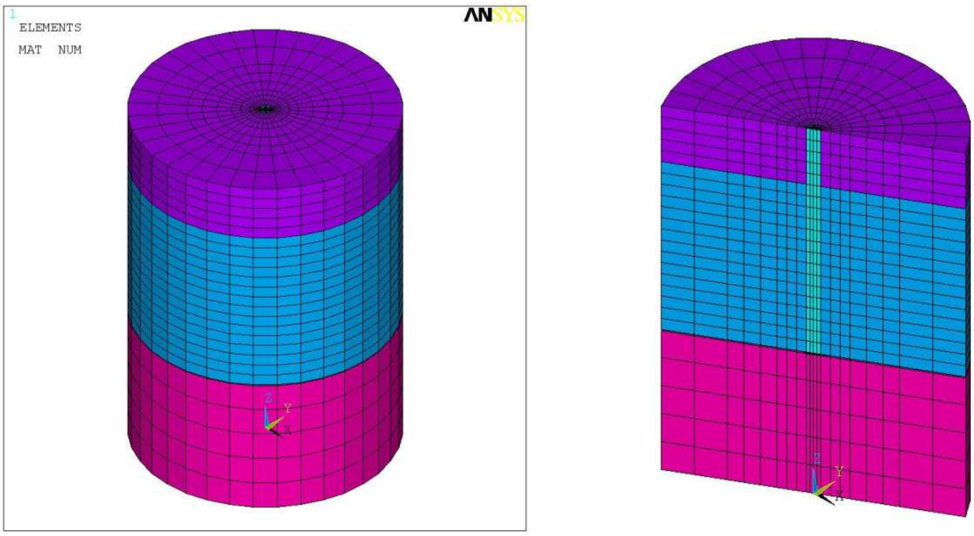

Obrázok 2 - 3D model a rez modelom

Na nasledujúcom obrázku, grafe a tabuľke sú uvedené výsledky a porovnanie vodorovných priehybov piloty vo vrstevnatom podloží.

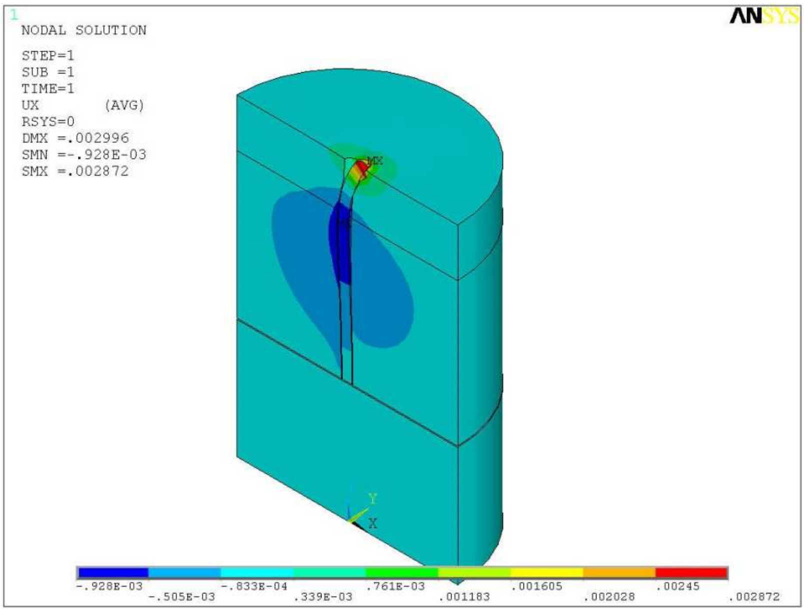

Obrázok 3 - Vodorovné deformácie piloty vo vrstevnatom podloží

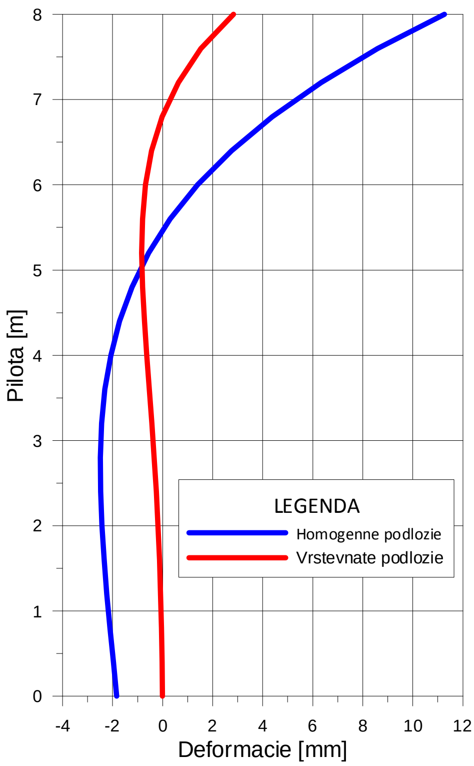

Obrázok 4 - Vodorovné deformácie po výške piloty

Na výsledkoch, uvedených na obr. 3 a obr. 4 je zrejmé, že vodorovné deformácie piloty v homogénnom prostredí nesúdržnej zeminy sú rádovo väčšie ako deformácie piloty vo vrstevnatom prostredí. Vyplýva to z nízkej hodnoty modulu pružnosti nesúdržnej zeminy a tým pádom je menší odpor nesúdržnej zeminy voči zatlačeniu tuhej konštrukcie piloty do zemného masívu.

Tabuľka 16 Vodorovné deformácie po výške piloty

Bod modelu	Vzd.od päty [m]	Deformácia [m] vrstevnaté podložie	Deformácia [m] homogénne podložie
3	8.0	0.11260E-01	0.28295E-02
403	7.6	0.85929E-02	0.15315E-02
803	7.2	0.63376E-02	0.62735E-03
1203	6.8	0.43816E-02	-0.26820E-04
1603	6.4	0.27509E-02	-0.44052E-03
2003	6.0	0.13982E-02	-0.68882E-03
2403	5.6	0.30497E-03	-0.80727E-03
2803	5.2	-0.56185E-03	-0.83535E-03
3203	4.8	-0.12291E-02	-0.80037E-03
3603	4.4	-0.17253E-02	-0.72655E-03
4003	4.0	-0.20763E-02	-0.63161E-03
4403	3.6	-0.23065E-02	-0.52925E-03
4803	3.2	-0.24380E-02	-0.42882E-03
5203	2.8	-0.24906E-02	-0.33650E-03
5603	2.4	-0.24820E-02	-0.25564E-03
6003	2.0	-0.24273E-02	-0.18745E-03
6403	1.6	-0.23394E-02	-0.13146E-03
6803	1.2	-0.22290E-02	-0.86162E-04
7203	0.8	-0.21045E-02	-0.49475E-04
7603	0.4	-0.19727E-02	-0.18091E-04
8003	0.0	-0.18379E-02	0.74792E-05

7 Záver

Modelovanie vrstevnatého podložia spolu s kontaktom piloty a okolitých vrstiev zeminy podstatne lepšie vystihuje skutočné pôsobenie piloty v zemnom masíve. Získané výsledky sa približujú k reálnym podmienkam na stavenisku. Vrstevnatosť podložia je bežným javom, s ktorým sa stretávame na akomkoľvek stavenisku. Preto je vhodné venovať mu náležitú pozornosť. V ďalších výpočtoch by bolo vhodné venovať sa ostatným spôsobom podopretia päty piloty (kĺbové podopretie resp. votknutie päty piloty) a zmeneným rozloženiam vrstiev podložia.

Literatúra

ANSYS ® User’s Manual for Revision 12, Swanson Analysis Systems, Inc.

ČSN 73 1002: Pilotové základy, 1989.

JENDŽELOVSKÝ, N., PREKOP, Ľ., 2014: Interaction between a Bended Pile and the Layered Subsoil. In: 14th International Scientific Conference VSU 2014, Sofia, Bulgaria, June 5-6, 2014. Vol. I pp. I-203-206. ISSN 1314–071X.

KOLLÁR, P., MISTRÍKOVÁ, Z.: 1985. Spolupôsobenie ohybom namáhaných pilót s pružným polpriestorom – piloty voľné v päte. Inžinierske stavby 01/1985, strany 29–39.

KUZMA, J. - HRUŠTINEC, Ľ., 2003: Interaction between Spread Foundations and Subsoil. In: Proceedings of the 13th Europan Conference on Soil Mechanics and Geotechnical Engineering. Praha: Czech Geotechnical Society CICE. ISBN 80-86769-04-6, p. 239-244.

MAJDÚCH, D.: 1984. *Zásady vystužovania betónových konštrukcií*. Bratislava, Alfa, 368 strán.

TURČEK, P., SLÁVIK, 2002. Zakladanie stavieb, Vydavateľstvo STU v Bratislave, 2002, ISBN 80-227-1699-5.

Poďakovanie
Príspevok bol vypracovaný v rámci grantovej úlohy VEGA, projekt č.1/0629/12.

Kontaktná adresa:
Ing. Ľubomír Prekop, PhD.
lubomir.prekop@stuba.sk
Katedra stavebnej mechaniky
Stavebná fakulta STU
Radlinského 11
813 68 Bratislava

PROPOJENÍ SYSTÉMU STRENGTH SE SYSTÉMEM ANSYS

ZDENĚK RAMÍK, STANISLAV VEJVODA

VÍTKOVICE ÚAM a.s., Mezírka 775/1, 602 00 Brno

Abstract: STRENGTH software developed in VÍTKOVICE ÚAM Company enables engineers to perform simple strength assessment and fatigue life assessment. System STRENGTH is based both on the theoretical background and the whole life experiences in Nuclear and Classic Power Plant pressure vessel components assessment of professor Vejvoda. This paper deals with the data exchange between FEM system ANSYS and STRENGTH. Nodal temperatures and stress or strain tensors computed in ANSYS are possible to import to both STRENGTH engines FatigueV and MonotonV. Total cumulative damage calculated for mesh nodes up to 32 thousand in STRENGTH version 7.04 may be exported directly into ANSYS for display.

Keywords: Fatigue, STRENGTH, ANSYS

1 Úvod

Výchozím stavem pro rozvoj programového systému STRENGTH jsou teoretické práce pana prof. Ing. Stanislava Vejvody CSc. Systém STRENGTH ideově navazuje na předchozí systémy HOROTE a STATES, jejichž autorem a vedoucím řešitelského týmu byl také pan Vejvoda.

STRENGTH je zaměřen zejména na posuzování mezních stavů pevnosti tlakových nádob, potrubí a aparátů. Hodnocení na prostou pevnost se provádí ve zvolených řezech kolmých na střednici stěny nádob nebo potrubí. Na únavu se posuzují vybrané body ležící na povrchu. Většina norem předpokládá hodnocení napětí nebo poměrných deformací vypočtených za předpokladu platnosti elastického stavu v celém rozsahu zatěžování. V takovém případě programy systému STRENGTH pro přibližný výpočet poměrných deformací a napětí pro namáhání v pružně plastickém stavu použijí princip Neubera.

Mezi některé současné možnosti systému STRENGTH patří volba posouzení na nízkokmitovou únavu, vysokokmitovou únavu a dvoufrekvenční zatěžování. Volba křivky životnosti: Langer, Manson-Coffin, Wöhler a volba chování materiálu: stress-strain křivka, materiál typu Ramberg-Osgood , materiál se zpevněním nebo materiál bez zpevnění.

2 Struktura systému STRENGTH

Pohled na prostředí systému STRENGTH po spuštění je ukázán na obrázku 1. Nápověda je realizována hypertextovými helpy.

Vstupní data se ve verzi 7.04 připravují pomocí libovolného textového editoru např. notepadu. Alternativní zadávání uživatelských vstupních dat pomocí dialogů roletových menu se připravuje v další verzi. Uživatelské zadání pro posouzení statické pevnosti a pro posouzení na únavu je kontrolováno z hlediska úplnosti a formální správnosti. Převodník U2I.exe data následně převede do interního formátu pro zpracování ve výkonné části.

Výkonná část systému STRENGTH tj. motory (enginy) FatigueV.exe a MonotonV.exe i převodníky jsou realizované jako tzv. konzolové aplikace. To umožňuje, aby kromě interaktivního prostředí STRENGTH mohly být motory přímo spuštěny z prostředí ANSYSu. Veškerá hlášení o běhu výkonné části a převodníků včetně případných varování a chyb se zapisují na konec textového souboru Strength.err.

Výsledky se zapisují rovněž do textových souborů. Možnost spouštění modulů výkonné části včetně “run-string” parametrů příkazové řádky nebo dávky usnadňuje automatické testování systému STRENGTH.

Testovací příklady systému STRENGTH jsou autorizovány a postupně doplňovány, každá nová revize výkonných modulů musí v mezích zaokrouhlovací chyby a formátu zobrazení čísel úspěšně projít všemi testy.

Obrázek 24 – Interaktivní prostředí systému STRENGTH

3 Použití systému STRENGTH

Z dílen vítkovického Energetického strojírenství byly pro Kalininskou jadernou elektrárnu v Rusku dodány v roce 2013 vysokotlaké ohříváky určené k ohřevu napájecí vody v systému regenerace páry turbínového okruhu. Na obrázku 2 je ukázán vysokotlaký ohřívák o hmotnosti 110 tun během expedice.

Systém STRENGTH byl ve společnosti VÍTKOVICE ÚAM a.s. použit při posouzení statické pevnosti a životnosti vysokotlakých ohříváků a pro posouzení kumulace poškození materiálu jeho trubkového svazku při dvoufrekvenčním zatěžování vlivem provozních změn tlaku a teploty včetně dynamických účinků vysokofrekvenčního kmitání trubek.

Obrázek 25 – Vysokotlaký ohřívák napájecí vody

4 Vstupní data

Uživatelská vstupní data STRENGTH byla navržena s ohledem na obsahovou srozumitelnost z hlediska pojmů únavové pevnosti a aby byla uživatelsky jednoduchá a vhodná z hlediska přenosu dat z MKP systému ANSYS. Data je možné připravit pomocí textového editoru. Vstupní data jsou zapsány v textovém souboru, délka jednotlivých řádků nepřesahuje 80 znaků. Na řádcích označených v prvním sloupci vykřičníkem jsou komentáře. Vkládat komentáře je možné na začátku souboru a mezi ukončené příkazy. Vysvětlující text je možné přidat také za příkaz *end. U některých příkazů lze po zadání parametrů příkazu za lomítko uvést další vysvětlívky.

Klíčová slova ve vstupních datech jsou rozpoznány většinou dle prvních pěti znaků. Pro lepší čitelnost lze užít kombinace malých a velkých písmen a přidat další znaky. Textové řetězce jsou ohraničeny jednoduchými uvozovkami (alt 39). Číselné hodnoty v zadání jsou zapsány volným formátem, oddělovačem čísel je jedna nebo více mezer. Textový soubor ukázaný v tabulce 1 obsahuje úplné zadání pro výpočet nízkocyklové únavy.

Tabulka 17 Uživatelská vstupní data STRENGTH pro únavu

```
!*       10        20        30        40        50        60        70
!*234567890123456789012345678901234567890123456789012345678901234567890123456789012
!************************************************************************
!*  programovy system STRENGTH  verse 7.03              03.07.2013      *
!* (c) prof.Vejvoda a kol.                                               *
!*----------------------------------------------------------------------*
!*  U_VTO7_2.fxt     (uzivatelska vstupni data, prevodnik: U2I.exe)     *
!*                   =>interni vstupni data pro engine: FatigueV.exe    *
!*  Last UpDate  Z.R.           verse 7.03              04.07.2013      *
!************************************************************************
!
! Charakteristika ulohy: Nizko-kmitova unava, Neuber ,2 materialy, 13 bodu
!                        pro VTO-7, prevod dat dle Pavel & Martin Rysavy
!                        teploty a napeti pres INCLUDE
!
*STRENGTH  7.03
!
*TITLE
  'vto7'             / nazev ulohy
!
*FatigueV
  'NKU'              / nebo: 'VKU','DFZ'
  'MaxTau'           / nebo: 'Tresca', 'Mises'
  'Neuber'           / nebo: 'Wekv'
  'Langer'           / nebo: 'Manson-Coffin', ('Wohler')
  'zpevneni'         / nebo: 'Ramberg-Osgood', 'bez_zpev'
  '3D'               / nebo: 'Axisym', 'Plane','Single-axis'
  'Stress'           / nebo: 'Strain'
  'bez_konc'         / nebo: 'Koncentrace-souc'
  'ZS_konc'          / nebo: 'JZ_nomin'
  'SI'               / nebo: 'USA'
  'InterAtomEnergo'  / nebo: ''
!
*PARAmetry zadani a vypoctu
  'F_VTO7_2'  / max. 8 znaku ,default 'Fatigue7'
      0       / pocet JZ
      9       / pocet ZS
      9       / pocet teplotnich poli (vypoctenych)
      0       /  - " - (konstantnich)
      5       / pocet Zateznych Bloku
      2       / pocet druhu materialu
     13       / pocet bodu
      0       / pocet bodu se zadanou koncentraci napeti
      0       / pocet superponovanych kmitu
!
*MATErial
 1 5 '08Ch18N10T'
  'Teplota   Rk   Rm       E   Z'
        20  196  491  205000  40
       100  186  456  200000  40
       200  176  417  190000  40
       300  162  358  180000  40
       350  157  333  175000  40
```

```
 2 5 '22K'
  'Teplota   Rk   Rm       E   Z'
        20  215  430  200000  35
       100  196  392  195000  35
       200  186  392  190000  33
       300  186  353  180000  31
       350  177  343  175000  31
!
*BLOCKs
  'ZS'
  'Bl.  Opak. PocetZS  SeznamZS'
    1      1      14   1  2  1  3  1  4  1  5  1  6
                       7  8  9  1
    2      2       5   1  2  1  3  1
    3     20       9   1  4  1  5  1  6  7  9  1
    4     39      10   1  4  1  5  1  6  7  8  9  1
    5    632      59   1  6  7  8  7  8  7  8  7  8
                       7  8  7  8  7  8  7  8  7  8
                       7  8  7  8  7  8  7  8  7  8
                       7  8  7  8  7  8  7  8  7  8
                       7  8  7  8  7  8  7  8  7  8
                       7  8  7  8  7  8  7  9  1
  'Bl. navazuje na ZB v cas. okamziku'
    1    0    0
    2    1   14
    3    1   14
    4    1   14
    5    1   14
!
*TENZor
   INCLUDE  'napeti2.ixt'
!
*TEMPerature
   INCLUDE  'teploty2.ixt'
!
*FACTors
   'safety' 2  10       / n_Sig, n_N
   'fiw'    1.0         / default
     2  'zmen'          / pokud beze zmen,tento radek a dalsi zadani odpada
     'c. bodu     fiw'
        1         0.6
       13         0.6
*MISCellaneous
   'EN'   200000.0
   'I_MAT'   2
    1  'zmen'          / pokud beze zmen,tento radek a dalsi zadani odpada
    'c. bodu   c. materialu'
       1          1
*FORM
    0    0    1
!
*END  uzivatelska data pro FatigueV, verze 7.03
!
```

5 Napětí a teploty exportované z ANSYSu

Data zatěžovacích stavů (případně jednotlivých zatížení) jsou číslována. Počet složek tenzoru napětí odpovídá volbě 3D, viz tabulka 1. První číslo na řádku označuje číslo uzlu sítě MKP, pro který byly hodnoty vypočteny. Všechny číslelné hodnoty mohou být zapsány ve volném formátu.

Tabulka 18 Vkládaný soubor napeti2.ixt (zkráceno)

```
  'ZS' 1
   64246 0.000       0.000       0.000       0.000       0.000       0.000
 1647529 0.000       0.000       0.000       0.000       0.000       0.000
 1648802 0.000       0.000       0.000       0.000       0.000       0.000
 1648812 0.000       0.000       0.000       0.000       0.000       0.000
 1650656 0.000       0.000       0.000       0.000       0.000       0.000
 1650899 0.000       0.000       0.000       0.000       0.000       0.000
 1662603 0.000       0.000       0.000       0.000       0.000       0.000
 1663238 0.000       0.000       0.000       0.000       0.000       0.000
 1750828 0.000       0.000       0.000       0.000       0.000       0.000
 1796157 0.000       0.000       0.000       0.000       0.000       0.000
 2173569 0.000       0.000       0.000       0.000       0.000       0.000
 2174184 0.000       0.000       0.000       0.000       0.000       0.000
 3028645 0.000       0.000       0.000       0.000       0.000       0.000
  'ZS' 2
   64246  -56.874     -15.212     -200.25    -0.69249     -1.5014      13.208
```

```
1647529  -27.266     -11.613      420.78      9.0977     0.16827     0.81166
1648802   250.55      604.25      111.00      351.85     -1.1650    -0.67466
1648812   5.7426     -171.94      40.859      21.063    -0.20146     0.29608
1650656   236.08      564.94      91.451     -330.64     -1.4029     0.64340
1650899  -50.141     -188.50      23.366     -89.550    -0.86695    -0.23593
1662603   27.888     -188.16     -49.754     0.22166     -88.943     0.15383
1663238   111.04      595.13      260.14      1.0931     -353.94    -0.74193
1750828   62.375     -8.2798      60.696    -0.54864E-01  3.1780    -0.11560E-01
1796157   293.84     -10.714      27.724      21.836      1.5089      130.66
2173569 -0.66796     0.11541      22.311     0.13611    -0.36468      1.1964
2174184 -0.57467      7.6481      3.0142     0.33303    -0.27395E-01 0.56244
3028645   267.59      6.8812      116.78    -0.40318      6.8837     -1.0216
 'ZS' 3
  64246   23.684    -0.78046      113.64    -0.94767E-01  1.1293     -7.5691
1647529 -0.16489    -0.19891      7.8793     0.25430     0.76821E-01 -0.13556
1648802  -46.577     -94.293     0.71433E-02 -57.259     0.37246     0.15215
1648812  -9.3922      320.07      41.378     -39.740    -0.26463     0.11893
1650656  -45.334     -91.886    -0.76131E-01  55.720     0.34697    -0.18577
1650899   84.144      350.69      78.914      164.34     0.44110     0.10167E-01
      ...
      ...
 'ZS' 4
      ...
      ...
 'ZS' 5
      ...
      ...
 'ZS' 6
      ...
      ...
 'ZS' 7
      ...
      ...
 'ZS' 8
      ...
      ...
 'ZS' 9
  64246  -29.454     -10.427     -136.51     0.58136     -3.6348      7.0534
1647529   5.2698      5.7644      36.590      1.7285     0.35804     0.59892E-01
1648802  -1.4327     -21.464     -7.0820     -10.309     0.54682     0.83608E-01
1648812   6.0997      147.34      86.529     -16.488     0.53012     0.16133
1650656  -9.1987     -39.482      10.642      24.214     0.37285    -0.12350
1650899   45.362      167.12      100.01      74.257     0.60355    -0.14280
1662603   90.532      136.37      37.634    -0.40937      59.700     0.21987
1663238   2.3256     -25.726     -6.1489     -12.116      14.809      6.3239
1750828   22.478      7.5424      22.491     -3.0902     0.73710E-01 0.89881E-01
1796157   34.281      5.9981      10.076      2.9762    -0.63260      12.519
2173569  -3.2977     -1.5891      185.07    -0.14995     -1.3706      2.1652
2174184  -1.2680      39.390      96.998     0.49079E-01 0.90520E-01  1.5068
3028645   46.772      16.260     -39.890     -2.8068      20.906     -3.0345
```

Tabulka 19 Vkládaný soubor teploty2.ixt (zkráceno)

```
'TE' 1
  'konst'  20.0
'TE' 2
  'konst'  40.0
'TE' 3
  'konst'  40.0
'TE' 4
  'konst'  40.0
'TE' 5
  'konst'  40.0
'TE' 6
  64246      183.54
1647529      194.38
1648802      186.69
1648812      191.12
1650656      169.15
1650899      190.28
1662603      190.46
1663238      178.26
1750828      181.92
1796157      194.40
2173569      193.27
```

```
 2174184      192.88
 3028645      176.96
 'TE' 7
       ...
       ...
 'TE' 8
       ...
       ...
 'TE' 9
   64246     159.24
 1647529     169.48
 1648802     170.41
 1648812     117.80
 1650656     154.55
 1650899     118.29
 1662603     118.38
 1663238     162.17
 1750828     162.00
 1796157     169.47
 2173569     115.86
 2174184     116.10
 3028645     149.22
```

6 Zobrazení výsledků v ANSYSu

V tabulce 4 je uveden výpis výsledků STRENGTH ve formátu určeném pro import do ANSYSu. Stejný formát byl použit při posouzení 7723 povrchových bodů sítě MKP modelu VTO-K-7 vstupního nátrubku na nízkocyklovou únavu, jak je ukázáno na obrázcích 3 a 4.

Podrobné posouzení bodu s nejvyšší vypočtenou kumulací poškození s číselnými hodnotami včetně zadaných vstupních napětí se zapisuje do samostatného výsledkového textového souboru.

Tabulka 20 Vypočtené celkové kumulace poškození, formát pro ANSYS

```
!
!  *************************************************************************
!  *                                                                       *
!  *                                                                       *
!  *                 S T R E N G T H   verse 7.04  2 0 1 4                 *
!  *                                                                       *
!  *                                                                       *
!  *                 VITKOVICE UAM a.s                                     *
!  *                                                                       *
!  *************************************************************************
!
!
!  =========================================================================
!           U N A V A - E T A P A   I N I C I A C E   D E F E K T U
!  -------------------------------------------------------------------------
!  PROGRAM STANDARDISOVAN KOMISI C.5 NA CSKAE PRAHA POD C. 523 DNE 15.3.1991
!  =========================================================================
!
!  vto7                                                  05.03.2014, 10:04
!
!  -------------------------------------------------------------------------
!  POUZITE VYPOCETNI POSTUPY:
!
!  - JEDNOTKY ....................................MPa, mm, stupen C
!  - TEORIE PEVNOSTI .............................MAX. SMYKOVYCH NAPETI
!  - KONCEPCE VYPOCTU PRUZNE
!        PLASTICKE DEFORMACE .....................NEUBER
!
!  - ZAVISLOST NAPETI-DEFORMACE ..................SE ZPEVNENIM
!  - KRIVKA ZIVOTNOSTI (NKU) .....................typ LANGER
!  - KRIVKA ZIVOTNOSTI A HYPOTEZA
!        KUMULACE POSKOZENI (VKU) .................NTD INTERATOMENERGO
!  -------------------------------------------------------------------------
!
!
!  VSTUPNI DATA JSOU ULOZENA V SOUBORU: F_VTO7_2.DAT (F_VTO7_2.DAU)
```

```
!
!
!
!  V Y S L E D K Y   V Y P O C T U
!  ------------------------------
 BF,   64246, TEMP, 0.25456         ! Kumulace poskozeni v bode c. INTE:     1
 BF, 1647529, TEMP, 0.01117         ! Kumulace poskozeni v bode c. INTE:     2
 BF, 1648802, TEMP, 0.30309         ! Kumulace poskozeni v bode c. INTE:     3
 BF, 1648812, TEMP, 0.00799         ! Kumulace poskozeni v bode c. INTE:     4
 BF, 1650656, TEMP, 0.19429         ! Kumulace poskozeni v bode c. INTE:     5
 BF, 1650899, TEMP, 0.02551         ! Kumulace poskozeni v bode c. INTE:     6
 BF, 1662603, TEMP, 0.01732         ! Kumulace poskozeni v bode c. INTE:     7
 BF, 1663238, TEMP, 0.25271         ! Kumulace poskozeni v bode c. INTE:     8
 BF, 1750828, TEMP, 0.00179         ! Kumulace poskozeni v bode c. INTE:     9
 BF, 1796157, TEMP, 0.00471         ! Kumulace poskozeni v bode c. INTE:    10
 BF, 2173569, TEMP, 0.00349         ! Kumulace poskozeni v bode c. INTE:    11
 BF, 2174184, TEMP, 0.00180         ! Kumulace poskozeni v bode c. INTE:    12
 BF, 3028645, TEMP, 0.12640         ! Kumulace poskozeni v bode c. INTE:    13
!
!
!  NEJVYSSI VYSLEDNA KUMULACE POSKOZENI D= 0.30309 JE V BODE:    3
!
!  KONEC VYPISU VYSLEDKU PROGRAMU FatigueV verze 7.04
```

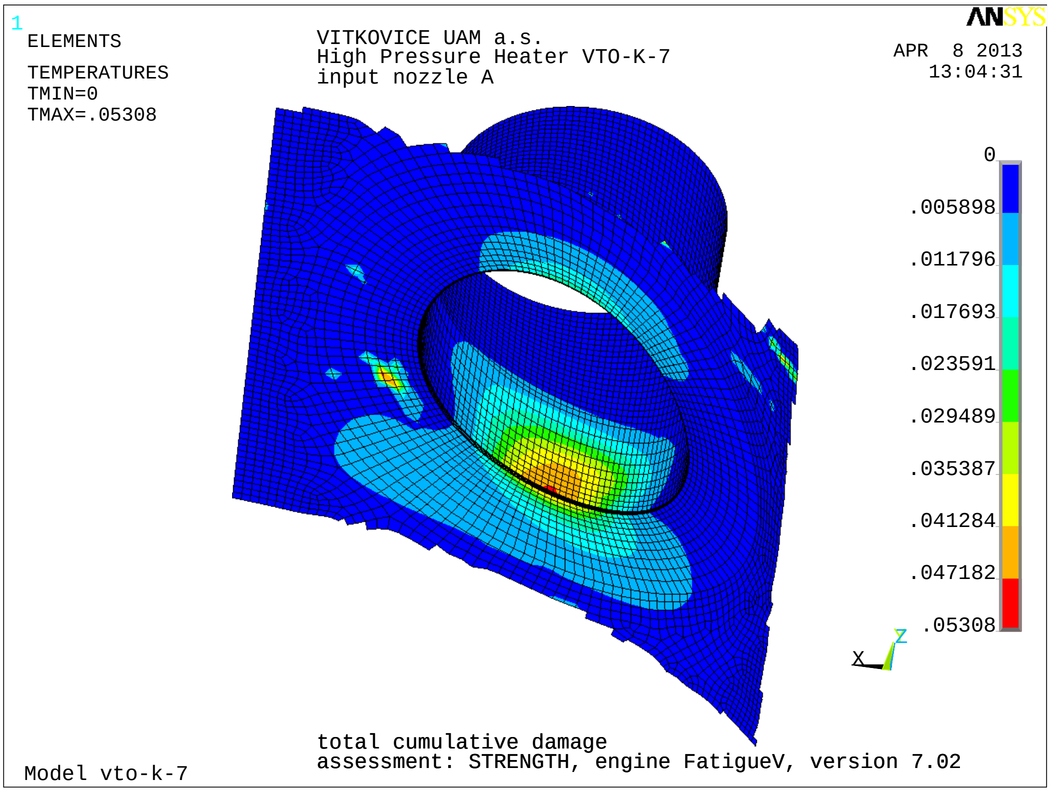

Obrázek 26 - Vypočtené kumulace poškození vstupního nátrubku

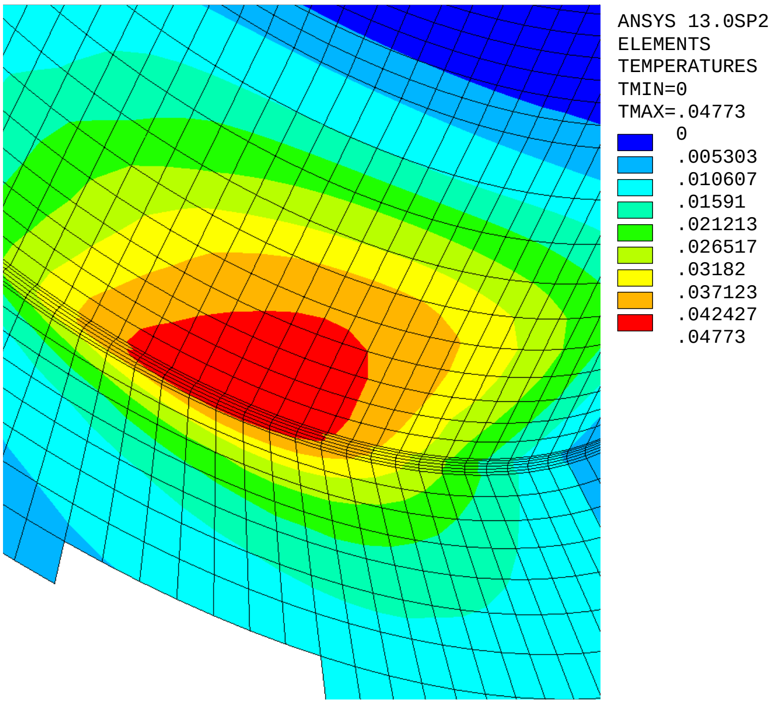

Obrázek 27 - Vypočtené kumulace poškození, detail

7 Závěr

Alternativní zadávání vstupních dat systému STRENGTH pomocí dialogů roletových menu v interaktivní části systému se připravuje v další verzi.

V systému STRENGTH bude postupně naprogramováno také posouzení na únavu podle následujících norem a předpisů: ČSN EN 1993-1-9 (Navrhování ocelových konstrukcí – Únava), ČSN 27 7008 (Navrhování ocelových konstrukcí rypadel, nakladačů a zakladačů), ČSN EN 12952-3 (Vodotrubné kotle a pomocná zařízení, Příloha B).

Po realizaci nabídky spolupráce s SVS FEM v oblasti přípravy a přenosu dat z ANSYSu do STRENGTH se usnadní přenos vypočtených teplot, složek napětí a deformací (jednotlivé „LOAD-CASE" nebo „LOAD-STEP") a zadání vstupních dat pro STRENGTH i vykreslení výsledků bude možné z nabídkových menu prostředí Classic i WorkBench.

Literatura

VEJVODA S.., POLÁK J., 1986. Využití koncepce ekvivalentní energie při výpočtu tlakových nádob na únavu, Strojírenství, ročník 1986, číslo 36, stránky 295-299,SNTL.

VEJVODA S., VĚCHET J., ŠÍMA J.,1983, Předpisy pro výpočet pevnosti zařízení a potrubí jaderných elektráren (komentář k souboru NTD INTERATOMENERGO), Normalizace v jaderné technice, ročník 1983, číslo 5, stránky 1-117, ISSN 0139-8881.

Hodnocení pevnosti zařízení a potrubí jaderných elektráren typu VVER, sekce III., Normativně technická dokumentace A.S.I, Praha, Brno 1996, Identifikační číslo NTD ASI-III-Z-5/96.

VEJVODA S., 2002, Stavba procesních zařízení. Hodnocení odolnosti materiálů tlakových nádob proti jejich poškozování v provozních podmínkách., Brno: CERM, 107 stran, ISBN 80-214-2302-1.

KLESNIL M., LUKÁŠ P., 1975, Únava kovových materálů při mechanickém namáhání. Praha: ACADEMIA, 222 stran, 509-21-857.

MACKERLE Z., VEJVODA S., 2012, Mezní stavy pevnosti. Podklady pro program FatigueV k posouzení na únavu. Zpráva společnosti VÍTKOVICE ÚAM a.s., arch. č. V2986/12.

RAMÍK Z., 2013, STRENGTH 7.04 – vstupní data. Zpráva společnosti VÍTKOVICE ÚAM a.s., arch.č. V3007/13, revize 1.

RAMÍK Z., 2012, Mezní stavy pevnosti. Etapa c) Zpracování algoritmů programu FatigueV a vytvoření beta verze software FatigueV. Zpráva společnosti VÍTKOVICE ÚAM a.s., arch.č. V2995/12.

RYŠAVÝ P., RYŠAVÝ M., 2013, Posouzení statické pevnosti a životnosti vysokotlakých ohříváků VTO-K-6 a VTO-K-7. Zpráva společnosti VÍTKOVICE ÚAM a.s., arch. č. V2942/12.

PŘICHYSTAL I., NOVOTNÝ J., 2013, Analýza proudění páry v mezitrubkovém prostoru vysokotlakého ohříváku. Zpráva společnosti VÍTKOVICE ÚAM a.s., arch. č. V3033/13.

Kontaktní adresa: VÍTKOVICE ÚAM a.s., Ruská 2887/101, Vítkovice, 703 00 Ostrava
Ing. Zdeněk Ramík, e-mail: zdenek.ramik@vitkovice.cz, tel. 725 404 729
Prof. Ing. Stanislav Vejvoda, CSc., e-mail: stanislav.vejvoda@vitkovice.cz, tel. 602 505 339
VÍTKOVICE ÚAM a.s., Mezírka 775/1, 602 00 Brno, Česká republika

DESIGN OPTIMIZATION OF FOUNDATION SLAB IN INTERACTION WITH SUBSOIL

MARTIN ŠTIGLIC

Slovak University of Technology in Bratislava
Faculty of Civil Engineering

Abstract: The paper is aimed at design optimization of foundation slab, which interacts with elastic subsoil. Examines the impact of cave in to the base plate. Skeleton of high-rise building, foundation slab and subsoil are modeled using finite element software ANSYS and optimization analysis is performed by ANSYS Workbench extension Design Exploration.

Keywords: FEM, optimization, subsoil, foundation slab

1 Introduction

The interaction between subsoil and foundation slab belongs to nonlinear problems, which appear in construction practice. Slab bends down or buckles out of the plane and comes into contact with the subsoil. Operators appearing in the control equations are nonlinear and of fourth order. When modeling unilateral bond, we consider nonsmooth analysis with various inequalities and in optimization with constraints in the form of inequalities. However, when modeling the slab on subsoil, the applied load cause the effect of penetration or unsticking and it is necessary to take care how the unilateral bond should be modeled. Software ANSYS has lot of algorithms and offers several possibilities how modeling the contact of two adjacent bodies.

One of the problems related to unilateral bond and subsoil-structure interaction is interaction when cave in occurs. This situation can occur anywhere in the world where mining operations finished. Old mining shafts kept in some regions the ground with old underground corridors. These may be disrupted and unstable corridors, deep ground dips, flooded areas. Around them the subsoil could be unstable and cave in could occurs. The hole remains under the foundation slab when cave in occurs and it can damage the entire structure. The task of this study is to investigate the impact of cave in of the area under each support columns and then optimize the foundation slab for the worst case.

2 Case study

2.1 Model

The three-storey structure is built on a concrete slab Img. 1 with dimensions of 32 x 17.6 x 0.7 m and stored on an elastic foundation with dimensions of 42 x 27.6 x 5 m.

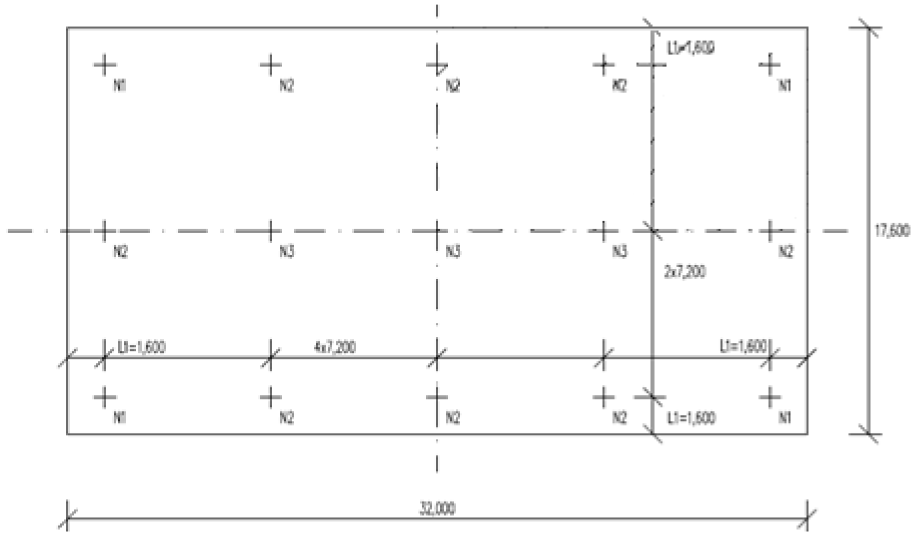

Image 28 – Foundation slab plan

2.2 Finite element model

The frame structure is modeled using BEAM188 elements. SHELL181 element with a thickness of 0.2 m was used for the storey plate. The same element with a thickness of 0.7 m was also used for the foundation slab. Subsoil was considered as elastic half-space and modeled using SOLID186 elements. Elements CONTA174 and TARGE170 were used to modeling the interaction of subsoil and foundation slab.

Material for each part of the structure is considered as linear elastic material with properties shown in the Tbl.1.

Table 21 Linear elastic materials properties

	Young's modulus E (MPa)	Poisson ratio v	Density (kg/m^3)
Slab	30000	0,18	2300
Subsoil	80	0,3	2000
Frame	30000	0,18	2300

Img. 2 shows the space structure and its mesh. Regular square grid was chosen for better and faster solutions convergence. Element edge length 0.8 m was set for the foundation plate, to ensure better interconnection with beam elements and regular square grid.

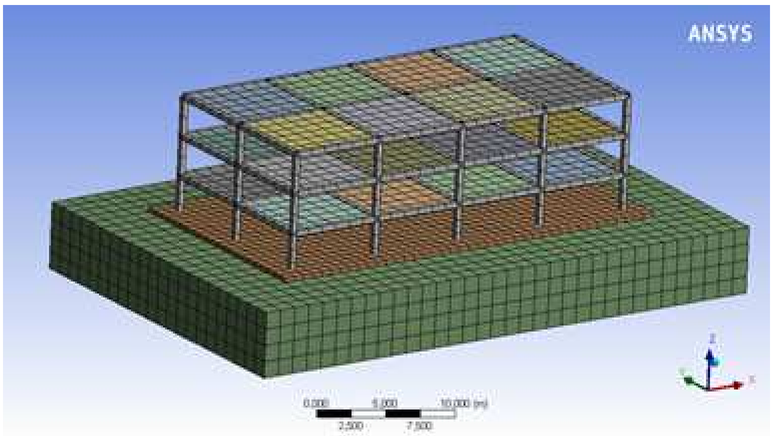

Image 2 – Space structure mesh

Each floor was loaded with the value of 20 kN/m^2. Slab was anchored at one point to avoid displacement in the X-axis and Y-axis. Subsoil was fixed around perimeter and at the bottom avoiding all displacements. The calculation takes into account the construction and subsoil self-weight. Gravitational acceleration was set up to the value 9.81 m/s^2. Cave-in was modeled as a displacement 2 m of square against Z-axis direction.

2.3 Analysis and results

Cave in can occur at any place under the foundation slab. This case study is focused on cave in simulated with square surface with dimensions 3.2 m x 3.2 m in places, where columns of construction are associated with base plate. Maximum slab penetration/unstick and maximum tension in the slab layers (top, middle, bottom) was examined for each location under a column. The results are summarized in Tab. 2 and shown in the graph on Img. 3 and Img. 4

Table 2 Results for each case of cave in

Support No.	**Max. penetration**	**Max. unstick**	**Max. stress top**	**Max. stress middle**	**Max. stress bottom**
	[mm]	[mm]	[MPa]	[MPa]	[MPa]
1	27,28	1,71	8,9982	4,8432	9,0197
2	18,53	5,93	10,0550	5,0627	10,1330
3	16,93	1,64	9,0503	4,9041	9,0706
4	18,75	5,92	10,0920	5,1473	10,1710
5	28,66	1,70	9,4429	4,8593	9,4657
6	21,36	6,09	11,2590	5,3082	11,3660
7	16,30	8,44	15,3290	5,1949	15,3970
8	15,30	3,65	14,3940	5,2580	14,4480
9	16,26	8,43	15,3180	5,1233	15,3860
10	22,00	5,76	11,3340	5,2455	11,4420
11	28,46	1,61	9,3154	4,8580	9,3398
12	19,62	5,64	10,2170	5,1966	10,2970
13	17,72	1,42	9,1850	5,0524	9,2062
14	19,17	5,63	10,2080	5,1996	10,2880
15	31,56	1,30	9,9581	5,3520	9,9871

From graphs, it can be seen, that on slab can be considered with symmetry and also that anchor on one slab point has little influence on results.

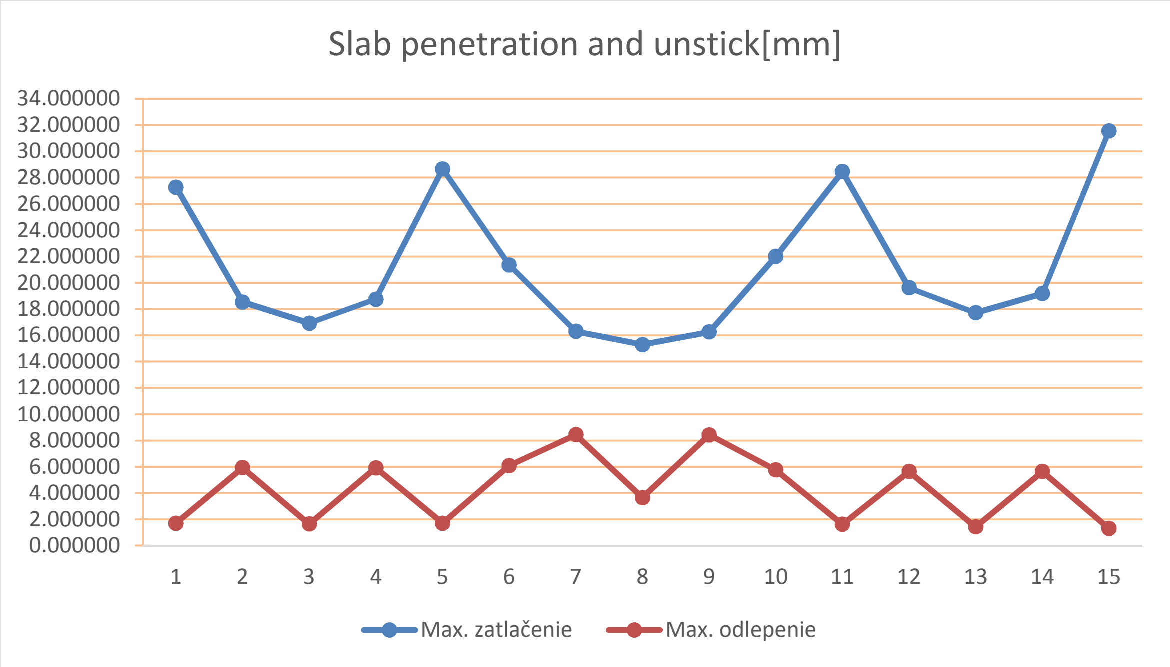

Image 3 – Maximum slab penetration and unnstick

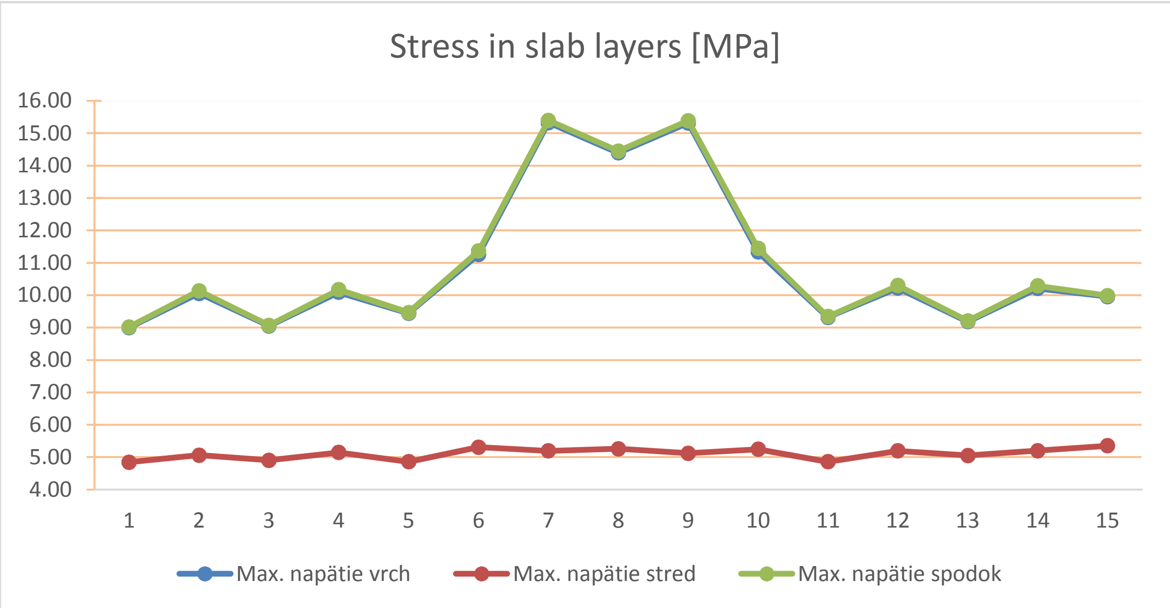

Image 4 – Maximum stress in slab layers

2.4 Design optimization

The worst case from analysis was chosen for the optimization. When looking at graph of stress Img. 4 it can be seen, that the greatest tension on the bottom slab layer is, when cave in occurs under a column number 7 and 9. Column number 7 was chosen to optimization. On Img. 5 are shown the places, at which occur the maximum penetration (on the left) and maximum stress (on the right).

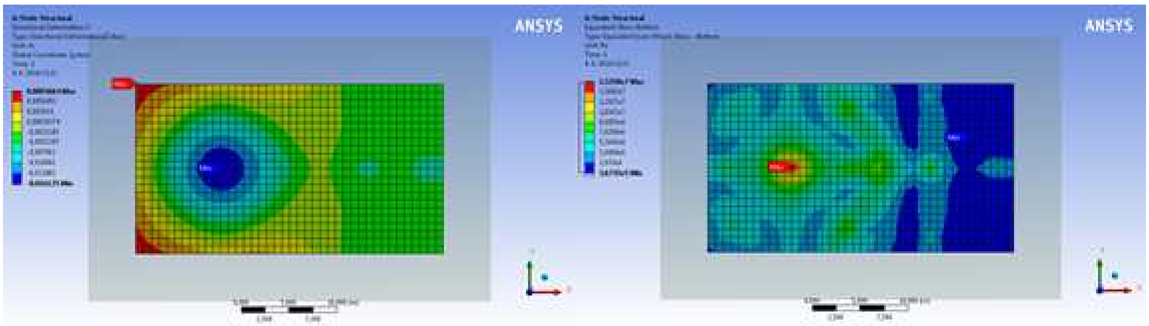

Image 5 – Maximum penetration (left) and maximum stress (right) in slab

Foundation slab thickness was optimized. The conditions were minimize slab volume and do not exceed the maximum tension stress. When considering a thickness of 0.7 m then critical damage occurs. Ideal slab thickness 2.46 m for critical case of cave-in was found by optimization analysis. At this value, the stress on the lower layer is close to 2.2 MPa.

3 Conclusion

The aim of the study was to investigate the effects of cave in under different structure columns and for the worst case optimize the thickness of the foundation slab with condition for maximum tension stress of concrete. In designed slab thickness, the concrete failure would occur in any case of cave-in and would be the most critical in case of No. 7 and No. 9. Slab thickness 2.46 m was determined by optimization and satisfy all conditions. In this case, the slab reinforcement was not taken into account and it was considered only with pure concrete slab. The question is, whether it is better/cheaper to use more concrete or use reinforcement. Also could be considered with solid finite elements for foundation slab because thickness 2.46 m is for shell element very large.

References

ARORA, J. , 2007 Optimization of Structural and Mechanical Systems, World Scientific Pub. Co. Inc, 595 s. ISBN 9812569626

KIKUCHI, N. – ODEN, J. T., 1995 Contact Problems in Elasticit. Philadelphia : SIAM, 495 s. ISBN: 0898714680

CHRISTENSEN, P. W. – Klarbring, A., 2009, An Introduction to Structural Optimization. Springer, 214 s. ISBN 978-1-4020-8666-3

JENDŽELOVSKÝ, N., 2009, Modelovanie základových konštrukcií v MKP. Bratislava, 94 s. ISBN 978-80-227-3025-9

ANSYS Help, Theory Reference for the Mechanical APDL and Mechanical Applications (ANSYS manual)

Acknowledgement
This paper was supported by Grant Agency VEGA, projects No. 01/0629/12.

Contact address:
Ing. Martin Štiglic
Slovenská technická univerzita v Bratislave, Stavebná fakulta, KSME, Radlinského 11, 813 68 Bratislava

OPTIMALIZÁCIA DOSKY NA PRUŽNOM PODLOŹÍ

KATARÍNA TVRDÁ
Slovak University of Technology Bratislava, Department of Structural Mechanics

Abstract: This paper deals with an problem on thickness of a plate using the first order method, while maintaining different restrictive conditions. The optimization analysis is based on a reduction of the thickness in the individual points. The aim is to obtain a minimum volume of the plate. Finally some results of optimal design are presented.

Keywords: static analysis, optimization, finete element method, plate, Winkler foundation

1 Úvod

Význam optimalizácie niektorých parametrov konštrukcií sa v celosvetovom meradle neustále zvyšuje. Zaoberajú sa ňou popredné univerzity vo svete hlavne pri riešení konkrétnych úloh pre prax najmä v odvetví letectva, lodnej výstavby ako automobilový priemysel. Význam optimalizácie tuhostí konštrukcie rastie aj stavebníctve. Najväčší význam nadobúda optimalizácia konštrukcií uložených na podloží. Hrúbka dosky na Winklerovom podloží sa zmenšuje až po minimálnu predpísanú hrúbku v závislosti od cieľovej funkciea optimalizačných parametrov, ktoré sa stanovia v optimalizačnej analýze. Pri výpočte môžeme využiť celú radu komerčných softwarových balíkov, ak máme k nim prístup, alebo si tím odborníkov vypracuje vlastný balík programov.

Riešenie každej hornej stavby je nutné uvažovať vždy v kontakte s podložím. Riešením týchto konštrukcií sa venuje pomerne veľa autorov. Z nich spomeniem najmä Jendželovský (2009), Mistríková (2007), Frydrýšek (2006), Jančo (2013), Kollár (2000), Eisenberger, Yankelevsky a ďalší. Podložie predstavuje neohraničenú oblasť, v kontakte s konštrukciou však uvažujeme určitú ohraničenú časť. Dodnes najrozšírenejším a najviac používaným je jednoparametrický Winklerov model podložia. Pasternakov a Vlasovov model patria medzi dvojparametrické modely podložia, ktoré zavádzajú aj vplyv okolia základu pomocou šmykových síl. Patria sem aj modely Filonenko-Boroditsch, Hetényi a ďalší. Potom pristúpili modely založené na teórii pružného polpriestoru. Najznámejší je Boussinesque vzťah pre deformáciu pružného polpriestoru. Dnes sa najviac používa pri riešení úloh MKP.

2 Optimalizačný proces

V optimalizačnom procese vo všeobecnosti vystupujú tri typy parametrov, ktoré charakterizujú návrhový proces: návrhové premenné, stavové premenné a cieľová funkcia. Nezávislými parametrami v optimalizačnej analýze sú návrhové premenné. Vektor návrhových premenných možno zapísať v tvare:

$$\mathbf{x} = \{\mathbf{x_1}\, \mathbf{x}_2\, \mathbf{x}_3 \cdots \mathbf{x}_n\} \tag{1}$$

Návrhové premenné musia vyhovovať ***n*** obmedzeniam s hornou a dolnou hranicou, ktoré sú:

$$\underline{\mathbf{x}}_i \le \mathbf{x}_i \le \overline{\mathbf{x}}_i \qquad (i = 1, 2, 3, \dots, n), \tag{2}$$

kde **n** je počet návrhových parametrov, premenných.

Obmedzenia (hranice) návrhových premenných sú často nazývané hraničnými podmienkami a definujú tzv. prípustný priestor. Optimalizačnú úlohu možno formulovať takto:

Minimalizujme

$$f = f(\mathbf{x}) \tag{3}$$

s podmienkami

$$g_i(x) \le \overline{g}_i \qquad (i = 1,2,3,\cdots,m_1) \tag{4}$$

$$\underline{h_i} \le h_i(x) \qquad (i = 1,2,3,\cdots,m_2) \tag{5}$$

$$\underline{w_i} \le w_i(x) \le \overline{w}_i \qquad (i = 1,2,3,\cdots,m_3) \tag{6}$$

kde:

f	je cieľová (účelová) funkcia,
g_i, h_i, w_i	sú stavové premenné, predstavujúce dolné a horné hranice,
$m_1 + m_2 + m_3$	je počet stavových premenných s rôznymi hornými a dolnými limitnými hodnotami.

Rovnice (3) až (6) predstavujú optimalizačný problém s obmedzeniami, ktorého cieľom je minimalizovať cieľovú funkciu *f* pod obmedzeniami predpísanými rovnicami (2), (4), (5) a (6).

a. Aproximačná metóda

Túto metódu možno charakterizovať ako zdokonalenú optimalizačnú metódu nultého rádu, ktorá vyžaduje iba veľkosti závislých premenných (účelová - cieľová funkcia a stavové parametre) a nie ich derivácie. Závislé premenné sú najprv aproximované metódou najmenších štvorcov a problém minimalizácie s obmedzeniami sa konvertuje do podoby neviazaného problému použitím penalizačných funkcií. Ich minimalizácia potom prebieha iteračným postupom, pokiaľ nie je dosiahnutá konvergencia alebo je signalizované ukončenie. Pri tejto metóde každá iterácia je ekvivalentná jednému kompletnému cyklu analýzy.

Aproximácie funkcie

Prvý krok v minimalizačnom probléme s obmedzeniami vyjadrenými rovnicami (3) až (6) spočíva v aproximácii každej závislej premennej, označenej symbolom ˆ. Pre cieľovú funkciu, a podobne aj pre stavové parametre, platí

$$\widehat{f}(x) = f(x) + \Delta\,, \tag{7}$$

$$\widehat{g}(x) = g(x) + \Delta\,, \tag{8}$$

$$\widehat{h}(x) = h(x) + \Delta\,, \tag{9}$$

$$\widehat{w}(x) = w(x) + \Delta\,, \tag{10}$$

kde: Δ je chyba.

Komplexnejšou formou aproximácie je úplná kvadratická reprezentácia s diagonálnymi členmi, napr.:

$$\widehat{f} = a_0 + \sum_i^n a_i x_i + \sum_i^n \sum_j^n b_{ij}\; x_i\; x_j \tag{11}$$

V programe ANSYS sa aktuálna hodnota každej premennej v príslušnej iterácii vytvára pomocou programu, pričom užívateľ má k dispozícii určité kontroly. Na určenie koeficientov a_i a b_{ij} v rovnici (11) je použitá metóda náhradných štvorcov. Druhá mocnina chyby cieľovej funkcie má tvar

$$E^2 = \sum_{j=1}^{n_d} \phi^{(j)} (f^{(j)} - \widehat{f}^{\;(j)})^2 \tag{12}$$

kde:

$\varphi^{(j)}$ je váha prislúchajúca návrhovej množine j

n_d je aktuálny počet návrhových množín.

b. Optimalizačná metóda prvého rádu

Táto optimalizačná metóda využíva druhotné (sekundárne) informácie. Podmienený problém je transformovaný do nepodmieneného problému cez penalizačné funkcie. Vytvárajú sa aj derivácie cieľovej funkcie a penalizačných funkcií stavových parametrov, potrebné na nájdenie smeru v návrhovom priestore. V každom iteračnom kroku sa hľadajú zostupné smery hľadania cieľovej funkcie dovtedy, kým nie je dosiahnutá konvergencia. Každá iterácia je zložená z poditerácií, ktoré obsahujú hľadanie smeru a gradientu hľadaných funkcií. Inými slovami, každá iterácia optimalizačnej metódy obsahuje niekoľko iteračných cyklov. V porovnaní s podproblémovou aproximačnou metódou táto metóda je často výpočtovo náročná, ale presnejšia.

Nepodmienené cieľové funkcie

Nepodmienená verzia problému je formulovaná nasledovne:

$$\mathbf{Q}(\mathbf{x}, q) = \frac{f}{f_0} + \sum_{i=1}^{n} P_x(x_i) + q\left(\sum_{i=1}^{m_1} P_g(g_i) + \sum_{i=1}^{m_2} P_h(h_i) + \sum_{i=1}^{m_3} P_w(w_i)\right) \tag{13}$$

kde:

Q je bezrozmerná, nepodmienená cieľová funkcia,

P_x, P_h, P_g, P_w sú penalizačné funkcie aplikované na viazaný podmienený návrh a stavové premenné,

f_o je referenčná hodnota cieľovej funkcie, ktorá je vybratá z aktuálnej návrhovej množiny.

Pri návrhových parametroch sa používajú externé penalizačné funkcie (P_x). Na obmedzenia stavových parametrov sú použité penalizačné funkcie (P_g, P_h, P_w), napr. pre obmedzenia stavových parametrov s hornou hranicou, penalizačná funkcia má tvar:

$$P_g(g_i) = \left(\frac{g_i}{g_i + \alpha_i} \right)^{2\lambda} \tag{14}$$

kde:

λ je veľké celé číslo, takže funkcia bude veľmi veľká, ak je prekročené obmedzenie a veľmi malá, ak nie je prekročená obmedzujúca podmienka.

3 Optimalizácia hrúbky dosky v jednotlivých bodoch

V tejto časti je uvedený príklad optimalizácie dosky využitím metódy prvého rádu (kap.2), využitím softwéru ANSYS, ktorá okrem neznámej funkcie využíva ja jej prvú deriváciu na rozdiel od aproximačnej metódy alebo nultého rádu (kap.2).

Ide o základovú dosku objektu, ktorý má 7 nadzemných a jedno podzemné podlažie. Doska je vyrobená z betónu triedy C25/30 a je uložená na stredne uležaných štrkoch a pieskoch. Materiálové charakteristiky boli uvažované nasledovne: E_x = 31 e^6 kPa, v = 0.2 a modul pružnosti podložia c = 7 e^4 kN/m^3.

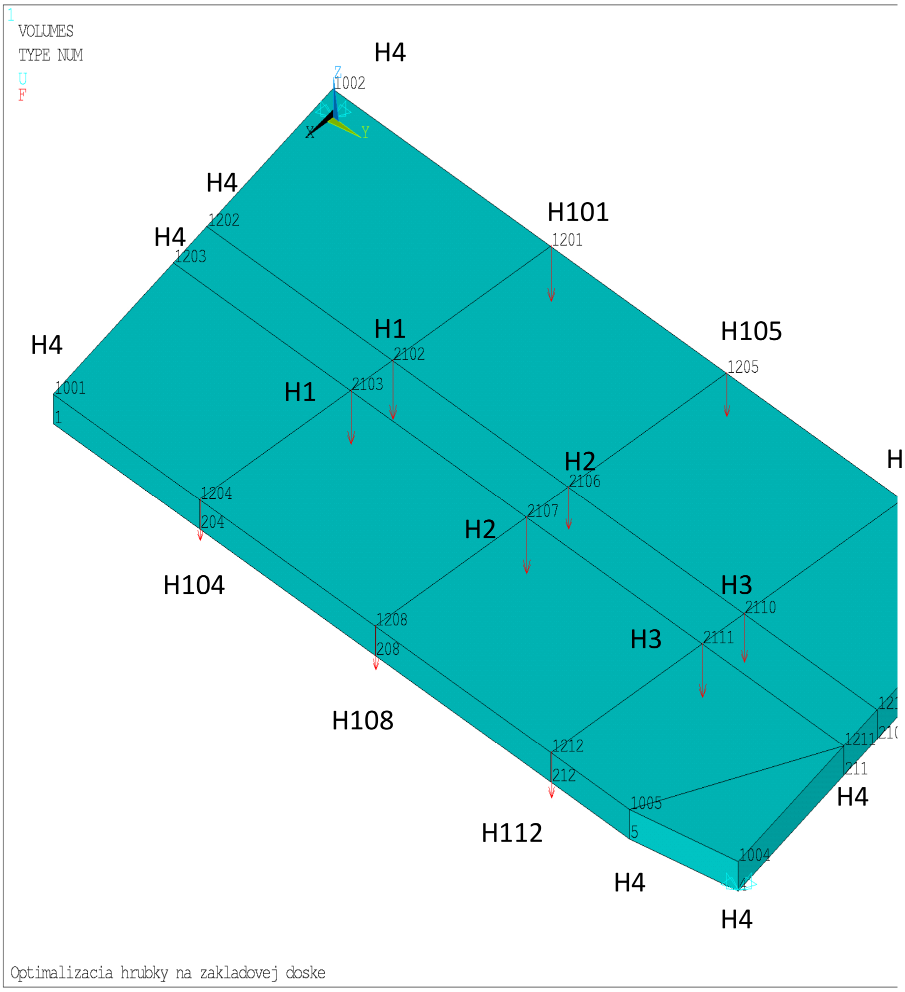

Obrázok 1 Vytvorenie statického modelu – definovanie objemov

Základová konštrukcia môže byť modelovaná z rôznych prvkov, ktoré ponúka knižnica programu Ansys. Tak isto je možné uvažovať rôzne prvky, ktorými je možné modelovať kontakt s podložím. Bližšie v prácach Hruštinec (2003), Jendželovský (2009), Prekop (2012).

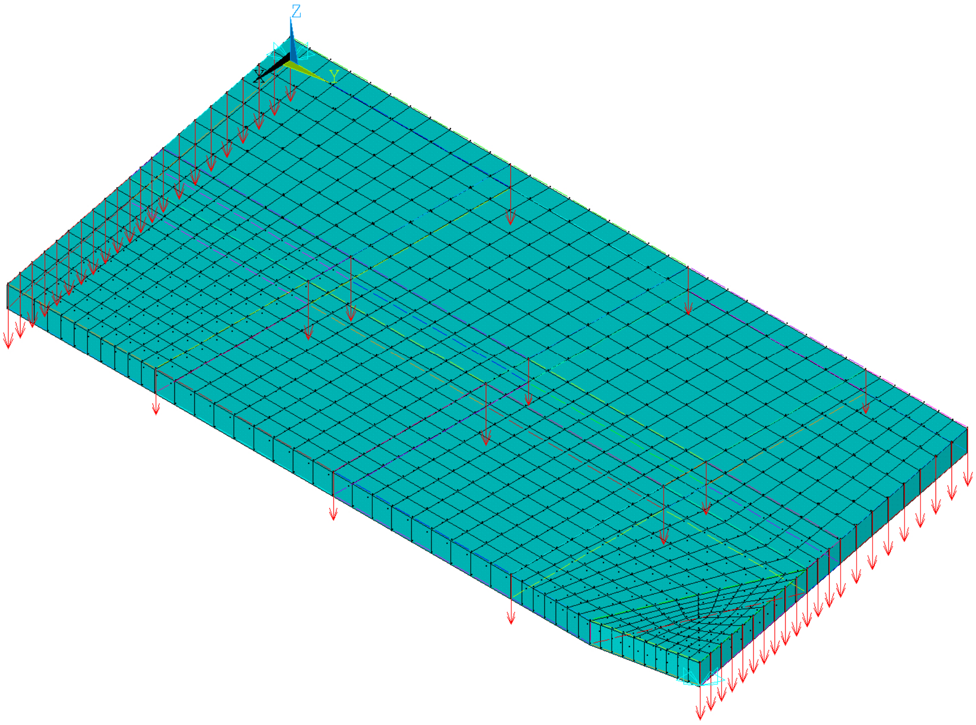

Obrázok 2 Modelovanie prvkov a definovanie zaťaženia

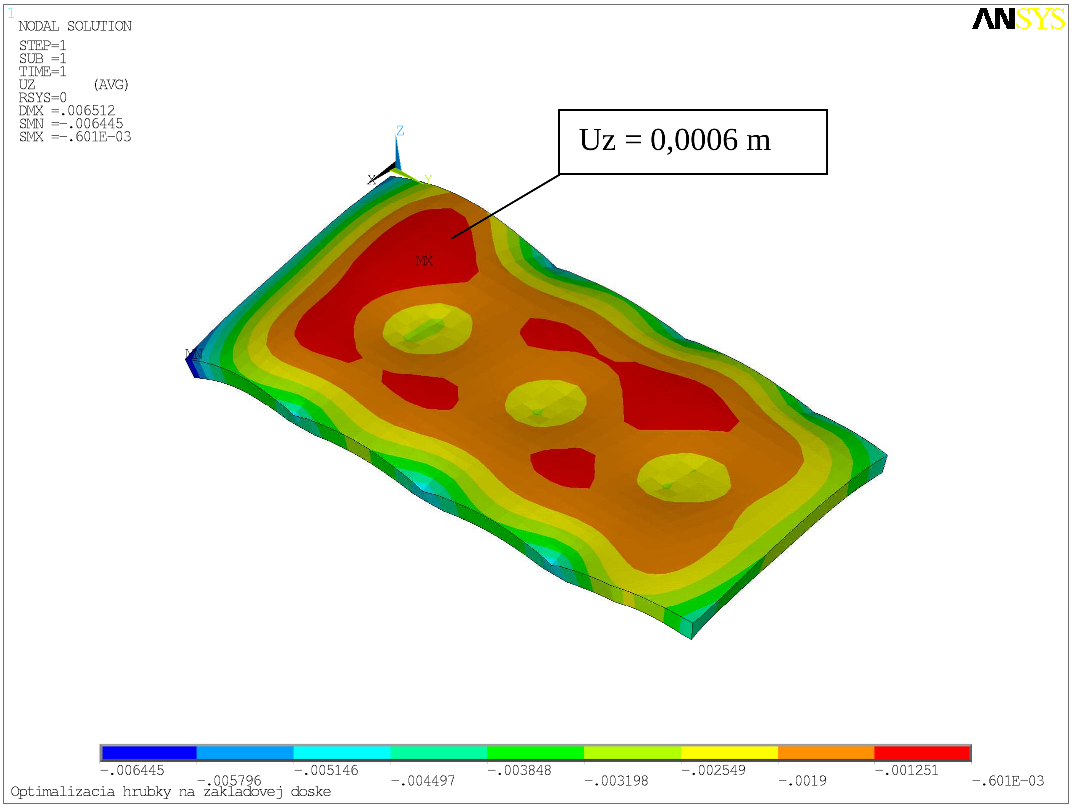

Obrázok 3 Zvislé posuny v smere z

- Modelovanie podložia je možné robiť aj pomocou polpriestoru, priradí sa mu modul pružnosti zeminy a vytvoria sa pevné prepojenia (couplingy), teda na doske a podloží sa v bodoch pod sebou priradia rovnaké zvislé deformácie uz.

- Iný spôsob modelovania podložia je pomocou kontaktných prvkov CONTA 173 a TARGE 170.
- Shell63 – prvok má priamo zabudované zadávanie podložia.
- Pomocou prvkov LINK11, ktorým sa priradia vlastnosti pružiny k.
- Iné.

V tomto prípade, pri modelovaní základovej konštrukcie boli použité prvky SOLID185 pre modelovanie dosky a pre modelovanie podložia prvky SURF154 s tuhosťou podložia. Prvok SOLID185 sa vyberal kvôli optimalizačnej procedúre (výhodný pre optimalizáciu objemu). Optimalizácia základovej dosky je prevedená na statickom modeli uvedenom na Obrázok 1.

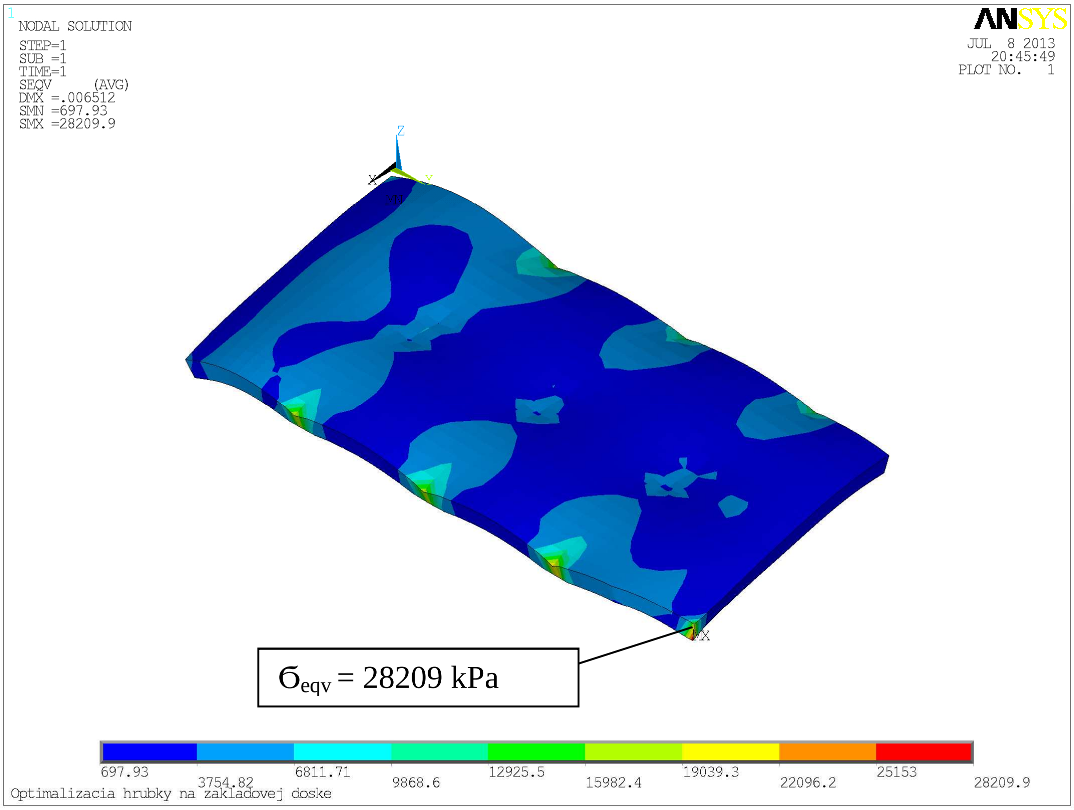

Obrázok 4 Priebeh Von Misesove napätia

Optimalizácia je riešená programom Ansys, minimalizoval sa objem základovej konštrukcie a to v jednotlivých hrúbkach ako je to dané na Obrázok 1 a to v pozíciách H.

Hrúbka dosky v jednotlivých bodoch označených písmenom H sa menila od 0.5 m do 1.5 m, pričom napr. v bodoch označených H4 bola rovnaká hrúbka. Ako obmedzujúce parametre bolo nastavené von Misesove napätie stanovené na 25 MPa.

Pre optimalizáciu sa použila metóda prvého ráda (First order method), ktorá používa pri výpočte aj prvú deriváciu funkcie. Počet cyklov bol stanovený na 16. Po optimalizačnej procedúre, ktorá využíva aj statickú analýzu bol vybratý optimalizačný návrh 16.

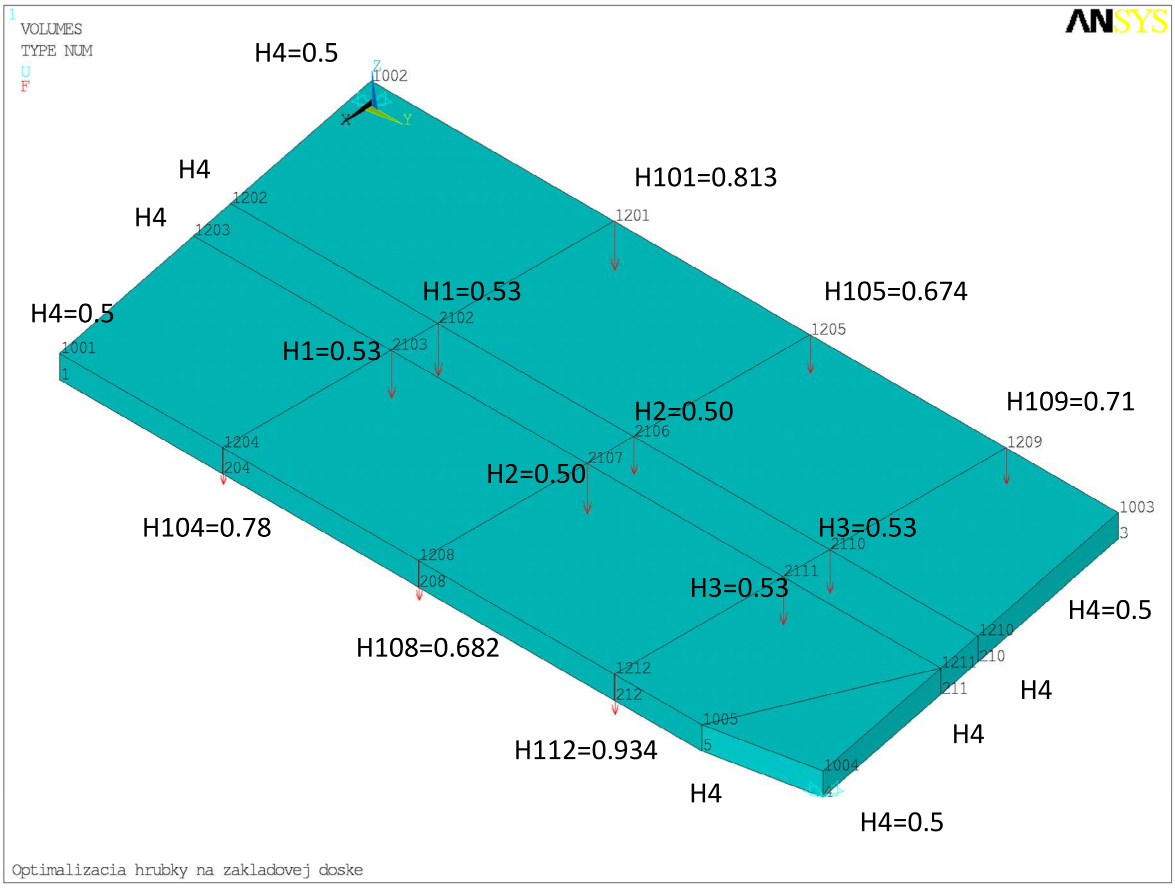

Obrázok 5 Výsledný návrh hrúbok v desiatich optimalizovaných bodoch – návrh 1

Tabuľka 1 Tabuľka výsledných hrúbok

parameter	označenie	Návrh 1/set 16	Návrh 2/set 19
STRS – napätie /kPa/	SV	24755	24939
DEFL – priehyb /m/	SV	$7.866\ e^{-3}$	$7.723\ e^{-3}$
H1– hrúbka /m/	DV	0.530	0.500
H2	DV	0.500	0.509
H3	DV	0.532	0.500
H4	DV	0.500	0.500
H6	DV	0.500	0.723
H7	DV	0.500	0.675
H8	DV	0.500	0.712
H9	DV	0.500	0.774
H101	DV	0.814	0.866
H104	DV	0.780	0.814
H105	DV	0.674	0.578
H108	DV	0.682	0.682
H109	DV	0.709	v633
H112	DV	0.934	0.907
TVOL -objem	OBJ	303.03	306.22

Výsledný návrh hrúbok je zobrazený na Obrázok 4 a je spracovaný aj v Tabuľke 1. Tá istá doska bola optimalizovaná na max. von Misesovo napätie 25 MPa, ale oproti optimalizačnej analýze na Obrázok 4 pribudli ďalšie 4 hrúbky v mieste mimo zaťaženia a výpočet prebehol pre 14 optimalizačných hrúbok (Obrázok 6).

Najlepšie bolo vytvorené riešenie v 19 iteračnom kroku. Výsledky sú spracované v Tabuľka **1** a na Obrázku 6.

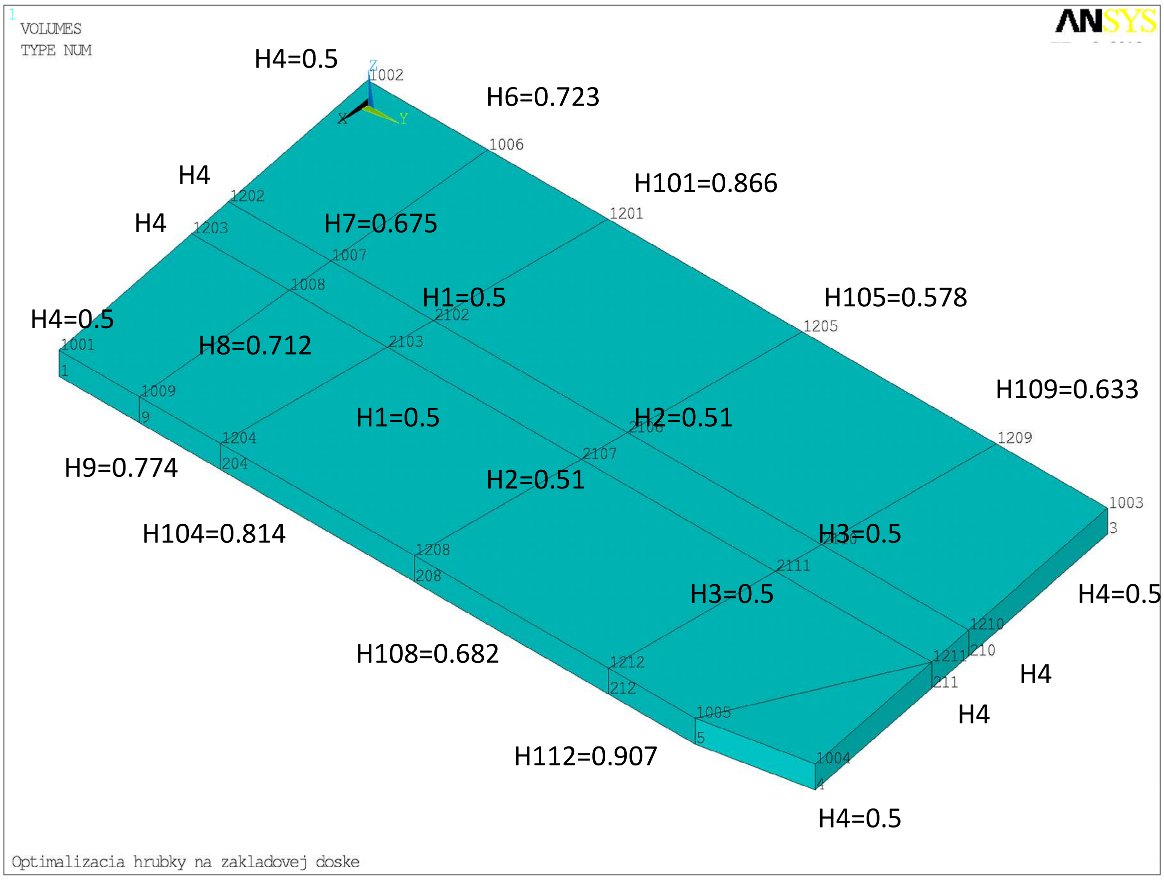

Obrázok 6 Výsledný návrh hrúbok v štrnástich optimalizovaných bodoch – návrh 2

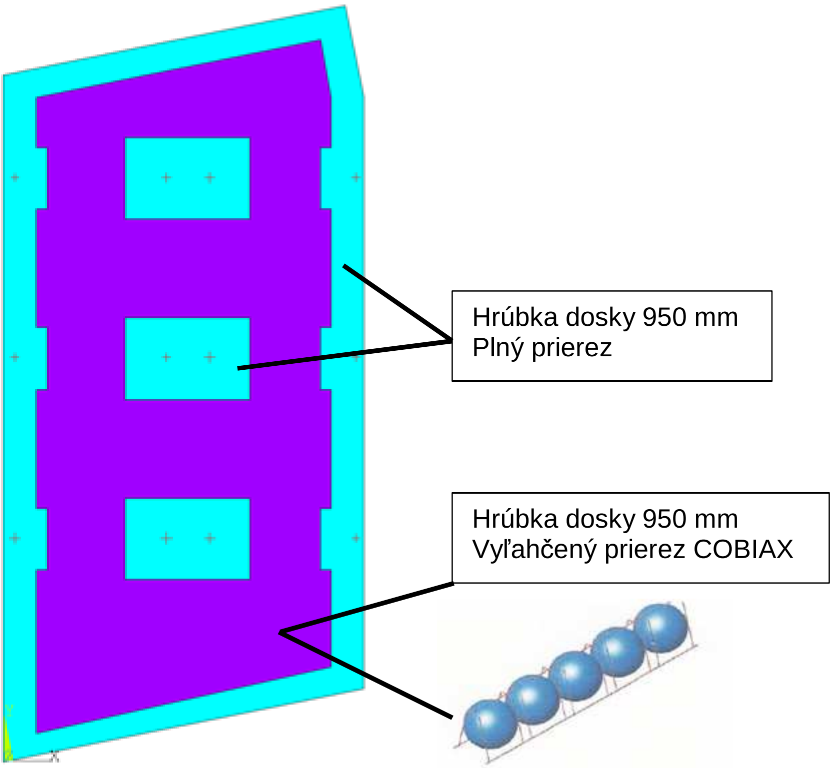

Obrázok 7 Výsledný návrh hrúbky dosky navrhnutý projektantom

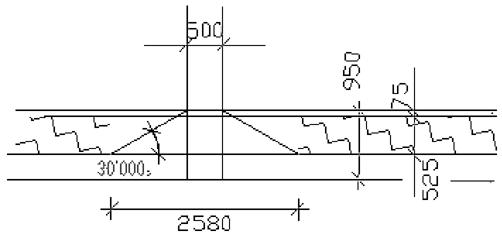

Obrázok 8 Rez základovou doskou navrhnutou projektantom

Hrúbka dosky je 950 mm pozostáva z dvoch vrstiev (Obrázok 7). Prvá vrstva hr. 350 mm je vybetónovaná skôr. Na túto sa položia gule Cobiax priemeru ϕ = 450 mm, čím sa vytvorí druhá vrstva hrúbky 600 mm. V oblasti blízko stĺpov je doska plná (Obrázok 8).

4 Záver

Záverom môžeme povedať, že ku každej optimalizačnej analýze treba pristupovať citlivo a zhodnotiť každú konštrukciu pred samotnou optimalizáciou. Niekedy nie je možné započítať aj vlastnú tiaž konštrukcie, pretože výpočet diverguje vzhľadom k znižovaniu hrúbky v jednotlivých bodoch. Pri optimalizácii hrúbky dosky na základe objemu, ako obmedzujúcu podmienku môžeme dať okrem napätia napr. aj priehyb, a pod. Takýmito postupmi je možné získať konkrétne návrhy konštrukcií.

Literatúra

FRYDRÝŠEK K., 2006. Nosníky a rámy na pružném podkladu 1, monografie, VŠB-TU Ostrava, pp.463. ISBN 80-248-1244-4

HRUŠTINEC Ľ., 2003. *Analýza spolupôsobenia plošného základu s podložím*. 1.vyd. Bratislava : Nakladateľstvo STU, (Edícia vedeckých prác; Zošit č. 12). 184 s. ISBN 80-227-1957-9

JANČO R., 2013. *MKP v riešení nosníkov a rámov na pružnom podklade*. Bratislava: STU v Bratislave, 109 s. ISBN 978-80-227-3880-4

JENDŽELOVSKÝ N., 2009. Modelovanie základových konštrukcií v MKP. 1.vyd. Bratislava: STU v Bratislave, 94 s. ISBN 978-80-227-3025-9

KOLLÁR P., TVRDÁ K., 2000. Viscoelastic Contact Problems of Plate Strip with Variable Stiffness and of Half-space , Antisymmetric problem. *Building Research Journal*, Volume 48, Nr.1.

MISTRÍKOVÁ Z., JENDŽELOVSKÝ N., 2007. Vplyv modelov podložia na deformáciu a napätosť základovej dosky. *Civil and Enviromental Engineering*. Vol.3., Issue 2 str.139-148

PREKOP Ľ., 2012. *Nelineárna analýza podzemných stien v interakcii s podložím.* - 1.vyd. Bratislava : Nakladateľstvo STU, (Edícia vedeckých prác; Zošit č. 118), 111 s. ISBN 978-80-227-3825-5

Poďakovanie

Článok vznikol za pomoci Grantovej agentúry VEGA v Slovenskej republike č. 1/1186/12.

Kontaktná adresa:

doc. Ing. Katarína Tvrdá, PhD., katarina.tvrda@stuba.sk, Slovak University of Technology, Faculty of Civil Engineering, Department of Structural Mechanics, Radlinského 11, 813 68 Bratislava, Slovakia

EXPERIMENTS WITH the influence of a Magnetic Field on the Speed of Temperature Change

ELIŠKA VLACHOVÁ-HUTOVÁ, KAREL BARTUŠEK, PAVEL FIALA

Department of Theoretical and Experimental Electrical Engineering,
Brno University of Technology, Czech Republic

Abstract: The paper presents the micro/nanoscopic model of a material inserted in a magnetic field. The model accepts the time component of an electromagnetic field from the perspective of the relative motion of systems. The relatively moving systems were derived and tested , Fiala P., 2011, and the influence of the motion on the superposed electromagnetic field was proved to exist already at relative motion speeds in the order of units of ms^{-1}. In micro- and nanoscopic objects such as biological tissues, the effect of an external magnetic field on the growth and behaviour of the biological system needs to be evaluated. We designed the model based on a description using Maxwell's equations of the electromagnetic field, and we also extended the monitored quantities to include the various flux densities; moreover, the time flux density $\tau(t)$ was monitored as a quantity. This quantity was then experimentally examined on the physical problem of the speed of heating a defined volume of a homogeneous material in relation to the magnitude and type of the surrounding magnetic field. Experiments were conducted with growth properties of simple biological samples in pre-set external magnetic fields

Keywords: Tissue, external magnetic field, time flux density

1 Introduction

When the temperature in animal cells and organisms containing water drops below 0±C, the water will freeze, resulting in the death of the living structures. Experiments performed on living organisms show that a magnetic field reduces the effects of hypothermia affecting the cells of these living organisms and decreases the mortality in the cells. This fact is caused by a large number of influences, which include the effect of an external magnetic field, its form, and distribution over the space in which the microscopically conceived system is located. Due to the effect of the external magnetic field, the hypothetical particles of the model of the system (a homogeneous material, a heterogeneous structure – biological units – a cell,...) change their dynamics, thus changing the entire microscopically interpreted system.

This paper analyzes the influence of a magnetic field on inanimate objects. Using physical parameters, we created a mathematical model which describes the rate of temperature change in the defined material sample. Experimental measurement of the temperature change of a copper sensor in a stationary homogeneous and gradient magnetic field was performed. Up to 10 times, the sample was cooled down to the nitrogen boiling point (-195:80±C to 77.35 K); at the pre-selected time, the sample was then removed and placed in an area where it was heated to the temperature of -20±C. Using the measuring centre and 4 temperature sensors (2 sensors measuring the temperature of the sample and 2 others for the measurement of the ambient temperature), we recorded the temperature change in the sample and the time required to heat it. This experiment was repeated in the presence of two magnetic fields. The results of the experiment were consistent with the mathematical model and contribute to the description of physical processes during the cooling of the biological tissues.

2 MODEL: the electromagnetic field and particles

For a model with distributed parameters of the electromagnetic field, it is possible to use partial differential equations based on the theory of the electromagnetic field to formulate a coupled model with concentrated parameters (in our case, particles). The model scale at the level of nanometers was also determined using the partial differential equations. The forces acting on a moving electric charge in the electromagnetic field can be expressed by means of the formula

$$f_{\mathrm{e}} = \rho\left(\boldsymbol{E}+\boldsymbol{v}\times\boldsymbol{B}\right) \text{ in } \Omega, \tag{1}$$

where $\boldsymbol{B}$ is the magnetic flux density vector in the space of a moving electrically charged particle with the volume density ρ, $\boldsymbol{v}$ is the mean velocity of the particle, $\boldsymbol{v}=\mathrm{d}\boldsymbol{s}/\mathrm{d}t$, $\boldsymbol{s}$ is the position vector from the beginning of the coordinate system o, t is the time, $\boldsymbol{E}$ is the electric intensity vector, and Ω is the definition region of the independent variables and functions. Then the specific force acting on the moving electrically charged particles with the charge q_{e}, number N_{e}, and – in the monitored area – volume V is

$$\int_0^\Omega \frac{f_{\mathrm{e}}}{q_{\mathrm{e}}}\mathrm{d}V = \left(\boldsymbol{E}+\boldsymbol{v}\times\boldsymbol{B}\right) \text{ in } \Omega. \tag{2}$$

For the quantum mechanical model described by the concentrated parameters, this force will initiate a change of the charged particle energy W_{e}, thus causing a change of particle oscillation frequency ω. The process can be written in the form

$$\Delta\omega_0 = \frac{\partial\omega}{\partial W_{\mathrm{e}}}\Delta W_{\mathrm{e}}\,, \tag{3}$$

where ω_0 is the oscillation frequency of the electrically charged particle, $\Delta\omega_0$ is the change of the particle oscillation frequency, ΔW_{e} is the change of the energy of the electrically charged particle. The change of the oscillation frequency of the electrically charged particle can be directed upwards in the damping of the electric charge movement or downwards during its acceleration. The dependence of an electrically charged particle frequency on the steady-state values of the electromagnetic field can be expressed as

$$\omega_0 \approx \sqrt{\frac{\left|q_{\mathrm{e}}\left(\boldsymbol{E}+\boldsymbol{v}\times\boldsymbol{B}\right)\right|}{m_{\mathrm{e}}s}}\,, \tag{4}$$

where s is the characteristic mean distance of the oscillation of a particle with the electric charge q_{e} which moves at a steady-state velocity $\boldsymbol{v}$, m_{e} is the mass of an electrically charged particle in the magnetic field with magnetic flux density $\boldsymbol{B}$. The numerical model in Ω is based on the formulation of the electromagnetic field equations for the quantities of the intensities and inductions

$$rot\,\boldsymbol{E} = -\frac{\partial\boldsymbol{B}}{\partial t} + rot\left(\boldsymbol{v}\times\boldsymbol{B}\right)\cdot \quad rot\,\boldsymbol{H} = \boldsymbol{J} + \frac{\partial\boldsymbol{D}}{\partial t} + rot\left(\boldsymbol{v}\times\boldsymbol{D}\right) \tag{5}$$

$$div\,\boldsymbol{B} = \boldsymbol{0}\ ,\ div\,\boldsymbol{D} = \rho\ , \tag{6}$$

where $\boldsymbol{H}$ is the magnetic field intensity vector, $\boldsymbol{J}$ the current density vector, and $\boldsymbol{D}$ the electric flux density vector. Respecting the continuity equation

$$div\,\boldsymbol{J}_T = -\frac{\partial\rho}{\partial t} \text{ where } \boldsymbol{J}_T = \boldsymbol{J}+\rho\boldsymbol{v}+\mathrm{j}c\rho\boldsymbol{u}_{\mathrm{t}}\,, \tag{7}$$

where j is the symbol of the imaginary component of the quantity complex shape and c is the velocity of light module in the vacuum, the above-written formulas (5) will assume the form

$$rot\,\boldsymbol{E}=-\frac{\partial\boldsymbol{B}}{\partial t}+rot\left(\boldsymbol{v}\times\boldsymbol{B}\right)-\frac{1}{\gamma}rot\left(\rho\boldsymbol{v}+\mathrm{j}c\rho\boldsymbol{u}_t+\boldsymbol{J}\right),$$

$$rot\,\boldsymbol{H}=\gamma\boldsymbol{E}+\rho\boldsymbol{v}+\gamma\left(\boldsymbol{v}\times\boldsymbol{B}\right)+\mathrm{j}c\rho\boldsymbol{u}_t+\frac{\partial\boldsymbol{D}}{\partial t}+rot\left(\boldsymbol{v}\times\boldsymbol{D}\right). \quad (8)$$

Here, γ is the conductivity of the environment from the macroscopic point of view. After connecting the macroscopic concept of the EMHD model with the microscopic approach, the coupling with the moving particle and its dynamics will manifest itself in the current flux $\boldsymbol{J}_\mathrm{T}$ from the expression (7):

$$\boldsymbol{J}_\mathrm{T}=\gamma\boldsymbol{E}+\rho\boldsymbol{v}+\mathrm{j}c\rho\mathbf{u}_t+\frac{\gamma}{q_e}\left(\frac{m_e\mathrm{d}\boldsymbol{v}}{\mathrm{d}t}+l\boldsymbol{v}+k\int_t\boldsymbol{v}\mathrm{d}t\right), \quad (9)$$

where m_e is the quantity of the model with concentrated parameters – the particle mass which is given by the formula

$$m_e=m_0\left(1-\frac{v^2}{c^2}\right)^{-\frac{1}{2}}, \quad (10)$$

where l is the damping coefficient, and k is the coefficient of stiffness of the ambient environment. The material relations for the macroscopic part of the model are represented by the expressions

$$\boldsymbol{B}=\mu_0\mu_r\boldsymbol{H}\ ,\ \boldsymbol{D}=\varepsilon_0\varepsilon_r\boldsymbol{E}\ , \quad (11)$$

where the indexes of the quantities of the permeabilities and permittivities r denote the quantity of the relative value and the 0 value of the quantity for the vacuum. The linkage between the macroscopic and the microscopic (dynamics of particles in the electromagnetic field) parts of the model is described by the relations of force action on the individual electrically charged particles in the electromagnetic field, and the effect is respected of the movement of the electrically charged particles on the surrounding electromagnetic field from (8).

$$rot\,\boldsymbol{E}=-\frac{\partial\boldsymbol{B}}{\partial t}+rot\left(\boldsymbol{v}\times\boldsymbol{B}\right)-\frac{1}{\gamma}rot\left(\rho\boldsymbol{v}+\mathrm{j}c\rho\boldsymbol{u}_t+\boldsymbol{J}+\frac{\gamma}{q_e}\left(\frac{m_e\mathrm{d}\boldsymbol{v}}{\mathrm{d}t}+l\,\boldsymbol{v}+k\int_t\boldsymbol{v}\,\mathrm{d}t\right)\right)$$

$$rot\,\boldsymbol{H}=\gamma\boldsymbol{E}+\rho\boldsymbol{v}+\gamma\left(\boldsymbol{v}\times\boldsymbol{B}\right)+\frac{\gamma}{q_e}\left(\frac{m_e\mathrm{d}\boldsymbol{v}}{\mathrm{d}t}+l\,\boldsymbol{v}+k\int_t\boldsymbol{v}\,\mathrm{d}t\right)+\mathrm{j}c\rho\boldsymbol{u}_t+\frac{\partial\boldsymbol{D}}{\partial t}+rot\left(\boldsymbol{v}\times\boldsymbol{D}\right). \quad (12)$$

The coupling of both models is formulated using equation(9) and the formula

$$q_e\left(\boldsymbol{E}+\boldsymbol{v}\times\boldsymbol{B}\right)+\frac{q_e}{\gamma}\left(\rho\boldsymbol{v}+\mathrm{j}c\rho\mathbf{u}_t-\frac{\partial(\varepsilon\boldsymbol{E})}{\partial t}\right)=\frac{m_e\mathrm{d}\boldsymbol{v}}{\mathrm{d}t}+l\boldsymbol{v}+k\int_t\boldsymbol{v}\mathrm{d}t\,. \quad (13)$$

The effect of the behaviour of the macroscopic model describing the mass with the quantum mechanical model of elements of the system can be observed using the fluxes of quantities. The known quantities are magnetic flux ϕ, current flux I, and electric flux having the magnitude q:

$$\phi=\iint_\Gamma\boldsymbol{B}\cdot d\boldsymbol{S}\ ,\ I=\iint_\Gamma\boldsymbol{J}\cdot d\boldsymbol{S}\ ,\ q=\iint_\Gamma\boldsymbol{D}\cdot d\boldsymbol{S}\ , \quad (14)$$

where $\boldsymbol{S}$ is the vector of the oriented boundary (in a 3D model of the plane), and Γ is the boundary of the area Ω , in which the flux is evaluated. If there is a moving element of the system in the model with a scale difference expressed in orders, it is easier to describe the state and effect of the superposed electromagnetic field by expressing the time flux density τ. The time flux can be different or inhomogeneous in parts of the area Ω. It is then possible to write

$$t = \iint_{\Gamma} \tau \cdot d\boldsymbol{S} \cdot \qquad (15)$$

After expanding the expression with the time flux density for the Cartesian coordinate system o, x, y, z, we have

$$t = \iint_{\Gamma} \frac{\boldsymbol{u}_z}{dz} \frac{1}{v_z(t)} \cdot (d\,\boldsymbol{x} \times d\,\boldsymbol{y}), \qquad (16)$$

where $\boldsymbol{v}(t)$ is the instantaneous velocity vector, $v(t)$ is the module of the instantaneous velocity vector, and $d\boldsymbol{x}$, $d\boldsymbol{y}$, $d\boldsymbol{z}$ are the vectors of differences in the coordinate system. Then the time flux density in the direction of the z-axis is

$$\tau_z = \frac{1}{v_z(t)dz} \boldsymbol{u}_z, \qquad (17)$$

where $\boldsymbol{u}_z$ is the base vector of the applicable coordinate system. To respect the other directions, we can write

$$\tau = \frac{1}{v_x(t)dx} \boldsymbol{u}_x + \frac{1}{v_y(t)dy} \boldsymbol{u}_y + \frac{1}{v_z(t)dz} \boldsymbol{u}_z, \qquad (18)$$

where $\boldsymbol{u}_x$, $\boldsymbol{u}_y$ are the base vectors of the coordinate system. Time density depends on the instantaneous velocity of the particle motion in the quantum mechanical model and on the element of length. If there occur regions with different instantaneous velocities at elementary sections within the area Ω of the system described by the quantum mechanical model (atoms, molecules etc.), then the space is characterized by an uneven time flux density according to the expression (18). The relation between the time flux density τ and the quantities of the electromagnetic field of the model of the system (12) is evident. The impact of a specific force on the moving electric charge qe can be defined according to the above-shown formulas (1) and (13). To evaluate the effect of the properties of the distribution of the magnetic field having a magnetic flux density $\boldsymbol{B}$ and to assess the influence of the electric charge q_e moving at the instantaneous velocity $\boldsymbol{v}$ in this field, the expressions (1), (2) for the area Ω can be formulated as

$$\boldsymbol{E} = q_e(\boldsymbol{v} \times \boldsymbol{B}) \text{ in } \Omega. \qquad (19)$$

Then, for the motion of the electrically charged particle along the element of the closed curve $d\ell$ (according to the microscopic interpretation), it is possible to rewrite the above formula (19) as

$\boldsymbol{E}\,d\ell = q_e(\boldsymbol{v}\,d\ell \times \boldsymbol{B})$ in Ω, and after modification from the formulas (17), (18) we have

$$\frac{\boldsymbol{E}}{q_e} d\ell = (\tau^{-1} \times \boldsymbol{B}) \text{ in } \Omega. \qquad (20)$$

If an electrically charged particle moves in the magnetic field having a magnetic flux density $\boldsymbol{B}$, and if the dimensions of the area Ω are multiply larger than the electrically charged particle or groups of particles, it is necessary to consider the questions of how the motion of the particle is influenced and what the observable oscillation changes are, namely the time flux density changes in parts of the area Ω. According to formula (3), respecting the conservation of the external energies (heat; motion), it is possible to say that the properties of the charged particles depend on the characteristics of the external magnetic field. There are three basic variants of the state of the macroscopically interpreted distribution of the external magnetic field having a magnetic flux density $\boldsymbol{B}$:

1. The external magnetic field exhibits low values of magnetic flux density $\boldsymbol{B}$, and its distribution is homogeneous on the microscopic scale. We then have B=min, $\partial B_x/\partial x = 0$, $\partial B_y/\partial y = 0$, $\partial B_z/\partial z = 0$ or, in at least one direction of the coordinate system and respecting the curl character of the field, formula (6).

2. The external magnetic field exhibits higher values of magnetic flux density $\boldsymbol{B}$, and its distribution is homogeneous on the microscopic scale. Then we have B=max, $\partial B_x/\partial x=0$, $\partial B_y/\partial y=0$, $\partial B_z/\partial z=0$ or, in at least one direction of the coordinate system and respecting the curl character of the field, formula (6).

3. The external magnetic field in inhomogeneous on the macroscopic scale. Then we have $\partial B_x/\partial x\neq 0$, $\partial B_y/\partial y\neq 0$, $\partial B_z/\partial z\neq 0$ and, respecting the curl character of the field, (6).

3 Numerical model analysis

We performed a simple analysis of FeNdB permanent magnet blocks having the dimensions of 15x10x40 mm, surface magnetic flux density of B_r=1.2 T, and intensity of H_{co}=850 kA/m. The analysis was carried out with the ANSYS FEM tool and solved as a stationary electromagnetic task.

Fig. 1 shows a configuration with the minimum and, in a certain part, homogeneous magnetic field. The setup for an inhomogeneous magnetic field with a high gradient distribution is presented in Fig. 2.

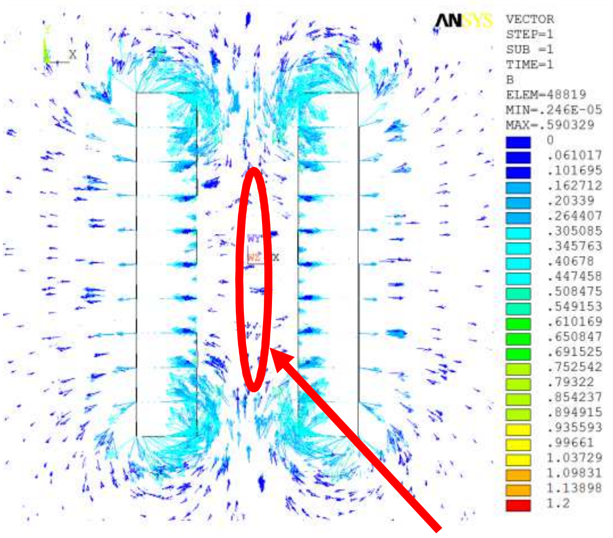

Fig. 1. Permanent magnet configuration: a weakly homogeneous field.

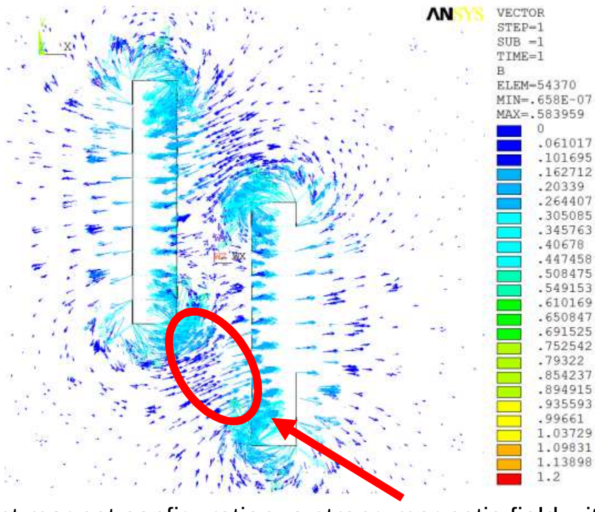

Fig. 2. Permanent magnet configuration: a strong magnetic field with a high gradient.

A similar analysis related to a different type of FeNdB permanent magnet blocks having the dimensions of 24x5x25 mm, surface magnetic flux density of B_r=1.02 T, and intensity of H_{co}=720 kA/m is shown in Fig.3, Fig. 4 and Fig.5.

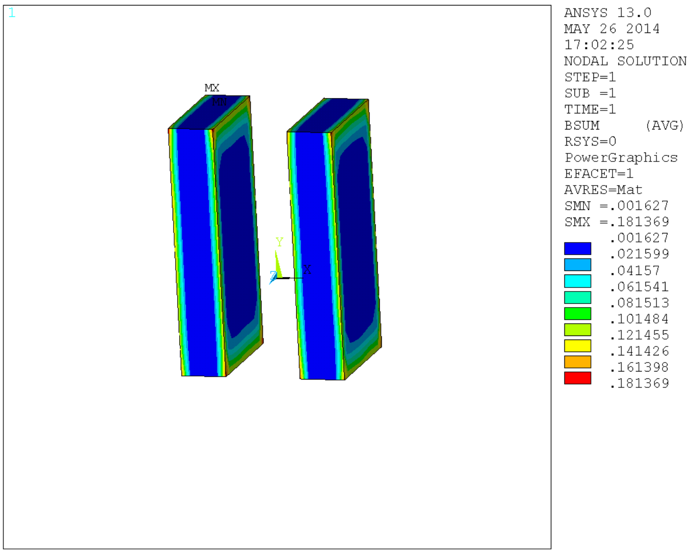

Fig. 3. Permanent magnet configuration: a weakly homogeneous field. The parameters are as follows: surface magnetic flux density B_r=1.02 T, and intensity H_{co}=720 kA/m; distribution of magnetic flux density B[T].

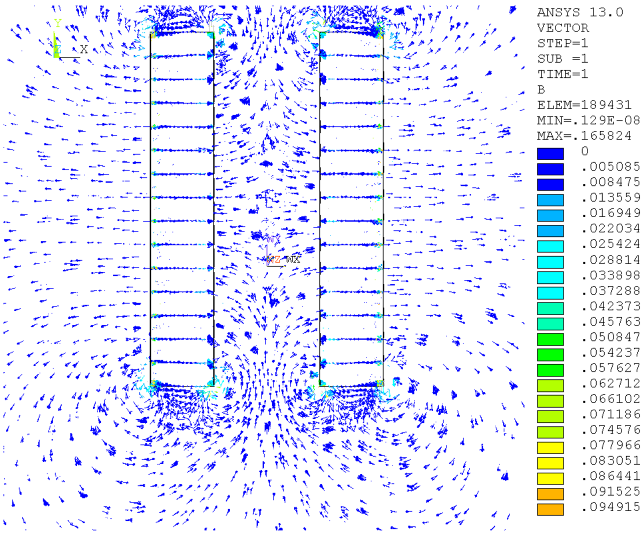

Fig. 4. Permanent magnet configuration: a weakly homogeneous field. The parameters are as follows: surface magnetic flux density B_r=1.02 T, and intensity H_{co}=720 kA/m; distribution of vector magnetic flux density B[T].

During the experiment, an element evaluating the observed macroscopic behaviour of mass was inserted in the red-marked areas.

4 Expriments

The verification of the difference in the properties of the microscopic model of mass under the pre-defined condition of the external magnetic field was performed using a copper element having the dimensions of 10x10x10 mm. We used FeNdB permanent magnet blocks with the following parameters: dimensions of 15x10x40 mm; surface magnetic flux density of B_r=1.2 T; and intensity of H_{co}=850 kA/m.

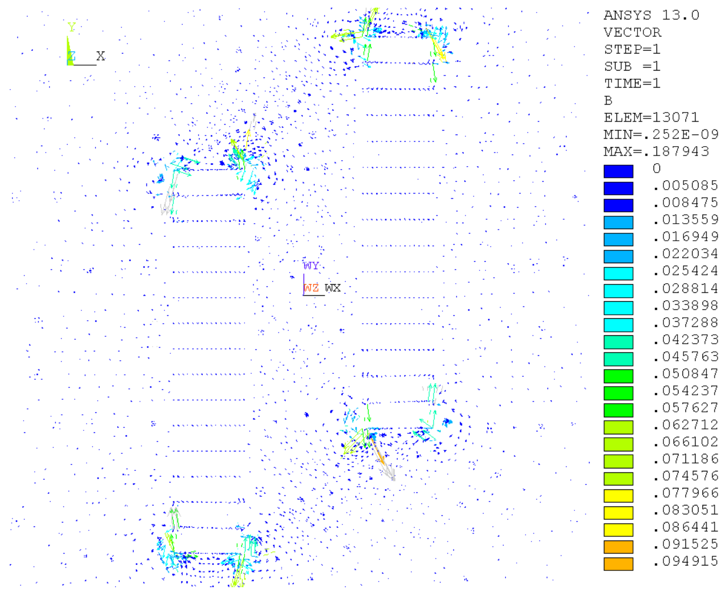

Fig. 5. Permanent magnet configuration: a magnetic field with a high gradient. The parameters are as follows: surface magnetic flux density B_r=1.02 T, and intensity H_{co}=720 kA/m; distribution of vector magnetic flux density B[T].

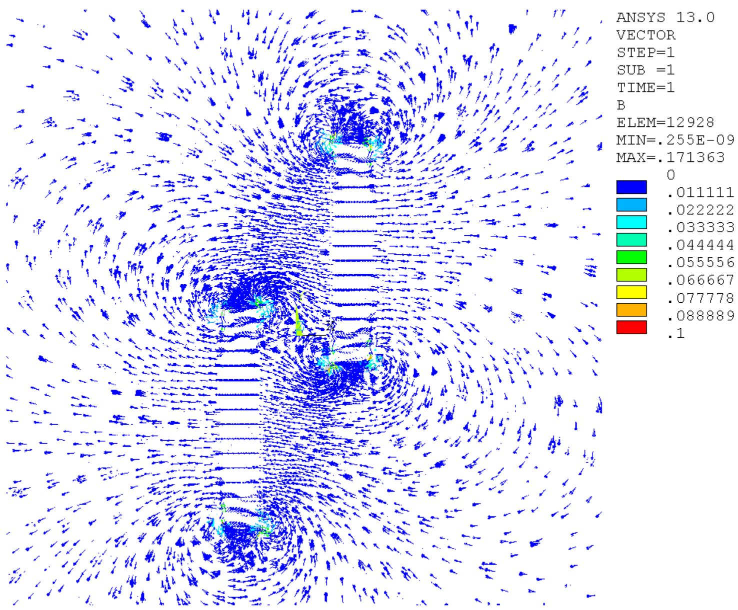

Fig. 6. Permanent magnet configuration: a strong magnetic field with a high gradient. The parameters are as follows: surface magnetic flux density B_r=1.02 T, and intensity H_{co}=720 kA/m; distribution of vector magnetic flux density B[T].

The copper element was cooled down to -193°C and then heated at the ambient temperature of 20°C. The heating period was measured repeatedly, starting from -180°C and proceeding to -20°C. These limits had been chosen with respect to suppressing the systematic measurement error in the experiment; the actual experiment is shown in Fig. 7. The aim of the experiment was to compare three different settings of the external magnetic field according to the section 2 above and to indicate their impact on the speed of heating. If, in any of the cases, under repeated measurement in the given space there occurs a decrease of the statistically significant deviation of the heating period with respect to the reference measurement, it is possible to assume according to formula (16) that a lower time density was reached in the sample than in the reference measurement.

Conversely, with a significantly longer heating time there occurs an increase of the time density in the measured sample as compared to the reference measurement.

Fig. 7. Configuration of the permanent magnets during the experiment

5 Comparison of the analysis

It follows from the conducted experiments that, in a strong magnetic field with a high gradient character of the magnetic flux density ***B*** , d*B/dx*200 Tm^{-1} is the lowest density of the time flux τ (setting 3, section 2). A higher value of the time flux density τ can be found in a magnetic homogeneous field with a low magnetic flux density ***B***, *B*2µT (setting 1, section 2), and the highest value is detected in a homogeneous magnetic field with the magnitude of the Earth's field -*B*50µT. (setting 2, section 2) .

6 Conclusion

A model of the macroscopic setting of a magnetic field was formulated, and the time flux density τ was observed within the microscopic concept of the quantum mechanical model of mass. Time flux density is a quantity introduced to monitor the influence of an external magnetic field on the behaviour of elements of mass or their groups at the level of atoms. The experiment showed a simple task of evaluating the behaviour of anorganic mass during changes in the energy of the sample. The aim of the research was to prepare the already built-up model for use in classifying the behaviour of simple biological materials in an externally defined magnetic field.

Tab. 1: Data of the comparison of the different settings

Homogeneous field		
Measurment no.	min	s
10	0:06:20	380
9	0:06:11	390
8	0:06:12	390
7	0:06:10	376
6	0:06:21	373
5	0:06:18	371
4	0:06:12	366
3	0:06:14	354

Gradient field		
Measurment no.	min	s
10	0:06:15	375
9	0:05:21	321
8	0:05:02	302
7	0:05:10	310
6	0:05:15	315
5	0:05:07	307
4	0:04:47	287
3	0:04:43	283

No external field		
Measurment no.	min	s
10	0:06:30	390
9	0:06:16	376
8	0:06:13	373
7	0:06:11	371
6	0:06:06	366
5	0:05:54	354
4	0:05:50	350
3	0:06:25	385

2	0:06:24	350
1	0:06:16	385
Average:	0:06:16	373,5
Median:	0:06:15	374,5
Standard deviation:	5,25E-05	13,11678
Maximum:	0:06:24	390
Minimum:	0:06:10	350

2	0:04:02	242
1	0:03:44	224
Average:	0:04:57	296,6
Median:	0:05:02	304,5
Standard deviation:	4,22E-04	39,90789
Maximum:	0:06:15	375
Minimum:	0:03:44	224

2	0:06:25	385
1	0:06:16	376
Average:	0:06:13	372,6
Median:	0:06:13	374,5
Standard deviation:	1,31E-04	12,39516
Maximum:	0:06:30	390
Minimum:	0:05:50	350

Acknowledgement - The research described in the paper was financially supported by a grant of the Czech Science Foundation, no. GACR 13-09086S, a project of the BUT Grant Agency, no. FEKT-S-14-2545/2014, and projects from the Education for Competitiveness Operative Programme, nos. CZ.1.07.2.3.00.20.0175 and CZ.1.07/2.3.00/30.0005

REFERENCES

Fiala, P Szabo, Z Friedl, M., 2011, EMHD Models Respecting Relativistic Processes of Trivial Geometries, Progress In Electromagnetics Research Symposium Proceedings, Suzhou, China, Sept. 12-16.

Ing. Eliška Vlachová-Hutová, Department of Theoretical and Experimental Electrical Engineering, Brno University of Technology, Technická 3082/12, 616 00 Brno, Czech Republic

Prof. Ing. Karel Bartušek, DrSc., Department of Theoretical and Experimental Electrical Engineering,Brno University of Technology, Technická 3082/12, 616 00 Brno, Czech Republic

doc. Ing. Pavel Fiala , Ph.D, Department of Theoretical and Experimental Electrical Engineering,Brno University of Technology, Technická 3082/12, 616 00 Brno, Czech Republic

MODELOVANIE VYĽAHČENÝCH DOSIEK V PROGRAME ANSYS

NORBERT JENDŽELOVSKÝ, KRISTÍNA VRÁBLOVÁ

Stavebná fakulta STU, Katedra stavebnej mechaniky, Radlinského 11, 813 68 Bratislava
Slovenská republika

Abstract: This article deals with modeling of biaxial voided flat slabs in ANSYS softwere. Slab have been voided by plastic hollow spheres. Slabs have been modeled by 3D elements SOLID 187. Bending moments and z-direction displacements of biaxial voided slab and solid slab have been compared.

Keywords: biaxial voided slab, sphere voiders, FEM modeling,ANSYS

1 Úvod

Stropné konštrukcie sú neoddeliteľnou súčasťou nosných konštrukcií budov. V súčasnej dobe požiadavky na veľkosti ich rozpätia narastajú a s nimi aj potreba nových a nekonvenčných riešení. Významnú zložku zaťaženia konštrukcií tvorí vlastná tiaž a preto masívne železobetónové dosky pri potrebe veľkých rozpätí nahrádzajú práve vyľahčené dosky. Vyľahčenie stropných konštrukcií má pozitívny vplyv nielen na samotnú konštrukciu stropu, ale aj na celú stavbu, pretože znižuje jej hmotnosť, znižuje aj náklady na konštrukciu zvislých nosných konštrukcií a základových konštrukcií.

2 Súčasné typy vyľahčených dosiek

Moderná doba priniesla riešenie obojsmerne vyľahčených stropných dosiek, kde je vyľahčenie realizované plastovými prvkami rôznych tvarov. Medzi hlavné výhody vyľahčených dosiek patrí:

- Pri približne rovnakej tuhosti dosky jej hmotnosť nižšia o 30%.
- 20% úspora betónu pri nosných prvkoch (stĺpy, základy...)
- Zníženie objemu, alebo úplne vylúčenie použitia prievlakov.
- Umožnenie väčších rozpätí.
- Menšie priehyby.
- Menšie zotrvačné sily pri seizmickej analýze.

V tomto článku sa venujeme doskám obojstranne vyľahčenými plastovými guľami, systém Bubbledeck a Cobiax. Medzi systémy, ktoré umožňujú vyľahčenia aj inými tvarmi plastových prvkov, patria systémy BeePlate alebo U-Boot.

BubbleDeck

Táto technológia bola vynájdená v roku 1990 Jorgenom Breuningom. Duté plastové gule, resp. elipsoidy, sú uložené medzi spodnú a hornú výstuž dosky, čo vytvára bunkovú štruktúru, správajúcu sa ako plná monolitická doska. Medzí prvé aplikácie BubbleDeck patrí Millennium Tower, 35-poschodová budova v Holandsku dostavaná v roku 2000 (Obr.1).

Obrázok 29 - Millennium Tower, Holandsko

BubbleDeck sa dodáva v troch variantoch: filigránová doska s poukladanými plastovými guľami, ktoré sa už iba zalievajú bez potreby spodného debnenia. Ďalej ako výstužné koše s plastovými guľami, ktoré sa ukladajú do pripraveného debnenia. Tretí variant je plne prefabrikovaná vyľahčená doska.

Cobiax

Cobiax Technologies je dcérskou spoločnosťou singapurskej spoločnosti Tiong Seng Holdings Limited so sídlom vo Švajčiarsku a pobočkami v Nemecku a Rakúsku. Hlavnou činnosťou skupiny Cobiax je výskum a vývoj bi-axiálnych plochých dutých dosiek, hodnotové inžinierstvo a predaj produktov pre medzinárodné projekty. Podobne ako pri systéme BubbleDeck, komponenty Cobiax sú plastové duté gule, resp. rotačné elipsoidy, ktoré vytvoria prázdny priestor. Tieto plastové prvky sú umiestnené medzi vrchnú a spodnú vrstvu betónovej dosky a slúžia ako náhrada za, z hľadiska statiky, nepotrebnú časť betónu. (Obr.2)

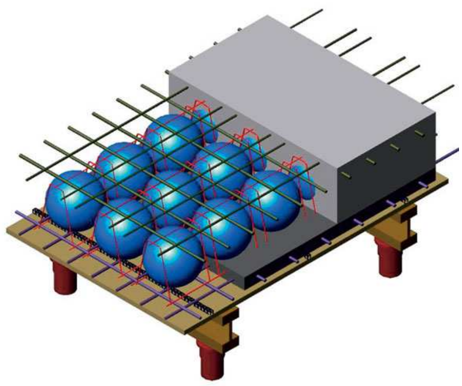

Obrázok 2 - Systém Cobiax

Typy dodávaných vyľahčovacích prvkov, odporúčané hrúbky dosiek a redukcia hmotnosti na štvorcový meter sú uvedené v Tabuľke 1, prevzatej z firemnej literatúry (2).

Tabuľka 1: Typy vyľahčovacích prvkov Cobiax

Typ	Hrúbka dosky	Priemer gule	Redukcia hmotnosti na m2
	mm	mm	kN/m2
CBCM-S-100	200	100	1,30
CBCM-S-180	300	180	1,91
CBCM-E-225	350	225	2,38
CBCM-E-270	400	270	2,68
CBCM-E-315	450	315	3,34
CBCM-E-360	500	360	3,82
CBCM-E-405	550	405	4,29
CBCM-E-450	600	450	4,77

3 Modelovanie vyľahčených dosiek

Modelovanie vyľahčených dosiek je možné dvomi rôznymi spôsobmi. Vyľahčenú dosku môžeme modelovať ako plnú dosku so zníženou tuhosťou a redukovanou vlastnou tiažou, za pomoci plošných doskových konečných prvkov (2D plocha) alebo vytvoriť 3D model dosky priamo s geometrickými tvarmi vyľahčovacích prvkov. Pre naše účely je vhodnejšie modelovať dosku priamo s vyľahčovacími prvami. Pre porovnanie sme vytvorili aj model plnej dosky, bez vyľahčovacích prvkov, s rovnakými rozmermi a okrajovými podmienkami

Parametre modelu

Riešená konštrukcia bola železobetónová doska štvorcového pôdorysu s rozmermi 8x8 m. Hrúbka dosky bola 350 mm a bola vyľahčená prvkami tvaru gule priemeru 225 mm s osovou vzdialenosťou gúľ 250 mm (Obr.3). Okrajové podmienky modelovanej dosky boli na dvoch okrajoch podopretá, t.j. na ľavom okraji zabránené posunom u_x, u_y, u_z a na pravom okraji bolo zabránené posunom u_y a u_z. Druhé dve strany dosky boli nepodoprené. Druhý model bola plná doska, ktorá mala rovnaké rozmery aj okrajové podmienky.

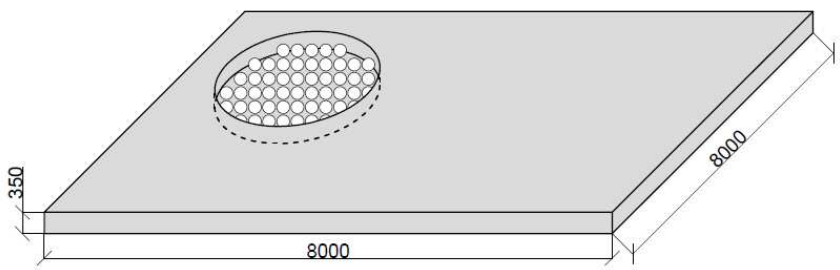

Obrázok 3 - Rozmery dosky

Modelovanie vyľahčenej dosky v programe ANSYS

Na numerické riešenie problému pomocou MKP sme zvolili systém ANSYS. V programe ANSYS sme vytvárali model z 3D konečných prvkov SOLID 187. Model bol vytvorený iba z betónu bez uváženia vystužovacích prvkov tak, že sme zadali materiálové vlastnosti železobetónu C20/25: modul pružnosti E= 30GPa, poissonove číslo ν= 0.2 a objemovú tiaž γ= 24kN/m^3.

Model sme konštruovali vytváraním objemov tak, že sme najskôr vytvorili jeden základný kváder veľkosti 250x250x350 mm, od ktorého sme odčítali objem vyľahčujúceho telesa- gule priemeru 225 mm. Ďalej sme vytvorili hardpointy, presne definované body, ktoré sa využívajú pre meshovanie, pretože sme potrebovali hodnoty napätí a priehybov práve v týchto bodoch dosky. Tento modul (Obr.4) sme vymeshovali z konečných prvkov SOLID 187 a následne kopírovali v dvoch vodorovných smeroch, aby sme vyplnili rozmer dosky 8 x 8m.

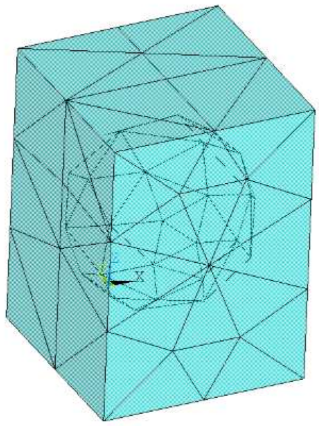

Obrázok 4 - Vymeshovaný modul

Pre správne spolupôsobenie modelu sme museli zjednotiť body s rovnakými súradnicami. Následne sme zadali okrajové podmienky. Dosku sme zaťažovali dvomi zaťažovacími stavmi: vlastnou tiažou a rovnomerným spojitým zaťažením 3 kN/m^2. Ako bolo vyššie spomenuté, vytvorili sme aj jednoduchší model plnej dosky. Na oboch modeloch sme analyzovali výsledky priehybov a normálových napätí. Tieto výsledky sa analyzovali zvlášť pre zaťaženie vlastnou tiažou a zvlášť pre rovnomerné spojité zaťaženie. Výsledky sme analyzovali v reze vedenom stredom dosky od jednej podopretej hrany k druhej. Zaujímali nás výsledky v spodnej časti dosky.

Pre jednoduchosť modelovania dosky v budúcnosti sme si pripravili makro pre parametrické modelovanie dosky. Vo vstupoch stačí zadať: hrúbku dosky, priemer vyľahčovacej gule, rozpätie dosky a osovú vzdialenosť vyľahčovacích prvkov. Následne stačí makro spustiť v príkazovom riadku.

4 Porovnanie priehybov dosky

Výsledky sú rozdelené do 4 skupín: vlastná tiaž plnej dosky (VLT-P), vlastná tiaž vyľahčenej dosky (VLT-V), plná doska zaťažená rovnomerným spojitým zaťažením (Q-P) a vyľahčená doska zaťažená rovnomerný spojitým zaťažením (Q-V).

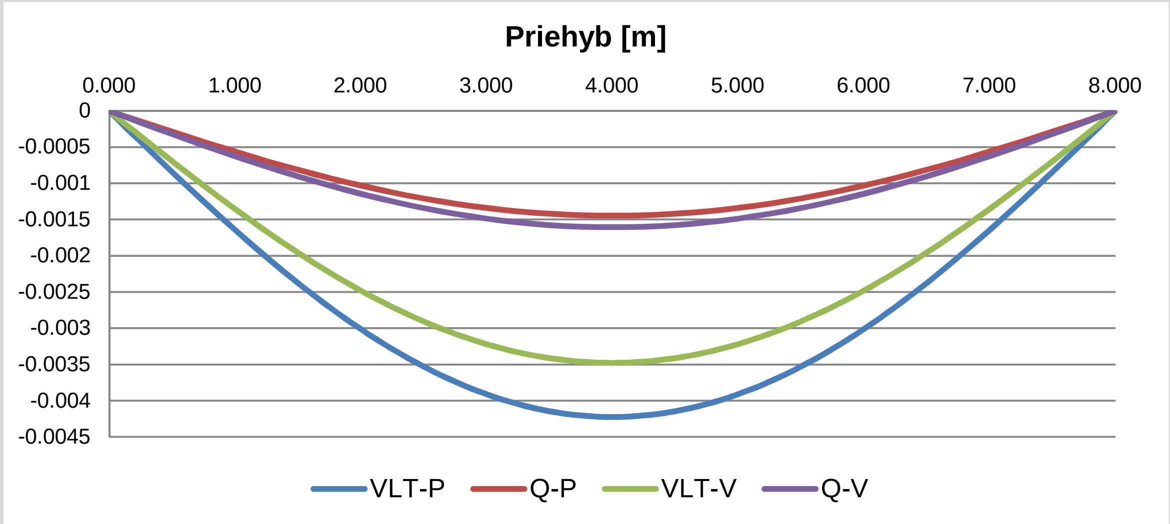

Obrázok 5 - Priehyby dosiek

Z výsledkov zvislých deformácií môžeme vidieť, že ak je spojité zaťaženie iba 3 kN/m^2 rozhodujúce zaťaženie bude tvoriť vlastná tiaž. Priehyb vyľahčenej dosky od vlastnej tiaže bol o 17,67% menší ako pri plnej doske. Pri spojitom zaťažení sa prejavila menšia tuhosť vyľahčenej dosky a priehyb bol väčší o 10,67%. V tomto prípade (spojité zaťaženie 3 kN/m^2 a vlastná tiaž spolu) je úspora v priehyboch vyľahčenej dosky 10,36%.

5 Výsledky ohybových momentov

Pri analýze výsledkov ohybových momentov v doske sme narazili na menší problém, pretože ANSYS pre 3D prvok SOLID 187 takéto výsledky neposkytuje. Vieme však získať hodnoty napätí v jednotlivých bodoch dosky. Keďže napätie počítame zo známeho vzorca teórie pružnosti:

$$\sigma = \frac{M}{I}.z, \tag{1}$$

kde *M*- ohybový moment na doske, *I*- moment zotrvačnosti dosky a *z*- je vzdialenosť od ťažiska. Po úprave vzťahu (1) ohybový moment môžeme vypočítať ako:

$$M = \frac{\sigma}{z}.I. \tag{2}$$

Problém nastáva pri počítaní momentu zotrvačnosti vyľahčenej dosky. Ako sme už popisovali v predchádzajúcej časti, pri meshovaní modulu sme vytvorili hardpointy, tieto hardpointy sme umiestnili na hornú a dolnú podstavu kvádra do ťažiska a stredu hrán. Pre výpočet momentov zotrvačnosti sme vytvorili makro v programe MathCad, kde sme prierez rozdelili, podľa toho, v ktorých miestach poznáme hodnoty napätí a počítali sme so zjednodušenými prierezmi. Do momentu zotrvačnosti prierezu sme započítavali vyšrafované plochy, ktoré sú znázornené na obrázku 6.

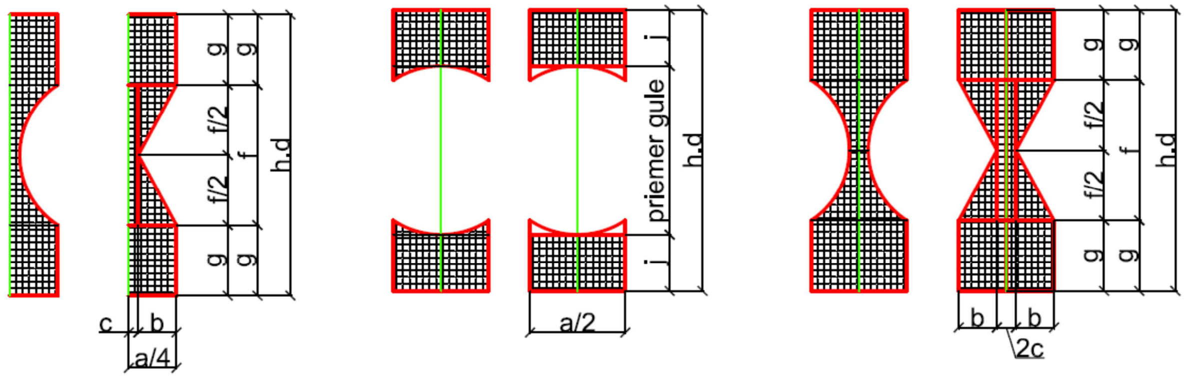

Obrázok 6 - Zjednodušenie prierezu dosky pre výpočet momentov zotrvačnosti

Momenty zotrvačnosti, vypočítané v programe MathCad sme zoradili do tabuľky v programe Excel aj s príslušnými hodnotami normálových napätí, prevzatých z ANSYSu a podľa vzorca (2) sme dopočítali hodnoty ohybových momentov. Vlnovkovitý priebeh ohybových momentov vyľahčenej dosky je zapríčinený pravidelným striedaním sa hodnoty momentu zotrvačnosti v mieste plného prierezu a mieste, kde ju umiestnený vyľahčovací prvok. Pri porovnaní plnej a vyľahčenej dosky môžeme sledovať rovnaký trend ako pri priebehu priehybov, pričom úspora vyľahčenej dosky v porovnaní maximálnych ohybových momentov je 14,12%.

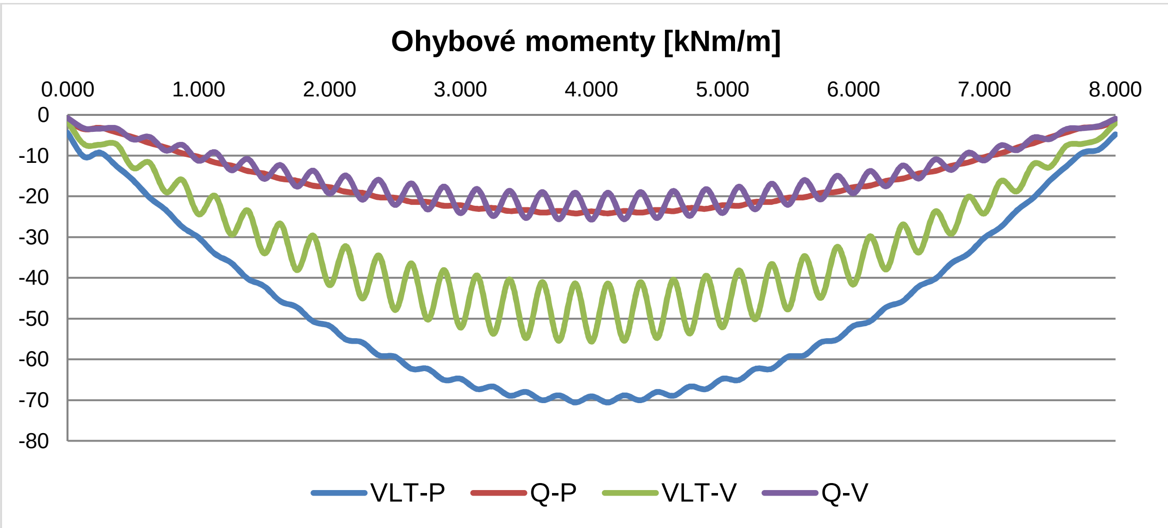

Obrázok 7 – Priebeh ohybových momentov

6 Záver

Podarilo sa nám vytvoriť makro v programe ANSYS pre rýchle vytváranie modelu vyľahčených dosiek, čo nám v budúcnosti značne uľahčí prácu. Taktiež sme vytvorili makro na výpočet ohybových momentov, ktoré sú v praxi nevyhnutné pre návrh výstuže.

V závere sme v tabuľke porovnali hodnoty maximálnych priehybov, napätí a ohybových momentov na oboch doskách. Z tabuľky je zrejmé, že ohybové momenty od rovnomerného spojitého zaťaženia sú takmer zhodné (rozdiel 6 %), čo potvrdzuje, že vyľahčené dosky sú schopné preniesť rovnaké zaťaženie ako plné dosky. Rozdiely v priehyboch sú trochu väčšie, čo je spôsobené menšou tuhosťou vyľahčenej dosky, na druhej strane úspora vyľahčených dosiek je vo vlastnej tiaži.

Tabuľka 2 Porovnanie ohybových momentov, napätí a priehybov plnej a vyľahčenej dosky

		Priehyb	**Napätie**	**Ohybové momenty**
		[m]	[kPa]	[kNm/m]
Plná doska	Vlastná tiaž	-0,00422	3456,3	-70,566
	q= 3 kN/m2	-0,00145	1185,0	-24,194
	Spolu	**-0,00567**	**4641,3**	**-94,760**
Vyľahčená doska	Vlastná tiaž	-0,00348	2811,5	-55,652
	q= 3 kN/m2	-0,00161	1299,6	-25,725
	Spolu	**-0,00508**	**4111,1**	**-81,376**

Literatúra.

ANSYS Release 11.0 Documentation for ANSYS

BubbleDeck Voided Flat Slab Solutions- Technical Manual & Documents, 2008

Cobiax, Brochure

http://www.bubbledeck.com/

http://www.stavcontact.sk/cobiax/index.html

IBRAHIM, ALI, SALMAN, *Flexural capacities of reinforced concrete two-way Bubbledeck slabs of plastic spherical voids,* Diyala Journal of Civil Engineering Sciences, 2013, str. 9-20

MOTA, M., Voided two-way flat slabs, Structures Congress, 2013, str. 1640-1649

SMUTEK, M., *Vyľahčované železobetónové stropné dosky,* Stavebné materiály, 2010

Poďakovanie

Tento príspevok vznikol za finančnej podpory grantovej agentúry MŠ SR, ako projekt VEGA 115721-1369 Mladý výskumník.

Kontaktná adresa:
prof. Ing. Norbert Jendželovský, PhD.
Stavebná fakulta STU, Katedra stavebnej mechaniky, Radlinského 11, 813 68 Bratislava
Slovenská republika

Ing. Kristína Vráblová
Stavebná fakulta STU, Katedra stavebnej mechaniky, Radlinského 11, 813 68 Bratislava
Slovenská republika

AXIAL DIFFUSER DEVELOPMENT USING ANSYS SOFTWARE TOOLS

LUKÁŠ ZAVADIL[1], TOMÁŠ KRÁTKÝ[1], VÍT DOUBRAVA[2]

[1]Centre of Hydraulic Research, [2]SIGMA Research & Development Institute

Abstract: This article describes development of an axial diffuser for a diagonal pump. Based on an older design, a parametric model was created, using DesignModeler and BladeModeler. Then a sensitivity analysis was performed with Design Exploration module. As a result, better hydraulic parameters were achieved.

Keywords: diffuser, flow, efficiency, pump, TBR

1 Introduction

Hydraulic design of an axial diffuser for a centrifugal pump is relatively complicated task. To support the impeller's characteristics, it has to meet multiple criteria. First, the diffuser should guarantee sustaining a wide operational range, especially in the case of a semi-axial pump with variable pitch impeller. Further, the diffuser needs to transform as much of the circumferential velocity component as possible into axial one to function properly. Otherwise the radial velocity increases friction losses in the outlet pipe with elbow and influences pump performance negatively. There is also a choice between constant-thickness and profiled blade and the manufacturing price vs. hydraulic performance trade-off. Theoretical analysis about axial diffusers design is not a purpose of this article, though. Instead, it focuses on showing practical aspects of such hydraulic design realization in ANSYS software tool environment.

2 Axial diffuser design using a parametric model

2.1 Original pump geometry

As an original design, a semi-axial pump with variable pitch impeller and with welded segmented outlet elbow has been chosen. The diagonal-type eight-blade impeller is followed by the axial diffuser with nine constant-thicknes blades and six-segment elbow. At the end of the elbow, the fluid leaves the pump in a direction perpendicular to the axis of rotation. The meridian of the original pump leaves no other choice than making a diffuser by casting.

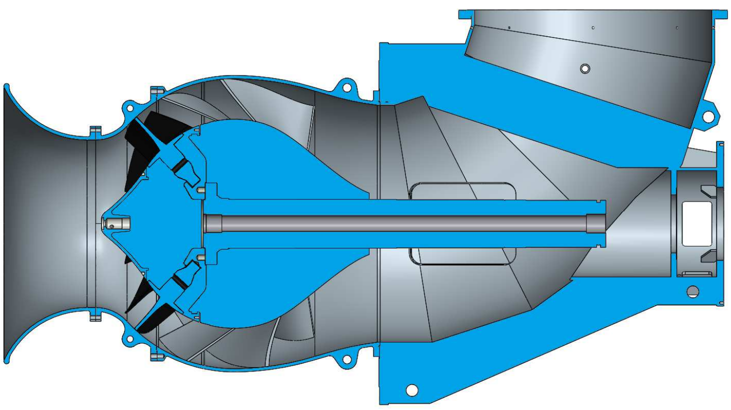

Image 30 – Original pump geometry

2.2 Goal of the new axial diffuser design

Apart from “mere” increased efficiency, another reason for a new design was simplified shape allowing for a lower manufacturing cost. To accomplish this, placing blades between two coaxial cylinders has been chosen as the best option. Meridional dimensions are based on the impeller outlet dimensions and the aim was finding a simplified design while maintaining or improving the hydraulic parameters.

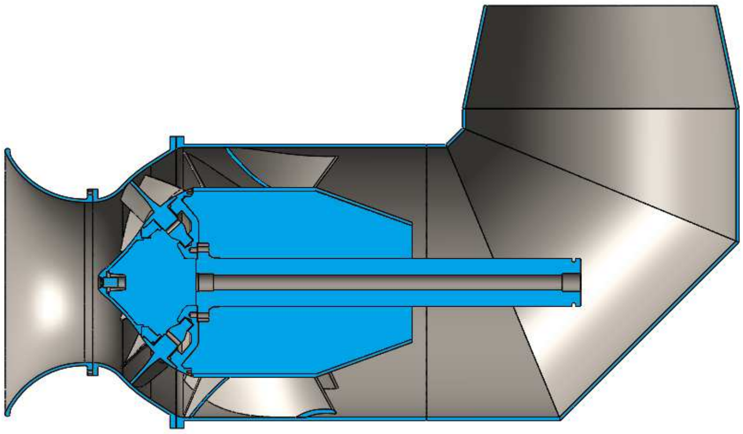

Image 31 – The pump with a new diffuser design

2.3 Parametric model of the axial diffuser

Using ANSYS DesignModeler and ANSYS BladeModeler modules, a parametric model of the meridional cross-section and blades was created. Leading edge and trailing edge positions and theta reference angle were driven by parameters. Blade was defined as a constant-thickness one, on two camberlines, with three values of β angle on each (where β represens the angle between…). In total, there were 13 parameters – a compromise between precise shape variations and computational demands. The mesh was generated in ANSYS Turbogrid and ICEM. Most parts of the mesh remained fixed, only diffuser domain had to be remeshed for each geometry change.

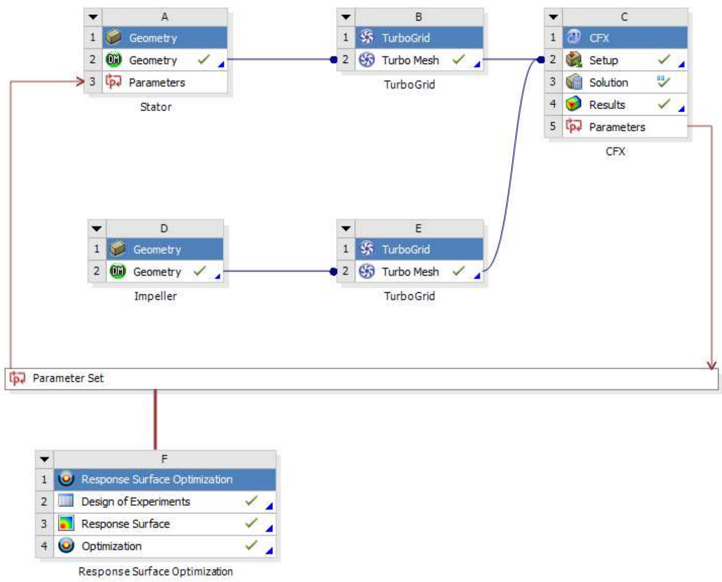

Image 32 – ANSYS Workbench project scheme

2.4 Boundary conditions and solver settings

The boundary conditions can be seen in Image 4. The „*Total Pressure*“ condition was set for the inlet, outlet was defined by the mass flow rate. For modelling the non-stationary interaction between the stator and rotor parts of the pump, two stator/rotor interfaces were placed in the assembled geometry. One interface is between the inlet part and the impeller passage and the second one between the impeller and diffuser passages. The impeller casing was modelled as a counter-rotating wall in the rotating frame.

To reduce computing time as much as possible, only an axisymmetric variant of the original geometry was considered. It was sufficient for different diffuser geometries comparison and allowed for employing the TBR (Transient Blade Row) method offered by CFX. Thanks to this it was possible to consider only one passage – a dramatical reduction in computing time. The periodic boundary conditions had to be set as well.

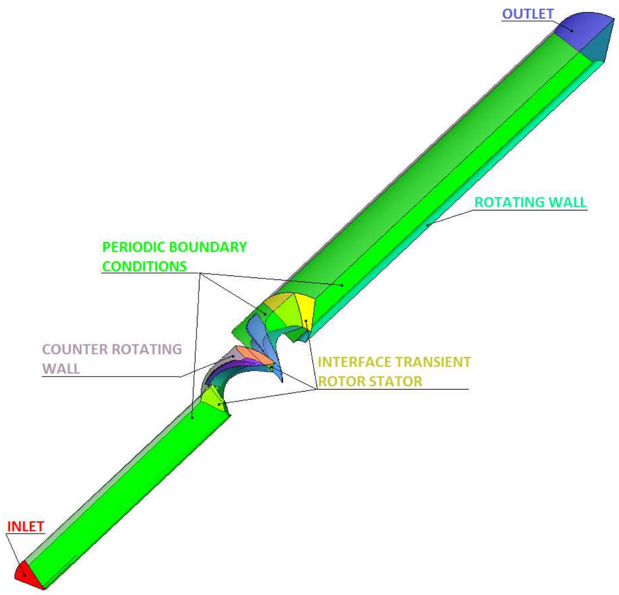

Image 33 – Selected boundary conditions

The whole analysis was performed as fully transient. Timestep was chosen with respect to count of impeller and diffuser blades. It should also represent rotation from 1° to 4°. In our case (8 blades on impeller, 9 blades on Difusser) 8.9.2 = 144 timesteps per a rotation meet these criterion – one timestep represents 2.5° and has this value:

$$\Delta t = \frac{1}{i \cdot n \cdot p} = \frac{1 \cdot 60}{18 \cdot 294 \cdot 8} = 0.00141723\ (s) \tag{21}$$

with *p (1)* being the impeller blades count, *i* (1) being the numer of timesteps per passage and *n* (rpm) the rotor rotation speed.

As a turbulence model, SST (Shear Stress Transport) model has been chosen. It was described by *Menter* and based on two-equation *k-ω* model. In general, SST is the recommended choice for modelling fluids in geometries containing rotating parts.

3 Hydraulic design in ANSYS

The parametric model allows for easy design changes. The best approach to utilize this advantage is to compute enough samples for performing sensitivity analysis. After deciding importance of individual design parameters, the model can be “fine-tuned” with the most important ones.

3.1 Generating samples

For generating optimal samples distribution, DOE (Design Of Experiment) part of ANSYS Response Surface Optimization was used. To utilize our limited number of licences better, we opted for bypassing Workbench. DOE table was used for wbjn scripts and with runwb2 command, def files were generated. This way it was easier to prepare the run at once and avoid reserving meshing and CFX-Pre licences for longer than necessary.

3.2 Computation and results evaluation

Cfx5solve command was employed for running the generated def files. For all of them the same initial res file was used. Some settings were done with ccl files. With cfx5mondata command, the monitored expressions values were extracted from the results in a form of csv files. Then it was easy to load them in Excel and compute two-periods averages.

These average values were then inserted back into Response Surface Optimization and sensitivity analysis could be performed.

4 Computed variants and results

Based on experiences and estimations, the range for parameters was set and a first sample table was generated. After computing the samples, it became obvious that the "optimal" area lied outside of the selected range. Only one of the samples lying on the borders showed good results.

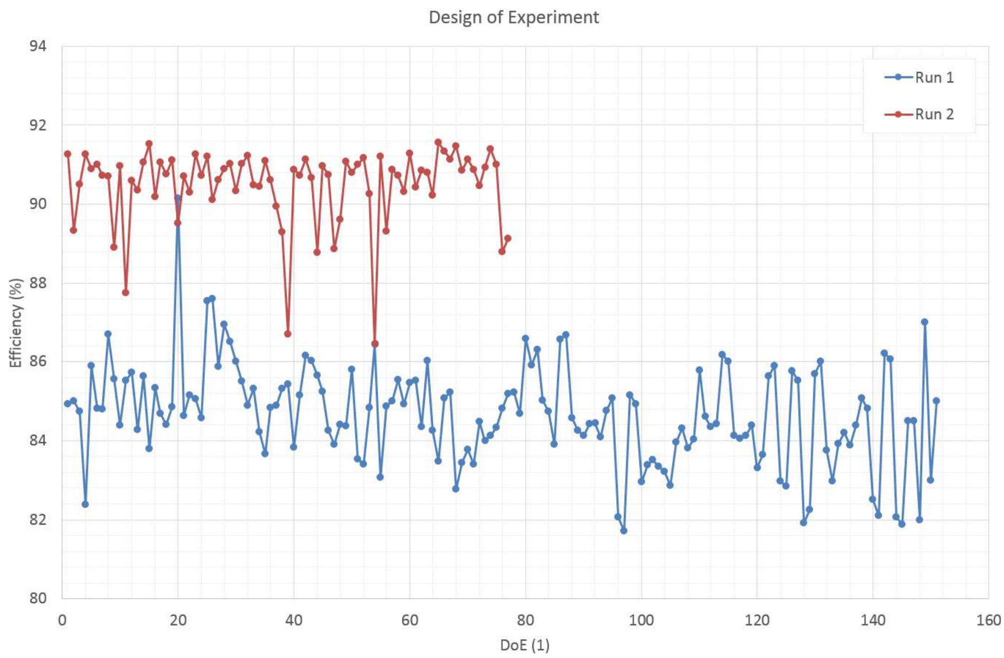

Image 5 – DOE results

Thus, based on the sensitivity analysis results, a better range was selected and another DOE table was generated and computed. This time, the results improved quite a bit. From these results, the best variant has been chosen as a "candidate model".

Also, just for the sake of comparison, the vast computing capacity of CERIT cluster, only available for non-commercial use, has been employed for comparing data obtained by sensitivity analysis with the "real" computed results. As it can be seen in the following figures, with sub-optimal area choice the efficiency-dependance-on parameters can differ a lot from the statistically estimated values.

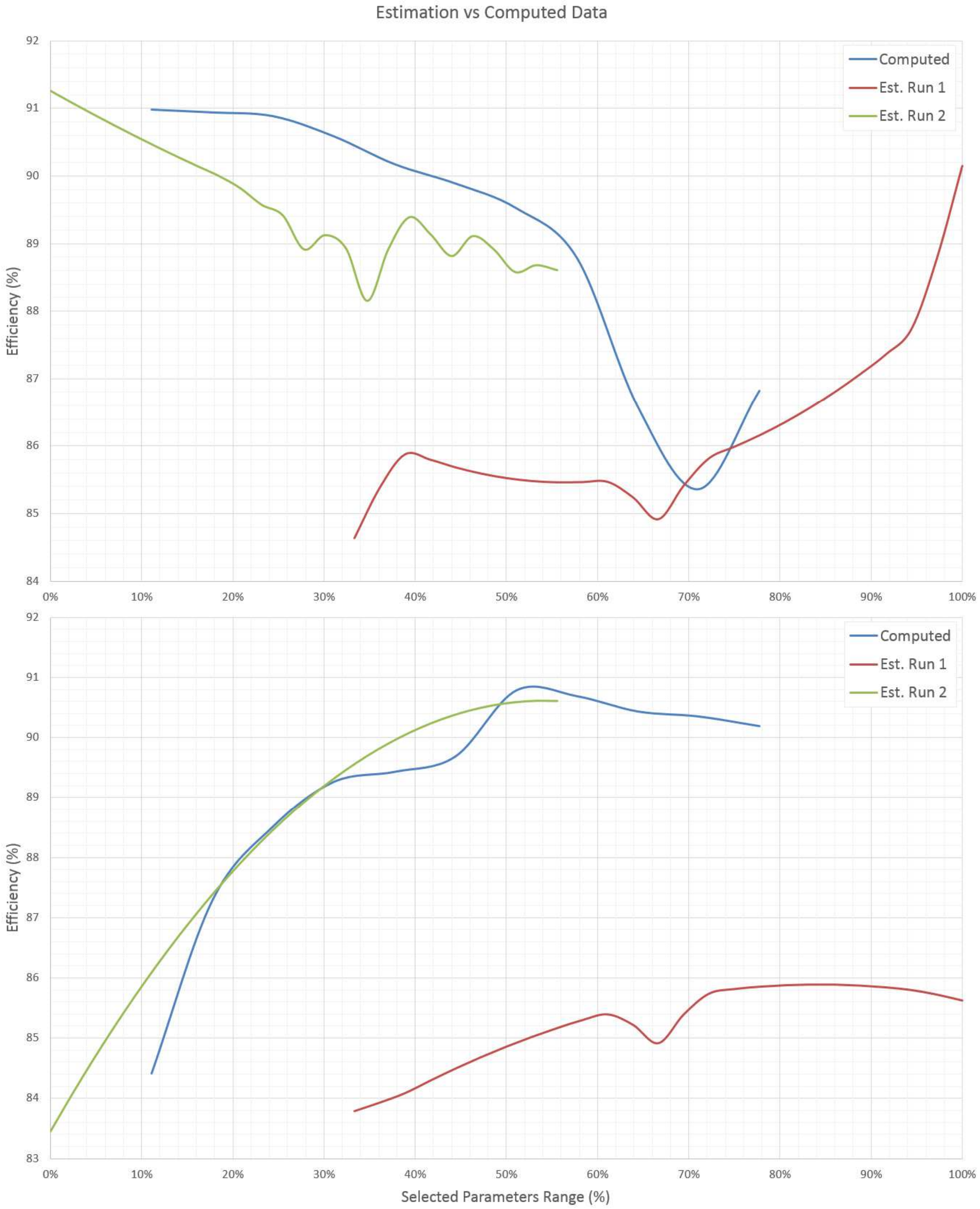

Image 6 – Sensitivity analysis of efficiency/selected parameters dependancy vs computed data

5 Results obtained by numerical simulations

To verify results obtained by the simplified axisymmetric model, the full geometry, including the elbow and suction bell, was assembled for the chosen candidate. The same configuration was used for the original axial diffuser geometry computations, thus it was suitable for a mutual comparison. As can be seen from the results, the goal was met. The optimized diffuser showed better performance then the original one. The improvement was accomplished mostly thanks to decreasing the radial velocity component, which resulted in lower performance losses in both the diffuser and the elbow.

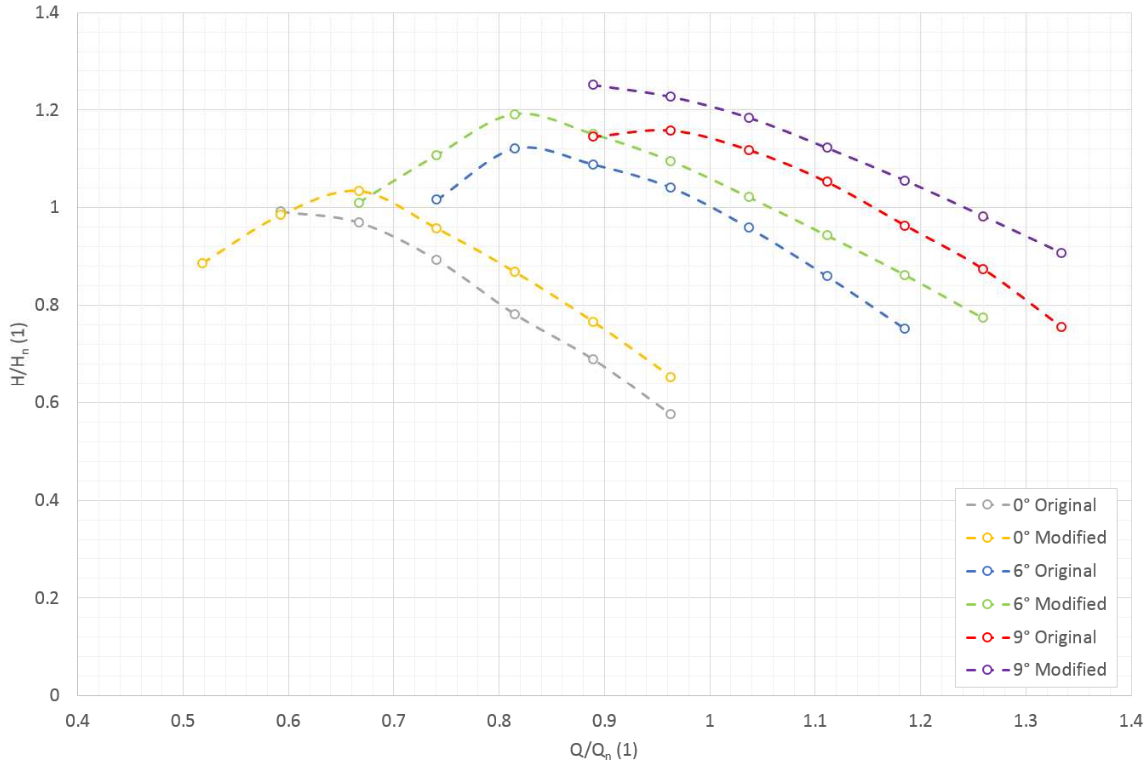

Image 7 – Q-Head characteristics comparison

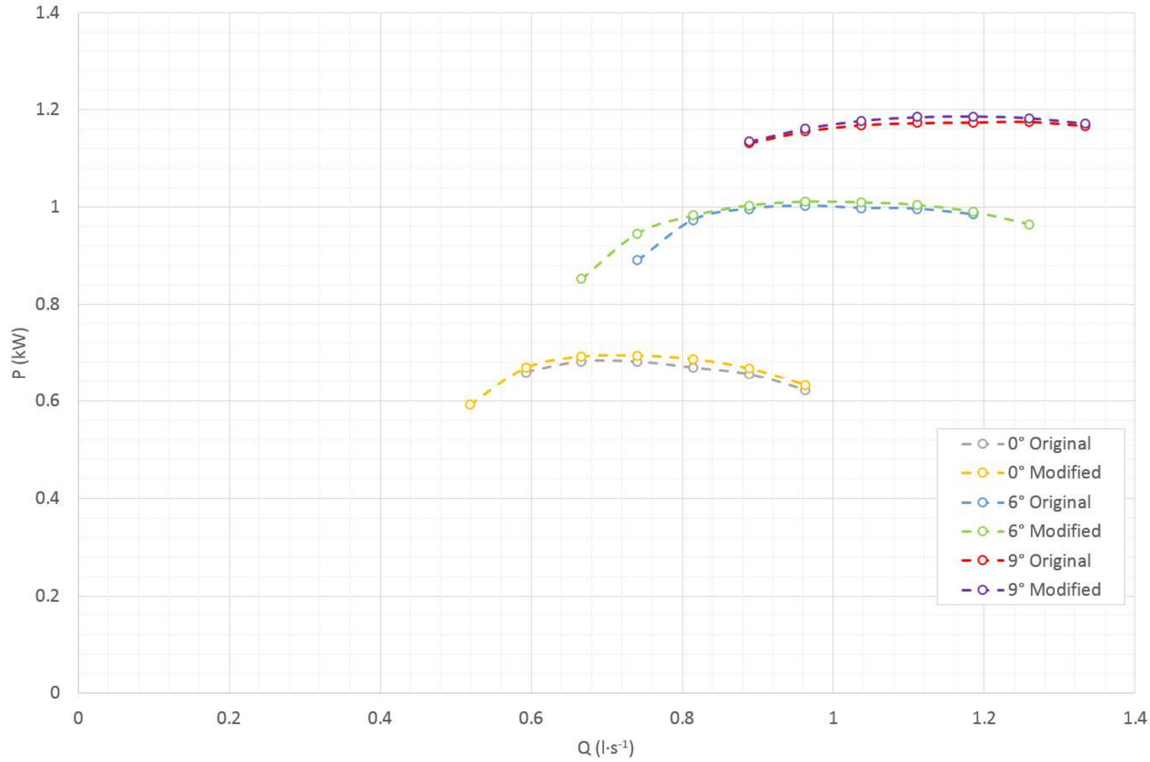

Image 8 – Q-Power characteristics comparison

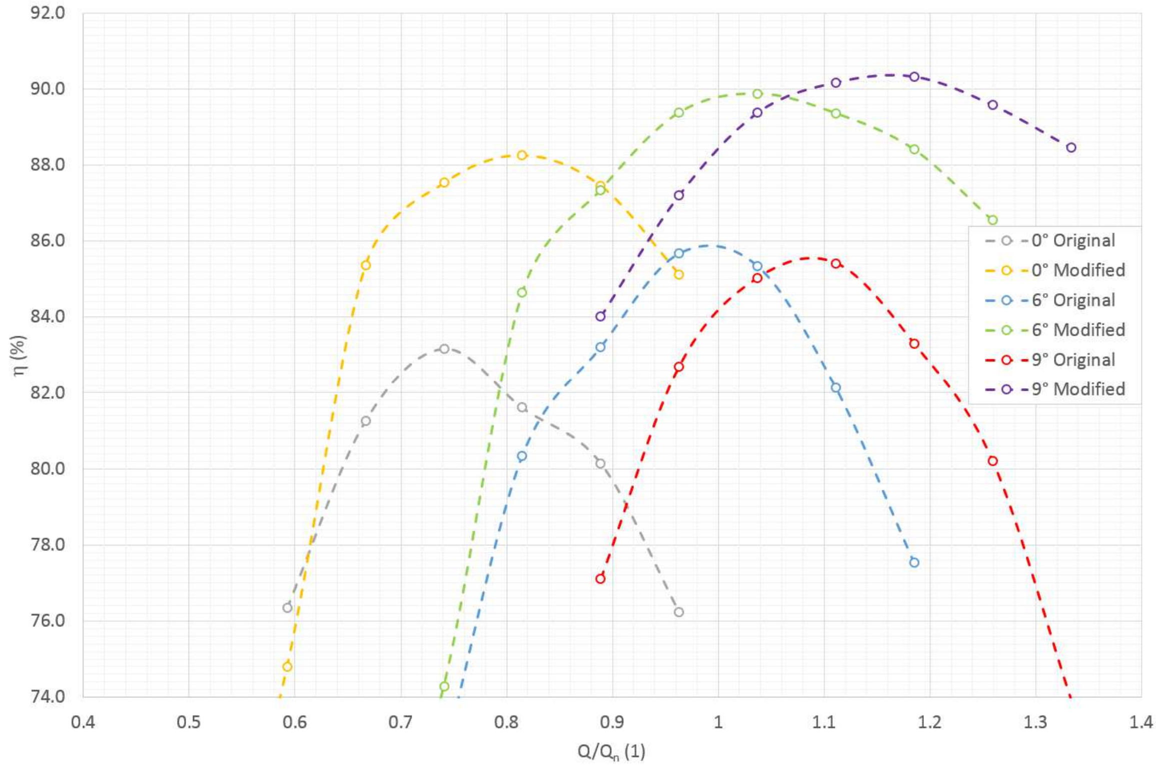

Image 9 – Q-Efficiency characteristics comparison

6 Conclusions

The achieved results clearly show that hydraulic design using ANSYS software tools can be very effective and proficient. Even with our limited experiences in this area we managed to improve the original design in a few weeks. Especially the increased efficiency plays a big role for pumps exceeding 5 MW of power input. There are still many questions left for the future, though. Especially defining the right parameters for the hydraulic design and correct evaluation of the pump performance (cavitation properties, characteristics over wide range of flow rate Q) certainly represent a major challenge.

References

GÜLICH J. F., 2010. *Centrifugal Pumps*. Berlin: Springer, 998 pages. ISBN 978-3-642-12823-3

Acknowledgement

Access to computing and storage facilities owned by parties and projects contributing to the National Grid Infrastructure MetaCentrum, provided under the programme "Projects of Large Infrastructure for Research, Development, and Innovations" (LM2010005), is greatly appreciated.

Contact address:
Ing. Lukáš Zavadil, Ph.D.
Centre of Hydraulic Design s.r.o., Jana Sigmunda 190, Lutín, 783 49

Mgr. Tomáš Krátký
Centre of Hydraulic Design, s.r.o., Jana Sigmunda 190, Lutín, 783 49

Ing. Vít Doubrava
SIGMA Research and Development institute, s.r.o., Jana Sigmunda 79, Lutín, 783 49

Title: 22nd SVSFEM ANSYS Users' Group Meeting and Conference 2014

Date and place of the event: 25th – 27th of June 2014, Jasná, Slovak Republic

Publisher: SVS FEM spol. s r.o., SVS FEM s.r.o., Škrochova 3886/42, 615 00 Brno-Židenice

Editor: doc. Ing. Petr Koňas, Ph.D.

Pages: 172

Edition: 1.

Year: 2014, Brno, Czech Republic

ISBN: 978-80-905525-1-7